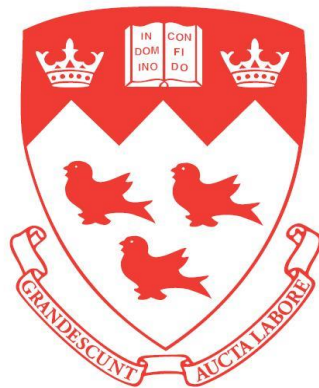


High-Efficiency III-Nitride Tunnel Junction Light-Emitting Nanowire Heterostructures

Sharif Md. Sadaf



Department of Electrical and Computer Engineering
Faculty of Engineering, McGill University, Montréal
June 2017

A thesis submitted to McGill University in partial fulfillment of the requirements of
the degree of Doctor of Philosophy

© Sharif Md. Sadaf 2017

Dedication

This thesis is dedicated to my parents

Abstract

The current III-nitride-based solid-state lighting technology relies on the use of a driver to convert alternating current (AC) to low-voltage direct current (DC) power, a resistive p -GaN contact layer to inject positive charge carriers (holes) for blue light emission, and phosphors to down-convert blue photons into green/red light, which have been identified as some of the major factors limiting the device efficiency, light quality, and cost. In this thesis, we demonstrated that multiple-active region phosphor-free InGaN nanowire white LEDs connected through a polarization engineered tunnel junction can fundamentally address the afore-described challenges. Such a p -GaN contact-free LED offers the benefit of carrier regeneration, leading to enhanced light intensity and reduced efficiency droop. Moreover, through the monolithic integration of p -GaN up and p -GaN down nanowire LED structures on the same substrate, we have demonstrated, for the first time, AC operated LEDs on a Si platform, which can operate efficiently in both polarity (positive and negative) of applied voltage.

We have also demonstrated, for the first time, an n^{++} -GaN/Al/ p^{++} -Al(GaN) backward diode, wherein an epitaxial Al layer serves as the tunnel junction. The stand-alone n - p - n nanowire backward diode showed record low resistivity $\sim 1.5 \times 10^{-4} \Omega \cdot \text{cm}^{-2}$. Additionally, the monolithic metal/Al(GaN) tunnel junction InGaN/GaN nanowire light emitting diodes (LEDs) exhibited a low turn-on voltage (~ 2.9 V), reduced resistance, and enhanced power, compared to nanowire LEDs without the use of Al tunnel junction or with the incorporation of an n^{++} -GaN/ p^{++} -GaN tunnel junction. This unique Al tunnel junction overcomes some of the critical issues related to conventional GaN-based homo or polarization engineered tunnel junction designs, including stress relaxation, wide depletion region, and light absorption, and holds tremendous promise for realizing

low resistivity, high brightness III-nitride nanowire LEDs in the visible and deep ultraviolet spectral range. Moreover, the demonstration and characterization of monolithic integration of metal and semiconductor nanowire heterojunctions provides a seamless platform for realizing a broad range of multi-functional nanoscale electronic and photonic devices.

To date, semiconductor light emitting diodes (LEDs) operating in the deep ultraviolet (UV) spectral range (210-280 nm) exhibit very low efficiency, due to the presence of large densities of defects and extremely inefficient *p*-type conduction of conventional AlGa_N quantum well heterostructures. We have demonstrated that such critical issues can be potentially addressed by using nearly defect-free AlGa_N tunnel junction core-shell nanowire heterostructures. The core-shell nanowire arrays exhibit high photoluminescence efficiency (~80%) in the UV-C band at room temperature. With the incorporation of an epitaxial Al tunnel junction, the *p*-(Al)Ga_N contact-free nanowire deep UV LEDs showed nearly one order of magnitude reduction in the device resistance, compared to the conventional nanowire *p-i-n* device. The unpackaged Al tunnel junction deep UV LEDs (operating at ~275 nm spectral range) exhibit an output power >8 mW and a peak external quantum efficiency ~0.4%, which are nearly one to two orders of magnitude higher than previously reported AlGa_N nanowire devices. We have also studied AlGa_N nanowire LEDs at ~242 nm spectral range. With the use of *n*⁺-Ga_N/Al/*p*⁺-AlGa_N tunnel junction (TJ), the device resistance is reduced by one order of magnitude and the light output power is increased by two orders of magnitude. For unpackaged TJ devices, an output power up to 0.4 mW and EQEs in the range of 0.004-0.006% are measured under pulse biasing condition. Detailed studies further suggest that the maximum achievable efficiency is limited by electron overflow and poor light extraction efficiency due to the TM polarized emission in the UV-C band.

In a nutshell, this dissertation work presents some of the grand challenges of III-nitride optoelectronics, and critically contributes to solve the challenges by novel device design using tunnel junction.

Abrégé

La technologie d'éclairage à l'état solide à base de nitrures du groupe III nécessite l'usage d'un convertisseur de courant alternatif (AC) en courant continu à basse tension (DC), un contact en p-GaN résistive pour injecter des charges positives (trous) pour les émissions de lumière bleue et des luminophores pour convertir les photons bleus en lumière verte ou rouge. Ces facteurs sont limitants à l'efficacité des dispositifs, la qualité de la lumière, et les coûts de production et d'opération. Dans cette thèse, nous avons démontré que les diodes électroluminescentes (LEDs) blanches à base de nanofils en InGaN sans phosphore, à multiples zones actives, et reliées par une jonction tunnel peuvent aborder les défis décrits précédemment. Une telle LED sans contact en p-GaN offre une meilleure intensité lumineuse et une efficacité plus élevée. De plus, grâce à l'intégration monolithique des structures en nanofils de p-GaN avec des polarités opposées sur le même substrat, nous avons démontré, pour la première fois, des LEDs à courant alternatif sur une plateforme de Si, fonctionnant en appliquant une tension négative et positive.

Nous avons également démontré, pour la première fois, une diode inversée en n⁺⁺ GaN / Al / p⁺⁺ Al(Ga)N, dans laquelle une couche épitaxiale en Al sert de jonction tunnel. La diode inversée n-p-n offre une faible résistivité record d'environ $1,5 \times 10^{-4} \Omega \cdot \text{cm}^{-2}$. De plus, les diodes électroluminescentes en Al(Ga)N avec la couche métallique ont une faible tension d'enclenchement ($\sim 2,9$ V), une résistance réduite et une puissance plus élevée par rapport aux LEDs à base de nanofils sans l'usage de la jonction tunnel d'Al ou l'incorporation d'une jonction tunnel n⁺⁺ GaN / p⁺⁺ GaN. Cette jonction tunnel d'Al unique peut résoudre certains des problèmes critiques liés aux jonctions tunnel conventionnelles à base de GaN, y compris la relaxation du stress matériel, une grande région d'épuisement et l'absorption de la lumière. Elles promettent la

réalisation de LEDs à faible résistivité, meilleure luminosité dans la gamme spectrale visible et ultraviolette. De plus, la démonstration et la caractérisation de l'intégration monolithique de nanofils à base de métaux et semi-conducteurs constituent une plateforme directe pour la réalisation d'une panoplie de dispositifs électroniques et photoniques multifonctionnels à l'échelle nanométrique.

À ce jour, les LEDs semi-conductrices fonctionnant dans la gamme spectrale ultraviolette profonde (UV) (210-280 nm) souffrent d'une très faible efficacité, en raison de la présence de grandes densités de défauts et d'une transmission de type p extrêmement inefficace pour les puits quantiques conventionnels en AlGa_N. Nous avons démontré que ces problèmes critiques peuvent être résolus en utilisant des tunnels jonctions de nanofils en AlGa_N avec une hétérostructure core-shell libres de défauts matériels. Les réseaux de ces nanofils présentent une efficacité élevée de photoluminescence (~ 80%) dans la bande UV-C à température ambiante. Grâce à l'incorporation d'une jonction tunnel épitaxiale à base d'Al, les LEDs ultraviolettes profondes à p-(Al)Ga_N libres de contacts montrent une réduction d'un ordre de grandeur de la résistance par rapport aux dispositifs p-i-n classiques à nanofils. Les LEDs UV non-encapsulées avec jonction tunnel en Al (fonctionnant à une portée spectrale d'environ 275 nm) présentent une puissance de sortie > 8 mW et une efficacité quantique externe d'environ 0,4%, soit près d'un à deux ordres de grandeur supérieurs à celles des dispositifs de nanofils en AlGa_N obtenus dans le passé. Nous avons également étudié les LEDs à nanofils d'AlGa_N ayant une portée spectrale d'environ 242 nm. Avec l'usage de la jonction tunnel n⁺ Ga_N / Al / p⁺ AlGa_N, la résistance des dispositifs est réduite d'un ordre de grandeur et la puissance de sortie lumineuse augmente de deux ordres de grandeur. Pour les dispositifs à jonction tunnel non-encapsulés, une puissance de sortie jusqu'à 0,4 mW et une efficacité quantique externe dans la plage de 0,004 à 0,006% sont mesurées avec une source de

courant à pulsations. Des études détaillées suggèrent en outre que l'efficacité maximale réalisable est limitée par un débordement (overflow) d'électrons et une faible efficacité d'extraction de la lumière en raison de l'émission polarisée TM dans la bande UV-C.

En bref, cette thèse présente certains des grands défis des dispositifs optoélectroniques en III-nitrures et contribue de manière critique à résoudre ces défis grâce à la conception de nouveaux dispositifs à l'aide de la jonction tunnel.

Acknowledgement

First and Foremost, I thank the Almighty, Allah for giving me the opportunity, strength, knowledge, and perseverance to pursue my doctoral study. I express my sincere gratitude to my advisor Prof. Zetian Mi for giving me the chance to work in the exciting field of III-nitride nanowire devices. It was great working with him as his Ph.D. student during the last five years. He has created a well-equipped and productive research environment at McGill University. Over the years, he had provided all the resources for his students to work on different challenging projects. I have learned how to identify critical research problems and write manuscripts effectively from him. Throughout this dissertation work, I have got tremendous support from him starting from conceiving the idea, designing the experiments and technical writing. He kept his faith in me even at the darkest part of my research and gave me intellectual freedom. His devotion to III-nitride nanowire research is incredible. I would like to thank my co-adviser Prof. Ishiang Shih for his comments and suggestions on the thesis work. I sincerely thank Prof. Thomas Szkopek for his insightful comments on my work and stimulating discussions. He has been an extremely reliable source of semiconductor device physics knowledge. Prof. Shih and Prof. Thomas also graciously allowed me to use their measurement facilities on numerous occasions.

Dr. H.P.T Nguyen deserves a big thank, and I am grateful to him for teaching me the MBE growth and device fabrication. Dr. Hieu laid a solid foundation at McGill University for nanowire LED research, and from which my work presented in this dissertation could have smoothly followed. I thank Dr. Yong-Ho for his support throughout, we attended many growths and TEM sessions together. I learned the aesthetics and details of TEM imaging from him. Dr. Yong-Ho worked closely with me for different projects and delicately taught me schematic drawing. He has also

helped me to draw schematics presented in this thesis. I am also grateful to Dr. S. Zhao for UV LED growth. I am indebted to Dr. Ashfiqua Connie, as she is the one who explained every aspect of visible and UV LED device characterizations lucidly, and most importantly she was there whenever I needed her help. Also, she explained some of the critical details of device characterizations that could not be grasped so easily without her explanation and experience. I would like to thank Dr. Junjie Kang, during his stay at McGill he helped to do AC LED measurement, and LED encapsulation. I have had the privilege to work with the most talented and hard-working crew at McGill university. Every result presented in this dissertation was accomplished with the help of my fellow labmates and cleanroom staffs. I thank Dr. G. Kibria, Dr. S. Arafin, Dr. Lu Li , Dr. Q. Wang , Dr. K. H Li, Dr. Hadi, Dr. Mehrdad, Dr Omid, Dr. S. Fan. Dr. Bandar, Dr. Sheng, Dr. Yichen, Dr. Binh, Dr. Ikwhang Chang, Xianhe Liu, Renjie Wang, Yuanpeng Wu, Srinivas Vanka, Nhung Tran, Roksana Rashid, Yongjie Wang, Pegah Gamari, and F. Choudhury. I am grateful to Dr. Matthieu Nannini, as he taught me some critical aspects of semiconductor processing. I thank other cleanroom staffs, including Donald Berry, Dr. Lino Eugene, Alireza Mesger, Dr. Sasa Ristic, Jun Li, Dr. Zhao Lu, Robert Gagnon and Christophe Clemente (UDeM) for their support. I thank Jean-Phillipe Masse (UDeM) and David Liu for TEM imaging. I thank Ibrahim Fakih for helping me in low temperature measurements. A very special thanks to David Laleyan for translating the abstract into French. I am grateful to Md. Samiul Alam for critically proofreading my thesis. I sincerely thank the Department of Electrical and Computer Engineering at McGill University.

I am grateful to my parents, who have provided me with high-quality education, moral and emotional support in my hard and good times. I am also grateful to my sister and other family members who have supported me along the way. I thank my friend Md. Sazzad Hossain and other

friends at McGill University who have supported me a lot. I sincerely thank my wife Shawana Khan for her support, encouragement, patience, and love. She made tremendous sacrifice for the sake of my research. Albeit, the Ph.D. study would have been undoubtedly more difficult without her support. On the whole, she has been an excellent source of my strength ever since we tied the knot.

Last but no means the least, I thank Natural Sciences and Engineering Research Council of Canada and the Fonds de recherche sur la nature et les technologies for their financial support on this research.

Contribution of Authors

The candidate and Prof. Zetian Mi worked together for this dissertation starting from conceiving the idea, designing the experiments, and writing the manuscripts. The full dissertation, however, includes the contributions of many present and past group members at MBE lab, McGill University. All the samples for MBE growth were prepared by the candidate. The MBE growths of tunnel junction dot-in-a-wire InGaN/GaN visible LED were performed by the candidate, Dr. H.P.T Nguyen and Dr. Y.-H Ra. The growths of tunnel junction double heterostructure AlGaIn-based UV LED were performed by the candidate and Dr. S. Zhao. The photoluminescence experiments were performed by the candidate together with Dr. A. Connie, Dr. J. Kang, Y. Wu, X. Liu and Dr. S. Zhao. The SEM imaging was carried out by the candidate. The XRD results analyses were performed by the candidate and Mr. Christophe Chabanier at INRS. The TEM analyses were performed by the candidate, Jean Phillippe Masse (at UDeM) and Dr. David Liu at Facility for Electron Microscopy Research (FEMR), McGill University. All the device fabrications were carried out by the candidate at McGill Nanotools Microfab. All the device electrical characterizations were performed by the candidate. All the electroluminescence characterizations were carried out by the candidate and Dr. A. Connie. Alternating current (A.C) LED measurements were carried out by the candidate and Dr. J. Kang. The absolute light output power measurements for visible/deep LEDs were carried out by the candidate, Mr. Y. Woo and Dr. S. Zhao.

Table of Content

Abstract.....	i
Abrégé	iv
Contribution of Authors.....	x
Table of Content.....	xi
List of Figures.....	xviii
List of Tables	xxviii
List of Acronyms.....	xxix
Chapter 1	1
Introduction.....	1
1.1 Solid-State Lighting	1
1.1.1 LED Basics	2
1.1.2 White LED	3
1.2 Current Status of III-nitrides based LEDs.....	4
1.3 LED History	6
1.4 Challenges in Current III-Nitride Photonics Research.....	9
1.4.1 Polarization Fields	9
1.4.2 Green Gap	13
1.4.3 Efficiency droop.....	14

1.4.4	Defects and Dislocations.....	15
1.4.5	Auger Recombination	16
1.4.6	Electron overflow.....	17
1.4.7	Poor Hole Transport and Hole Injection Efficiency	18
1.4.8	Issues with <i>p</i> -doping	18
1.4.9	Issues with Resistive <i>p</i> -Al(Ga)N Contact.....	20
1.4.10	Issues with Substrates	20
1.5	Ultraviolet LEDs	22
1.5.1	Ultraviolet LEDs: The Challenges.....	23
1.5.2	Crystal Quality and Internal/External Quantum Efficiency.....	24
1.5.3	Carrier Injection and Operation Voltage.....	24
1.5.4	Light Extraction	25
1.6	Nanowires.....	26
1.7	III-nitride Tunnel Junctions.....	28
1.7.1	Tunnel Junctions in LEDs.....	29
1.7.2	Polarization Engineered Tunnel Junction	30
1.8	Organization of the Thesis	34
Chapter 2		37
MBE Growth, Processing and Characterization of InGaN/Al(Ga)N Nanowire Heterostructures		37

2.1	III-nitride Nanowire Growth by MBE	37
2.1.1	GaN Nanowire Growth	39
2.1.2	Nanowire Density, Coalescence and Defects	45
2.1.3	Growth of InGaN/Al(GaN) dot-in-a-wire structure.....	47
2.1.4	Si-/Ge-doped GaN Base.....	47
2.1.5	InGaN/GaN Dots (active region) Growth.....	48
2.1.6	Mg-doped AlGaN Blocking Layer and Core-Shell Nanowire	49
2.1.7	Mg-doped GaN Cap.....	50
2.1.8	n^{++} -GaN/InGaN/ p^{++} GaN tunnel junction growth.....	50
2.1.9	n^{++} -GaN/Al/ p^{++} GaN tunnel junction growth	51
2.2	UV Nanowire LED Growth	51
2.3	Characterizations of Nanowires	53
2.3.1	Characterization of as grown nanowires by SEM.....	53
2.3.2	Characterization of as-grown nanowires by TEM	53
2.4	Device Fabrication	54
2.4.1	Surface Planarization	55
2.4.2	Device Contact and subsequent processing	57
2.4.3	UV LED Fabrication.....	58
2.5	Photoluminescence Study	59
2.5.1	Band-to-Band Direct Transition	60

2.5.2	Excitonic Transition.....	60
2.5.3	Band-Edge to Donor/Acceptor Transition.....	61
2.5.4	Donor-Acceptor Pair Transition.....	61
2.5.5	Non-Radiative Recombination.....	61
2.6	Electroluminescence Study.....	62
2.6.1	IQE and EQE.....	62
2.7	Summary.....	64
Chapter 3	65
Multiple-Active Region InGaN/GaN Tunnel Junction Nanowire White-Light Emitting		
Diodes..... 65		
3.1	Design and Band diagram.....	66
3.2	Growth and Characterization.....	69
3.3	Fabrication Process.....	72
3.4	Current-Voltage Characteristics.....	73
3.5	Electroluminescence and Light Output Characteristics.....	75
3.6	Multiple Active Region LEDs.....	77
3.7	Summary.....	79
Chapter 4	80
Alternating-Current InGaN/GaN Nanowire White-Light Emitting Diodes: An Application		
of Nitride Tunnel Junction..... 80		

4.1	Growth and Characterization	81
4.2	Summary	84
Chapter 5		85
Molecular Beam Epitaxial Growth and Characterization of Monolithic <i>n</i>-GaN/<i>Al</i>/<i>p</i>-AlGaN		
Nanowire Heterostructure		85
5.1	Design and SEM.....	88
5.2	MBE Growth	89
5.3	TEM Characterizations	90
5.4	X-ray Diffraction Analysis.....	94
5.5	Summary	96
Chapter 6		97
Record Low Resistance AlGaN Nanowire Backward Diode for High Efficiency III-Nitride		
Photonic Devices.....		97
6.1	Design and Growth.....	99
6.2	Schematic Band Diagram.....	101
6.3	Device Fabrication	103
6.4	Current-Voltage Characteristics	103
6.5	Summary	109

Chapter 7	110
Monolithically Integrated Metal/Semiconductor Tunnel Junction Nanowire Light Emitting Diodes	110
7.1 Design and Growth.....	112
7.2 Characterization of Nanowire Heterostructure	114
7.3 Device Fabrication	117
7.4 Electrical and Optical Characterizations	118
7.5 Summary	121
Chapter 8	122
An AlGa_N Core-Shell Tunnel Junction Nanowire Light Emitting Diode Operating in the Ultraviolet-C Band.....	122
8.1 Design and Growth.....	124
8.2 Photoluminescence Characterization	126
8.3 Structural Characterization.....	128
8.4 Device Fabrication and Electrical Characterization.....	130
8.5 Electroluminescence Characterization:	132
8.6 Polarization Measurement.....	134
8.7 Summary	135
9 Chapter 9.....	137

Sub-milliwatt AlGa_N Nanowire Tunnel Junction Deep Ultraviolet Light Emitting Diodes on Silicon Operating at 240 nm	137
9.1 Design, Growth and Optical Characterization	138
9.2 Device Fabrication and Electrical Characterization.....	140
9.3 Electroluminescence Characterization	141
9.4 Optical Polarization.....	143
9.5 Output Power and EQE	144
9.6 Summary	146
10 Chapter 10	147
Conclusions and Future Works	147
10.1 Summary	147
10.2 Suggested Future Works	149
10.2.1 Self-organized Al(Ga) _N /Al _N Quantum Dots/Discs in Nanowires	149
10.2.2 Tunnel Junction III-Nitride Visible Nanowire Laser Diodes	151
10.2.3 Tunnel Junction III-Nitride UV Nanowire Laser Diodes	153
10.2.4 Tunnel Junction III-nitride Solar Cells	154
10.2.5 Ga _N Nanowire Vertical Transistor on Si Substrate	156
10.2.6 Selective Area Growth of Tunnel Junction InGa _N /Al(Ga) _N Core-Shell LEDs...	158
11 List of Publications	160
12 Bibliography	164

List of Figures

Figure 1.1: A schematic illustration of a double-heterostructure LED in operation powered by a battery	2
Figure 1.2: Schematic energy band diagram structure for a (a) homojunction LED and (b) double-heterostructure LED	3
Figure 1.3: Different ways of generating white light from InGaN LEDs: (a) combination of red, green, and blue LEDs, (b) UV GaN LED with three phosphors, and (c) blue InGaN LED with yellow phosphor	3
Figure 1.4: In-plane lattice parameters and band gaps for GaN(0 0 0 1) and its related alloys. The lattice parameters and band gaps for common substrates, 4H-SiC (0 0 0 1), 6H-SiC (0001) and Si (1 1 1), are also included	4
Figure 1.5 LED prediction until 2035	5
Figure 1.6: Summary of key contributions to the efficient blue LEDs	8
Figure 1.7: Origin of polarization in GaN due to non-centro symmetry and associated electric field	10
Figure 1.8: (a) Effect of spontaneous and piezoelectric polarization on the band diagram of InGaN/GaN MQW (b) and (c) origin of positive and negative sheet charge at the last GaN barrier and EBL layer	13

Figure 1.9: Maximum external quantum efficiency (EQE) of different commercial nitride and phosphide LEDs(spheres), illustrating the green gap problem.....	14
Figure 1.10: (a) Plot of the external quantum efficiency (EQE) of commercial III-nitride LED devices, measured using EL at 350 mA b) Plot of the internal quantum efficiency (IQE) of III-nitride QW structures, measured using PL, versus emission wavelength.....	15
Figure 1.11: The wide range of important applications of UV LEDs.....	22
Figure 1.12: Reported external quantum efficiencies for AlGa _N , InAlGa _N , and InGa _N quantum well LEDs emitting in the UV spectral range.....	23
Figure 1.13: Variation of the critical thickness of the misfitting layer growing on a top of a nanowhisker as a function of whisker radius.....	27
Figure 1.14: Schematic drawing of the crystal structure of wurtzite Ga-face and N-face Ga _N	31
Figure 1.15: Polarization induced sheet charge density and directions of the spontaneous and piezoelectric polarization in Ga- and N-face strained and relaxed AlGa _N /Ga _N heterostructures.....	32
Figure 2.1: (a) Tilted SEM image of a Ga _N compact film (b) Tilted SEM image of Ga _N nanocolumn (c) growth phase diagram of Ga _N at a fixed N ₂ plasma condition (flow and power).	40
Figure 2.2 HRTEM images collected on dedicated samples grown for 7 and 16 min, revealing the following respective Ga _N island shapes at the onset of the nucleation process: spherical cap-shaped island and NW. The NWs are hexahedral. The shape of spherical caps is outlined for the sake of clarity .	42

Figure 2.3 : (a) Kinetics of the atoms on the substrate during the nucleation process and early stage of nanowire growth. (b) Different diffusion process and Ga impingement process related to the growth of GaN nanowire 43

Figure 2.4: Schematic of the nanowire growth process including adatom adsorption, desorption, diffusion and nucleation by MBE process 44

Figure 2.5: HAADF image of self-organized QD formation 48

Figure 2.6: Surface planarization by polyimide resist layer of different height/shape nanowires. 54

Figure 2.7: Step by step nanowire LED fabrication process. 58

Figure 2.8: Different donor-acceptor recombination and other transition process 60

Figure 3.1: Schematic and energy band diagram of tunnel junction (TJ) integrated dot-in-a-wire LEDs. (a) Schematic illustration of the dot-in-a-wire LEDs, including LEDs A, B, C and D. (b) Schematic representation of the fabricated large area nanowire LEDs. (c) Simulated energy band diagram of GaN/InGaN/GaN tunnel junction showing carrier generation and injection process under reverse bias. 67

Figure 3.2: (a) Equilibrium energy band diagram of three reversely biased tunnel junctions connected in series. Multiple quantum dots are incorporated in each active region. The inset shows the radiative recombination rate in the active region. (b) Simulated electron and hole concentration inside the tunnel junctions and active regions. 68

Figure 3.3: 45° tilted SEM images of conventional dot-in-a-wire LED A (left) and SAR tunnel junction dot-in-a-wire LED B (right). Scale bar represents 500 nm..... 70

Figure 3.4: Structural characterization by SEM, TEM and photoluminescence. (a) A 45° tilted scanning electron microscopy (SEM) image of MAR TJ dot-in-a-wire LED. The scale bar denotes

1 μm . (b) Room temperature photoluminescence spectra of LED C and LED D. (c) HR-TEM shows MAR TJ dot-in-a-wire LED structure. (d) High angle annular dark field (HAADF) image showing the MAR tunnel junction dot-in-a-wire LEDs with the presence of tunnel junctions and quantum dot active regions. EDXS line profile along c-axis (growth direction) showing In peaks in the tunnel junctions and Ga dips and In peaks in dot region (lower panel). (e) EDXS elemental mapping image of tunnel junction region shows the In, Ga, and N variation. Scale bar presents 30 nm. 71

Figure 3.5: Current-voltage (I-V) characteristics of tunnel junction dot-in-a-wire LEDs. (a) I-V characteristics of LEDs A, B, and C measured at room temperature. (b) Temperature-dependent I-V characteristics of LED C. 73

Figure 3.6: (a) Simulated I-V comparison of LED B and LED C. (b) Simulated L-I comparison of LED B and LED C. 74

Figure 3.7: Electroluminescence characteristics of tunnel junction dot-in-a-wire LEDs. (a) Light-current (L-I) characteristics of LEDs A, B and C. (b) Relative external quantum efficiency (EQE) of LEDs A, B C. The inset shows the relative EQE comparison as a function of input power measured at room temperature. 75

Figure 3.8: Electroluminescence spectra of LED A, B, and C. 76

Figure 3.9: HAADF image of tunnel junction MAR nanowire LED structure (LED D) and EDXS analysis showing In concentration variations in the device active regions. 77

Figure 3.10: Phosphor-free white light emission of tunnel junction MAR dot-in-a-wire LEDs. (a) Electroluminescence spectra LED D measured under different injection currents. The inset shows the device optical image. (b) Correlated color temperature (CCT) properties. 78

Figure 3.11: (a), SEM image of LED D. (b), I-V characteristics of LED D. (c) L-I characteristic of LED D..... 79

Figure 4.1: Alternating current tunnel junction dot-in-a-wire LED arrays. (a) Two-step selective area growth of *p*-GaN up and *p*-GaN down AC nanowire LEDs on Si substrate. *p*-Up nanowire LED arrays were first grown on the opening areas of SiO_x coated Si substrate. Then the SiO_x and the nanowires on top were selectively removed using chemical etching. The *p*-up nanowire LED structures were then covered with SiO_x and additional opening areas were created prior to the growth of the *p*-down nanowire LED structures. Subsequently, the SiO_x and the nanowires on top were selectively etched. This leads to the formation of *p*-up and *p*-down nanowire LED arrays on the same Si chip. (b), (c) Device schematics. (d) 45° tilted SEM images of as grown *p*-GaN up and *p*-GaN down nanowire LED structures. (e) Optical micrograph of green light emitting nanowire LED arrays on Si under AC biasing conditions..... 82

Figure 4.2: SEM image of as grown AC nanowire LED arrays on a Si substrate. The scale bar represents 50 μm..... 83

Figure 4.3: I-V characteristics of *p*-GaN up (left) *p*-GaN down (right) LEDs on Si..... 84

Figure 5.1: (a) Schematic diagram of different epitaxial Al/Al(Ga)N nanostructures grown on Si substrate. (b) An SEM image of nanostructure A taken with a 45° angle..... 88

Figure 5.2: (a) High-resolution transmission electron microscopy (HR-TEM) image of nanostructure B. 90

Figure 5.3: (a) STEM image of a full nanostructure C (thick Al) (b) and (c) EDXS point analysis of the Al layer (point B in b) and *p*-AlGa_{0.5}N region (point C), *n*-Ga_{0.5}N region (point A) and Al layer in sidewall region (point D). 92

Figure 5.4: (a) STEM image of a full nanostructure A (thin Al) (b) and (c) EDXS point analysis of the tunnel junction, Al layer (point B in b) and p -AlGa_{0.85}N region (point C), n -Ga_{0.15}N region (point A) and Al layer in sidewall region (point D).....92

Figure 5.5: (a) STEM image of a nanostructure C (thick Al layer) and different line profile analyses along the nanowire length and lateral dimension.....93

Figure 5.6: Symmetric $\theta/2\theta$ XRD scan in Bragg reflection.....95

Figure 6.1: (a) Schematic diagram of four different composition AlGa_{0.85}N backward diodes (BD A, BD B, BD C, BD D) (b) An SEM image of AlGa_{0.85}N backward diode taken with a 45° angle..... 99

Figure 6.2: Schematic energy band diagram of (a) n^{++} -Ga_{0.15}N/Al/ p^+ -Al_{0.15}Ga_{0.85}N backward diode structures (BD A) (b) n^{++} -Ga_{0.50}N/Al/ p^+ -Al_{0.50}Ga_{0.50}N backward structure (BD B) (c) n^+ -Al_{0.50}Ga_{0.50}N /Al/ p^+ -Al_{0.50}Ga_{0.50}N backward structure (BD C) (d) n^+ -AlN/Al/ p^+ -AlN backward structure (BD D). 102

Figure 6.3: a) I-V characteristics comparison of n^{++} -Ga_{0.15}N/Al/ p^+ -Al_{0.15}Ga_{0.85}N backward diode structure (BD A) and n^{++} -Ga_{0.50}N/Al/ p^+ -Al_{0.50}Ga_{0.50}N (BD B), the inset shows the I-V plots in semi-log scale. b) Specific resistance vs Current density plot of n^{++} -Ga_{0.15}N/Al/ p^+ -Al_{0.15}Ga_{0.85}N backward diode structure (BD A)..... 104

Figure 6.4: I-V characteristics comparison of n^+ -Al_{0.50}Ga_{0.50}N /Al/ p^+ -Al_{0.50}Ga_{0.50}N backward structure (BD C) and n^+ -AlN/Al/ p^+ -AlN backward structure (BD D), the inset shows the I-V plots in semi-log scale. 107

Figure 6.5: (a) Temperature dependent I-V characteristics comparison of n^{++} -Ga_{0.15}N/Al/ p^+ -Al_{0.15}Ga_{0.85}N backward diode structure (BD A). 108

Figure 7.1: Schematic energy band diagram of (a) conventional p^{++}/n^{++} GaN tunnel junction and (b) n^{++} -GaN/Al/ p^{++} -GaN tunnel junction structures. 110

Figure 7.2: (a) Schematic diagram of Al tunnel junction (TJ) dot-in-a-wire LED (LED A), n^{++} -GaN/ p^{++} -GaN tunnel junction LED (LED B), conventional nanowire LEDs without the use of any tunnel junction (LED C) grown on a Si substrate. (b) PL spectra of Al TJ dot-in-a-wire LEDs (LED A) measured at room temperature. (c) An SEM image of Al-interconnect TJ dot-in-a-wire LEDs (LED A) taken with a 45° angle. 114

Figure 7.3: (a) STEM image of a single Al tunnel nanowire LED structure (LED A). (b) HAADF (left) and EDXS line profile (right) across the InGaN/GaN quantum dots. (c) HR-TEM image of the Al tunnel junction (left) and EDXS point profiles (right) of the tunnel junction region and p -GaN region. 115

Figure 7.4: I-V characteristics of the Al tunnel junction dot-in-a-wire LED (LED A), n^{++} -GaN/ p^{++} -GaN tunnel junction LED (LED B), and conventional nanowire LED without the use of any tunnel junction (LED C). 117

Figure 7.5: (a) L-I characteristics of the Al tunnel junction (TJ) dot-in-a-wire LED (LED A), n^{++} -GaN/ p^{++} -GaN tunnel junction LED (LED B), and conventional nanowire LED without the use of any tunnel junction (LED C). (b) Electroluminescence (EL) spectra of the Al tunnel junction dot-in-a-wire LED (LED A) under pulsed biasing condition (10% duty cycle). Inset: the optical micrograph of the Al tunnel junction dot-in-a-wire LED (LED A) showing strong green light emission. 119

Figure 7.6: Electroluminescence (EL) spectra of LED B and LED C under pulsed biasing condition (10% duty cycle). 120

Figure 7.7: Relative external quantum efficiency (EQE) of the Al-tunnel junction nanowire LEDs (LED A) measured under CW biasing condition..... 120

Figure 8.1: (a) Schematic diagram of Al tunnel junction (TJ) AlGa_N UV LED (LED A). (b) Schematic diagram of standard *p-i-n* AlGa_N UV LED without the use of any tunnel junction (LED B). (c) An SEM image of nanowires in an Al TJ AlGa_N UV LED structure taken with a 45° angle. 125

Figure 8.2: (a) Room temperature photoluminescence spectrum, and (b) Internal quantum efficiency vs. excitation power measured at room temperature for the AlGa_N tunnel junction nanowire LED heterostructure. The inset shows the PL spectra measured under an excitation power of 0.13 mW at 293 K and 15 K..... 127

Figure 8.3: (a) STEM image of a single Al tunnel junction AlGa_N UV LED structure (LED A). (b) STEM image of the Al-tunnel junction. (c) EDXS point analysis of the tunnel junction region (point B in b) and *p*-AlGa_N region (point A in b). (d) EDXS line profile analysis along the lateral dimension of the *p*-AlGa_N segment (line1-2 in a)..... 129

Figure 8.4: (a) Schematic illustration of the fabricated large area AlGa_N nanowire tunnel junction UV LED. (b) I-V characteristics of the AlGa_N tunnel junction UV LED (LED A) and the standard *p-i-n* UV LED without the use of any tunnel junction (LED B). 130

Figure 8.5: (a) Electroluminescence (EL) spectra of the Al tunnel junction AlGa_N UV LED (LED A) under CW biasing condition. The inset shows the EL spectrum in log scale. (b) Output power vs injection current for Al tunnel junction AlGa_N UV LED (LED A) and standard *p-i-n* AlGa_N UV LED (LED B) under pulsed biasing (2% duty cycle). The inset shows an optical image of LED A under an injection current of 8 A/cm². (c) External quantum efficiency (EQE) and output power

of Al tunnel junction AlGa_N UV LED under CW condition. (d) Wall plug efficiency (WPE) of Al tunnel junction AlGa_N UV LED under CW condition..... 132

Figure 8.6: (a) Electroluminescence spectra of LED A under an injection current of 8 A/cm² for TM and TE polarized emission. (b) Light intensity vs. injection current for TM and TE polarized emission. 135

Figure 9.1: (a) Schematic of AlGa_N nanowire standard UV LED structure. (b) Schematic of AlGa_N nanowire TJ UV LED structure. (c) SEM image of AlGa_N nanowires in the standard UV LED structure. (d) SEM image of AlGa_N nanowires in the TJ UV LED structure. The images were taken with a 45-degree tilting angle. The scale bar in both images are 1 μm. 139

Figure 9.2: Room-temperature PL spectra measured from AlGa_N nanowire standard and TJ UV LED structures. 140

Figure 9.3: (a) Room-temperature I-V characteristics of standard and TJ UV LEDs, with the inset showing the plots in a semi-log scale. (b) Room-temperature EL spectra measured from standard and TJ UV LEDs, with the inset showing the optical image of light emission from the device top. Device size: 500 μm × 500 μm. 141

Figure 9.4: (a) Room-temperature EL spectra measured from a TJ UV LED under CW biasing, with injection currents varying from 2 to 60 mA. The device size is 500 μm × 500 μm. The inset shows a scan up to 650 nm under an injection of 20 mA. (b) The derived EL peak position (filled circles) and spectral linewidth (filled triangles) as a function of injection current. 142

Figure 9.5: (a) EL spectra under an injection of 20 mA for TM and TE polarizations. (b) Light intensity vs. injection current for TM and TE polarizations..... 143

Figure 9.6: Room-temperature output power and EQE of TJ UV LEDs. Symbols: filled and open circles are for output power under CW and pulse biasing, respectively; filled triangles are for EQE under CW biasing. Device size: 1 mm × 1 mm.	144
Figure 10.1 Schematic illustration of High Power Tunnel Junction AlInGaN/AlN QDs UV nanowire LEDs on Si or Sapphire substrate. Band diagram of the GaN/AlGaN tunnel junction is also shown.	151
Figure 10.2: Schematic illustration of InGaN/GaN QDs visible nanowire edge-emitting laser.	152
Figure 10.3 Schematic illustration of AlGaN/AlN QDs UV nanowire edge emitting laser.	153
Figure 10.4 Schematic illustration of single junction and multi-junction InGaN nanowire solar cell.	155
Figure 10.5 (a) Schematic illustration of vertical n-GaN/i-GaN/n-GaN nanowire growth on Si substrate. (b) Illustration of vertical nanowire transistor fabrication.	157
Figure 10.6 a) Schematic illustration of InGaN/GaN dot-in-a-wire heterostructures for photonic crystal laser. (b) SEM image of hexagonally packed nanowires which have diameters ~260 nm, and pitch ~345 nm. (c) Illustration of the fabrication of electrically injected dot-in-nanowire photonic crystal lasers.	158

List of Tables

Table 1.1 Effect of lattice non-ideality on the magnitude of spontaneous polarization in III-nitrides	10
Table 1.2 Piezoelectric constants of wurtzite AlN and GaN used in the calculation.....	10
Table 1.3 Substrates used for the growth of III-nitride LEDs	21
Table 6.1 Specific resistivity values of different planar/nanowire tunnel junction devices	105

List of Acronyms

AC	Alternating Current
BEP	Beam Equivalent Pressures
BD	Backward Diode
CFL	Compact Fluorescent Lighting
CBE	Chemical Beam Epitaxy
CIE	Commission International De L'eclairage Chromaticity Diagrams
CVD	Chemical Vapor Deposition
CW	Continuous Wave
DC	Direct Current
DLD	Deep Level Defect
DH	Double Heterostructure
EBL	Electron Blocking Layer
EDXS	Energy Dispersive X-Ray Spectrometry
EL	Electroluminescence
ELO	Epitaxial Lateral Overgrowth
FWHM	Full-Width-at-Half Maximum
HRTEM	High Resolution Transmission Electron Microscopy
HEMT	High Electron Mobility Transistor
HAADF	High Angle Annular Dark Field

HVPE	Hydride Vapor Phase Epitaxy IQE Internal Quantum Efficiency
ITO	Indium Tin Oxide
LED	Light Emitting Diode
LEEBI	Low Energy Electron Beam Irradiation
LD	Laser Diode
MAR	Multiple Active region
MBE	Molecular Beam Epitaxy
MOCVD	Metal-Organic Chemical Vapor Deposition
MOVPE	Metal Organic Vapor Phase Epitaxy
MQW	Multi-Quantum Well
NW	Nanowire
PALE	Pulse Atomic Layer Deposition
PECVD	Plasma Enhanced Chemical Vapor Deposition
PAMBE	Plasma Assisted-Molecular Beam Epitaxy
PL	Photoluminescence
QCSE	Quantum Confined Stark Effect
QD	Quantum Dot
QW	Quantum Well
RF	Radio Frequency

RHEED	Reflection High Energy Electron Diffraction
RTA	Rapid Thermal Annealing
SAR	Single Active Region
SAG	Selective Area Growth
SEM	Scanning Electron Microscopy
SRH	Shockley-Read-Hall
SQW	Single Quantum Well
SSL	Solid State Lighting
STEM	Scanning Tunneling Electron Microscope
TE	Thermionic Emission
TE	Transverse Electric
TM	Transverse Magnetic
TAT	Trap Assisted Tunneling
TEM	Transmission Electron Microscopy
TJ	Tunnel Junction
UHV	Ultra High Vacuum
UV	Ultraviolet
VCSEL	Vertical Cavity Surface Emitting Laser
VLS	Vapor-Liquid-Solid
XRD	X-Ray Diffraction

Chapter 1

Introduction

1.1 Solid-State Lighting

Over the last few years, semiconductor light-emitting diodes (LEDs) have become the major component of the current solid-state lighting (SSL) technology. Compared to the conventional energy inefficient incandescent (~5% efficiency) and fluorescent lighting technologies (~20% efficiency), LED light bulbs or lamps can, in principle, operate at an efficiency level of 100% [1, 2]. SSL technology generates visible light with reduced heat generation and much less energy consumption. In incandescent lighting, electric current flows through a tungsten filament to heat it up sufficiently enough that it glows. In this process, a substantial amount of input energy or power is converted to heat and infrared emission rather than the desired visible light emission.

Associated with this process is an energy loss of ~90% or more (only about 10% of the energy is used to make visible light). An alternative to this inefficient incandescent lighting, compact fluorescent lighting (CFL), has been on the market for quite some time. But CFL usage has also been limited due to toxic mercury-related complexity in their design prototype; it also suffers from parasitic energy losses [3]. Furthermore, both incandescent and CFL lighting contribute to increased emissions of pollutants such as CO₂ and SO₂ and nuclear waste. [3, 4]. These are identified as critical roadblocks for efficient SSL technology. Therefore, there has been a growing demand for low-cost, highly efficient, environment friendly and phosphor free (to avoid down conversion loss) visible light sources.

These long- standing critical problems can potentially be solved by adopting energy efficient light-emitting diodes (LEDs). As shown in Fig. 1.1, in solid-state LEDs, electrons (from n -type semiconductors) recombine radiatively with holes (p -type semiconductors) to emit photons or visible light (blue, green, red or white), directly converting electricity into light. Current energy efficient, environment friendly SSL technology largely depends on the development of emerging LED technology.

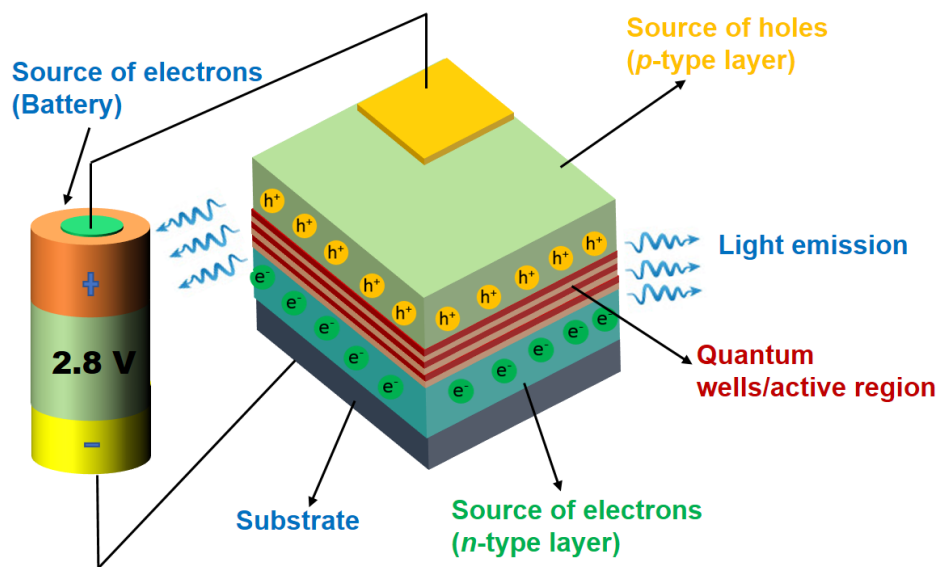


Figure 1.1: A schematic illustration of a double-heterostructure LED in operation powered by a battery [5].

1.1.1 LED Basics

An LED is a light source that directly converts electrical energy into light with rectifying characteristics. However, an LED will emit light after reaching a certain threshold voltage below which it will conduct a small amount of current. In addition to being an efficient light source, an LED can also be used as a circuit element. As shown in Fig.1.2a, light emission can be achieved by electron–hole recombination at the junction between the p - n junctions in a semiconductor (homojunction).

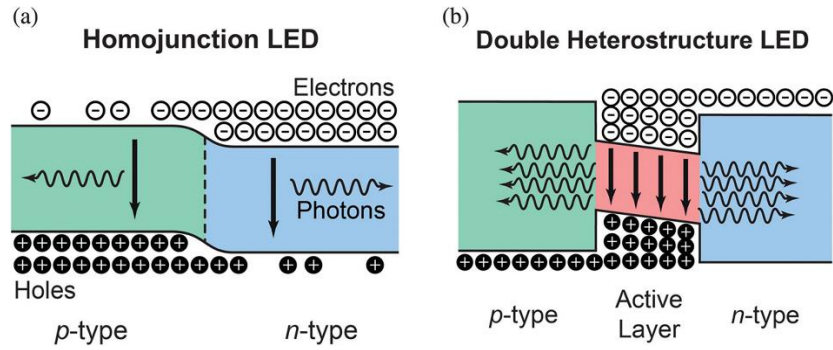


Figure 1.2: Schematic energy band diagram structure for a (a) homojunction LED and (b) double-heterostructure LED [5].

As can be seen in Fig.1.2b, a double heterostructure LED emits photons more efficiently as electron and holes are confined to an active region with a smaller bandgap compared to the n -type and p -type cladding layers. The emitted photons have an energy approximately equal to the band gap of the active material. In addition, heterostructure LEDs with InGaN/GaN quantum wells (QW)/quantum dots (QD) have been reported as having improved performance.

1.1.2 White LED

White light can be produced from LEDs by different methods [6], as shown in Fig. 1.3, Firstly, by combining blue, green, and red (RGB) emissions to generate white light. In this process, photon down-conversion loss can be potentially avoided.

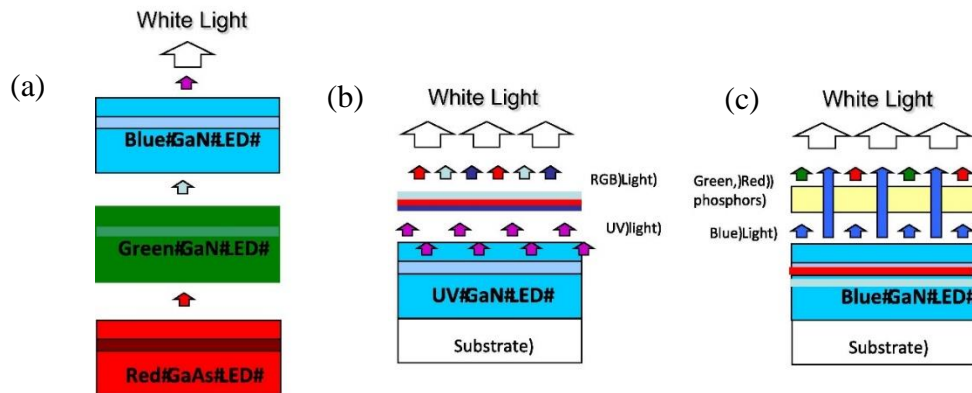


Figure 1.3: Different ways of generating white light from InGaN LEDs: (a) combination of red, green, and blue LEDs, (b) UV GaN LED with three phosphors, and (c) blue InGaN LED with yellow phosphor [6].

However, this process requires complicated balancing of the RGB output over the temperature and over the optical lifetime that further requires sophisticated optical feedback driver electronics. Secondly, the UV/blue emitters excite red, green, and blue phosphors, similar to how fluorescent lamps generate white light [7]. This process is by far the most reproducible and stable. There is a significant photon down-conversion loss from UV to blue, green, and red light emission [7]. The most common approach for making white LEDs is to use yellow emitting phosphor YAG:Ce with a blue LED chip. In this method, phosphorus is typically mixed with epoxy or silicone gel encapsulant that surrounds the LED chip [8].

1.2 Current Status of III-nitrides based LEDs

In recent years, III-nitride materials (AlN, GaN, InN) and their alloys have been extensively used in SSL technology due to the direct band gap and the tunability of the band gap from ultraviolet, AlN (6.2 eV) to near infrared wavelengths InN (0.7 eV) [9]. As shown in Fig. 1.4, InGaN alloys can cover the entire visible spectrum, enabling high efficiency LEDs [10-16], laser diodes (LDs)

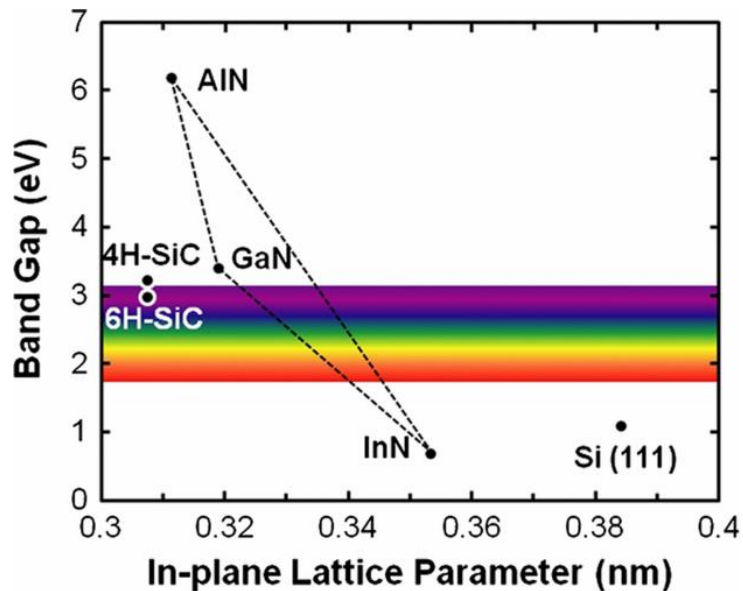


Figure 1.4: In-plane lattice parameters and band gaps for GaN(0 0 0 1) and its related alloys. The lattice parameters and band gaps for common substrates, 4H-SiC (0 0 0 1), 6H-SiC (0001) and Si (1 1 1), are also included [9].

[17-20], solar cells [21-25], photo-detectors [26-30] and sensors [31, 32]. AlGaN alloys cover the full ultraviolet spectrum that enables short wavelength solid state ultraviolet light emitters.

In 2014, the Nobel Prize in Physics was awarded to Shuji Nakamura, Isamu Akasaki, and Hiroshi Amano for their pioneering work on InGaN-based blue light-emitting diodes. Although Nakamura *et al.* demonstrated the first blue LEDs, it opened up new research avenues to realize nitride based longer wavelength green, yellow, and red emitting LEDs and primarily white LEDs. III-nitride is a unique materials system and has widespread applications in both optoelectronic and electronic devices.

A high breakdown field (~ 5 MV/cm) [33, 34], wide bandgap, and high electron saturation velocities ($\sim 2.5 \times 10^7$ cm/s) [35, 36] are essential properties for high-power and high-frequency devices. Since the first demonstration of AlGaN/GaN high electron mobility transistor (HEMT) in 1993 [37] and InGaN-based blue light-emitting diodes in the 1990s, nitride materials systems have been extensively studied for high electron mobility transistor applications [37-41]. These properties give nitrides such enormous functionalities that make it a viable replacement for the currently ubiquitous Si technology.

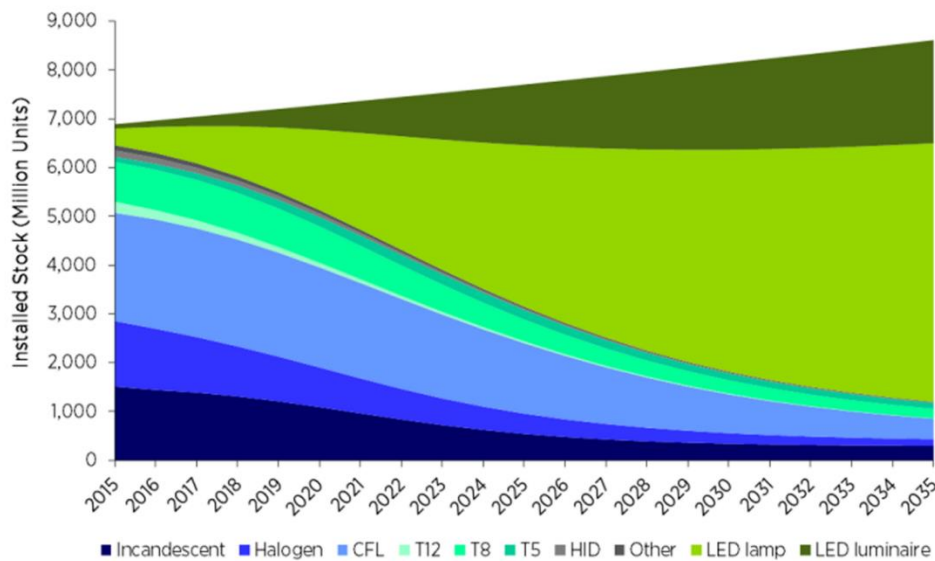


Figure 1.5 LED prediction until 2035 [44]

The United States (U.S.) Department of Energy (DOE) has been at the forefront of the SSL technology evolution. Since 2002, the DOE has supported studies forecasting the market penetration of LEDs in general illumination applications. These reliable forecasts provide a comprehensive overview of the normal path of LED adoption within the U.S. and estimate the approximate energy savings offered by LED products to the year 2035. In 2015, the total energy consumption in the United States was 97.8 quads of primary energy according to the EIA's AEO 2015. The U.S. Department of Energy (DOE) SSL Program calculated that in 2015, lighting consumed 5.8 quads of energy and accounted for roughly ~6% of the total energy and 15% of the total electricity consumed in the U.S. [42, 43].

LEDs have exceeded many conventional lighting technologies with regards to energy efficiency, lifetime, versatility, and overall color quality. LEDs are also attractive owing to their increasing cost competitiveness. It is expected that LED technology will continue to improve, with increasing efficiency and decreasing prices [44]. It was reported that in spite of the increasing number of lighting products installed in the U.S. (up from 6.9 billion in 2015 to 8.6 billion in 2035), the lighting market model predicts that LED adoption will result in a continued reduction in energy use over time. However, the energy consumption of the U.S. lighting stock would continue to increase, up to 6.7 quads in 2035, if SSL is not adopted. As shown in Figure 1.5, LEDs already offers 0.3 quads, or 280 trillion BTU (tBTU) of energy savings in 2015.

1.3 LED History

The first visible, red light emitting LED was developed and demonstrated by Nick Holonyak and co-workers at General Electric, U.S. in 1962 [45]. This demonstration was based on GaAsP on a GaAs substrate. During that time or even earlier, green emission was demonstrated based on GaP

[46]. In the early 1990s, relatively high-efficiency GaAlAsP and AlInGaP LEDs were demonstrated with yellow and red emissions. Interestingly, early GaP or GaAsP based LEDs showed luminous efficacy of about 0.02 lm/W whereas later GaAlAs(P) based LEDs showed luminous efficacy of about 10 lm/W. Finally, current AlInGaP LEDs show luminous efficacy of about > 150 lm/W.

Efficient and cost effective white light emission has been severely limited by several factors. First, phosphor assisted down conversion needs relatively shorter wavelength blue LEDs, but existing efficient (at yellow and red spectral regions) GaAlAsP and AlInGaP LEDs and/or semi-efficient GaAs and InP based materials cannot emit at such short wavelength range (blue spectral region). The material that enabled the development of blue LEDs was gallium nitride (GaN). However, the development of GaN-based blue LEDs had been limited due to GaN crystal growth/deposition and efficient *p*-type doping.

In 1969, Maruska and Tietjen at RCA Laboratories demonstrated the successful growth of single crystal GaN on a sapphire substrate by hydride vapor phase epitaxial (HVPE) growth technique [47]. Later, Yoshida *et al.* developed GaN films using an AlN buffer layer on sapphire by reactive molecular beam epitaxy (MBE) in 1983 [48]. A few years later in 1986, Amano *et al.* grew GaN films with a low-temperature AlN buffer layer by using metal organic chemical vapor deposition (MOCVD) [49]. After successful demonstration of high-quality GaN films by MBE and MOCVD, Amano *et al.* demonstrated the first *p*-type Mg-doped GaN by using post growth low-energy electron beam irradiation (LEEBI) treatment in 1989 [50]. Later, Nakamura *et al.* achieved better *p*-type GaN films with improved hole concentration and mobility using post thermal annealing under an NH₃ ambient gas [51]. As shown in figure 1.6.

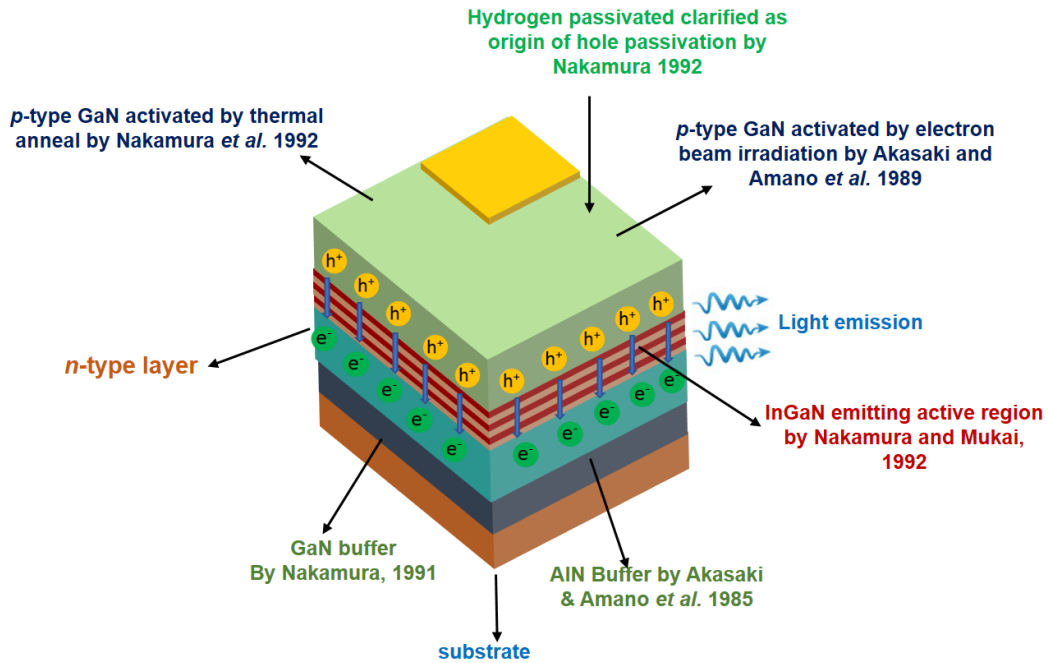


Figure 1.6: Summary of key contributions to the efficient blue LEDs [5].

After the successful demonstration of GaN growth and efficient *p*-type doping, Nakamura *et al.* developed *p-n* junction GaN LED in 1991 [52]. However, *p-n* junction GaN LEDs showed poor light output power $\sim 42 \mu\text{W}$ and external quantum efficiency $\sim 0.18\%$ at 430 nm emission wavelength. Subsequently, Nakamura *et al.* demonstrated *p-GaN/n-InGaN/n-GaN* double heterostructure blue LEDs in 1993 with improved performance [53]. In 1994, Nakamura *et al.* demonstrated commercially available blue LEDs with a *p-AlGaN* electron blocking layer. This modified LED showed output power of 1.5 mW and an EQE of 2.7% at 450 nm emission wavelength [54]. Finally, in 1995, Nakamura *et al.* demonstrated bright blue, green, and yellow emission LEDs with InGaN quantum-well (QW) structures [55]. Later, they showed super bright blue and green single quantum well (SQW) LEDs [56].

The first blue-emitting InGaN lasers were demonstrated by Nakamura *et al.* in 1996 [57]. Shortly after that, Nishia Chemical Corporation showcased the first white LEDs [58]. Recently, Osram, Philips and Nichia have developed and continued to use GaN-on-sapphire LED technology.

However, Cree has developed GaN-on-SiC technology, whereas Soraas has recently started growing GaN-on-GaN.

1.4 Challenges in Current III-Nitride Photonics Research

1.4.1 Polarization Fields

III-nitride materials system including InN, GaN, AlN and their ternary alloys crystallize in wurtzite and zinc-blende crystal structure. However, compared to zinc-blende, thermodynamically stable wurtzite crystal structure with alternating planes of metal (Ga, In, Al) and N atoms are preferred for device applications. Due to the large electronegativity and small size of N atoms compared to metal atoms, the bonds formed between Ga/Al/In and N shows polar (large ionicity) characteristics along the [0001] direction.

As shown in Fig.1.7, each GaN unit cell contains a charge dipole formed due to the spatial separation of negative charge (electron cloud) and positive charge (the nuclei). Due to these minute displacements of the electron cloud and positively charged nuclei, a surface polarization charge as high as $P_{sp}/e \sim 1.8 \times 10^{13}/\text{cm}^2$ was estimated for GaN, whereas for AlN, a charge density of $\sim 5 \times 10^{13}/\text{cm}^2$ was estimated. Given the sheet charge density in semiconductors is $\sim 10^{15}/\text{cm}^2$, roughly one out of 100 atoms can be assumed to be contributing to the polarization charge. An electric field of $\sim 1\text{-}10$ MV/cm is associated with these polarization sheet charges [59]. These polar dipoles cancel each other out in the bulk material, yet forms negative/positive sheet charges at the surfaces.

Table 1.1 Effect of lattice non-ideality on the magnitude of spontaneous polarization in III-nitrides [59]

Material	AlN	GaN	InN
c_0/a_0	1.6010	1.6259	1.6116
$P_{sp}(\text{C/m}^2)$	-0.081	-0.029	-0.032

Table 1.2 Piezoelectric constants of wurtzite AlN and GaN used in the calculations [59]

Material	$e_{31} (\text{C/m}^2)$	$e_{33} (\text{C/m}^2)$	$C_{13} (\text{Gpa})$	$C_{33} (\text{Gpa})$
GaN	-0.49	0.73	103	405
AlN	-0.60	1.46	108	373

Wurtzite hexagonal close packed crystal structures exhibits spontaneous polarization, due to the non-centrosymmetric nature of the ions. Conversely, spontaneous polarization is negligible in symmetric zinc-blende crystal structures. The Ga atom terminated surface (Ga-polar) develops a negative sheet charge, and alternatively, The N atoms terminated surface (N-polar) shows a positive sheet charge at the interface.

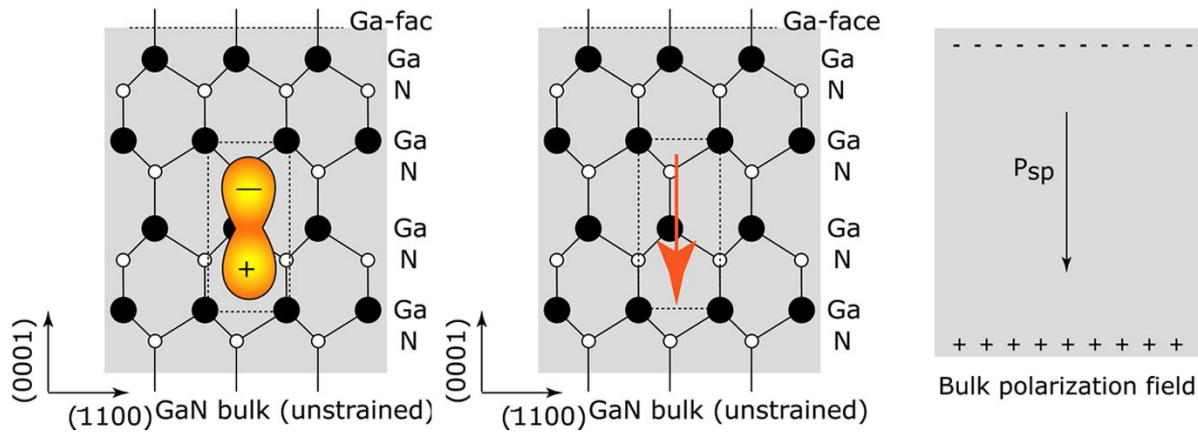


Figure 1.7: Origin of polarization in GaN due to non-centro symmetry and associated electric field [59]

In addition to spontaneous polarization, there is a net charge (positive or negative) due to the piezoelectric polarization at the strained AlGa_N/Ga_N or InGa_N/Ga_N heterointerfaces. Such strain-induced piezoelectric polarization can be calculated with the piezoelectric constants in table 1.2 and the following equation:

$$P_{pz} = e_{33}\varepsilon_3 + e_{31}(\varepsilon_1 + \varepsilon_2) \quad (1)$$

Where $\varepsilon_3 = (c - c_0)/c_0$ represents the strain along the c-axis or [0001] direction, and $\varepsilon_1 = \varepsilon_2 = (a - a_0)/a_0$ is the in-plane isotropic strain. Here, c_0 and a_0 are the final out of plane and in plane lattice parameters of the strained crystal. However, in the wurtzite crystal structure, out of plane and in plane lattice parameters are related and can be expressed by the following equation:

$$\frac{c_0 - c}{c} = -\frac{2C_{13}}{C_{33}\frac{a_0 - a}{a}} \quad (2)$$

Where C_{13} and C_{33} are the in plane and out of plane elastic constants, respectively (Table 1.2). By combining equations (1) and (2) the net strain induced piezoelectric polarization along the [0001] can be expressed by the following formula:

$$P_{pz} = \frac{2(a_0 - a)}{a} \left(e_{31} - e_{33} \frac{C_{13}}{C_{33}} \right)$$

As shown in Table 1.2, in wurtzite III-nitrides, e_{31} is always negative, while e_{33} , C_{13} and C_{33} are always positive, therefore $(e_{31} - e_{33} \frac{C_{13}}{C_{33}})$ will always be a negative number. Hence, P_{pz} in III-N is always negative for layers under tensile stress ($a > a_0$), and positive for layers under compressive stress ($a < a_0$) as shown in Table 1.1. However, spontaneous polarization, P_s in III-N is always negative. For layers under tensile stress, P_s and P_z are parallel to each other and for layers under compressive stress, the two polarizations are anti-parallel. This polarization

(spontaneous+piezoelectric) charge further leads to a high polarization field that is a prerequisite for developing nitride based high electron mobility transistors (HEMTs) and recent polarization engineered tunnel junctions. The charges related to piezoelectric polarization arise at the interface of lattice-mismatched materials.

Piezoelectric polarization associated large strain at the heterointerfaces leads to anion to cation displacement. The piezoelectric polarization field is stronger than the spontaneous polarization field in visible InGaN-based LEDs and lasers, and such a strong field plays an important role in device performance. These piezoelectric charges and resulting large piezoelectric fields (of about 2 MV/cm) have been exploited in many devices using III-nitrides. In the InGaN/GaN-based light-emitting diodes, this piezoelectric polarization becomes more problematic since it largely facilitates electron escape from the active region to the *p*-side region. As shown in Fig. 1.8, polarization induced sheet charge related band bending in the InGaN/GaN active region favors electron leakage or overflow from the active region reducing radiative recombination [4].

This electron leakage further leads to the efficiency droop problem. Furthermore, the presence of the polarization field in InGaN/GaN multi-quantum wells (MQW) causes the quantum confined Stark effect (QCSE) that reduces the overlap potential (spatial separation) of electron and hole (band bending in the opposite direction) wave functions in the LED active region [60, 61]. This QCSE effect reduces the radiative recombination probability and leads to increased carrier loss and degrades the overall performance of the LED [60].

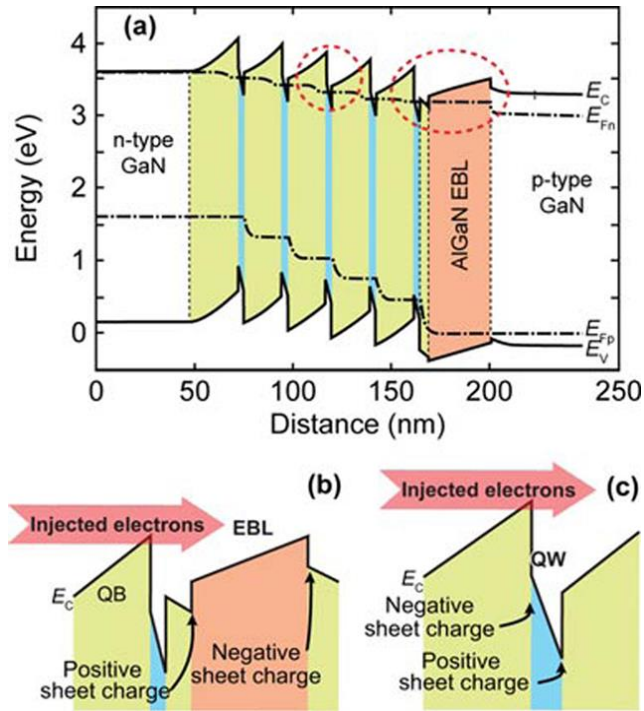


Figure 1.8: (a) Effect of spontaneous and piezoelectric polarization on the band diagram of InGaN/GaN MQW (b) and (c) origin of positive and negative sheet charge at the last GaN barrier and EBL layer [4].

1.4.2 Green Gap

The development of efficient III-nitride green light emitters is limited at longer wavelengths (> 500 nm) due to the presence of a large polarization field and associated degradation of radiative recombination.

This is a well-known problem in current lighting technology and is hence termed as the “green gap” [62]. As shown in Fig. 1.9, InGaN-based planar LEDs show high EQE in the blue and violet wavelength range, but show a significant drop in the green spectral range. This overall degradation is associated with high In related material quality degradation. AlInGaP based material shows improved light performance in the longer wavelength red spectral region but poor performances in short wavelengths due to the indirect bandgap in this spectral range.

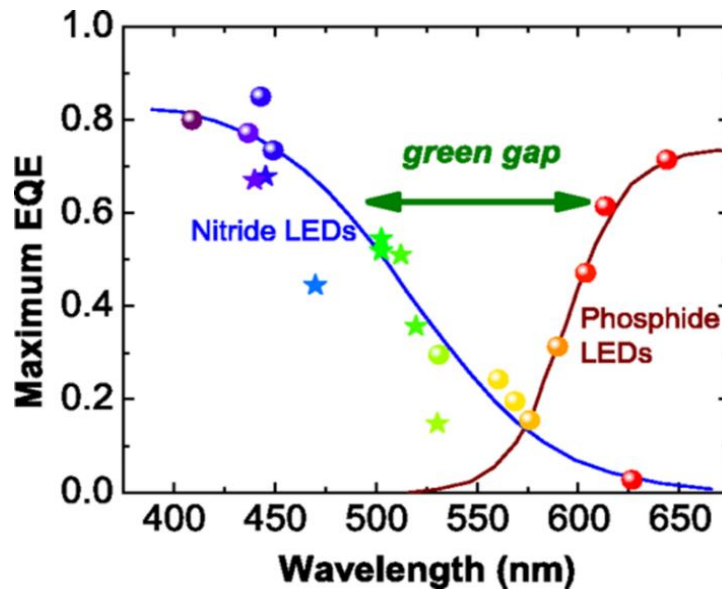


Figure 1.9: Maximum external quantum efficiency (EQE) of different commercial nitride and phosphide LEDs(spheres), illustrating the green gap problem [62].

1.4.3 Efficiency droop

In order to keep pace with the SSL technology roadmap; serious attention must be paid to certain existing bottlenecks. *Efficiency droop* is one of the grand challenges for efficient SSL technology, i.e. the decrease in external quantum efficiency (EQE) with increasing drive current [1]. Typically, high power LEDs show a peak in efficiency at low currents ~ 10 (A/cm^2), then the efficiency starts to fall. InGaN-based blue LEDs show much higher efficiency at low currents compared to longer wavelength green LEDs. Still, it suffers from $\sim 40\%$ or more efficiency reduction at a higher current density or desired drive current [4].

Such an efficiency degradation problem becomes more severe for longer wavelength green or red LEDs. This so-called “efficiency droop” is a major obstacle for the efficient advancement of the projected SSL technology. This problem has been the subject of extensive research for many years, the physical origin of this issue has not yet been properly identified. Several reasons and

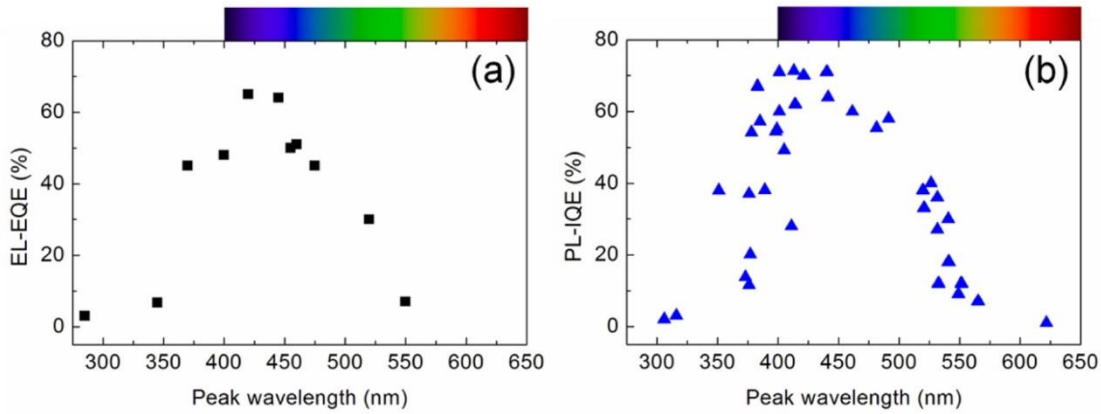


Figure 1.10: (a) Plot of the external quantum efficiency (EQE) of commercial III-nitride LED devices, measured using EL at 350 mA. (b) Plot of the internal quantum efficiency (IQE) of III-nitride QW structures, measured using PL, versus emission wavelength [63].

remedies have been suggested by different research groups and renowned LED companies. To date, defects and dislocations, Auger recombination, carrier delocalization, poor hole transport, and electron overflow are considered the primary causes of efficiency droop [1, 4, 64]. Typical EQE and IQE results of InGaN-based LEDs are depicted in Fig. 1.10a and 1.10b. As shown in Fig. 1.10, InGaN-based LEDs in the blue spectral range, ~420-450 nm, show high IQE >80% at low current densities. The development of ideal LEDs with IQE ~100% is limited by defects, and non-radiative Auger assisted recombination. An EQE value of higher than 60% was also reported for InGaN-based blue LEDs [63]. However, both IQE and EQE are significantly lower in the green and yellow spectral ranges. The degradation in IQE/EQE is primarily due to the presence of large densities of defects and dislocations in the longer spectral range.

1.4.4 Defects and Dislocations

Defects and threading dislocations are present in III-nitrides, and these defects often give rise to the efficiency droop problem. Threading dislocations are present due to the unavailability of lattice matched substrates, and the resulting propagating defect densities can be as high as $\sim 10^8$ - 10^{10} cm^{-2} [65-67]. The non-radiative recombination due to defects/states is termed Shockley-Red-Hall (SRH) recombination. Due to non-radiative states saturation at high injection current, SRH

recombination contributes to efficiency droop [68]. In general, threading dislocations introduce some acceptor like energy levels in the band gap through which defect-assisted Auger recombination takes place. Dislocations are also closely associated with *carrier delocalization*.

In general, at low drive current, electrons and holes are expected to be confined to localized potential minima within the QW caused by In fluctuations or QW thickness variations or related energy activated defects. Conversely, at high drive current, electrons and holes are delocalized from the previously confined potential minima and move to other regions where defect density is much greater and they recombine non-radiatively [4].

1.4.5 Auger Recombination

Auger recombination is a high carrier density, non-radiative process, and is considered as the most controversial mechanism causing efficiency droop. In the Auger process, an electron from the conduction band recombines with a hole in the valence band, and transfers the extra energy released by the process to a third carrier rather than emitting a photon. As the Auger process is a high carrier non-radiative recombination process, the Auger recombination process is proportional to the cube of the free carrier density (n). The contributions to efficiency droop largely depend on the value of the Auger recombination co-efficient C . Therefore, the Auger process can lower the efficiency when the LEDs are driven with a high current. To this end, it is very important to measure the exact Auger co-efficient for both planar and nanowire structures.

Previous reports suggest that only an Auger coefficient greater than $10^{-31}\text{cm}^6\text{ s}^{-1}$ can cause a significantly high efficiency droop [1]. The Auger recombination co-efficient has been previously measured in different active regions including a single quantum well (QW), multiple quantum wells (MQW) and double heterostructures (DH) [1, 69-75]. To date no convincing studies on the

direct measurement of the Auger recombination co-efficient have been reported. Recently, Auger coefficients of $6.1 \times 10^{-32} \text{ cm}^6\text{s}^{-1}$ were measured for nearly defect-free InGaN nanowires and $4.1 \times 10^{-33} \text{ cm}^6\text{s}^{-1}$ for InGaN/GaN in dot-in-nanowire grown on low-resistivity (001/111) silicon by catalyst-free plasma-assisted MBE, and no efficiency droop was evident up to an injection current of 400 A/cm^2 [76].

1.4.6 Electron overflow

Electron overflow or leakage, refers to the leakage or flow of electrons from the active region without being captured or radiatively recombined in the *p*-region. This carrier leakage is another major problem causing efficiency droop in III-nitride LEDs. In this context a large bandgap, i.e. AlGaIn electron blocking layer (EBL), is often incorporated between the last quantum well/dot and the *p*-GaIn region to reduce electron leakage [77, 78]. However, the EBL incorporation approach is not often useful in blocking electron leakage efficiently due to the large polarization field in the device active region. Due to the inefficient electron blocking capability of the EBL, electron leakage is considered one of the leading causes of efficiency droop.

Electron leakage becomes extreme when the injection current is stronger than the radiative recombination current [1]. Temperature dependent electroluminescence measurements in planar structures suggested that electron leakage could be the dominant efficiency droop mechanism [79, 80]. Also, in dot-in-a-wire QDs structures, it was proposed that the achievement of maximum quantum efficiency is limited by electron leakage rather than Auger recombination. By incorporating a *p*-type doped large bandgap AlGaIn (low Al%) electron blocking layer, efficiency droop was significantly reduced or eliminated [77].

1.4.7 Poor Hole Transport and Hole Injection Efficiency

Due to the heavy effective mass of holes and associated low hole mobility, hole transport in the active region is non-uniform. Only the quantum wells or dots close to the *p*-side delivers reasonable photon emission because of higher carrier density, as heavy holes cannot cover all the quantum wells or dots. Conversely, electrons have lower effective mass, and they move more smoothly across the quantum wells. In InAlGaN based optoelectronic devices, electrons typically have mobility of $\sim 200 \text{ cm}^2/\text{V}\cdot\text{sec}$ or more, and a high concentration of electron carriers is readily achievable due to high ionization efficiency and low ionization energy. In contrast, holes in GaN typically have ~ 20 times lower electron mobility ($10 \text{ cm}^2/\text{V}\cdot\text{sec}$), due to the large *p*-type dopant (Mg) ionization energy. This non-uniform carrier flow not only causes reduced radiative recombination, but also causes electron overflow and Auger recombination.

Several solutions have been suggested to overcome this problem. Until recently, a large bandgap EBL has been incorporated to reduce the electron leakage. In addition to reducing electron leakage, the EBL simultaneously hinders the free flow of holes from the adjacent GaN layer largely due to the relatively large valence band offset (ΔE_C) between AlGaN and GaN. Efficient *p*-type doping can reduce this hole injection barrier. Nonetheless, *p*-type doping efficiency also decreases with the increase of the bandgap of the EBL (AlGaN) and Al mole fraction. Therefore, to strike a balance between efficient hole transport and reduced electron leakage, an Al mole fraction $\sim 15\%$ is typical in the EBL design.

1.4.8 Issues with *p*-doping

As discussed in the previous section, the progress of III-nitride visible LED technology was limited in the 1970s and even in the early 1980s due to the lack of GaN film and efficient *p*-

doping. Yoshida *et al.* in 1983 and Amano *et al.* in 1986 demonstrated GaN films by MBE and MOCVD methods, respectively [48, 49]. These MBE and MOCVD GaN films were found to be unintentionally *n*-type doped due to the presence of oxygen impurities and nitrogen vacancies. In 1992, Nakamura *et al.* achieved an electron mobility of 900 cm²/V.s at room temperature (3000 cm²/V.s at 70 K) using a low-temperature GaN buffer layer [81].

In 1989, Amano *et al.* first demonstrated Mg-doped *p*-type GaN by post-growth low-energy electron-beam irradiation (LEEBI) treatment [50]. The hole concentration and mobility was measured to be $\sim 2 \times 10^{16}$ cm⁻³ and 8 cm²/V.s, respectively. In 1992, Nakamura *et al.* demonstrated *p*-type GaN films using NH₃ free post thermal annealing in N₂ ambient. In this thermally treated *p*-type GaN films, hole concentration and mobility was measured to be 3×10^{17} cm⁻³ and 10 cm²/V.s. After this study, Nakamura *et al.* explained that in environments containing NH₃, atomic hydrogen (NH₃ dissociation) as interstitial defects impedes the activation of Mg acceptors by forming Mg-H complexes. It was concluded that in conventional MOCVD GaN growth, Mg dopant activation was hindered because of the presence of H in the form of Mg-H complex that resulted in low hole concentration [82].

In the post-growth treatment in N₂ ambient, Hydrogen atoms were dissociated and removed from complex Mg-H [51]. After this discovery, Nakamura *et al.* was able to demonstrate the first successful LEDs and lasers with efficient *p*-type doping. Still, *p*-type doping density is low ($\sim 10^{17}$ cm⁻³) in conventional MOCVD growth techniques due to the high ionization energy of holes (~ 170 meV) [83]. Later in 2010, Bhattacharya *et al.* successfully demonstrated low temperature growth of *p*-doped GaN in nitrogen rich (in hydrogen-free ambient) plasma-assisted molecular beam epitaxy (PA-MBE) [84].

In this process, a doping density as high as $\sim 2 \times 10^{18} \text{ cm}^{-3}$ was reported. In MBE growth, electrically active hole concentrations in GaN have been limited to a low range ($\sim 10^{18} \text{ cm}^{-3}$) with a doping efficiency of $\sim 5\%$. Such a low doping efficiency is due to the high activation energy of the Mg acceptor level, lower solubility, and compensation from defects present in the structure. Recent reports have suggested that doping efficiency can be increased to as high as $\sim 10\%$ in GaN by periodic metal modulation epitaxy, where the hole concentration obtained was $\sim 1.5 \times 10^{18} \text{ cm}^{-3}$ through periodically modulating the metal (Ga) atoms and Mg dopants [83]. Current lighting technology still relies on the efficient activation of the *p*-type Mg dopants in GaN by forming shallow acceptor levels in GaN.

1.4.9 Issues with Resistive *p*-Al(Ga)N Contact

To make a perfect ohmic contact with a *p*-type semiconductor, ideally the metal work function must be greater than the semiconductor work function. GaN also has a large band gap ($\sim 3.4 \text{ eV}$) and electron affinity ($\sim 4.1 \text{ eV}$), and the *p*-GaN work function can be as high as $\sim 7.5 \text{ eV}$. Therefore, it is challenging to make an ohmic contact using existing low work function metals. In addition, due to the low ionization efficiency of Mg dopants, it is difficult to make tunnel contact of a heavily *p*-doped GaN cap layer.

1.4.10 Issues with Substrates

To date one of the primary concerns of III-nitride materials growth is the lack of a suitable lattice-matched, cost effective and large area substrate for mass production. Expensive GaN substrates have limited their usage in widespread lighting technology. Rather, lattice mismatched Sapphire, 6H-SiC, and Si have been used for heteroepitaxial III-nitride growth through the conventional MOCVD or MBE growth technique. These lattice mismatched heteroepitaxy methods result in the

formation of a large number of threading dislocations at the nitride/substrate interface. These threading dislocations later propagate through the active regions, and act as non-radiative recombination centers, thereby reducing LED performance.

Table 1.3 Substrates used for the growth of III-nitride LEDs

Substrate	Lattice constant (\AA^0)	Lattice mismatch to GaN (%)	Thermal conductivity ($\text{Wm}^{-1}\text{K}^{-1}$)
GaN	3.189	0	130
Silicon	5.43	17	3.59
Sapphire	2.747	13	7.5
6H SiC	3.081	3.4	490

As can be seen from the table 1.3, SiC has less lattice-mismatch to GaN and an almost similar thermal expansion co-efficient, but it still has limited usage due to its cost. For LED mass production, sapphire is still preferred in spite of its several disadvantages, i.e. large lattice mismatch, thermal co-efficient mismatch, and low thermal conductivity.

1.5 Ultraviolet LEDs

Ultraviolet light emitters have a wide range of critical applications, such as sterilization and disinfection, water and air purification, medical instrumentation, biological sensors, and protein analysis (shown in Fig. 1.11) [85]. Conventional Mercury and Xenon lamps are generally bulky and expensive, have limited lifespan, and require a high voltage to operate. Moreover, the emission wavelengths cannot be tuned, and they cause environmental pollution due to the presence of mercury in the lights [13].

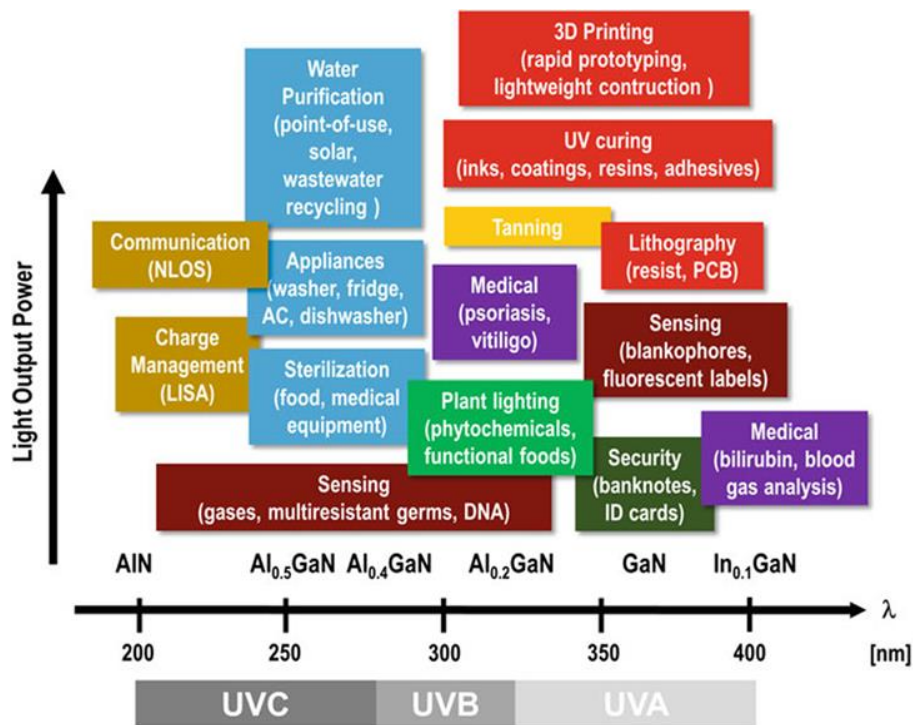


Figure 1.11: The wide range of important applications of UV LEDs [85].

UV-LEDs are compact, robust and have a long lifespan. LEDs are small in size, cheaper, and mercury-free, and can be operated at low or moderate DC voltage. III-nitride UV-LEDs also offer the tunability of emission wavelength through bandgap engineering and can be switched on and

off within a few tens of nanoseconds. It was projected by Yole Développement in 2012 that the UV LED market will grow 43% by 2017 and reach nearly 270 million dollars [111-113].

1.5.1 Ultraviolet LEDs: The Challenges

The UV emission wavelength can be tuned to cover wavelengths in the UV-A (315 – 420 nm), UV- B (280 – 315 nm), and UV-C (100 – 280 nm) spectral range. Depending on the spectral wavelengths UV LEDs have critical applications. As shown in Fig. 1.12, as we move closer to the deep UV range, it becomes more and more difficult to produce high efficiency LEDs [14]. The underlying reasons are summarized in the following paragraphs.

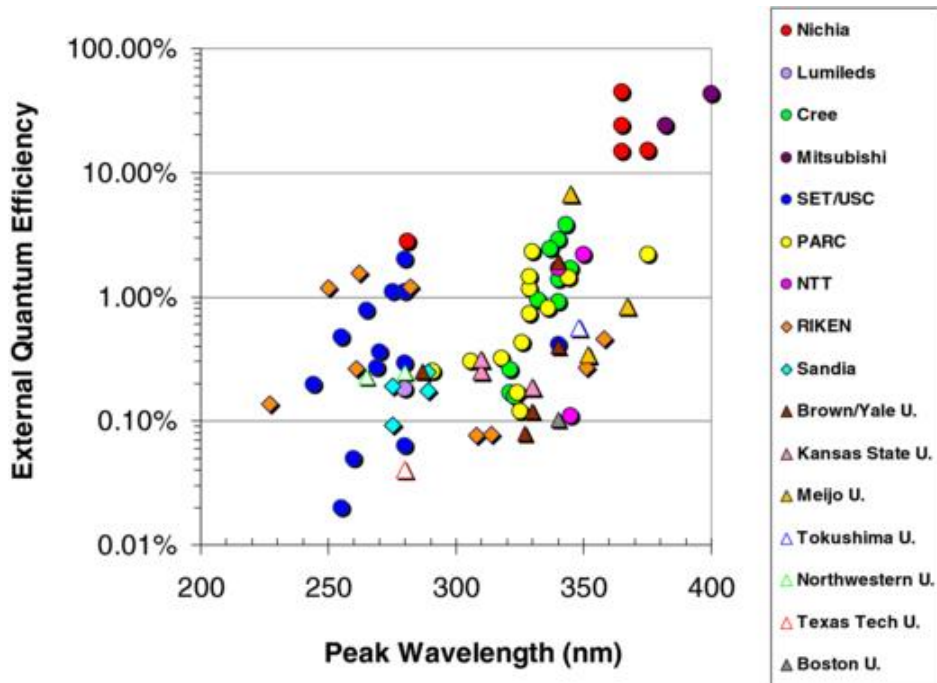


Figure 1.12: Reported external quantum efficiencies for AlGa_N, InAlGa_N, and InGa_N quantum well LEDs emitting in the UV spectral range [14].

1.5.2 Crystal Quality and Internal/External Quantum Efficiency

Relatively high defect densities in AlN and AlGaN materials grown on foreign lattice-mismatched substrates result in a low IQE. AlN layers grown on lattice-mismatched sapphire substrates result in dislocation densities as high as 10^{10} cm^{-2} [86-88]. These threading dislocations work as non-radiative recombination centers that cause a reduced internal quantum efficiency and EQE [89, 90]. Different approaches have been explored to reduce the dislocation densities in AlGaN and AlN layers grown on sapphire substrates, including the insertion of a low temperature AlGaN/AlN layer [91, 92], epitaxial lateral overgrowth (ELO) [93-96], and pulse atomic layer deposition (PALE) to grow high quality AlGaN [96-98].

Growth on nano-patterned sapphire substrates [99, 100], and growth through exploiting short period superlattices were also demonstrated. By exploiting the ELO technique, the dislocation density can be reduced down to 10^5 - 10^6 cm^{-2} from $\sim 10^8$ - 10^9 cm^{-2} , and from 10^{10} cm^{-2} to 10^9 cm^{-2} , respectively [96, 101].

1.5.3 Carrier Injection and Operation Voltage

In general, UV-LEDs suffer from poor carrier injection efficiency, and high device operation voltage. Such issues are fundamentally associated with a poor *p*-type conductivity of Mg-doped *p*-AlGaN [102, 103]. The ionization efficiency of the Mg-dopant acceptors decreases steadily with the Al-mole fraction in the Mg-doped AlGaN layer. For Mg-doped wide band gap AlN the acceptor level is found to be 510-600 meV above the valence band edge [104, 105]. Therefore, at room temperature a small percentage of Mg acceptors are ionized which results in very poor hole concentrations. Interestingly, at high Al mole fractions, Si-doping is very challenging for *n*-AlGaN [106-108].

Various approaches have been explored to improve the conductivity, for example, short period superlattices ($\text{Al}_x\text{Ga}_{(1-x)}\text{N}/\text{Al}_y\text{Ga}_{(1-y)}\text{N}$) [109, 110], polarization doping of graded $\text{Al}_x\text{Ga}_{(1-x)}\text{N}$ [104], and Mg-delta doping [111]. Additionally, efficient hole injection and electron leakage from the AlGaN active region is another big challenge. The development of an efficient injection scheme, especially for UV-B and UV-C LEDs, is critical due to the simultaneous improvement of electron leakage from the active region and efficient hole injection into the active region. To this end, several approaches including Mg-doped AlGaN electron blocking layers, AlN/AlGaN electron blocking heterostructures [112, 113], and AlGaN/AlGaN multi-quantum barriers [114] have been previously proposed.

1.5.4 Light Extraction

Unlike blue and near UV-LEDs, light extraction from deep UV-LEDs is not straight forward and fundamentally limits efficient light extraction for several reasons. Advanced packaging technologies such as high-index transparent silicones and polymers have been adapted and optimized mainly for blue LEDs. However, this technology is not well suited for AlGaN-based deep UV emitters due to high energy deep UV photons. Hence, several other techniques have been investigated to enhance the light extraction efficiency, including photonic crystals, roughening of the LED surfaces, patterned substrates, shaped LED dies, micro-pixel LEDs, and multi-directional reflectors [115-119].

Also, Ag and Al-based reflectors commonly used for blue LEDs cannot make low resistance ohmic contact to Mg-doped p -AlGaN. Nano-pixel LEDs somewhat overcome this problem as low resistance Pd/ p -GaN can be facilitated and UV-reflective aluminum reflectors can be utilised [120]. AlGaN alloys generally exhibit a large negative crystal field splitting (-219 meV), whereas GaN shows a positive crystal field splitting (38 meV) [121]. Due to the negative crystal field

splitting, the recombination between the electrons from the conduction band with the holes in the top valence band is polarized transverse magnetically (TM).

Also, this negative field splitting causes a rearrangement of the valence bands at higher aluminum mole fraction that results in a switch from transverse electric (TE) to transverse magnetic (TM) at a shorter wavelength [122]. Previous studies suggested that the TE to TM transition happens at an Al mole fraction of 0.25 [122]. However, the polarization characteristic and switching critically depends on the strain and internal electric field present in the structure [123-126].

1.6 Nanowires

Although tremendous progress has been made in the III-nitride materials systems, the applications of III-nitride planar devices have been limited predominantly due to the presence of large defect densities. Commercially available III-nitride planar devices are mostly grown on expensive sapphire or SiC substrates. To this end, III-nitride nanowires can potentially mitigate some of the problems associated with current nitride planar devices. III-nitride nanowires can be synthesized or grown in several ways, either by the top down or the bottom up approach.

Chemical vapor deposition (CVD) [127], metal organic chemical vapor deposition (MOCVD) [128, 129], metal organic vapor phase epitaxy (MOVPE), molecular beam epitaxy (MBE), and chemical beam epitaxy (CBE) generally fall into the bottom-up approach. In contrast, the top-down approach typically requires a masking layer and nanoscale patterning. Nanowires of desired size and shape can then be grown on these nanopatterns. III-nitride nanowire offers several unique benefits compared to their planar counterparts. These advantages include reduced threading dislocations on the top surface and polarization fields mostly due to the effective lateral stress relaxation on the sidewalls, and their potential to be grown on various cost-effective substrates.

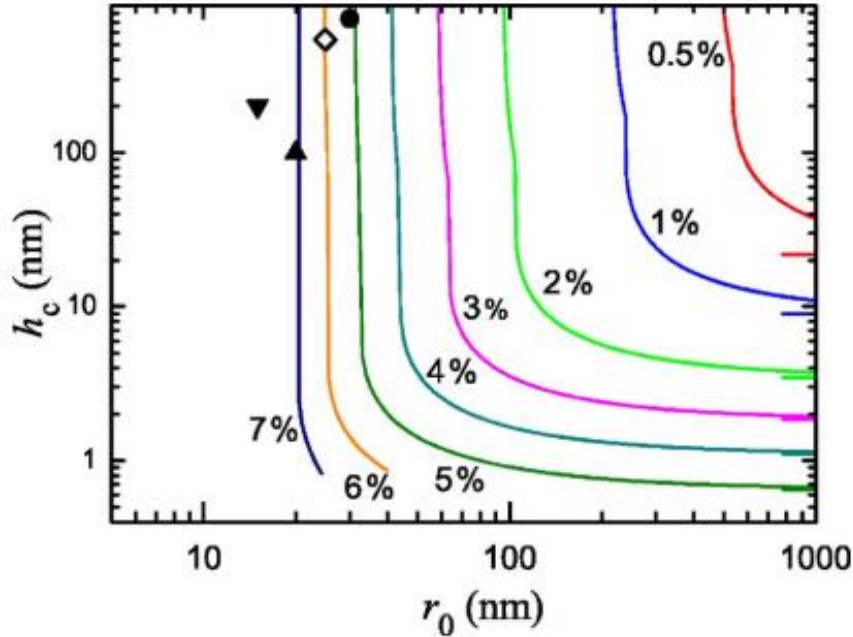


Figure 1.13: Variation of the critical thickness of the misfitting layer growing on a top of a nanowhisker as a function of whisker radius [133].

III-N nanowires in the form of wurtzite crystal (growth direction c-axis, $\langle 0001 \rangle$) structure grow vertically, perpendicular to the substrates. It shows a unique tendency to relax the strain in the free sidewalls (m-planes) even though significantly lattice mismatched heterostructures are formed [130-132]. Fig. 1.13 shows the dependence of strain accommodation on the nanowire radius [133].

The dependence of the critical thickness of the overlayer material grown on the nanowire radius is also shown. The different contour lines correspond to a different amount of lattice mismatch between the nanowire and overgrown material. For a certain degree of lattice mismatch, the area just above the contour line demonstrates the combination of the nanowire radius and overgrown material critical thickness that would lead to plastic deformation and associated extended defects. Conversely, the combination of the critical thickness and the nanowire radius below the contour line does not result in any plastic deformation.

Catalyst-free III-nitrides can be grown on various substrates including Si(111) [134], Si(001) [76], sapphire [135], polycrystalline metal [136-138] and amorphous films [139, 140]. Recent reports have suggested that III-nitride nanowires can be successfully grown on a cost effective, CMOS compatible Si substrate with much reduced defect densities [77, 141]. Further to these potential benefits, due to their small size, III-nitride nanowires hold tremendous promise for integration in state-of-the-art optoelectronic and electronic applications. For optoelectronic applications, several factors associated with III-nitride nanowires need a broad understanding. In the following paragraphs, some of the critical issues are discussed that may fully or partially eliminate some of the long-standing bottlenecks in present light-emitting diode technology.

1.7 III-nitride Tunnel Junctions

The scheme of tunnel junction (TJ) has been in use for a wide variety of electronic and optoelectronic device applications including LEDs, lasers, solar cells, transistors, etc. since shortly after their first demonstration by Leo Esaki in 1958 in heavily or degenerately doped Ge p - n junctions [142]. Efficient inter-band tunneling provides a unique means for carrier type conversion from electrons into holes and vice versa, which is beneficial for a broad range of optoelectronic and electronic devices. It also holds exceptional promise for novel optoelectronic device design.

In forward biased tunnel junctions, electrons tunnel into the empty states of degenerate (heavily doped) p -type semiconductors. In reverse biased tunnel junctions, electrons in the valence band of the p -type semiconductor tunnel into the empty states of the conduction band, leaving behind holes. Inter-band tunnel junctions have been investigated using relatively narrow band gap materials such as Ge, Si, GaAs and SiGe [143]. However, tunnel junctions using III-nitride materials system has been limited primarily due to inefficient p -type doping. Inter-band tunnel

junctions are useful for optoelectronic devices, for example multi-color LEDs [144], vertical cavity surface emitting lasers (VCSELs) [145], and multi junction solar cells [146].

1.7.1 Tunnel Junctions in LEDs

III-nitride based light-emitting diodes have resistive p -type material due to dopant solubility limitation. This resistive p -type material forms a poor ohmic contact in a light-emitting diode with high contact resistance. As previously mentioned, reverse biased tunnel junctions can act as a carrier type conversion center that enables the replacement of resistive p -Al(Ga)N contact with n -Al(Ga)N contact for visible and deep UV emitters. When the TJ is integrated with a single active region LED, in typical device operation, the LED is forward biased while the tunnel junction is reverse biased. The whole LED/ p - n junction structure serially connected with a low resistance TJ can be considered as a single LED, wherein the tunnel junction acts as a short circuit element and carrier conversion center. With the use of the tunnel junction, the resistive p -GaN contact layer can be replaced by an n -GaN contact, leading to a significantly reduced device resistance [147-151], voltage loss, and heating effect [145, 152].

The voltage drop or series resistance of the TJ is superimposed in the I-V curve of the TJ integrated single/multiple active region LEDs. In addition, the tunnel junction allows for the reduction of the thickness of the resistive p -Al(Ga)N layer that reduces the overall device series resistance. For deep UV emitters, TJ integration also enables the insertion of a relatively thin p -GaN layer in the UV LED design that absorbs UV light. Moreover, tunnel injection of holes into the Al-rich AlGaIn active region significantly reduces the hole injection bottleneck. The tunnel junction also enables stacking of multiple p - n junctions/LEDs [145, 148, 153], providing the unique opportunity for

repeated carrier usage [145, 152, 154]. As such, high power operation can be achieved at low injection current, leading to enhanced efficiency [155] and reduced efficiency droop [155, 156].

1.7.2 Polarization Engineered Tunnel Junction

As described in the previous section, III-V wurtzite crystal structures demonstrate high spontaneous and piezoelectric polarization along the c-axis [0001] direction. Spontaneous polarization exists along the (0001) (metal-polar) and (000-1) (N-polar) directions of wurtzite III-nitride crystals [157]. Strain induced piezoelectric polarization can either add to or subtract from the spontaneous polarization based on the composition and polarity (N-face or Ga-face). Due to the presence of high spontaneous and piezoelectric polarization, new tunneling heterostructures can be potentially enabled.

Due to this large polarization, high densities of sheet charges exist at the sharp interface of the polar heterointerface. Such a high density of polarization induced sheet charges between GaN/InGaN and GaN/AlGaN can be exploited to bend the energy band over a small distance (tunnel distance) depending on the polarity and composition (In% or Al%). This band bending enables the alignment of the conduction band and the valence band of GaN/Al(Ga)N with low tunneling barrier and height. As discussed in the previous section, non-centrosymmetric wurtzite crystals exhibit two different sequences of atomic layering in the two opposing directions, parallel to certain crystallographic axes.

For GaN wurtzite crystals, the sequence of the atomic layers of the components Ga and N is reversed along the [0001] and [000-1]. In the GaN crystal structure, the constituent atoms are arranged in bilayers. These bilayers are composed of two closely packed hexagonal layers or planes. One layer consists of cations and the other is formed by anions. As shown in Fig. 1.14, in

the case of GaN, a basal plane should be either Ga-face or N-face. For the Ga-face surface, a positive sheet charge forms at the bottom of the unit cell and a negative sheet charge at the top. For N-face surface, the polarization direction is reversed along $[0001]$ [158].

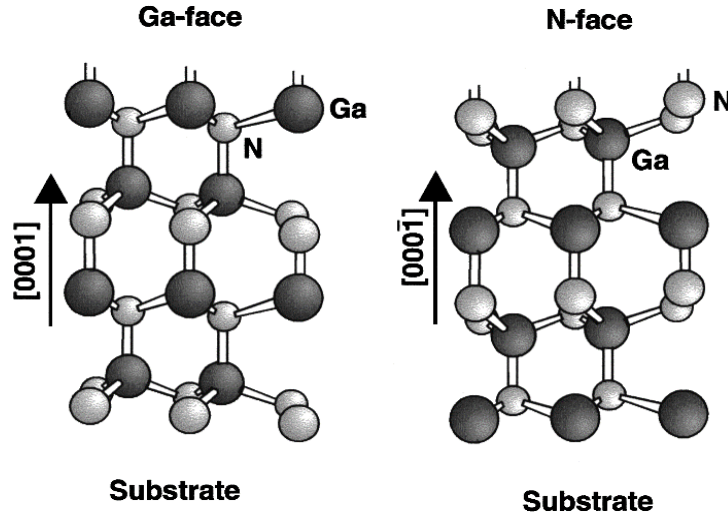


Figure 1.14: Schematic drawing of the crystal structure of wurtzite Ga-face and N-face GaN [157].

However, in bulk GaN these sheet charges cancel out, resulting in uncompensated spontaneous charges at the interface. Also, strain induced piezoelectric polarization is present in the strained heterointerfaces.

In pseudomorphic growth combinations, for example, GaN/AlGa_N or GaN/InGa_N exhibit non-zero macroscopic piezoelectric polarization. In the case of epitaxial films and metal face (Ga or Al) heterostructures (InGa_N/GaN or AlGa_N/GaN) grown on thick relaxed GaN films, for example, Al_xGa_(1-x)N or Al_xIn_(1-x)N ($x > 0.82$) the top layers will be under tensile strain. In this tensile strain case, both the piezoelectric and spontaneous polarization are in the same direction (aiding one another). Shown in Fig. 1.15, the piezoelectric and spontaneous polarization are anti-parallel for compressively strained In_xGa_(1-x)N or Al_xIn_(1-x)N (for $x \leq 0.82$) layers (opposing each other) [159].

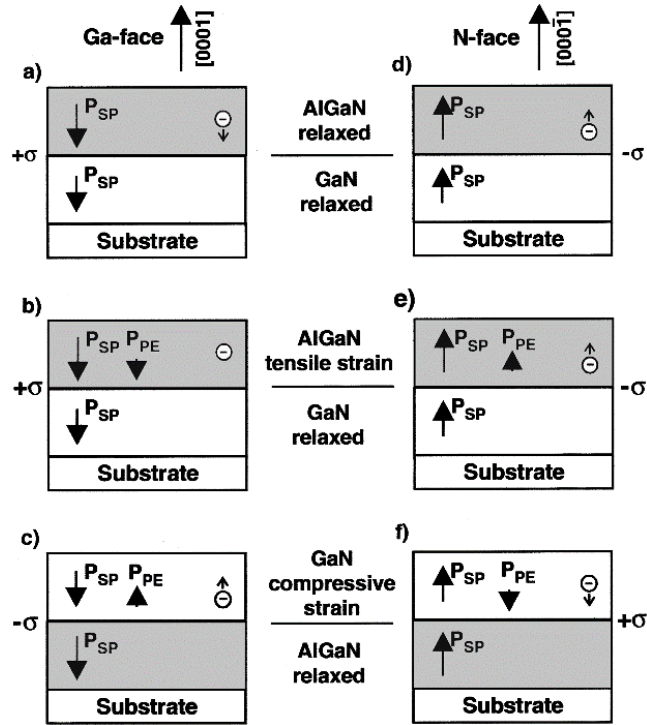


Figure 1.15: Polarization induced sheet charge density and directions of the spontaneous and piezoelectric polarization in Ga- and N-face strained and relaxed AlGaIn/GaN heterostructures [157].

However, if the polarity flips over from metal face to N-face, the piezoelectric, as well as spontaneous polarization charge signs change [160]. For InGaIn/GaN heterostructures, the piezoelectric polarization is the dominant contribution to polarization charge due to the large lattice mismatch, whereas spontaneous polarization dominates in AlGaIn/GaN heterostructures [161-164]. This unique polarization effect in nitrides has been utilized for the origin of 2-dimensional electron gas (2DEG) in AlGaIn/GaN high electron mobility transistors (HEMTs), eliminating the need for modulation doping [160, 165-169]. Recently, the polarization charge at the GaIn/InGaIn or AlIn/GaN heterointerface has been exploited to engineer the electrostatics of the junction for efficient inter-band tunneling [143].

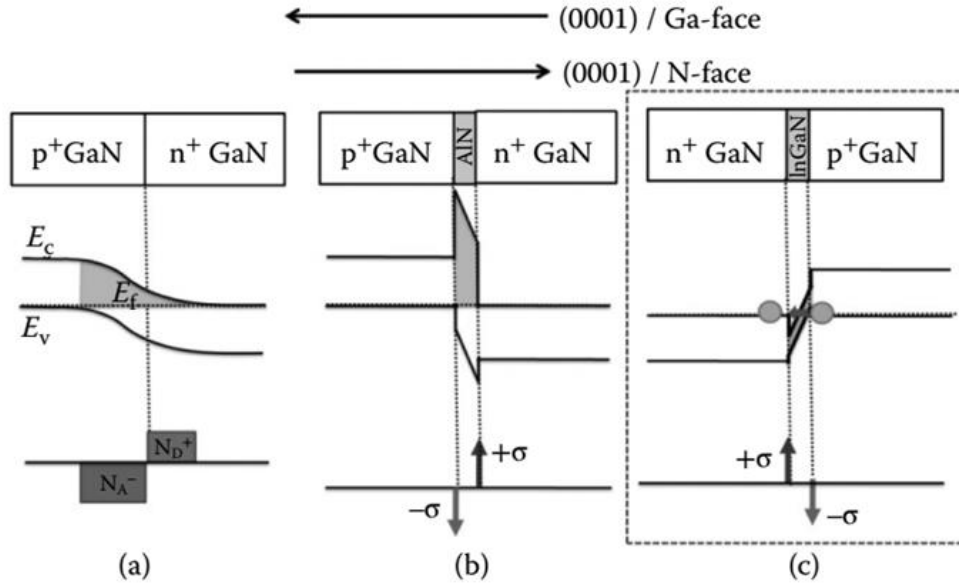


Figure 1.16: Charge and band diagram of a (a) conventional degenerately doped tunnel junction, (b) polarization engineered GaN/AlN tunnel junctions, and (c) GaN/InGaN tunnel junctions [143].

As shown in Fig. 1.16, for GaN/AlN/GaN heterostructure devices, using a wide band gap AlN as the barrier material polarization induced tunnel junction has been demonstrated by several groups [170-173]. It was found that even with a ~ 2.6 nm thin AlN barrier layer, the polarization sheet charge induced field is so high that it aligns the conduction and valence bands on either side [143]. Still, the large band gap of AlN limits the tunneling probability, and GaN/AlN/GaN devices demonstrate high tunneling resistance and low current density. With GaN/AlN/GaN heterostructures grown along the Ga-face orientation, the net positive and the net negative polarization charges were found at the bottom and the top of the GaN/AlN heterointerfaces, respectively. Therefore, the conduction and the valence bands can only be aligned for efficient tunneling when the top layer is p^+ -GaN. For GaN/InGaN/GaN structures, the positive polarization charge was found to lie at the top GaN/InGaN interface. Therefore, InGaN can be used as a barrier

material if the top layer is n^{++} -GaN for efficient inter-band tunneling. However, the tunneling probability depends on the thickness of the inserted barrier materials and barrier height (bandgap). Therefore, it is expected that compared to large band gap AlN or $\text{Al}_x\text{Ga}_{(1-x)}\text{N}$, lower band gap InGaN would perform well as an efficient tunnel barrier. Also, InGaN with large strain induced piezoelectric polarization is well suited for low resistance effective polarization engineered inter-band tunneling.

1.8 Organization of the Thesis

This thesis focuses on the development of various novel III-nitride nanowire tunnel junctions on a Si platform and its integration with full-color InGaN/Al(Ga)N visible light and UV LEDs. In this dissertation work, the design, MBE growth, fabrication, characterizations, and performance of different InGaN/GaN polarization engineered and monolithic Al/Al(Ga)N tunnel junctions have been extensively investigated. A large part of the thesis work was focused on the development of high-efficiency InGaN/GaN dot-in-a-wire nanowire LEDs integrated with polarization engineered and metal/semiconductor tunnel junctions. Additionally, we have focused on performance improvement of AlGaN-based LEDs operating in the ultraviolet (UV-C) band.

Chapter 1 provides a general overview of the status of III-nitride visible and UV LEDs and the advantages of III-nitride nanowires for light emitting device applications. The overall development of III-nitride LEDs/lasers is presented. The recent developments and limiting factors of both visible/UV LEDs are also described. Additionally, the usage of III-nitride tunnel junctions in various electronic and optoelectronic applications are described.

Chapter 2 presents the growth mechanism of catalyst free vertically aligned III-nitride nanowires by plasma-assisted molecular beam epitaxy. The detailed MBE growth of tunnel junction

InGaN/GaN dot-in-a-wire and AlGaN double heterostructure is described. The III-nitride nanowire LED device fabrication is briefly summarized. Additionally, the optical and electrical characterizations of InGaN/GaN and AlGaN nanowire heterostructures are presented.

Chapter 3 describes the first demonstration of tunnel junction InGaN/GaN dot-in-a-wire LEDs. The achievement of cascaded multiple-active-region InGaN/GaN dot-in-a-wire LEDs is also described. Monolithic multiple-wavelength LEDs are further presented in this chapter.

Chapter 4 reports on the first demonstration of alternating current (AC) operated nanowire LEDs on a Si platform. This study promises to offer the elimination of the AC/DC converter required in conventional LED lighting technology.

Chapter 5 discusses the unique molecular beam epitaxial growth of n -GaN/Al/ p -AlGaN nanowire heterostructure. Our detailed studies suggest that nearly dislocation/defect free GaN/Al/Al(Ga)N nanowires can be grown epitaxially on a Si substrate in an optimized growth condition.

Chapter 6 focuses on the first demonstration of an n^{++} -GaN/Al/ p^{++} -AlGaN backward diode, wherein an epitaxial Al layer serves as the tunnel junction. Here, we have demonstrated a record low resistivity Al/Al(Ga)N nanowire backward diode. The transport properties of the backward diode are discussed.

Chapter 7 presents the first demonstration of an n^{++} -GaN/Al/ p^{++} -GaN tunnel junction InGaN/GaN dot-in-a-wire LED. The performance of p -contact free InGaN/GaN nanowire LEDs are described in this chapter. Also, the performance of LED devices without the use of Al-tunnel junction or with the use of an n^{++} -GaN/ p^{++} -GaN tunnel junction is compared in this chapter.

Chapter 8 reports on the development of nearly defect-free AlGaN tunnel junction core-shell nanowire heterostructures. With the incorporation of an epitaxial Al tunnel junction, the *p*-(Al)GaN contact-free nanowire deep UV LEDs (operating in the ~275 nm spectral range) exhibit an output power >8 mW and a peak external quantum efficiency ~0.4%, which are nearly one to two orders of magnitude higher than for previously reported AlGaN nanowire devices.

Chapter 9 reports the first demonstration of core-shell AlGaN nanowire LEDs in the challenging ~242 nm spectral wavelength range with detailed optical and electrical characterizations.

Chapter 10 summarizes the dissertation work. Some future directions and works have been proposed to overcome some of the challenges of III-nitride light emitters. Additionally, some new device applications have been proposed using high-quality III-nitride nanowires.

Chapter 2

MBE Growth, Processing and Characterization of InGaN/Al(Ga)N Nanowire Heterostructures

In recent years, a broad range of III-nitride nanowire optoelectronic devices have been demonstrated, including LEDs [76, 77, 134], lasers [174], photodetectors [175, 176], and solar cells [177, 178]. Such high-purity optoelectronic devices are grown by molecular beam epitaxy (MBE) and metal organic chemical vapor deposition (MOCVD). Some critical issues associated with planar structures can be potentially addressed by utilizing one-dimensional III-nitride nanowires grown by MBE. Moreover, these nanowires can be grown on lattice mismatched, cost effective Si substrates, and also on other foreign substrates [76, 77, 134, 136, 179]. III-nitride nanowires also offer significantly reduced dislocation densities and strain relaxation on the sidewalls [180]. Also, such MBE grown nitride nanowire LEDs promise significantly improved light extraction because of the effective large surface to volume ratios.

In this chapter, we discuss the III-nitride MBE growth, device fabrication, and characterization. It is worth mentioning that a significant amount of time in this study has been spent on growth optimization through varying critical growth parameters and also device fabrication and characterization.

2.1 III-nitride Nanowire Growth by MBE

Among the bottom-up approaches for nanowire synthesis, MBE has been considered to be the most efficient growth technique for high quality, defect free nanowire growth on lattice

mismatched foreign substrates. Also, MBE is a versatile technique for epitaxial planar structure growth. Both nearly defect-free planar structures and nanowires can be grown in an ultra-high vacuum (UHV) ambient conditions. This UHV ambient condition mostly eliminates any impurities in the growth chamber and minimizes interactions between the molecular beam and the impurities. It also gives extreme flexibility to characterize the growth *in situ*.

In general, MBE has a lower growth rate compared to MOCVD. This slow growth rate enables the formation of self-organized InGaN/GaN dot-in-a-wire structures (to be described in a later section). Nearly dislocation and defect-free Al-rich AlGaN or AlN nanowires can also be grown on a Si substrate. All the III-nitride nanowires presented in this thesis were grown in Veeco GeN-II and Veeco Gen Xplore catalyst-free plasma-assisted MBE systems under nitrogen-rich conditions. The Veeco GeN-II MBE system at McGill University is equipped with Ga, Al, In, Mn, Mg, Si, and Ge Knudsen effusion cells. The Veeco GeN II MBE system consists of three main vacuum chambers, an intro chamber, a buffer chamber, and a growth chamber.

Typically, a base pressure of $\sim 10^{-10}$ Torr is maintained in the growth chamber using a cryo pump and an ion pump. However, during the growth, a pressure of $\sim 10^{-5}$ Torr is typical while only the cryo pump is functioning. A radio frequency (RF) plasma source of ~ 350 - 400 W and constant N_2 flow (0.4-1 sccm) are used for different III-nitride wide bandgap nanowire growth. The RF power supply dissociates stable N_2 molecules into nitrogen species (neutral atoms, ions, and active molecules). Generally, the atomic nitrogen is very reactive, and reacts readily with Ga, In, and Al to form stable nitride nanostructures.

In this study, all the III-nitride nanowires were grown on low resistivity *n*-doped (111) Si substrates. Prior to the loading into the intro chamber, the Si wafers were thoroughly cleaned to

remove any organic particles/dust using conventional solvents including acetone, methanol/IPA, and DI water. Afterwards, the wafers were soaked into the 10:1 hydrofluoric acid (HF) or 6:1 buffered oxide etchant (BOE) for 1 minute to remove the native oxides. The clean Si wafers were again degassed in the intro chamber for 1 hour at 200°C, and again in the Buffer chamber for 2 hours at 1000°C. Subsequently, the wafer was loaded into the growth chamber. All these transfers, from intro chamber to buffer chamber, and buffer chamber to growth chamber were carried with a magnetically coupled transfer rod. In the growth chamber, reflection high-energy electron diffraction (RHEED) reconstruction 7×7 pattern was observed at around ~ 800 °C.

The RHEED pattern can be used as a powerful tool to monitor the *in situ* oxide desorption of the substrate surface. The RHEED system also enables *in situ* monitoring of the surface properties. In addition, during the nanowire growth, spotty patterns (an array of dots) were observed in the RHEED screen. The general information of the nanowires, including the size, shape, orientation, and density can be derived from the size, shape and density of the dots on the RHEED screen. Before growth, the wafer holder is flipped from the loading position to a growth position which faces the impinging material sources. For excellent uniformity of the impinging material, the holder was designed in such a way that it provides continual azimuthal rotation of the sample. This is commonly known as ‘CAR’.

2.1.1 GaN Nanowire Growth

The III-nitride (Al,Ga,In)N nanowire growth can be initiated by depositing a few monolayers of Ga for ~ 6 secs before the nitrogen plasma strike. But some reports have suggested that Ga deposition is not essential for stable GaN nucleation. However, in this study, a few monolayers of Ga were deposited as a seed layer for stable GaN nucleation that subsequently led to stable GaN

nanowire growth. In the plasma assisted MBE, III/V (Ga/N) ratio and the growth temperature critically determined whether planar or columnar growth would take place.

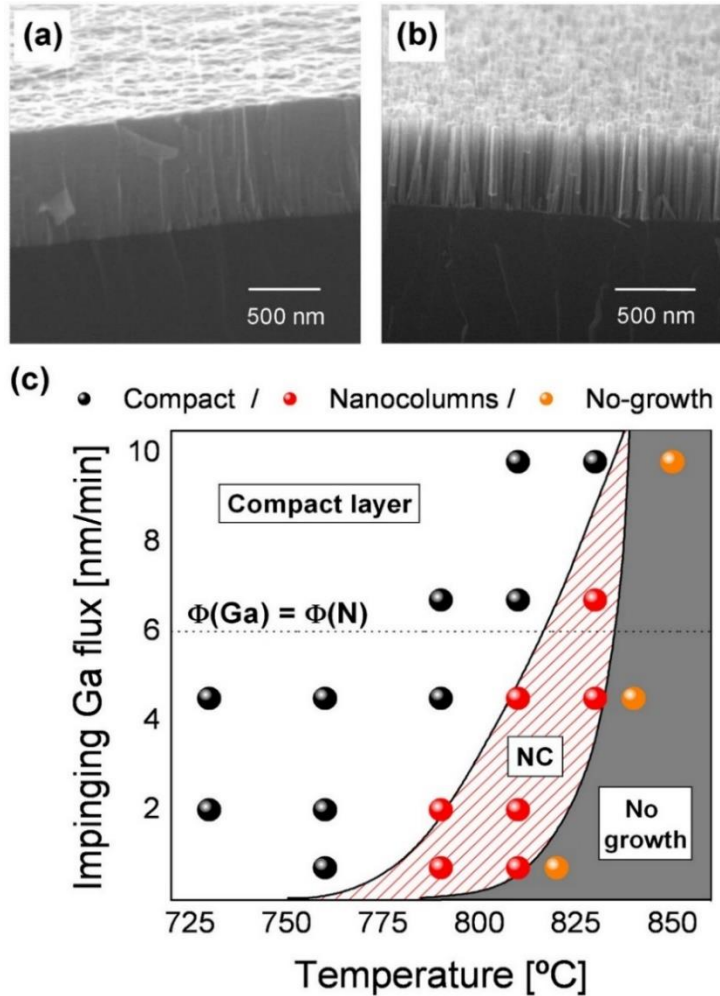


Figure 2.1: (a) Tilted SEM image of a GaN compact film (b) Tilted SEM image of GaN nanocolumn (c) growth phase diagram of GaN at a fixed N₂ plasma condition (flow and power) [181].

This critical growth phase diagram has been experimentally demonstrated by Calleja *et al* [181]. According to this result, depending on the III/V (Ga/N) flux ratio and the substrate temperature, the growth falls into three distinct regimes including, a) compact layer b) nanowire/nanocolumnar growth c) no growth regime (shown in Fig. 2.1 a,b,c) [181]. As presented in Fig. 2.1, at a high growth temperature all the impinging Ga atoms desorb and hence no growth occurs. And at too

low a growth temperature or with a too high Ga flux (Ga/N ratio higher than 1) compact layers form, as shown in Fig. 2.1a. At an intermediate growth temperature (between too high and too low) and under nitrogen-rich conditions (Ga/N ratio lower than 1) nanowire/nanocolumn growth occurs. If the substrate temperature is high enough, nanowires/nanocolumns can also be formed in a Ga-rich regime (Ga/N>1). The entire nanowire growth process primarily consists of nucleation and elongation/growth steps. The nucleation process of the nanowires is governed by the formation of nuclei of critical size.

In the early stages, the impinging Ga and N atoms can desorb from the surface and diffuse onto the surface or adsorb onto the surface by bonding with other atoms. This adsorption process leads to the formation of meta-stable nuclei. Then a cluster of previously bonded atoms form stable nuclei of critical size [182]. Stable nuclei then take the form of a semi-spherical shape. Also, an amorphous ~2-3 nm layer of SiN_x forms at the interface due to the reaction between the reactive Si substrate and the active nitrogen species at elevated temperatures [182, 183]. Such a SiN_x layer at the Si-GaN interface works as a compliant buffer and accommodates large lattice mismatch induced line dislocations and other defects [174].

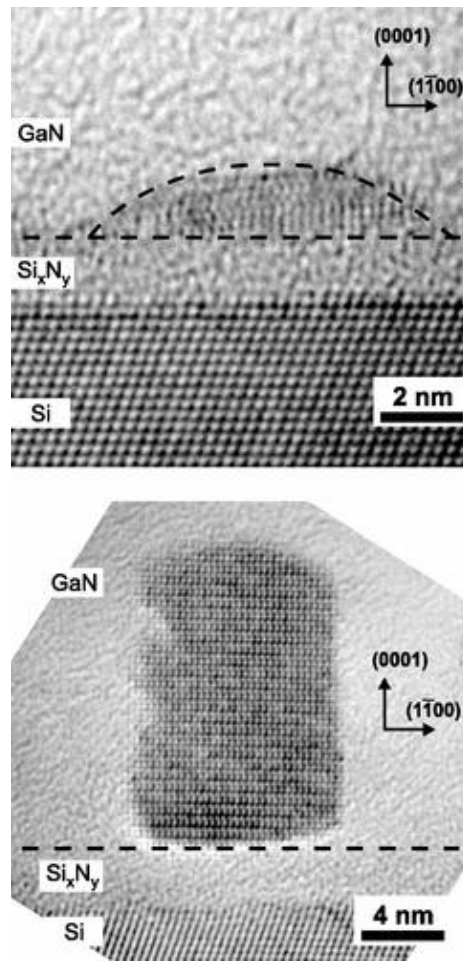


Figure 2.2 HRTEM images collected on dedicated samples grown for 7 and 16 min, revealing the following respective GaN island shapes at the onset of the nucleation process: spherical cap-shaped island and NW. The NWs are hexahedral. The shape of spherical caps is outlined for the sake of clarity [184].

Afterwards, a stable 3D GaN island start to form, and this spherical cap-shaped is nucleated on an amorphous SiN_x layer [183]. In the later stage, the stable GaN nuclei or island undergoes a shape transition, from a spherical cap shape to hexagonal nanowires (top c-plane facet and m-plane side facets) as shown in Fig. 2.2 [184]. If the Ga and N impingement continue, nanowires will grow further both vertically and radially, though the growth rate in both directions varies significantly. It has been reported that the vertical growth rate is about 33 times higher than the radial growth rate that eventually leads to high aspect ratio nanowires [185].

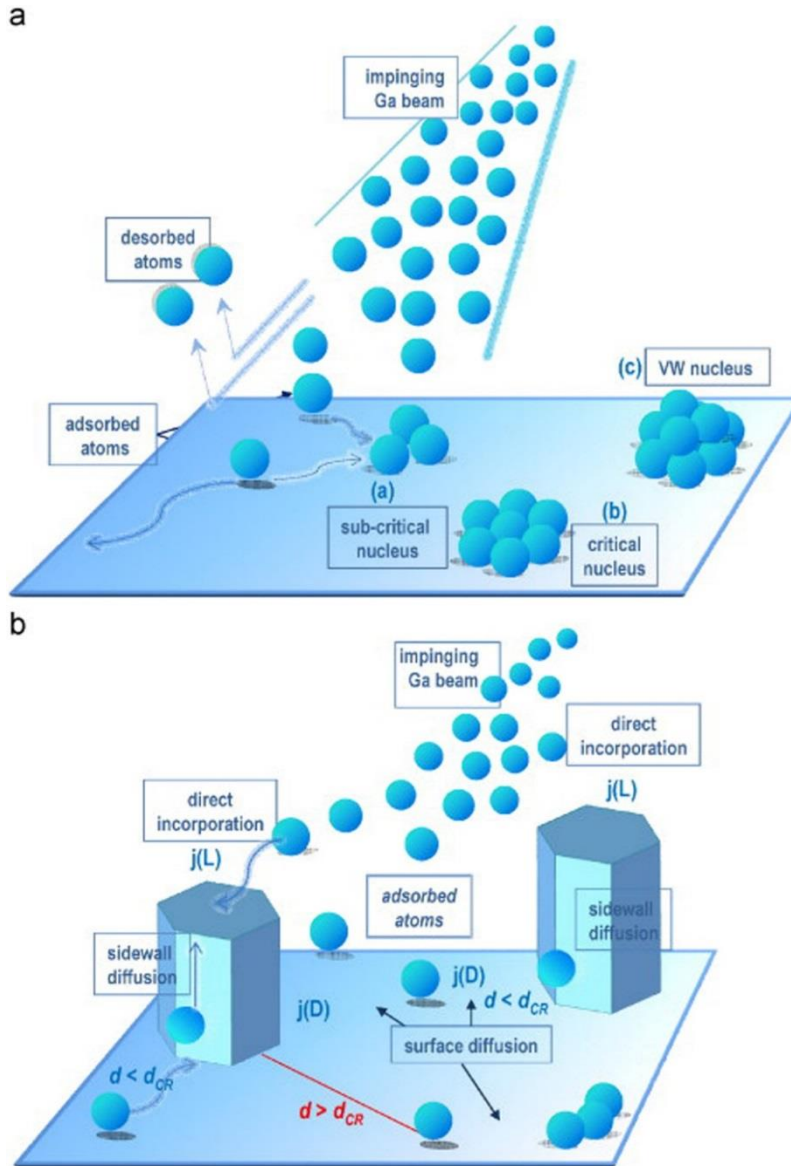


Figure 2.3 : (a) Kinetics of the atoms on the substrate during the nucleation process and early stage of nanowire growth. (b) Different diffusion process and Ga impingement process related to the growth of GaN nanowire [186].

As shown in Fig. 2.3a and Fig. 2.3b, the impinging Ga or N atoms can reach the top apex via different paths [186]. As shown in Fig. 2.4, these adatoms can arrive at the top plane (c-plane) directly and/or diffuse/climb along the side walls (non-polar m-planes) [186, 187]. This diffusion

driven process has been widely accepted and reported by various research groups as one of the major contributing factors for nanowire growth [186-193].

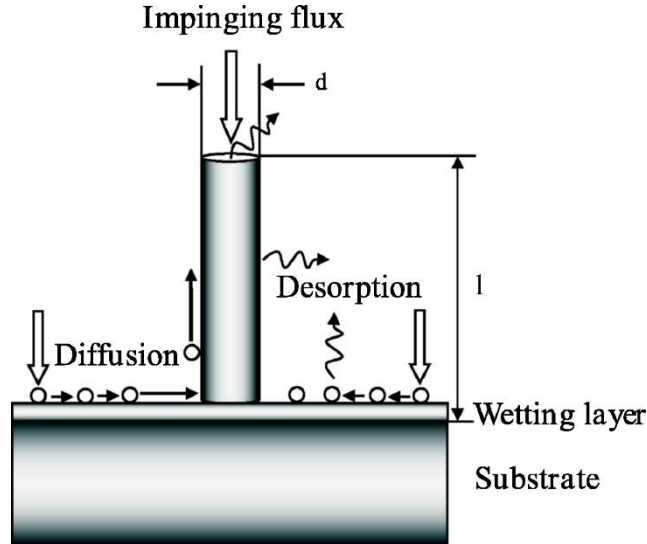


Figure 2.4: Schematic of the nanowire growth process including adatom adsorption, desorption, diffusion and nucleation by MBE process [187].

The amount of atoms present on the top c-plane can be higher than the impinging Ga atoms due to the direct diffusion through the m-plane side walls. It was also found that for a given Ga flux, the axial growth rate far exceeds the growth rate of the planar structures [192]. This is a direct consequence of the diffusion of Ga adatoms from the non-polar m-plane sidewalls. Despite the N-rich growth conditions, it has been found that the amount of N atoms is not proportionately enough, and hence, the axial growth rate is limited [190]. This is directly related to the different Ga and N adatoms diffusion length through the m-plane side walls. Even at high N-flux ($G/N < 1$) the amount of Ga far exceed the amount of N-present at the top planes (c-planes).

It was also suggested that the N and Ga adatoms sticking coefficients are not similar on the m-plane side walls, and this could be the driving force for the nanowire formation [193]. It was found

that the axial growth rate is proportional to the inverse diameter of the nanowire [187]. This suggests that previously grown nanowires with different diameters will receive a different amount of material for further growth, and that the growth rate will be different for different size nanowires. Consequently, thin nanowires will grow more quickly than thick nanowires, and the radial growth rate is dependent on the impingement on the sidewalls only, though it is much slower than the axial growth rate.

Plasma cell positioning also has a direct effect on the axial growth rate. In spontaneous nitride nanowire growth, both height and diameter can vary for several reasons. Firstly, nanowire growth is largely a statistical process, for instance, the GaN islands do not all nucleate and grow at the same time. Secondly, the growth rate is not similar for all the nanowires, and depends on the geometry of individual nanowires and their surroundings.

2.1.2 Nanowire Density, Coalescence and Defects

III-nitride nanowire density, grown on a Si substrate, by and large depends on the growth temperature and III/N ratio. In our study the nanowire density typically is in the range of $\sim 10^{10} \text{ cm}^{-2}$, it has been found that adjacent nanowires tend to coalesce together when the nanowire density is beyond $\sim 10^8 \text{ cm}^{-2}$. Coalescence generally takes place when the orientation between the adjacent nanowires is misaligned. This is due to the tilting about the normal to the Si substrate of an angle of a few degrees. Due to this mis-orientation or tilt, the neighboring nanowires touch or twist each other, and become a single nanowire entity with an increased diameter (top portion).

This mis-orientation could be due to surface roughness or thickness variation in the amorphous SiN_x interlayer [184]. Also, increased radial growth for long nanowires contributes to the coalescence. Because of the coalescence, a network of boundary dislocations form to

accommodate this twist/tilt associated strain [194-196]. If the strain cannot be accommodated elastically, basal planes stacking faults are formed at the coalescence joints [194]. Mg doping incorporation is also found to be difficult for coalesced nanowires due to triple twin domains [197, 198]. Conversely, high Mg flux also promotes lateral nanowire growth, in the form of coalescence.

III-nitride nanowire density also depends on the degree of coalescence [199]. It has been seen that nanowire density tend to increase at first, then gets saturated and subsequently decreases due to coalescence [184]. However, longer nanowires tend to show a higher degree of coalescence compared to shorter nanowires. Coalescence generally leads to defects (deep level traps), these defects act as non-radiative recombination centers [184, 194-196]. These factors severely degrade the optoelectronic device performance of III-nitride nanowires. However, the coalescence phenomenon can be potentially mitigated by increasing the growth temperature and/or III/V ratio which significantly reduces the density of nanowires [199].

Nanowires density depends on the density of the spherical cup shaped islands during the nucleation period. Afterwards, the III/V ratio and the growth temperature critically influence the spherical cup-shape transition, and therefore contribute to the decrease or increase of the density of the nanowires [200]. However, an intermediate degree of top surface coalescence (not too much, keeping the nanowire density high) is desirable for device processing (which will be discussed in the later section).

2.1.3 Growth of InGaN/Al(Ga)N dot-in-a-wire structure

In this thesis, various self-organized InGaN/Al(Ga)N quantum dot-in-a-wire based designs have been extensively studied. These designs included conventional p -GaN/i-(InGaN/Al(Ga)N/ dot-in-wire)- n -GaN nanowire LEDs, p^{++} -GaN/InGaN/ n^{++} -GaN tunnel junction integrated p -GaN down single active region InGaN/GaN dot-in-a-wire LEDs, and p^{++} -GaN/InGaN/ n^{++} -GaN tunnel junction integrated p -GaN down cascaded multiple active region LEDs.

In addition, p^{++} -Al(Ga)N/Al/ n^{++} -GaN tunnel junction integrated InGaN/GaN dot-in-a-wire and core-shell AlGaIn, p -GaN down LEDs were grown. These structures consisted of a Si-doped GaN base, self-organized p -type modulation doped InGaN/Al(Ga)N quantum dots, a Mg-doped GaN top/cap layer, heavily doped GaN/InGaN/GaN polarization engineered tunnel junctions, and epitaxial metal/semiconductor (Al/GaN) tunnel junctions. LED device performance critically depends on the growth of these individual segments.

2.1.4 Si-/Ge-doped GaN Base

To form the conventional dot-in-a-wire LED, a (111) ‘‘epi ready’’ n -doped Si substrate with a low resistivity $< 0.001 \Omega\text{-cm}$ was used. During Si-doped n -type GaN growth, the growth temperature was kept between 750°C to 850°C and the Ga flux was varied between 5×10^{-8} Torr to 1×10^{-7} Torr. In this growth condition, n -type GaN nanowire growth rate was typically 3 nm-5 nm/min, keeping an RF power of 350-400 W and a nitrogen flow rate of 0.6-1 sccm. For typical LED growth with good nanowire morphology, the Si cell temperature was kept at 1300°C to 1350°C , that gave an electron concentration of about $1 \times 10^{19} \text{ cm}^{-3}$. It is worthwhile mentioning that too high or too low Si/Ge doping significantly changes the nanowire morphology and also the nanowire density. Ge

doping was also used with a flux and cell temperature ($\sim 1100^\circ\text{C}$) equivalent to Si doping for *n*-type doping.

2.1.5 InGaN/GaN Dots (active region) Growth

Self-organized multiple InGaN/GaN quantum dots incorporated in the nanowires, serve as the device active region for efficient photon emission. These InGaN/GaN dots form the active region, where electrons and holes recombine and emit photons. In this study, 10 InGaN (3 nm)/GaN (3 nm) self-organized dots and 5 InGaN/GaN (3 nm)/GaN (3 nm) dots were grown for single active region and multiple active regions LEDs, respectively.

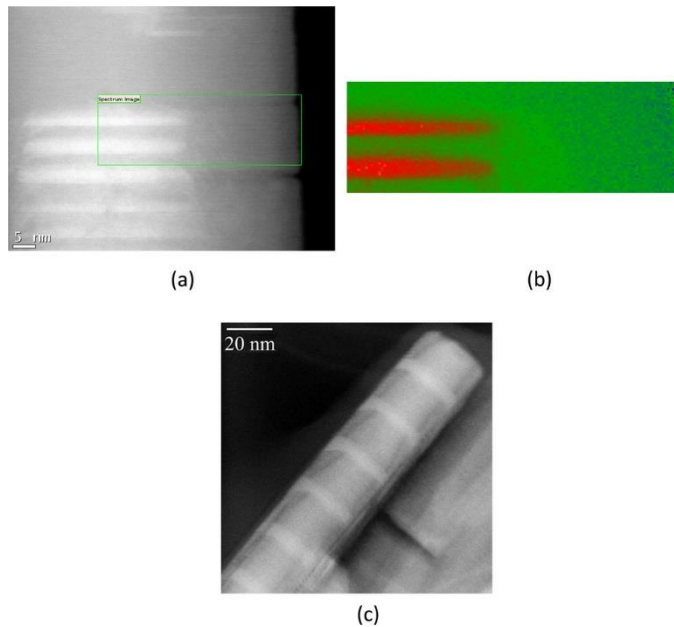


Figure 2.5: HAADF image of self-organized QD formation [201].

Blue, green, red, and/or white light emission can be achieved by varying the In composition of the dots in the range of ~ 10 -50%. While GaN is grown at $\sim 750^\circ\text{C}$ - 850°C , InGaN/GaN dots are grown at relatively low substrate temperatures of 570 - 690°C , to enhance the In incorporation into the dots. MBE grown InN decomposition temperature is about $\sim 470^\circ\text{C}$, and high-quality InGaN cannot

be grown below 500°C. Therefore, the InGaN/GaN growth temperature is a trade-off between In decomposition and high quality InGaN. As shown in the HAADF image (Fig. 2.5), in an optimized growth condition, InGaN/GaN QDs with diameter smaller than the nanowire is clearly demonstrated [201]. Such self-organized QDs can be achieved by varying the growth temperature and the In/Ga flux. In addition to substrate temperature, In flux is also important to get optimized radiative efficiency with the desired color emission. Too low a growth temperature leads to weak photoluminescence intensity due to In adatom related defects, and too high a growth temperature leads to inhomogeneous broadening due to In phase segregation. The InGaN/GaN quantum dots are also *p*-type modulation doped using Mg to enhance the hole injection and carrier transport process [134].

2.1.6 Mg-doped AlGaN Blocking Layer and Core-Shell Nanowire

Immediately after the InGaN/GaN QDs (active region), a large bandgap Mg-doped AlGaN blocking layer was incorporated. The thickness of the AlGaN electron blocking layer is about 8 nm-10 nm with an Al composition ~8%-20%. For high brightness core-shell LEDs, an AlGaN layer of ~80 nm-90 nm was formed in the formation of the AlGaN shell surrounding the InGaN/GaN dots (core region). The AlGaN shell can cover a large part of the nanowire structure due to the diffusion-controlled growth process. Al-content in the shell and the thickness of the shell layer can be controlled by growth duration and the Al/Ga flux ratio.

Here, large bandgap AlGaN offers superior carrier confinement by drastically reducing surface recombination. In addition, InGaN/AlGaN dot-in-a-wire core-shell nanowire structure was also exhibited. In this unique structure, during the AlGaN barrier growth, an AlGaN shell is also

spontaneously formed around the sidewall of the nanowire, which leads to drastically reduced non-radiative surface recombination.

2.1.7 Mg-doped GaN Cap

Compared to the Si doped *n*-type GaN nanowire growth, Mg-doped *p*-type GaN growth is much more challenging because of several factors. First, due to oxygen impurity incorporation and N vacancy, high *n*-type background doping is always present in GaN nanowires. Second, low ionization efficiency of Mg in GaN results in poor hole doping. Bhattacharya *et al.* demonstrated for the first time that MBE growth at relatively low growth temperature, and under N-rich growth conditions leads to a much higher hole concentration ($\sim 3 \times 10^{18} \text{ cm}^{-3}$) in Mg-doped GaN planar structure.

In this study, the Mg doped *p*-type GaN nanowire growth was done at a relatively low temperature and with a relatively high Mg flux to promote efficient Mg incorporation. During Mg-doped *p*-type GaN growth, the growth temperature was kept between 720°C to 790°C and the Ga flux is varied between 5×10^{-8} Torr to 1×10^{-7} Torr. For typical LED growth with good nanowire morphology, Mg cell temperatures were kept at 230°-275°C and this gave hole concentrations of about $\sim 1 \times 10^{18} \text{ cm}^{-3}$. In these growth conditions, *p*-type GaN nanowire growth rate is typically ~ 3 nm/min, with an RF power of 350 W and a nitrogen flow rate of 1 sccm.

2.1.8 *n*⁺⁺-GaN/InGaN/*p*⁺⁺GaN tunnel junction growth

In this study, in addition to conventional *p*-GaN up *p-i-n* nanowire LEDs, *n*-GaN up tunnel junction integrated nanowire LEDs were studied. In this polarization engineered tunnel junction, In concentration and InGaN thickness is critical for polarization induced band bending, and associated efficient inter-band tunneling. In this context, we have extensively studied the tunnel

junction LED performance by varying the In composition (20% to 40%) and InGaN thickness (2 nm to 6 nm).

Doping concentration and degeneracy in the n^{++} -GaN and p^{++} -GaN layers in the tunnel junction were controlled by the Si (n -doping) and Mg (p -doping) effusion cell temperatures. In addition, n^{++} -GaN (~ 10 nm-20 nm) and p^{++} -GaN (~ 20 nm-30 nm) layer thicknesses were carefully optimized based on the tunnel junction nanowire LED performance. Also, n^{++} -GaN, InGaN, and p^{++} -GaN layers were grown at 640°C-660°C. The integration of n^{++} -GaN/InGaN/ p^{++} GaN tunnel junctions for a wide range of nanowire LEDs applications are discussed in chapter 3 and chapter 4.

2.1.9 n^{++} -GaN/Al/ p^{++} GaN tunnel junction growth

For the n^{++} -GaN/Al/ p^{++} GaN tunnel junction growth, a thin Al epitaxial layer is epitaxially inserted in between the n^{++} -GaN and p^{++} GaN layers. Unique to this structure, the Al layer serves as a tunnel junction by forming an ohmic/quasi-ohmic contact to the heavily doped n^{++} -GaN and p^{++} GaN layer (to be discussed in the later chapters). The n^{++} -GaN and p^{++} GaN layer growth recipe is identical to the growth of the previously mentioned polarization engineered n^{++} -GaN/InGaN/ p^{++} GaN tunnel junction growth. The epitaxial metal Al layer was grown at relatively low temperature (~300°C to 550°C) with a thickness of (~1 nm to 6 nm). The integration of the n^{++} -GaN/Al/ p^{++} GaN tunnel junction into different visible/UV LEDs are discussed in chapter 7, 8 and 9.

2.2 UV Nanowire LED Growth

AlGaIn based high-efficiency UV LEDs have drawn considerable attention due to their broad range of important applications. In comparison to AlGaIn based planar UV LEDs, AlGaIn nanowires

have low defect densities, and it was previously demonstrated that Mg-dopant incorporation can be significantly enhanced in AlN/GaN nanostructures as compared to planar structures [202]. Compared to InGaN/GaN visible dot-in-a-wire LEDs, AlGaN based ultraviolet nanowire LEDs require more careful optimization of the growth parameter due to the large lattice mismatch between the AlGaN and the Si substrate, difficulty in impurity doping (specially *p*-type doping), and different growth kinetics of Al adatoms.

As discussed in the previous chapter, a large lattice mismatch results in a higher dislocation density and defects that ultimately leads to poor material quality. Different Al composition AlGaN nanowires growth processes generally involves the use of nitrogen (N) rich conditions to promote the formation and nucleation of nanowire structures [203]. However, in N-rich condition, Al-adatom migration is significantly reduced due to the strong bond between Al-N as compared to Ga-N [204]. This reduced Al adatom migration leads to non-uniform Al and Ga incorporation and associated compositional non-uniformity at the nano and atomic scale [202, 205-207]. In addition to *p*-type Mg doping, such non-uniform Al and Ga incorporation substantially hinder the wavelength tunability of AlGaN ternary nanowires. Such a bottleneck in wavelength tunability further limits the realization of deep UV nanowire LEDs in the shorter wavelength range.

In this thesis, it has been shown that MBE grown Al-rich AlGaN nanowires with a relatively uniform compositional distribution can be achieved by an optimized growth condition which is significantly different from the conventional nitrogen rich growth condition. This growth process involved the use of a GaN nanowire template to promote the formation of AlGaN nanowires, and subsequently, a low nitrogen flow rate was used to enhance the surface migration of the Al adatoms. In this optimized growth regime, a precise control on the optical bandgap of ternary AlGaN nanowires can be readily achieved by varying the substrate

temperature, instead of changing the Al and Ga beam equivalent pressures (BEPs).

2.3 Characterizations of Nanowires

2.3.1 Characterization of as grown nanowires by SEM

Scanning electron microscopy (SEM) is an excellent tool to characterize the III-nitride nanowires. SEM morphology of as-grown nanowire provide some qualitative information on the nanowire material quality, nanowire density, Si or Mg doping effects on the morphology, Ga/N ratio effect on the growth rate, nanowire diameter, and growth temperature/flux effect. Additionally, the effect of various lattice-mismatched substrates on the nanowire morphology can be identified. In our study, 45° tilted SEM microscopy was regularly performed after the nanowire growth using a HITACHI FE-SEM.

2.3.2 Characterization of as-grown nanowires by TEM

In the course of this study, transmission electron microscopy (TEM) was used on numerous occasions. TEM imaging gives a general idea about the crystalline quality of the nanowires, coalescence, elemental composition, defects/dislocations and nature of InGaN/(Al)GaN QD formation. In this study, polarization engineered tunnel junction cascaded nanowire LEDs and monolithic metal/semiconductor tunnel junction nanowire LEDs were also characterized. In general, a thin sample was prepared by mechanical grinding and ion milling for effective TEM analysis. For our TEM study, the nanowires were typically scratched-off from the Si or Sapphire substrate with a razor blade, and subsequently were dispersed on a Cu grid.

A single representative nanowire was used to characterize the crystalline quality and overall structure. In this study, various high-resolution TEM (HRTEM), high angle annular dark field

(HAADF), and energy dispersive X-ray spectrometry (EDXS) analyses were performed. Such TEM imaging is highly sensitive to the atomic number (Z) of the elements. Therefore, for III-nitride TEM analysis, only metal atoms are seen, and elemental mapping gives greater sensitivity to the detection of metal atoms. This atomic number dependent analysis is called Z-contrast mode.

2.4 Device Fabrication

While planar light-emitting diodes fabrication is a mature technology, nanowire LED processing and fabrication are still in its infancy. According to recent reports, both electroluminescence (EL)

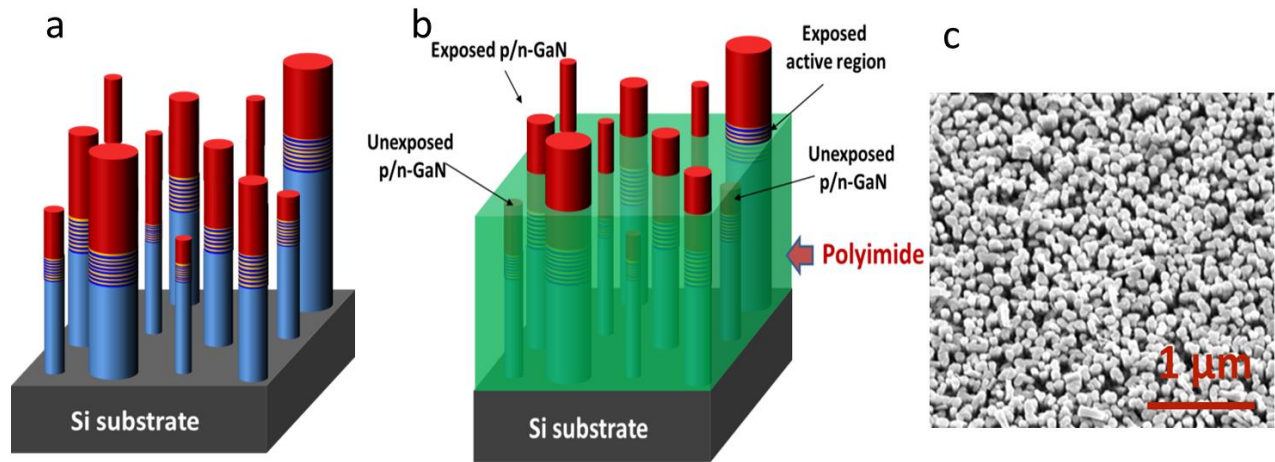


Figure 2.6: Surface planarization by polyimide resist layer of different height/shape nanowires.

intensity and current-voltage (I-V) characteristics can be severely affected by processing conditions [208-211]. However, current nanowire LEDs still rely on spontaneously grown self-assembled nanowire arrays. In this kind of growth, variations in the nanowires height, diameter, and the nanowires spacing are apparent. It was previously reported that only 1% of all the self-assembled nanowires effectively emit light [208-211]. Therefore, the number of electroluminescence nanowires has to be dramatically increased for this to be a practical lighting

application. In addition to improvement in growth, efficient carrier injection into the active regions also needs to be improved.

In this context, nanowire LED processing plays an important role, but several limiting factors need to be carefully addressed to solve processing related issues. Nanowire LEDs show a relatively high turn-on voltage and low output power compared to their planar counterparts. The relatively high voltage drop across the devices could be due to the *p*-region, active region, device fabrication, or from the nanowire growth itself. To this end, we found that during GaN nanowire growth ~2-3 nm of amorphous SiN_x was formed at the nanowire-Si substrate interface, which could lead to relatively high resistance for nanowire LEDs grown on a Si substrate [140, 212, 213].

During the device fabrication process, a polymer resist layer (polyimide) is often used to passivate and planarize the nanowires [77, 134] (Fig. 2.6). Due to variations in the height of the spontaneously formed nanowire arrays, some of the nanowire top surfaces may still be covered with some residual polymer, which leads to increased device resistance. These issues can potentially be addressed by developing highly uniform nanowire arrays using the selective area growth technique. The relatively low output power and low external quantum efficiency are directly related to the inefficient light extraction, due to the underlying Si substrate absorption, as well as the low carrier injection efficiency of nanowire LEDs. While these limiting factors are associated with some of the growth bottlenecks, of course some are also related to nanowire processing.

2.4.1 Surface Planarization

As mentioned earlier, spontaneously grown nanowires by MBE show variations in height and diameter. Therefore to make a uniform contact throughout the entire surface, the non-uniform

surface needs to be planarized. It is worth mentioning that the fill factor (nanowire surface coverage) is estimated to be ~30%-50% depending on the growth conditions. In this context, an insulating material is required to fill the gaps between the nanowires to avoid a short circuit path between the top metal (*p*-/*n*-GaN contact layer) and the bottom contact. Since this planarization is critical for effective visible LED fabrication and efficient light extraction, the refractive index and the transparency of the filling material in the visible spectral wavelength are very important.

Various filling materials including spin-on glass (SOG), parylene, HSQ, and polyimide have been successfully utilised in current InGaN/GaN nanowire LEDs [77, 134, 211, 214]. However, in this study, polyimide from HD microsystems (PI 2610) was used. This polyimide generally has a viscosity in the range of 25-30 poise and a dielectric constant of 2.9. Diluted polyimide was prepared by a standard process, and this dilution process helped to achieve different resist thicknesses which can be used for different nanowire LED fabrication, depending upon the nanowires height. For a standard nanowire LED fabrication, a polyimide resist layer was spin coated on to the sample. The spin coating time and spin speed were carefully calibrated to get a uniform polyimide resist layer. As such, a uniform thickness was achieved over the whole surface of the nanowires.

The polyimide effectively fills up the gaps between the nanowires, and a ~700-800 nm excess resist layer sits on the surface of the nanowires. Subsequently, the top of the nanowires was exposed by iterative O₂ plasma (RF power 100 W, 100 mTorr pressure) etch back process. In this process, the polyimide layer was etched, and the sample subsequently checked by SEM. This iterative etch-back process is considered to be the most time consuming and meticulous step. It is also worthwhile mentioning that the processed LED performance largely depends on this step.

These etch back steps were carried out in such a way that most of the nanowires were well exposed for carrier injection. Due to the non-uniform height and shape, some of the nanowires were buried by some residual polymer. In general, over etching leads to leaky LED devices and under etching leads to resistive LED devices. After the etch back process, the polyimide layer was hard baked at 300^o C for 25 mins. These issues can be potentially addressed by developing highly uniform nanowire arrays using the selective area growth technique.

2.4.2 Device Contact and subsequent processing

Due to variations in the height of the nanowires, the metal contact and associated surface coverage to nanowires ratio plays an important role for the device performance. Recently, Musolino *et al.* reported that instead of Ni/Au/ITO hybrid layer, solely using an ITO single layer can make better ohmic contact to the nanowires [211]. After the polyimide planarization step, the pattern of different mesa sizes (0.3×0.3 mm², 0.5×0.5 mm², 1×1 mm²) was defined by conventional optical lithography. The process is shown in Fig. 2.7.

Note that, a 37% HCl cleaning was performed to remove any residual oxides after the photolithography step. Subsequently, a thin layer of Ni/Au (5 nm/ 5 nm) or Ti/Au (5 nm/ 5 nm) was deposited by e-beam evaporation to serve as the *p*-/*n*-metal contacts. This 10 nm Ni/Au or Ti/Au layer has a transmittance of approximately 40%. After this, ~120-150 nm indium tin oxide (ITO) single layer was sputtered to serve as a current spreading layer. The Ni/Au/ITO or Ti/Au/ITO layer was then lifted off by acetone or AZ 1165 remover depending on the metal thickness. Later, a rapid thermal annealing (RTA) was performed in N₂ ambient at 500-600°C for 1 min to achieve low resistance alloyed contact. In addition, another RTA step was carried out for the ITO layer (5 mins, N₂ ambient), this annealing step improved the ITO transmission and

resistivity. Then a 100 nm SiO₂ layer was deposited by conventional PECVD technique for surface passivation. After that, another photolithography step was performed to open the window of the previously defined metal mesa. The mesa window was subsequently opened by a buffered oxide etchant (6:1). Finally, another optical lithography step was carried out to define the metal grid contact to the previously defined metal mesa. Ti/Au (20 nm/ 100 nm) was deposited to make the metal grid contact.

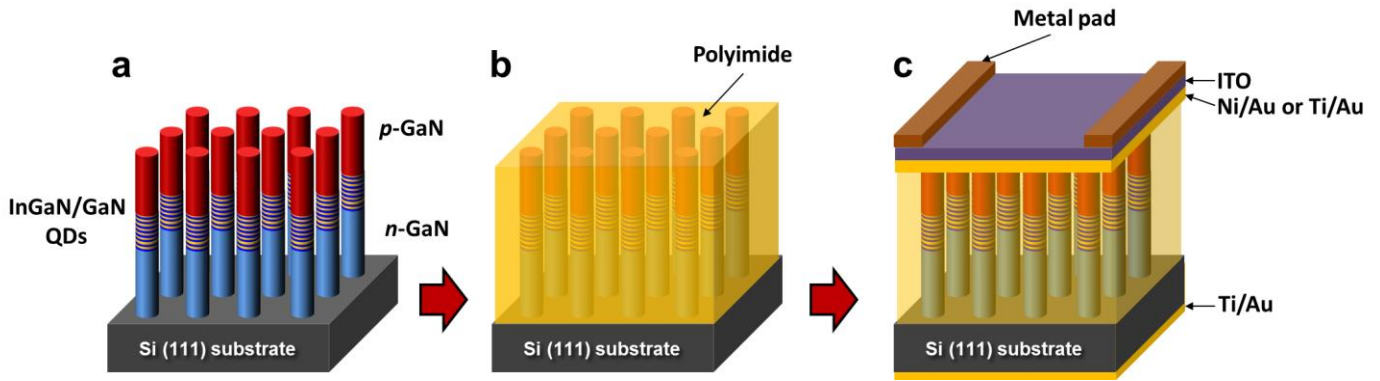


Figure 2.7: Step by step nanowire LED fabrication process.

2.4.3 UV LED Fabrication

As described in the previous section, for AlGaN-based deep UV-LED growth, different growth parameters were used, as such, the nanowire's top portion coalesced, and the nanowires were more or less uniform and flat. In this process, self-planarization occurs, and it by and large eliminates the need for any planarization process and associated usage of any filling material. For UV LED fabrication, we also do not need an ITO layer. Except for this planarization process and the ITO deposition process, UV LED fabrication is identical to that of the visible LED fabrication described in previous sections.

2.5 Photoluminescence Study

The optical properties of GaN nanowires can be characterized by a photoluminescence study. In this study, we used 325 nm and 405 nm lasers. Typically, photoluminescence is a non-contact, non-destructive technique of characterizing the electronic structures of different materials. In this process, light (photon) is directed onto a sample, upon photon absorption of an UV or visible photon with an energy greater than the band gap energy (the energy between the valence band and conduction band) of the material, an electron-hole pair is generated and the electron and hole are excited to states high up in the conduction and valence band.

The excited electron or hole will not remain in the initially excited states for long, and instead will very quickly relax back ($\sim 10^{-13}$ s) to the low energy state within their respective energy bands by emitting phonons. Consequently, the electron and hole finally arrive at the bottom of the conduction band and top of the valence band. After that, the electron-hole recombine radiatively with the emission of a photon (luminescence) and does not necessarily need to involve any phonon (for direct bandgap) for the conservation of momentum. In the nonradiative process, the electron's energy is transferred to the impurities or defects in the material and dangling bonds at the surface. In indirect bandgap material, both photons and phonons are associated with the conservation of momentum.

Radiative recombination takes place across the band gap of the material through various transition mechanisms. These transition processes are briefly discussed in the following sections and summarized in Fig. 2.8. Photoluminescence is an important tool to determine the bandgap of the materials, the impurity levels and defect detection, the recombination mechanism, and material quality dopant incorporation etc.

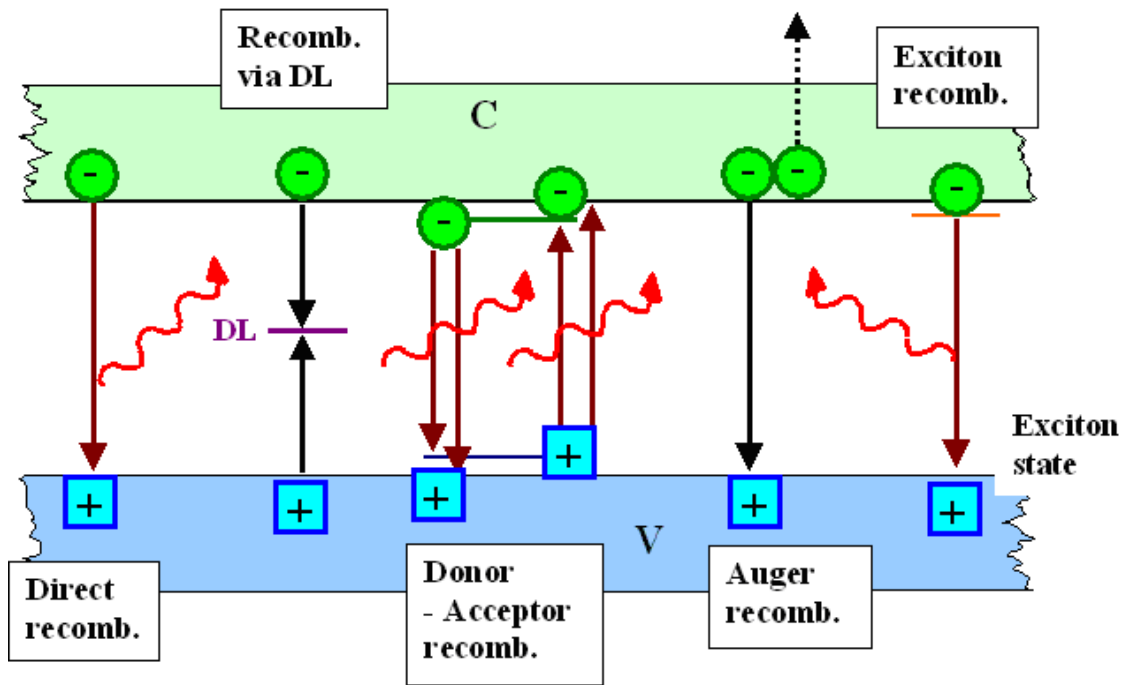


Figure 2.8: Different donor-acceptor recombination and other transition process [372].

2.5.1 Band-to-Band Direct Transition

Band-to-band transition generally refers to the radiative recombination of an electron in the conduction band with a hole in the valence band. This direct transition normally happens for direct band gap pure crystals at relatively high temperatures.

2.5.2 Excitonic Transition

Excitonic transitions are observed at low temperatures in a defect free pure crystal. The free exciton is generally composed of an electron in the conduction band, and a hole in the valence band bound together by the coulomb interaction. The exciton associated emission is sharp since the exciton levels are well defined. Bound excitonic transitions are observed in intentionally doped high purity material. The exciton can be bound with an impurity atom (either donor or acceptor). The energy of the free exciton is calculated to be $(h\nu = E_g - E_x)$, where E_g = electron energy in the conduction band edge, E_x = hole energy in the valence band edge. The energy of the bound exciton is lower than the

free exciton energy, and can be expressed as, ($h\nu = E_g - E_x - E_b$), here E_b refers to the binding energy of the exciton to the impurity. In contrast to band-to-band transition, excitonic transitions are often observed at low temperatures.

2.5.3 Band-Edge to Donor/Acceptor Transition

This process involves the transition of a free carrier from the conduction/valence bands to a bound acceptor/donor.

2.5.4 Donor-Acceptor Pair Transition

In donor-acceptor pair (DAP) transition, the recombination occurs when an electron moves from the neutral donor to the neutral acceptor. After the transition process, donor and acceptor are ionized, and then the coulomb attractive force acts between them. The DAP transition results in a broad emission spectrum.

2.5.5 Non-Radiative Recombination

In general, non-radiative recombination takes place in the presence of defects in the crystal. These defects include dislocations, vacancies, interstitials, and foreign atoms. Such defects have energy levels within the bandgap of the semiconductor. The transition between the carriers (electrons/holes) to these defects levels results in the emission of a phonon. Another non-radiative recombination process is Auger recombination. The Auger recombination process was explained in chapter 1.

2.6 Electroluminescence Study

While photoluminescence is a non-contact, non-destructive technique for optical characterization, electroluminescence (EL) is performed on a fully processed device. In contrast to PL, EL is simultaneously an optical and electrical phenomenon. Like PL, EL also involves radiative recombination of electrons and holes. A p - n junction is formed by doping different regions of a semiconductor, either by donor or acceptor (n - or p -) type doping. At the interface of the p - or n -doped semiconductor, excess electrons (in the n -side) and excess holes (in the p -side) are present.

There is a net diffusion of electrons and holes from either side and formation of an equilibrium condition. At the interface of a p - n junction, there is a net positive (negative) space charge in the n -(p -) side. Associated with this space charge, there is an electric field directed from the n - region to the p - region. This electric field prevents further diffusion in either side, the Fermi level is aligned in the n - and p -side. The space charge region is called the “depletion region” since there are no mobile carriers in this region, and the electric field is also confined to this depletion region. The doping levels can modulate the space charge region or the depletion region in the p - and n -sides. If a positive voltage is applied to this p - n junction, the electric field and depletion region is reduced, and hence the excess electrons (holes) are injected from the n -(p -) region to the p -(n -) region. Electroluminescence results from the radiative recombination of electrons and holes.

2.6.1 IQE and EQE

A light-emitting diode’s performance metric, namely internal quantum efficiency (IQE) and external quantum efficiency (EQE) can be calculated through photoluminescence and electroluminescence studies. In general, the number of emitted photons and the number of injected

charge carriers are important in assessing the quality of an LED. The IQE generally quantifies the efficiency of an LED by photon emission, and is expressed by the following equation:

$$IQE = \frac{\text{number of photons emitted from the active region (QW) per second}}{\text{number of electrons injected into the active region}}$$

$QW = \frac{P_{int}/(hv)}{\left(\frac{I}{e}\right)}$ Where, P_{int} represents the emitted optical power from the active region, I is the current injected into the active region, hv is the photon energy, and e represents the elementary charge. For an ideal LED, the IQE should be unity, meaning that for every electron-hole pair one photon would be emitted. In real device, because of re-absorption or internal reflection of the light, not all the photons created can escape out of the crystal. Therefore, the light extraction efficiency (η_{ext}) is also very important.

$$\eta_{ext} = \frac{\text{number of photons emitted into free space per second}}{\text{number of photons produced per second}} = \frac{L/(hv)}{P_{int}/(hv)}$$

Where L is the optical power emitted into free space. The product of internal and extraction quantum efficiencies gives the external quantum efficiency (EQE):

$$EQE = IQE \cdot \eta_{ext} = \frac{L}{hv} \left/ \left(\frac{I}{e}\right) \right. .$$

The IQE and EQE can be measured from different photoluminescence and electroluminescence measurements. The IQE can be measured from the temperature dependent PL/EL measurements. This measurement is based on the assumption that, at cryogenic temperatures, the defect-related recombination is nearly zero due to the thermal freeze out effect. Hence, the PL/EL intensity is at its maximum at low temperatures. In general, IQE is calculated as the ratio of the room temperature

integrated PL/EL intensity to the low temperature integrated PL/EL intensity. However, it has been reported that the PL intensity is not saturated at low temperatures for InGaN [215]. It is worthwhile mentioning that the IQE calculated in this method depends on the excitation level and the doping density of the material [216, 217].

2.7 Summary

In this chapter, a general overview of plasma assisted molecular beam epitaxial growth of III-nitride nanowire visible and deep UV LEDs has been presented. Various InGaN/Al(Ga)N quantum dot-in-nanowire visible LED growth details have been described. In addition, III-nitride deep UV LED growth optimization has been described. The III-nitride nanowire LED device fabrication, structural, electrical and optical characterizations were discussed. Details of the structural and optical characterizations procedures, including SEM, HR-TEM, EDX, IQE , EQE etc. were also discussed.

Chapter 3

Multiple-Active Region InGaN/GaN Tunnel Junction Nanowire White-Light Emitting Diodes

Some of the contents of this chapter were previously published *Nano Lett.*, 2015, 15 (10), pp 6696–6701[218].

As described in chapter 1, the efficiency of current LED lighting technology has been limited by several factors. First, the current LED lamps still rely on the use of phosphors to down-convert blue light into green and red light. Associated with this down-conversion process is an energy loss of ~30%, or more. Second, the performance of GaN-based LEDs has been limited by the inefficient current conduction of *p*-GaN, which typically has a resistance ~ 100 times higher than that of *n*-GaN [219], leading to poor current spreading [147, 220], reduced efficiency, and efficiency droop. These critical challenges can be potentially addressed by employing the scheme of tunnel junction and the integration with nanowire LED structures. Various design schemes, including GaN/Al(Ga)N/GaN [149-151, 173], GaN/InGaN/GaN [219-224], and GaN/GdN/GaN [145, 225] tunnel junctions have been implemented in GaN-based LED structures. However, the tunneling probability has been severely limited by the difficulty in creating a highly doped *p*-region [149, 222, 223]. Recently, it has been demonstrated that dopant incorporation can be significantly enhanced in nanowire structures, due to the much-reduced formation energy in the near-surface region [226-228]. Moreover, compared to conventional GaN quantum well devices, GaN nanowire LEDs can exhibit significantly reduced dislocation densities and polarization fields [76, 180, 186, 229-231]. Nanowire LEDs with tunable, multi-color emission have been demonstrated, which can

be epitaxially grown on extremely low cost, large area Si substrates [76, 77, 141, 232-236]. In spite of these intensive studies, the incorporation of tunnel junction in nanowire LEDs has not been reported to our knowledge.

In this context, we have investigated the incorporation of GaN/InGaN/GaN polarization-enhanced tunnel junction in nearly defect-free InGaN/GaN phosphor-free nanowire white LED heterostructures. We have demonstrated, for the first time, an entirely new *p*-contact free InGaN/GaN nanowire LED. With the use of tunnel junction interconnect, we have shown that multi-junction phosphor-free nanowire LEDs can exhibit improved light intensity and reduced efficiency droop. Due to the repeated carrier usage, such devices operate at low current and high voltage. This work offers a new avenue for realizing high efficiency LEDs that can operate under a large range of voltage biasing conditions and can possibly eliminate or greatly simplify the electrical driver required in today's LED lighting systems.

3.1 Design and Band diagram

Schematically shown in Fig. 3.1a, we have first studied four types of nanowire LEDs, including a conventional InGaN/GaN dot-in-a-wire *p*-GaN up LED (LED A), single active region (SAR) ($n=1$) tunnel junction dot-in-a-wire *p*-GaN down LED (LED B), and multiple-active region (MAR) ($n=3$) tunnel junction dot-in-a-wire LEDs (LEDs C and D).

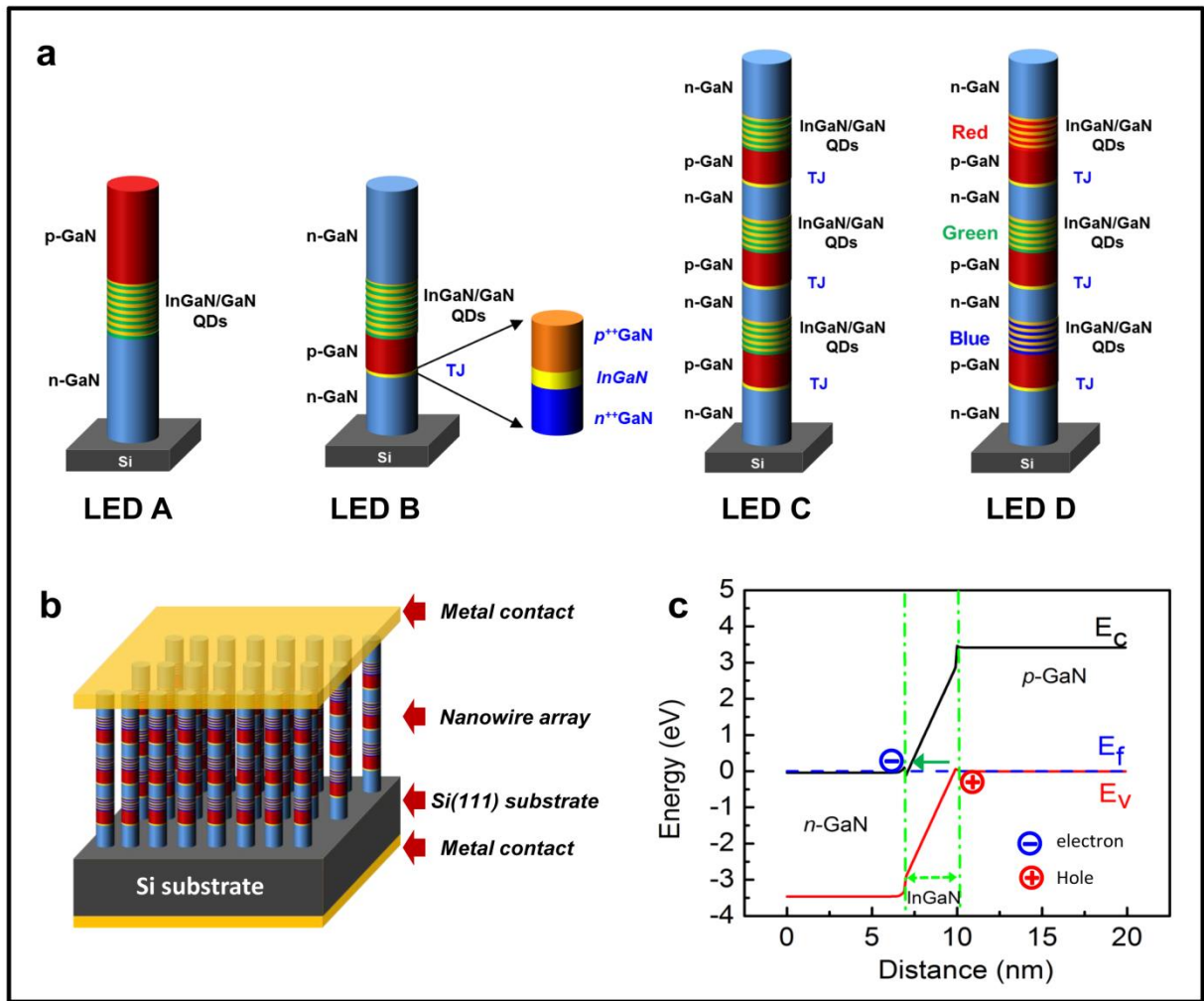


Figure 3.1: Schematic and energy band diagram of tunnel junction (TJ) integrated dot-in-a-wire LEDs. (a) Schematic illustration of the dot-in-a-wire LEDs, including LEDs A, B, C and D. (b) Schematic representation of the fabricated large area nanowire LEDs. (c) Simulated energy band diagram of GaN/InGaN/GaN tunnel junction showing carrier generation and injection process under reverse bias.

The device active region consists of multiple InGaN/GaN quantum dots. Each InGaN quantum dot has a height of ~ 3 nm and is capped by ~ 3 nm GaN layer. Each active region of LED C is nearly identical to that of LEDs A and B, with peak emission at ~ 540 nm. The multiple active regions of LED D are designed to emit at blue (~ 450 nm), green (~ 550 nm), and red (~ 620 nm) spectral range, respectively, thereby leading to phosphor-free white light emission. In order to compare the

intrinsic performance of these devices, no electron blocking layer was incorporated in the device active region. The GaN/InGaN/GaN tunnel junction consists of ~ 12 nm Si-doped GaN ($N_D \sim 5 \times 10^{19} \text{ cm}^{-3}$), 3 nm InGaN with In concentration of $\sim 32\%$ and 20 nm Mg-doped GaN ($N_A \sim 1 \times 10^{20} \text{ cm}^{-3}$). The doping together with In concentration and thickness were carefully optimized to maximize tunneling efficiency. The large area nanowire LED device is schematically shown in Fig. 3.1b.

Shown in Fig. 3.1c, electrons from the valence band of p -GaN tunnel into conduction band of n -GaN, and, as such, holes are injected into p -GaN and also into the device active region (quantum dots).

The use of tunnel junction increases the concentration of holes in the p -GaN, thereby minimizing the restriction of low hole injection efficiency in wide bandgap nitride materials. The injected holes recombine with injected electrons from n -GaN in the active region to give rise to efficient photon emission. This process repeats itself through the rest of the tunnel junctions and stacked active regions. Consequently, a single electron injection can lead to multiple photon emission in LEDs C

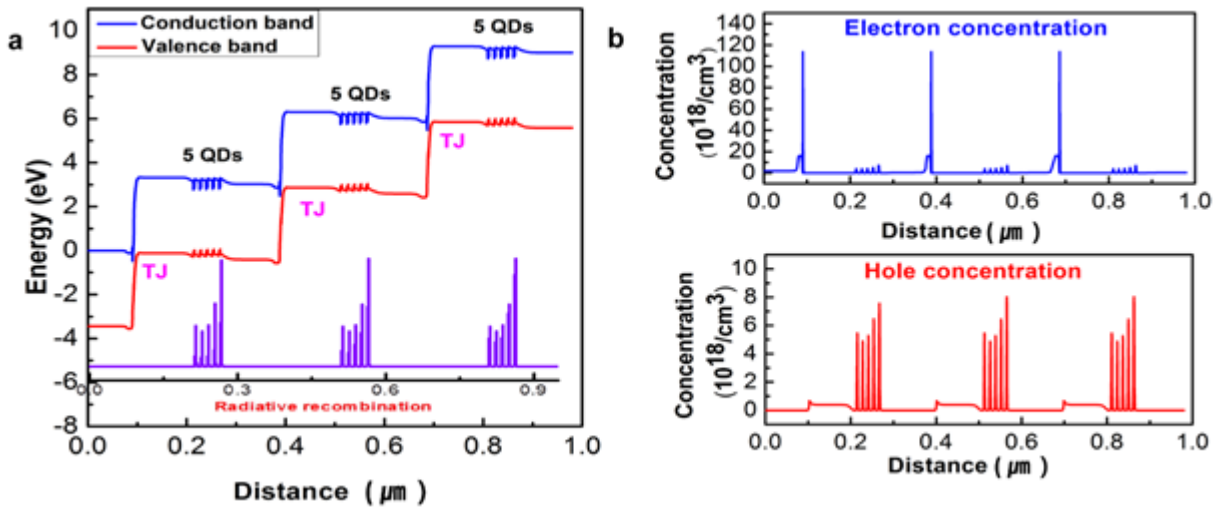


Figure 3.2: (a) Equilibrium energy band diagram of three reversely biased tunnel junctions connected in series. Multiple quantum dots are incorporated in each active region. The inset shows the radiative recombination rate in the active region. (b) Simulated electron and hole concentration inside the tunnel junctions and active regions.

and D, due to the repeated carrier regeneration in each tunnel junction. The output power, energy band diagram, and electron and hole distributions of the tunnel junction integrated dot-in-a-wire LEDs were numerically calculated using the APSYS simulation software (shown in Fig. 3.2)

3.2 Growth and Characterization

The nanowire LED structures were grown on *n*-Si (111) substrates by a Veeco Gen II plasma-assisted molecular beam epitaxy (PAMBE) system. The nanowires are of wurtzite crystal structure and possess N-polarity [237-239]. Self-organized InGaN/GaN dot-in-a-wire LED heterostructures were grown on *n*-Si (111) substrates by radio frequency PAMBE under nitrogen rich conditions. The substrate surface oxide was desorbed *in situ* at 770 °C. The growth conditions for Si-doped GaN nanowires included a growth temperature of 750 °C, with a nitrogen flow rate of 1.0 standard cubic centimeter per minute (sccm), a forward plasma power of 350 W, and Ga beam equivalent pressure of 6×10^{-8} Torr. The InGaN quantum dots were grown at relatively low temperatures (~650 °C) to enhance the In incorporation into the dots. Also, the In composition in the dots can be well controlled by varying the In and Ga beam flux. Each quantum dot layer was subsequently capped by a GaN layer of ~3 nm. In this experiment, 10 InGaN/GaN quantum dots were incorporated in each GaN nanowire for SAR devices, and 5 InGaN/GaN quantum dots were incorporated for MAR tunnel junction devices. During the growth of tunnel junction region, the substrate temperature was reduced to 650 °C.

The MAR tunnel junction LEDs were epitaxially grown by stacking the multiple active regions with tunnel junction interconnects. The dot-in-a-wire LEDs exhibit excellent structural properties. Shown in Fig. 3.4a is the scanning electron microscopy (SEM) image of the nanowire structures for LED C. The nanowire diameters and densities are in the ranges of ~40 to 100 nm and $\sim 1 \times 10^{10}$ cm⁻² (SEM images of LED A and LED B are shown in Fig. 3.3).

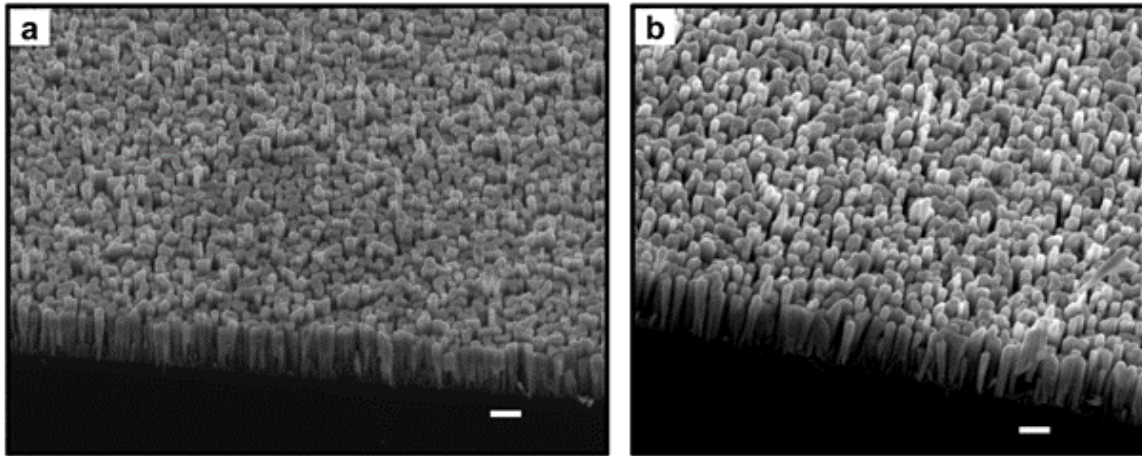


Figure 3.3: 45° tilted SEM images of conventional dot-in-a-wire LED A (left) and SAR tunnel junction dot-in-a-wire LED B (right). Scale bar represents 500 nm.

Fig. 3.4b illustrates the normalized photoluminescence (PL) spectra of LED C measured at room temperature, which is nearly identical to that measured from LEDs A and B. The peak at ~550 nm is related to the emission from the quantum dot active region; there are no noticeable additional peaks from the tunnel junctions. PL spectrum of LED D is also shown in the figure for comparison. The broad spectral linewidth (white-light emission) of LED D is due to the stacking of multiple active regions with different emission colors (indicated by the arrows in Fig. 3.4b). Structural properties of the tunnel junction LED heterostructures were characterized by scanning transmission electron microscopy (STEM), high angle annular dark field (HAADF) and energy dispersive X-ray spectrometry (EDXS) analysis. JEOL JEM-2100F equipped with a field emission gun with an accelerating voltage of 200 kV was used to obtain bright-field TEM images. The Ga and In L_{α} lines were used for the EDXS microanalysis.

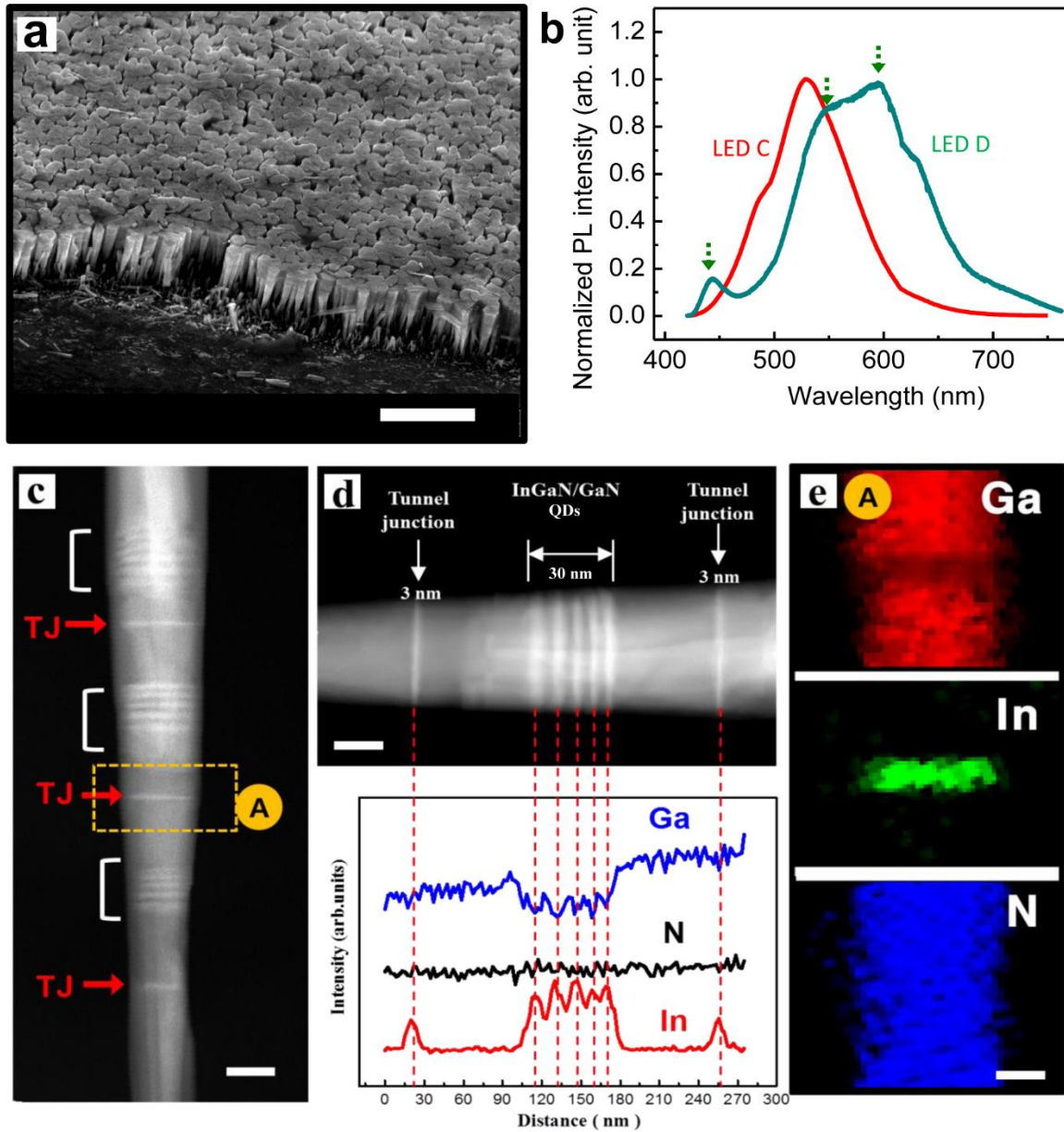


Figure 3.4: Structural characterization by SEM, TEM and photoluminescence. (a) A 45° tilted scanning electron microscopy (SEM) image of MAR TJ dot-in-a-wire LED. The scale bar denotes 1 μm. (b) Room temperature photoluminescence spectra of LED C and LED D. (c) HR-TEM shows MAR TJ dot-in-a-wire LED structure. (d) High angle annular dark field (HAADF) image showing the MAR tunnel junction dot-in-a-wire LEDs with the presence of tunnel junctions and quantum dot active regions. EDXS line profile along c-axis (growth direction) showing In peaks in the tunnel junctions and Ga dips and In peaks in dot region (lower panel). (e) EDXS elemental mapping image of tunnel junction region shows the In, Ga, and N variation. Scale bar presents 30 nm.

Fig. 3.4c shows the HAADF of the MAR tunnel junction nanowire structure (LED C). The presence of multiple quantum dot active regions can be clearly identified. No noticeable extended defects or misfit dislocations were observed. It is seen that multiple InGaN/GaN quantum dots are positioned in the center of the nanowires, due to the strain-induced self-organization [77]:[237]. The InGaN thickness is ~ 3 nm in each tunnel junction, shown in Fig. 3.4d. To further confirm compositional variations of the tunnel junction and active region, EDXS analysis was performed. The signal variations of Ga, In, and N across different tunnel junctions and the quantum dot active region along the growth direction of LED C are displayed in the lower panel of Fig. 3.4d. Clear In peaks reveals the existence of the InGaN layer in each tunnel junction. Also, we observed regular peaks and dips of In and Ga throughout the quantum dot region. The EDXS elemental mapping image of the tunnel junction region, illustrated in Fig. 3.4e, further provides unambiguous evidence for the presence of GaN/InGaN/GaN tunnel junction.

3.3 Fabrication Process

The nanowire LED fabrication process included the following steps. First, a polyimide resist layer was spin-coated to fully cover the nanowires, followed by O_2 plasma etching to expose the nanowire top surface. Thin Ni (8 nm)/Au (8 nm) and Ti (20 nm)/Au (120nm) metal layers were then deposited on the nanowire surface and the backside of the Si substrates to serve as *p*- and *n*-metal contacts, respectively. For the tunnel junction LEDs, thin Ti (8 nm)/Au (8 nm) was deposited on the nanowire top surface to serve as the *n*-metal contact. Following that, we used a 150 nm indium tin oxide (ITO) layer that was deposited by RF sputtering on the device top surface to serve as a transparent electrode and current spreading layer. The fabricated devices with metal contacts were annealed at ~ 500 °C for 1 min in nitrogen ambient, and the complete devices with ITO contacts were annealed at 300 °C for 1 hour in vacuum. We then used metal grid contact with

device sizes ranging from $1 \times 1 \text{ mm}^2$, $500 \times 500 \text{ }\mu\text{m}^2$ and $300 \times 300 \text{ }\mu\text{m}^2$. LEDs with chip areas of $\sim 500 \times 500 \text{ }\mu\text{m}^2$ were mostly measured and reported in this study.

3.4 Current-Voltage Characteristics

Fig. 3.5a shows typical current-voltage (I-V) characteristics of the three sets of devices, including conventional LED A, SAR tunnel junction LED B, and MAR (n=3) tunnel junction LED (LED C). The mesa size of the measured device is $500 \times 500 \text{ }\mu\text{m}^2$. The turn-on voltages and series resistances of the devices approximately scale with the number of active regions (n). It is also worthwhile mentioning that the relatively high turn on voltage for the presented single junction nanowire LEDs is partly related to the non-uniform current injection due to variations of the height of the spontaneously formed nanowire arrays as well as the presence of an SiN_x layer at the nanowire-Si interface [140, 212, 213, 240]. The measured voltage drop at 20 mA for LEDs A, B and C are 5.5 V, 4.9 V, and 16 V, respectively. Compared to LED A, LED B shows reduced turn on voltage, due to the efficient hole injection with the incorporation of tunnel junction and low contact resistance *n*-GaN.

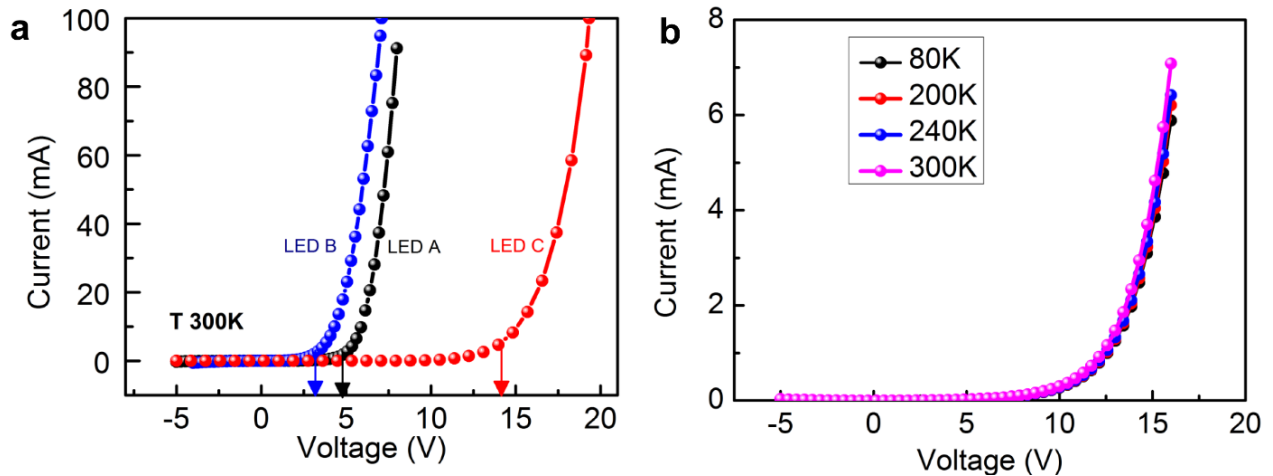


Figure 3.5: Current-voltage (I-V) characteristics of tunnel junction dot-in-a-wire LEDs. (a) I-V characteristics of LEDs A, B, and C measured at room temperature. (b) Temperature-dependent I-V characteristics of LED C.

Fig. 3.5b shows the temperature-dependent I-V curves for the multiple-stacked devices (LED C). There are no significant changes in the I-V characteristics, further confirming that the tunnel junction interconnect works well even at low temperature. We also modeled these tunnel junction integrated SAR and MAR dot-in-a-wire LEDs using APSYS simulation package. The simulation results are consistent with the experimental results, and show that the turn-on voltage and series resistance scale with the number of active regions.

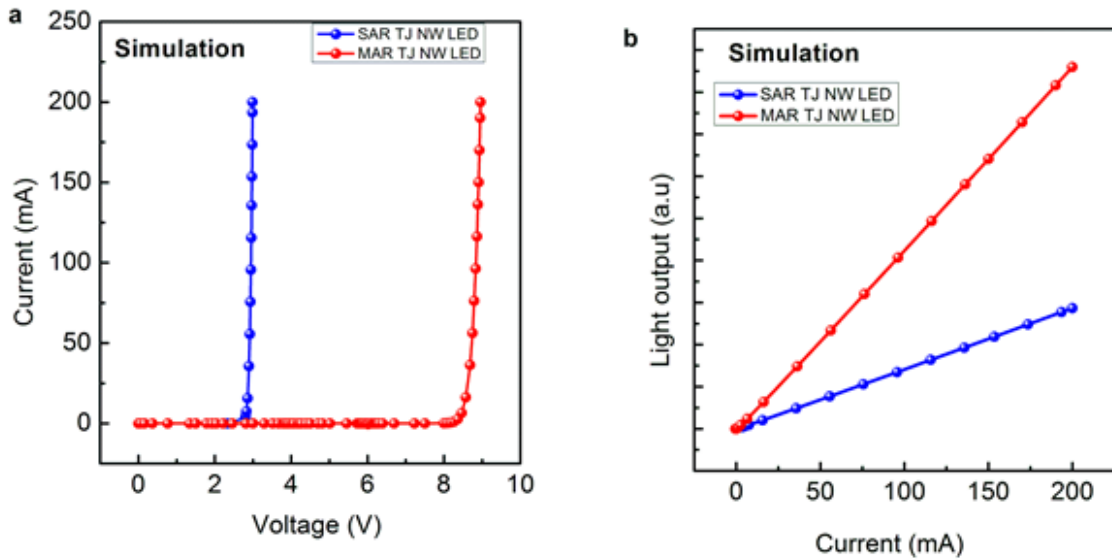


Figure 3.6: (a) Simulated I-V comparison of LED B and LED C. (b) Simulated L-I comparison of LED B and LED C.

In the simulation, 20% of the theoretical polarization induced sheet charge density was considered for tunnel junction integrated structures. An average In composition of 20% was used for the quantum dot active region. In this simulation, Auger co-efficient was assumed to be $1 \times 10^{-34} \text{ cm}^6 \text{ s}^{-1}$ while non-radiative surface recombination was not considered. The presence of multiple tunnel junction layers in the dot-in-a-wire LEDs can lead to significantly increased output power. Detailed simulation shows that the tunnel junction dot-in-a-wire LEDs can exhibit uniform electron and hole concentrations in the active region and significantly enhanced output power, compared to conventional InGaN/GaN LEDs.

3.5 Electroluminescence and Light Output Characteristics

Fig. 3.7a shows the light intensity vs. current characteristics of the devices. Electroluminescence (EL) spectra of LEDs are shown in Fig. 3.8. An optical image of the device is illustrated in the inset of Fig. 3.7a, showing green light emission. Compared to the reference LED A, SAR tunnel junction dot-in-a-wire LED B shows higher light intensity owing to the better current spreading through the low resistant *n*-GaN contact, and also the improved hole injection inside the dots [156, 221].

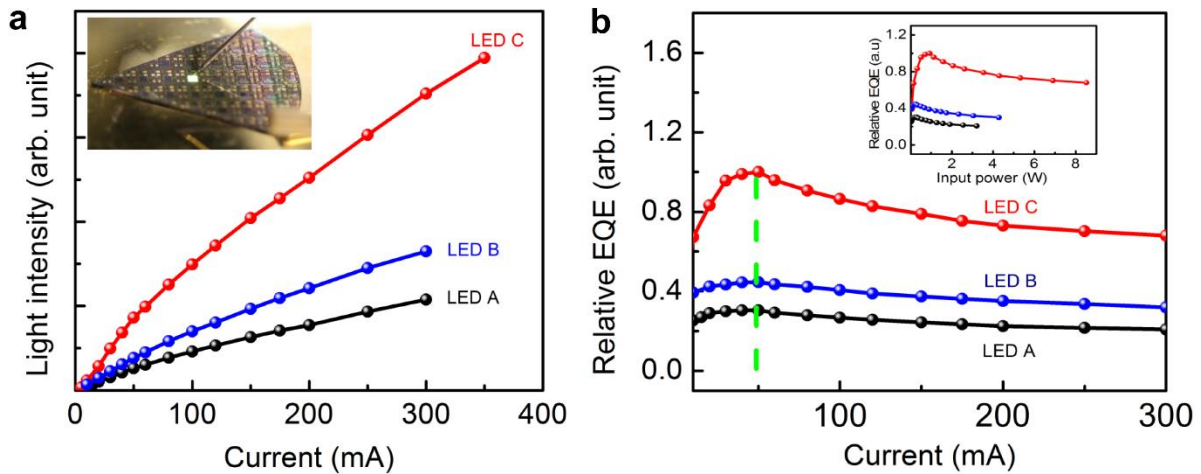


Figure 3.7: Electroluminescence characteristics of tunnel junction dot-in-a-wire LEDs. (a) Light-current (L-I) characteristics of LEDs A, B and C. (b) Relative external quantum efficiency (EQE) of LEDs A, B and C. The inset shows the relative EQE comparison as a function of input power measured at room temperature.

MAR tunnel junction dot-in-a-wire devices (LED C) shows significantly enhanced light intensity compared to the SAR tunnel junction devices (LED B), due to the repeated carrier regeneration at each tunnel junction and the resulting multiple opportunities for radiative recombination. These measurements are consistent with the simulated results.

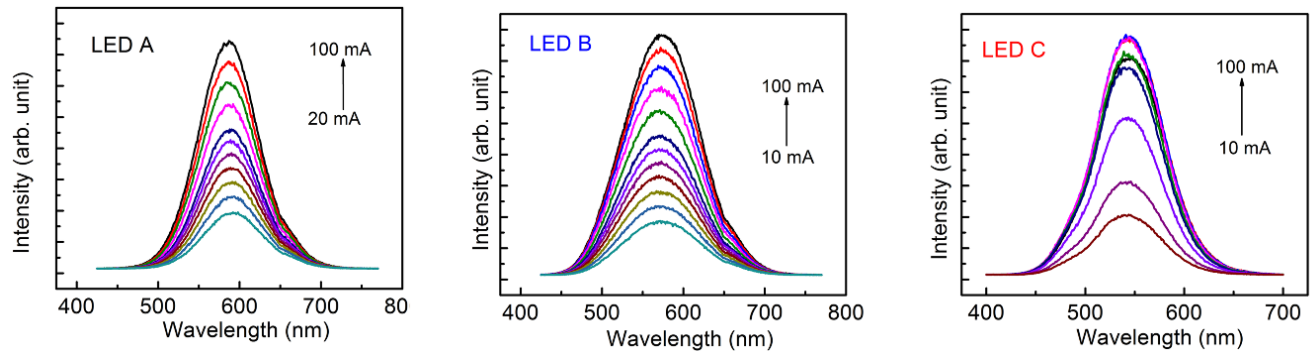


Figure 3.8: Electroluminescence spectra of LED A, B, and C.

Fig. 3.7b shows the external quantum efficiency (EQE) trend of the measured devices under pulsed biasing conditions (10% duty cycle). All of the devices show efficiency droop at high injection current. It is worthwhile mentioning that no electron blocking layers were incorporated in the device active regions. The intriguing part of the result is that, for LED C, the current corresponding to the maximum efficiency point is almost identical to LED A and LED B, suggesting that MAR tunnel junction LED C can be operated at a higher output power while maintaining the same level of efficiency loss of the conventional LEDs. This can be better illustrated in the variations of EQE vs. input power, shown in the inset of Fig. 3.7b. It is seen that efficiency droop occurs at higher input power for LED C, compared to LEDs A and B. An output power of a few mW was measured for the MAR tunnel junction LED C under an injection current of 350 mA. Recent studies have shown that the output power of axial nanowire LEDs can be drastically enhanced by incorporating a large band gap AlGaIn shell to minimize nonradiative surface recombination and increase carrier injection efficiency [141, 241].

3.6 Multiple Active Region LEDs

In general, stacking multiple quantum wells/dots in planar structures is not a suitable route to realize low current, high voltage operation since it also significantly increases the densities of defects and dislocations. Such issues can be fundamentally addressed in tunnel junction nanowire LED structures, as demonstrated in this work.

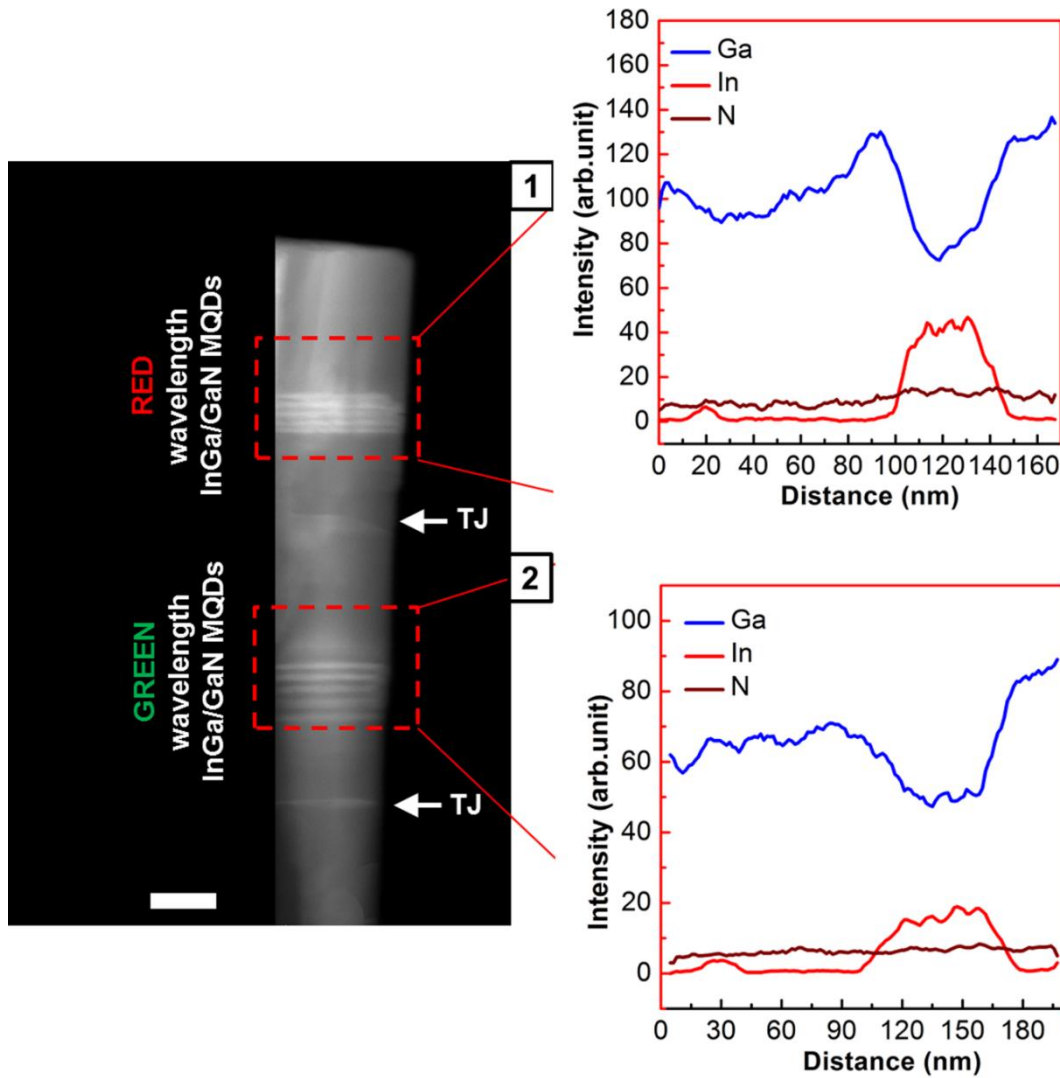


Figure 3.9: HAADF image of tunnel junction MAR nanowire LED structure (LED D) and EDXS analysis showing In concentration variations in the device active regions.

Moreover, such MAR tunnel junction nanowire LEDs can be designed to operate in a broad wavelength range, leading to phosphor-free white light emission. In LED D, the three interconnected active regions consist of blue, green, and red-emitting quantum dots, respectively, shown in Fig. 3.4b. The HAADF TEM image and EDXS line scan are shown in Fig. 3.9. Fig. 3.10a shows the EL spectra. Three distinct peaks positioned at around 445 nm, 570 nm, and 625 nm can be clearly measured. The resulting strong, nearly white-light emission is shown in the inset of Fig. 3.10a. No noticeable wavelength shift was measured with increasing injection current.

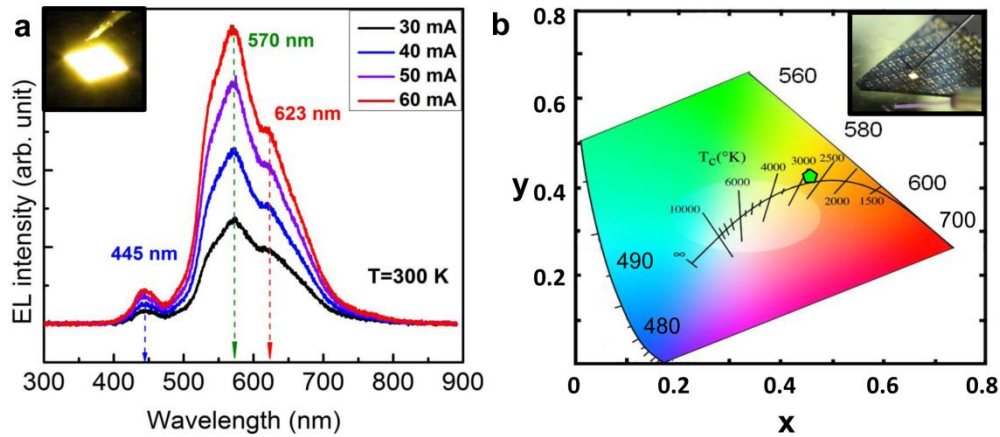


Figure 3.10: Phosphor-free white light emission of tunnel junction MAR dot-in-a-wire LEDs. (a) Electroluminescence spectra LED D measured under different injection currents. The inset shows the device optical image. (b) Correlated color temperature (CCT) properties.

The device emission characteristics are illustrated in the Commission Internationale de l'éclairage (CIE) chromaticity diagram, shown in Fig. 3.10b. The correlated color temperature is ~ 3000 K. The x and y values stay nearly constant in the range of 0.47 and 0.49 for injection currents varying from 20 mA to 250 mA. SEM image, I-V and L-I characteristics are shown in Fig. 3.11.

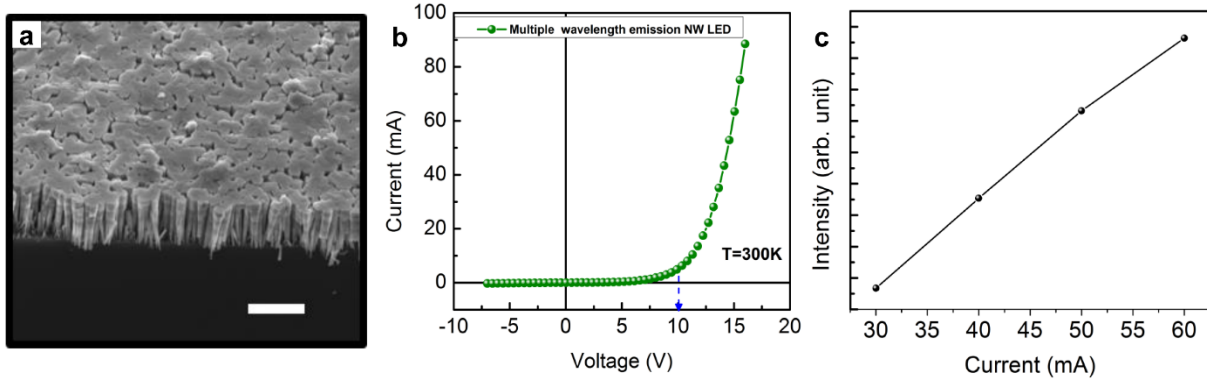


Figure 3.11: (a), SEM image of LED D. (b), I-V characteristics of LED D. (c) L-I characteristic of LED D.

3.7 Summary

In summary, we have developed polarization engineered InGaN/GaN tunnel junction nanowire LEDs that can eliminate the use of resistive *p*-GaN contact layers, leading to reduced voltage loss and enhanced hole injection. Moreover, by using tunnel junction interconnect, we have demonstrated multiple-active-region nanowire LEDs with significantly enhanced light intensity. Moreover, the demonstrated tunnel junction nanowire LED technology enables phosphor-free white emission and reduced efficiency droop.

Chapter 4

Alternating-Current InGaN/GaN Nanowire White-Light Emitting Diodes: An Application of Nitride Tunnel Junction

Some of the contents of this chapter were previously published *Nano Lett.*, 2015, 15 (10), pp 6696–6701 [218].

Generally, Light-emitting diodes are operated at direct-current (DC) power because of its intrinsic diode characteristic. InGaN/GaN-based LEDs have widespread important applications, and some of the applications critically require alternating-current (AC) power operated LED [242]. In this context, a rectifier is essential for AC-to-DC conversion [243]. However, this conversion process is very inefficient and leads to 20-50% energy loss [244]. Also, this process is costly, complicated, and plagued by low life time [245]. To date, however, a great attention has been paid to the improvement of efficiency (EQE/IQE) of InGaN-based light emitters, while the development of AC power LEDs has been sluggish. To this end, various micro-chip LED configurations, including series, antiparallel or Wheatstone bridge (WB) have been studied for efficient direct AC operation [245-248]. Nevertheless, in series/antiparallel configurations, half of the LEDs are OFF during positive half/negative half cycles. Hence, such AC LEDs suffer from low luminous efficiency since they require increased number of LEDs to get the same amount of light output. On the other hand, in Wheatstone bridge configuration, much-improved light efficiency can be achieved. Unlike conventional light bulbs, LEDs are low voltage devices and cannot operate on an alternating current voltage. As a consequence, an electrical circuit is required to convert AC power

to low-voltage DC power (typically 2-4V). Such a driver adds a significant level of complexity, cost, and efficiency loss to the LED devices and systems. we have demonstrated, for the first time, AC LEDs on a Si platform, which can operate efficiently in both positive and negative polarity of applied voltage. This work offers a new avenue for realizing high efficiency LEDs that can operate under a large range of voltage biasing conditions and can possibly eliminate, or greatly simplify the electrical driver required in today's LED lighting systems.

4.1 Growth and Characterization

Schematically shown in Fig. 4.1, with the use InGaN/GaN tunnel junction we have further demonstrated, for the first time, AC LEDs consisting of *p*-GaN up and *p*-GaN down tunnel junction dot-in-a-wire structures monolithically grown on the same Si chip using the technique of selective area growth. This AC operated nanowire LED array emits green light at positive and negative polarity of AC voltage. For the selective area growth of AC nanowire LEDs, a 100 nm SiO₂ was first deposited on Si substrate by plasma enhanced chemical vapor deposition (PECVD). Various openings with sizes from 300 × 300 μm² to 50 × 50 μm² were then defined on SiO₂/Si substrate by standard photolithography and wet etching process. Conventional *p*-GaN up InGaN/GaN nanowire LEDs was first grown. Subsequently, the sample was soaked in BOE solution to selectively remove SiO₂ and also nanowires on SiO₂. Prior to the second growth step, a SiO₂ layer was deposited onto the previously grown *p*-GaN up nanowire LEDs to protect these nanowires. The second reverse polarity *p*-GaN down nanowire LEDs were then selectively grown on the opening areas. Tunnel junction connects the *p*-GaN layer with the *n*-type Si substrate, thereby enabling reverse polarity LED operation. The selective area growth process is illustrated in Fig. 4.1a, b, and c.

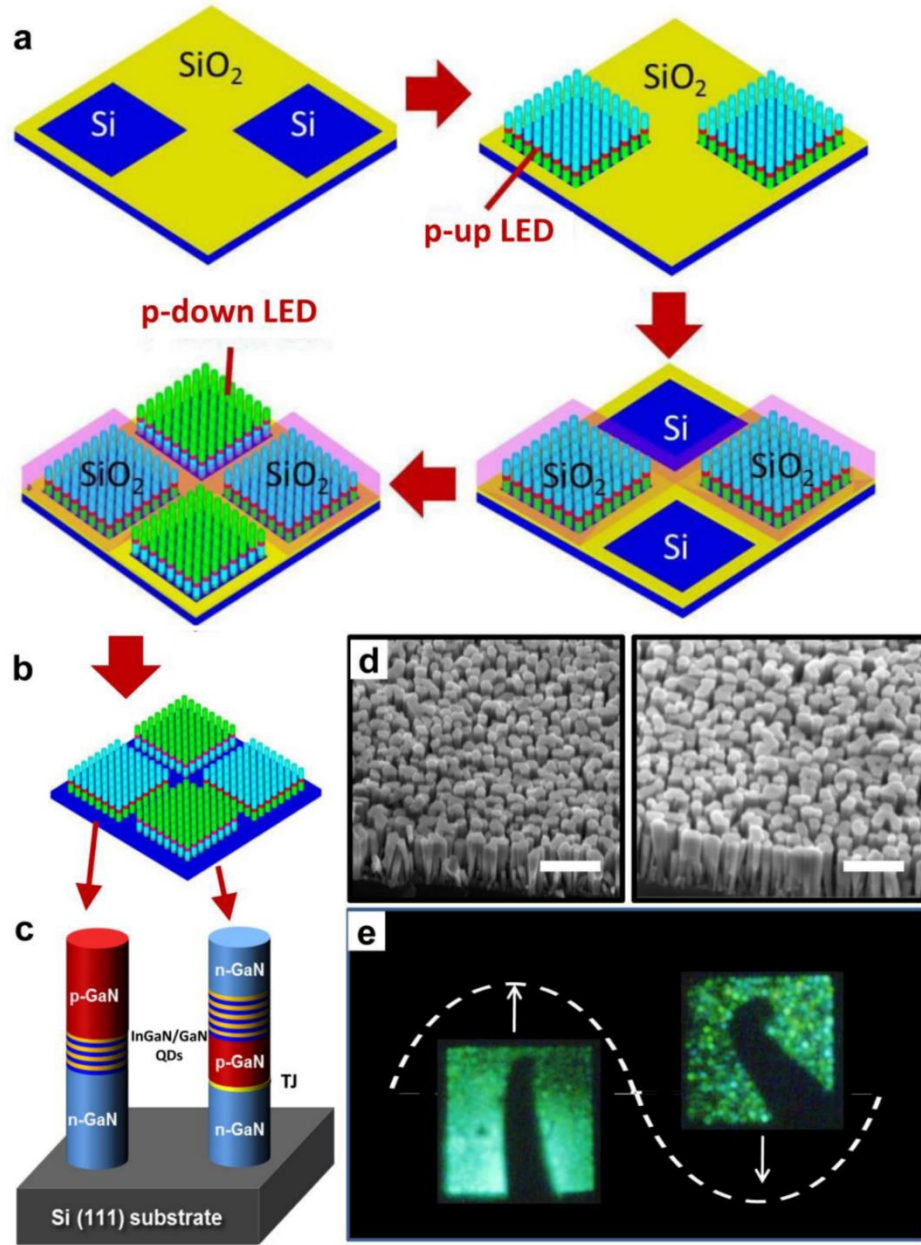


Figure 4.1: Alternating current tunnel junction dot-in-a-wire LED arrays. (a) Two-step selective area growth of p -GaN up and p -GaN down AC nanowire LEDs on Si substrate. p -Up nanowire LED arrays were first grown on the opening areas of SiO_x coated Si substrate. Then the SiO_x and the nanowires on top were selectively removed using chemical etching. The p -up nanowire LED structures were then covered with SiO_x and additional opening areas were created prior to the growth of the p -down nanowire LED structures. Subsequently, the SiO_x and the nanowires on top were selectively etched. This leads to the formation of p -up and p -down nanowire LED arrays on the same Si chip. (b), (c) Device schematics. (d) 45° tilted SEM images of as grown p -GaN up and p -GaN down nanowire LED structures. (e) Optical micrograph of green light emitting nanowire LED arrays on Si under AC biasing conditions.

SEM images of the nanowire devices grown on Si (111) substrates are also shown in Fig. 4.1d (also shown in Fig. 4.2 for SEM images of *p*-GaN up and *p*-GaN down AC LED devices). The electrical measurements were done with a frequency of 20-60 Hz at a peak to peak voltage of 10 V using an Agilent 6812B AC power source. Shown in Fig. 4.1e, both devices emit green color under AC operation.

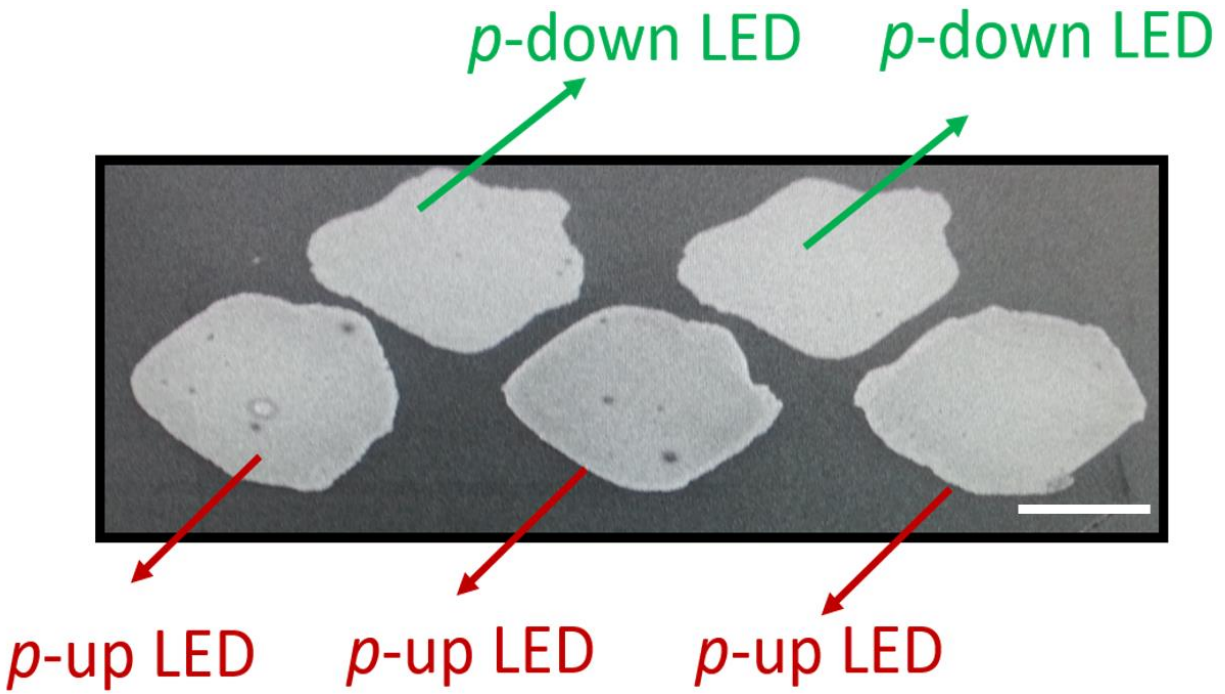


Figure 4.2: SEM image of as grown AC nanowire LED arrays on a Si substrate. The scale bar represents 50 μm .

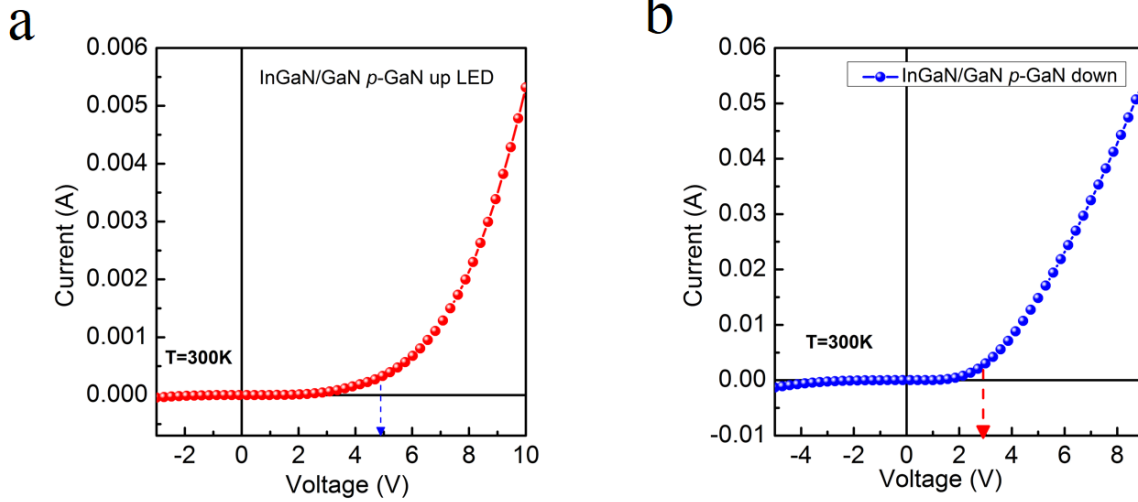


Figure 4.3: I-V characteristics of *p*-GaN up (left) *p*-GaN down (right) LEDs on Si.

At a frequency of 60 Hz, these devices are almost flicker free, and are suited for practical applications. These devices can also be operated independently by DC bias as shown in Fig. 4.3.

4.2 Summary

In this chapter, we have shown that AC-operated InGaN/GaN nanowire LED offers extreme flexibility in the operation voltage and can completely eliminate the use of an AC/DC converter required in conventional LED lighting technologies, thereby leading to reduced cost and further enhanced efficiency.

Chapter 5

Molecular Beam Epitaxial Growth and Characterization of Monolithic *n*-GaN/Al/*p*-AlGaN Nanowire Heterostructure

Epitaxy of dissimilar materials (distinctly different properties, crystal structures and lattice parameters) commonly known as ‘heteroepitaxy’ promises to introduce different novel functionalities [249]. Among the heteroepitaxial combinations, metal/semiconductor epitaxy holds tremendous promise for numerous electronic/optoelectronic applications [250]. Previously, various epitaxial metals/GaAs combinations, including Al/GaAs, Ag/GaAs, Fe/GaAs, Au/GaAs, Co/GaAs have been extensively studied by molecular beam epitaxy (MBE) to realize improved device characteristics and/or new functionalities [249, 251-253]. These extensive epitaxial metal/GaAs-based studies are primarily due to the importance of prototype III-V semiconductor GaAs and well-known GaAs-based device applications, relatively small lattice mismatch between common metals and GaAs and similar crystal structures. On the other hand, among the III-V semiconductors, Al(Ga)N- based semiconductors are considered ubiquitously ideal for a broad range of electronic and optoelectronic devices, whereas among the metals, Al is an important metal for electronic/optoelectronic devices due to CMOS compatibility, ohmic contact formation with wide bandgap semiconductors, and superconducting behavior [254]. To date, however, it has remained challenging to realize high quality epitaxy between metal and Al(Ga)N due to prohibitively large lattice mismatch [250, 255]. Yet, there have been few studies on the epitaxy of

metal/Al(Ga)N semiconductors, and these reports have been restricted to metal/Al(Ga)N planar structures [255].

In general, the performance of large lattice mismatched (~10% or more) epitaxial metal/semiconductors planar structures has been limited due to the presence of large densities of defects/dislocations [250, 251, 256]. Still, a few reports demonstrated that different metals ranging from Ni, Pd, Pt, Al, Ti, Hf, Fe and Mg can be grown epitaxially on GaN in both ultra-high vacuum and in conventional vacuum conditions with limited success [250, 251, 255-261]. It was also reported that various metal/GaN and/or metal/GaAs epitaxy is possible even with the presence of a thin native oxide on GaN or GaAs [255].

Previous reports suggest that GaN/metal/GaN sandwich structure can be realized in planar geometry without any noticeable intermixing. Even so, the interlayer metal suffers from two-dimensional tensile stress due to large lattice and thermal coefficient mismatch [262]. However, compared to planar structure, III-nitride nanowires exhibit significantly reduced defects and dislocations due to the effective lateral stress relaxation. In addition, because of the reduced dopant formation energy in nanowire structure, significantly improved dopant ionization can be realized. Given these advantages, III-nitride nanowires are considered promising in light-emitting diodes, lasers, power electronics etc [218]. Moreover, recent reports suggest that Al(Ga)N nanowires can be epitaxially grown on different metals and graphene [136, 263]. In addition, defect free, atomically clean monolithic metal/Al(Ga)N interface in nanowire heterostructure can be successfully employed to realize low resistance tunnel junction [259, 264, 265].

Until recently, comprehensive study of the epitaxial growth and characterization of Al/Al(Ga)N combination has remained elusive due to several reasons. First, Al is a face centered cubic metal

with relatively low melting point ($\sim 660^\circ\text{C}$) that limits Al growth/deposition temperature both *in situ* or *ex situ* [249]. Second, for direct epitaxial Al metal growth on GaN, GaN surface needs to be very clean and ultra-high vacuum is required to avoid GaN contamination. Third, close packed Al (111) plane has significantly large lattice-mismatch ($\sim 10.2\%$) with close packed GaN basal plane (0001) that induces tensile strain in the Al layer [255]. In addition, it was found that successful epitaxial growth of f.c.c Al metal on wurtzite GaN critically depends on the growth temperature, growth rate, ultrahigh vacuum condition, and the surface quality of the GaN layer [255]. However, it was reported that epitaxial Al layer can be formed on GaN at different temperatures, and the Al film quality by and large depends on the Al layer thickness and high quality epitaxy was observed after certain thickness limit [255]. Conversely, it was also reported that high quality GaN can be grown on various metal layers at different growth temperatures using MBE.

In this context, we have proposed and demonstrated, molecular beam epitaxial growth of Al metal on wide band gap *n*-GaN and *p*-AlGa_N on Al. We have extensively studied the epitaxy and other morphological/structural characterizations of Al/Al(Ga)_N nanowire by X-ray diffraction (XRD), scanning electron microscopy (SEM), and transmission electron microscopy (TEM). Our detailed studies suggest that high quality, defect free Al metal can be epitaxially grown on Al(Ga)_N with Al thickness ranging from ~ 1.6 nm to ~ 16 nm in the c-axis growth direction without any noticeable misfit dislocations. It is also observed that sufficiently thick large band gap Al(Ga)_N semiconductors can be epitaxially grown on Al metal. Such high-quality *n*-GaN/Al and Al/*p*-Al(Ga)_N interface suggests that dislocation/stacking-faults free interface can be realized in *n*-GaN/Al/*p*-Al(Ga)_N sandwich nanowire heterostructure due to effective stress relaxation in the sidewalls, pure growth ambient and slow growth rate.

5.1 Design and SEM

In this work, we have studied three different types of epitaxial n -GaN/Al/ p -AlGaN nanowire structures. These nanowire structures were grown under similar growth conditions except the Al growth duration was varied to examine the thickness dependence on the epitaxy of metal/semiconductor. Illustrated in Fig: 5.1a, which are denoted as epitaxial nanostructure A, nanostructure B and nanostructure C. The nanostructure A consists of 340 nm n -GaN, 25 nm n^{++} -GaN, 1.6 nm Al, 25 nm p^{++} -Al_{0.15}Ga_{0.85}N, 30 nm p -Al_{0.15}Ga_{0.85}N capping layer. The nanostructure B and C consist of similar structure except for the thickness of Al was increased to ~5 nm and ~16 nm, respectively.

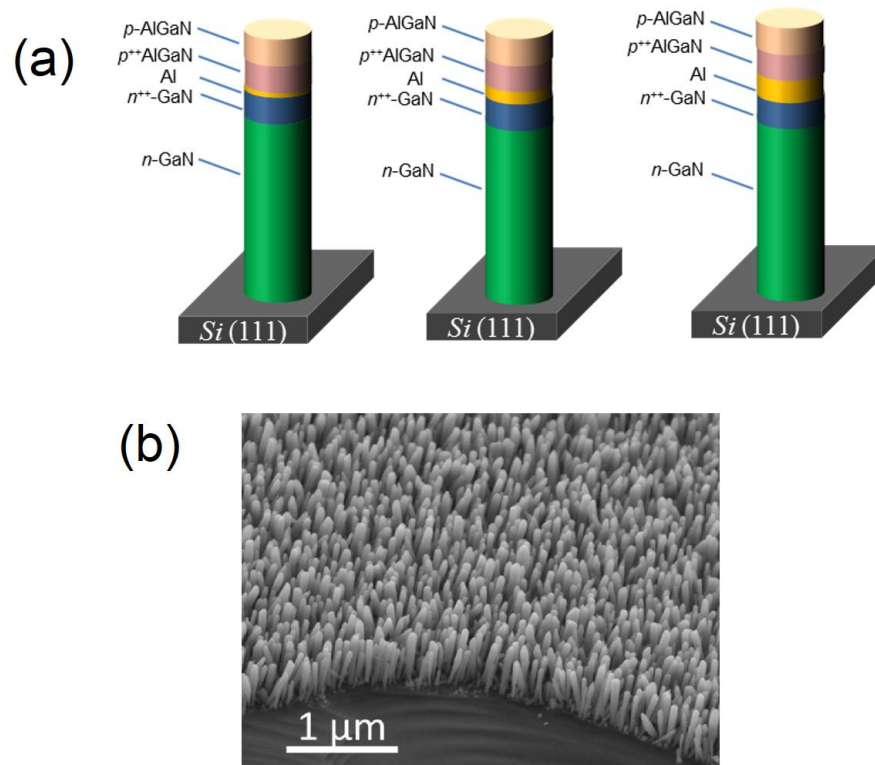


Figure 5.1: (a) Schematic diagram of different epitaxial Al/Al(Ga)N nanostructures grown on Si substrate. (b) An SEM image of nanostructure A taken with a 45° angle.

In order to study the intrinsic epitaxy of metal/semiconductor nanostructure, no additional layer (GaN capping or Al(Ga)N contact layer) was incorporated in this nanostructure and not suitable for subsequent device fabrication. Illustrated in Fig: 5.1b is the scanning electron microscopy (SEM) image of Al nanostructure A taken with 45° angle. As can be seen, the nanowires are vertically aligned on the Si substrate and exhibit relatively uniform height and size distribution.

5.2 MBE Growth

All the epitaxial metal/semiconductor nanostructures were grown by plasma-assisted MBE on *n*-Si (111) substrates under nitrogen rich condition without using any external metal catalyst. Prior to the loading into the MBE growth chamber, the thin native oxide on the Si substrate was removed by hydrofluoric acid (10%), and further *in situ* desorbed at ~770°C. The N₂ flow rate was kept at 1.0 standard cubic centimeter per minute (sccm), the forward plasma power of ~350 W was kept during the growth. It is worthwhile mentioning that MBE provides unique opportunity to realize *in situ* Al/III-nitride epitaxy since it has elemental Al source and this eliminates the need of *ex situ* Al deposition and GaN surface cleaning. The substrate temperature was kept at ~780°C for the growth of *n*-GaN. However, for the heavily doped *n*⁺⁺-GaN region, the growth temperature was lowered to 640°C. The different thickness of Al layers were grown at ~460° C and were subsequently capped with a thin layer of Ga. To avoid the formation of AlN or Al-rich AlGa₃N, the nitrogen plasma was turned off during the Al layer growth. It was previously reported that after a few monolayer (ML) growth (1 ML= 0.234 nm, planar distance between Al (111) planes), crystalline quality of epitaxial Al-layer improves and consistently shows similar epitaxial Al layer upto ~40 nm [255]. Therefore, it is expected that, high quality, defect free epitaxial Al-layers can be grown with different thickness. The substrate temperature was then increased to ~640°C for the growth of *p*-AlGa₃N and subsequently capped with another layer of *p*-Al_{0.15}Ga_{0.85}N. Doping

concentration and degeneracy in the epitaxial nanostructures were controlled by the Si (*n*-doping) and Mg (*p*-doping) effusion cell temperatures. Si and Mg doping concentrations in the heavily doped *n*-GaN and *p*-AlGaN segments of the nanostructure were in the ranges of 5×10^{19} and 1×10^{20} cm^{-3} , respectively. In this growth process, the Al and Ga beam equivalent pressure of 2.5×10^{-8} and 5×10^{-8} Torr were maintained, respectively.

5.3 TEM Characterizations

Structural properties of the different epitaxial Al/AlGaN nanowire heterostructure were subsequently investigated by scanning transmission electron microscopy (STEM) and high-resolution transmission electron microscopy (HR-TEM) using a JEOL JEM-2100F equipped with

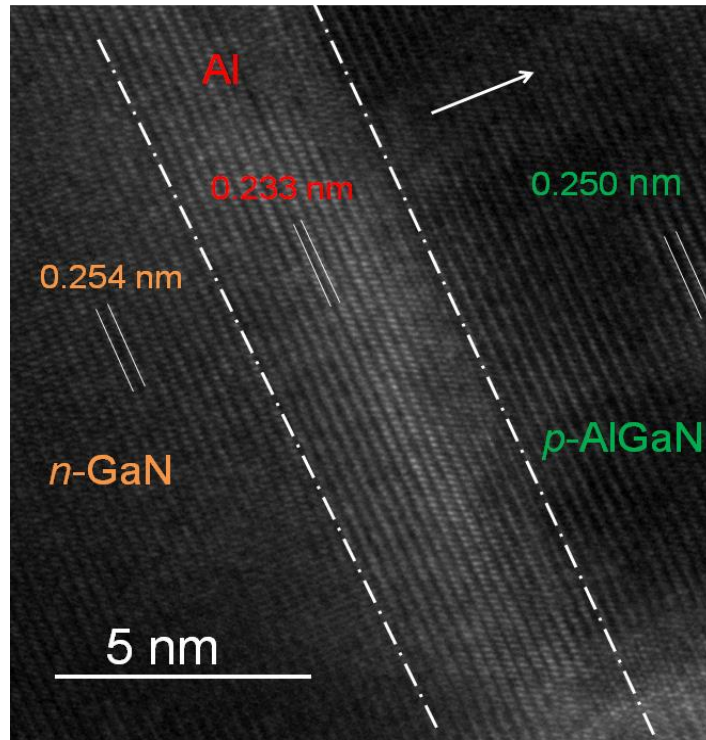


Figure 5.2: (a) High-resolution transmission electron microscopy (HR-TEM) image of nanostructure B.

a field emission gun operated at 200 kV. The sample was prepared by dispersing Al/AlGaN nanowires on a Cu grid, and high angle annular dark field (HAADF) STEM imaging was measured with an electron beam diameter of approximately 0.2 to 0.7 nm. Shown in Fig. 5.2, the interfaces between the epitaxial Al layer and subsequent *p*-AlGaN layer and/or bottom Al layer and *n*-GaN were characterized by high resolution transmission electron microscopy (HR-TEM). The detailed HR-TEM analysis further confirmed there were no noticeable stacking faults or threading dislocations formed at any of the interfaces, which is in direct contrast to planar Al/GaN interface. From the lattice fringe image as shown in Fig. 5.2, it is seen that the interplanar spacing is 0.233 nm in Al layer, which corresponds to Al (111) planar distance. However, the interplanar distance in *n*-GaN and *p*-Al(Ga)N are 0.254 nm and 0.250 nm, respectively, suggesting that *n*-GaN (0002) and *p*-Al(Ga)N (0002) planes are in hetero-epitaxial relationship with Al (111). It is worthwhile mentioning that the lattice constant of Al (111) is 0.289 nm, whereas the lattice constant of GaN (0002) plane is 0.319 nm. As such, the lattice-mismatch between the epitaxial Al (111) and Ga (0002) is ~10%. Such large lattice mismatch induced dislocations can be relaxed in the nanowire sidewalls, and dislocations/stacking fault free interfaces can be realized. We have also confirmed this heteroepitaxy by XRD (to be discussed in later section). Illustrated in Fig. 5.3a and 5.4a are the STEM images of Al/AlGaN nanowire structure (thick Al-layer and thin Al layer), wherein the different segments are identified. In high-magnification STEM images shown in Fig. 5.3b and 5.4b, the Al layer is clearly observed with ~16 nm thickness. Energy dispersive X-ray spectroscopy (EDXS) analysis was further performed to study the compositional variations of the epitaxial *n*-GaN/Al/*p*-Al_{0.15}Ga_{0.85}N nanostructure. To further understand the compositional variations, we have studied both thick and thin Al/AlGaN nanostructures by EDXS point analysis.

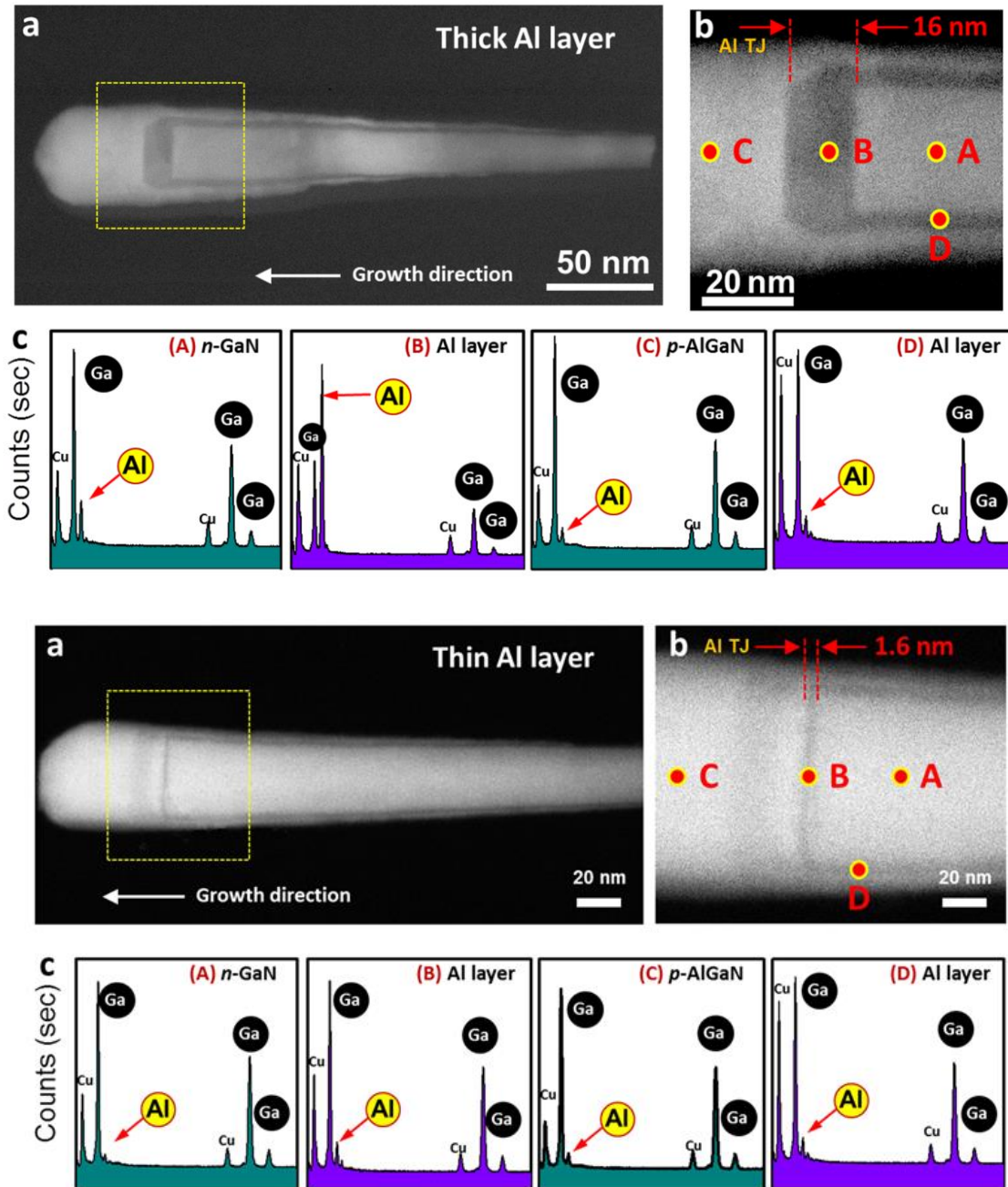


Figure 5.3: (a) STEM image of a full nanostructure C (thick Al) (b) and (c) EDXS point analysis of the Al layer (point B in b) and *p*-AlGaN region (point C), *n*-GaN region (point A) and Al layer in sidewall region (point D).

Figure 5.4: (a) STEM image of a full nanostructure A (thin Al) (b) and (c) EDXS point analysis of the tunnel junction, Al layer (point B in b) and *p*-AlGaN region (point C), *n*-GaN region (point A) and Al layer in sidewall region (point D).

An EDXS point analysis was done in the vicinity of the Al-layer, shown in Fig: 5.3c and 5.4c, which provided clear evidence for the presence of Al (both thick and thin). The GaN nanowire with Al layer is surrounded by an AlGaN shell which was formed during the epitaxy of subsequent p^{++} -Al_{0.15}Ga_{0.85}N segment and p -Al_{0.15}Ga_{0.85}N capping layer. It can also be seen that a thin layer of Al also forms in the sidewalls. EDXS point analysis was carried out in the p^{++} -Al_{0.15}Ga_{0.85}N layer, Al layer (in the sidewalls) and n -GaN layer. As can be seen in Fig. 5.3c, point analysis in the n -GaN region also gives sensitivity to Al which is higher than the Al-signal in the p -Al_{0.15}Ga_{0.85}N region.

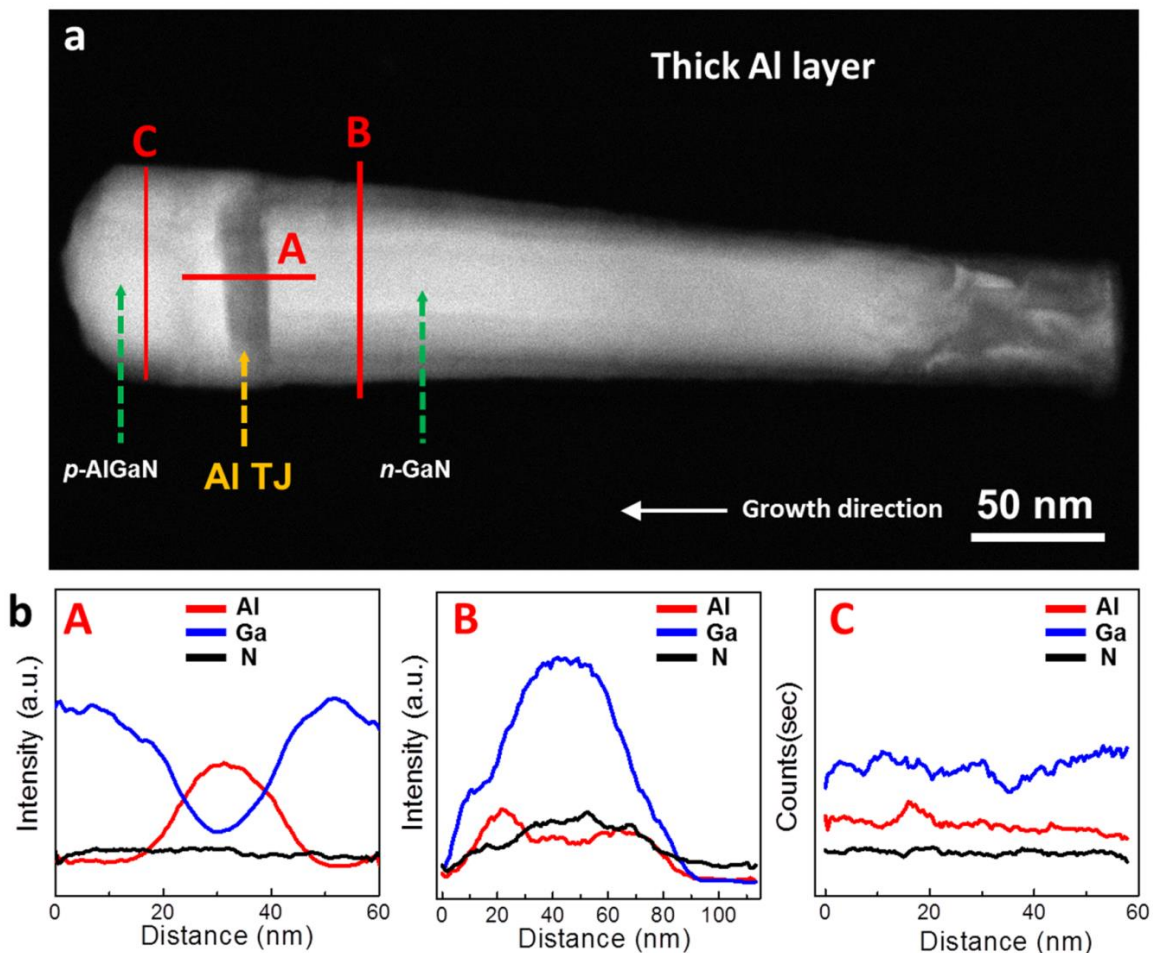


Figure 5.5: (a) STEM image of a nanostructure C (thick Al layer) and different line profile analyses along the nanowire length and lateral dimension.

Since the *n*-GaN region is surrounded by Al metal and *p*-Al_{0.15}Ga_{0.85}N shell, the electron beam directed perpendicular toward the *n*-GaN region gives collective sensitivity to Al which sums up to be greater than the Al-signal in the *p*-Al_{0.15}Ga_{0.85}N region. In consequence, even though the beam was directed toward the Al-layer, Ga and Cu signals were also detected from the surrounding AlGa_{0.85}N shell structure and Cu grid due to the transmitted beam.

We have performed EDXS line profile analyses along the lateral dimension of the different sections of the nanowire (line A, B, C). This lateral EDXS line scan (line scan B) unambiguously confirms the presence of Al-rich AlGa_{0.85}N shell. However, we have also performed line scans along the length of the nanowire (*n*⁺⁺-Ga_{0.85}N to *p*⁺⁺-Al_{0.15}Ga_{0.85}N through the Al layer). As can be seen in Fig. 5.5, line scan A unequivocally confirms the presence of Al layer, whereas line scan B also shows Ga rich *n*-Ga_{0.85}N in the center. Line scan C confirms the presence of low Al% *p*-AlGa_{0.85}N layer. It is worthwhile mentioning that due to the presence of very thin ~1.5 nm-2.5 nm Al layer (in thin Al layer, nanostructure A), similar line scans along the nanowire do not give greater sensitivity or signal for the presence of Al. Our detailed TEM study suggests that point analyses at different segments of the nanowires can reliably identify AlGa_{0.85}N segments and/or Al layer. Conversely, EDXS line analyses along the lateral dimension are best suited for identifying the Al-rich AlGa_{0.85}N shell region and along the nanowire direction through the Al layer confirms the presence of Al.

5.4 X-ray Diffraction Analysis

To further analyze the epitaxial relationship between Al metal and Al(Ga)N nanowires, the spontaneously grown large area nanowire samples were characterized by XRD. The XRD experiments were carried out with CuK α radiation using a Bruker D8 Advance system equipped with a Gobel mirror on the incidence beam and a series of Soller slits on the diffracted beam in

front of the detector . Fig. 5.6 shows the symmetric $\theta/2\theta$ scan performed to determine the out of plane orientation of Al/Al(GaN) nanowires.

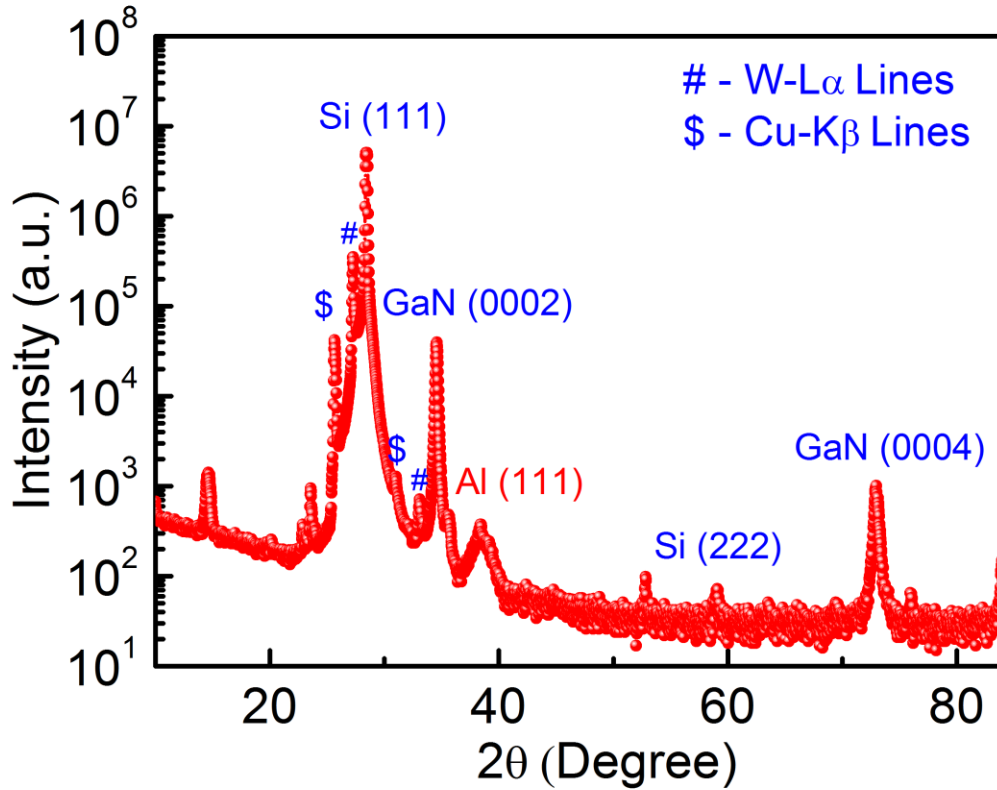


Figure 5.6: Symmetric $\theta/2\theta$ XRD scan in Bragg reflection.

Shown in Fig. 5.6, apart from the peaks from Si substrates , peaks from GaN (0002) and Al (111) are seen in Bragg condition. The presence of Al (111) and GaN (0002) peaks suggest that f.c.c Al (111) plane maintains an epitaxial relationship with GaN (0002) basal plane in the growth direction. It is worthwhile mentioning that the diffraction peak corresponds to Al (111) plane shifts toward higher angle is likely due to the tensile stress (>10% lattice mismatch) and/or thermal expansion co-efficient mismatch [256].

5.5 Summary

In summary, we have investigated unique molecular beam epitaxial growth of *n*-GaN/Al/*p*-AlGaN nanowire heterostructure. Our detailed studies suggest that, nearly dislocations/defects free GaN/Al/Al(Ga)N nanowires can be grown epitaxially on Si substrate in an optimized growth condition. We have also characterized and discussed the epitaxial Al-layer quality by S-TEM, HR-TEM and XRD. It is found that different thickness of the defect free Al layer can be epitaxially grown on Al(Ga)N nanowires. This study suggests that seamless Al/Al(Ga)N nanowire epitaxy would enable different novel functionalities and improve III-nitride based optoelectronic/electronic devices. It is envisioned that the metal/semiconductor nanowire epitaxy can be further improved by adopting selective area epitaxy where Al or other metals can be grown epitaxially on different semipolar or non polar Al(Ga)N nanowire facets [266].

Chapter 6

Record Low Resistance AlGaN Nanowire Backward Diode for High Efficiency III-Nitride Photonic Devices

III-nitride backward diodes (conduct more current at reverse bias) are in demand for a broad range of electronic and optoelectronic applications including visible and ultraviolet light-emitting diodes (LEDs), laser diodes (LDs), multi junction solar cells, vertical-cavity surface-emitting lasers (VCSELs) etc. [218, 221, 242, 259, 262, 264, 267-269]. As discussed in previous chapters, low resistance, efficient tunnel junctions or backward diodes integrated with photonic devices offer several potential benefits. Yet, demonstration of efficient, low resistance stand-alone tunnel junction (backward diode) using large bandgap AlGaN nanowire remains very challenging. Low resistance tunnel junction requires an ultrathin depletion width for efficient electron tunneling from the filled valence band to the empty conduction band.

To date, however, the resistance and the overall performance of III-nitride tunnel junctions has been severely limited by the *p*-type dopant solubility limitation, prohibitively large dopant ionization energy (200-600 meV) and wide band gaps (3.4 eV to 6.2 eV) [150]. It was previously reported that *p*-/*n*- doping concentration in the range of $\sim 10^{18} \text{ cm}^{-3}$ - 10^{19} cm^{-3} can significantly impact tunnel junction performance [218, 221, 225, 259, 268, 270-272]. It was also reported that low resistance can be achieved in GaN-based homo tunnel junction given that the *p*-doping concentration is high to shrink the depletion region [243, 270-273]. Moreover, previous studies

suggest that tunnel junction performance is severely limited in planar structure due to the presence of high density of defects and low p -type dopant ionization efficiency [274].

The current-voltage characteristics are further restricted in relatively wide bandgap Al(Ga)N-based tunnel junctions because of the poor dopant ionization efficiency and associated wide depletion region that inhibits efficient tunneling [242, 269, 275]. Due to the large lattice mismatch, medium to Al-rich AlGaN-based materials/devices suffer from high density of defects and dislocations compared to GaN or InGaN-based materials/devices grown on foreign substrates. Besides, p -type doping efficiency is by and large limited by Al-composition, and decreases with the increase of Al-mole fraction [202]. III-nitride nanowires exhibit reduced dislocation densities and polarization fields due to stress relaxation. The previous studies on the AlGaN-based planar tunnel junctions, however, mostly focused on the polarization engineering at the AlGaN/InGaN interfaces [242, 269]. Furthermore, the performance (specific resistivity and turn-on voltage) of those devices is limited by relatively inefficient p -type doping, large density of defects, and inefficient polarization engineering at the interfaces.

Contrary to planar structures, due to effective stress relaxation, it has remained challenging to realize polarization engineered tunnel junctions in the low-dimensional III-nitride nanowires. Additionally, significantly high absorption loss in InGaN inter-layer inhibits the seamless integration of polarization engineered Al(Ga)N/InGaN/Al(Ga)N tunnel junction with efficient light emitters. Recent studies have demonstrated that significantly enhanced Mg-dopant incorporation and resulting large hole concentration can be achieved in III-nitride nanowire grown by molecular beam epitaxy (MBE). In contrast to MBE, MOCVD process requires Mg dopant activation from Mg-H complex. Compared to planar structures, in low dimensional nanowires dopant formation energy is much reduced in the near surface region. Recently, n^{++} -GaN/Al/ p^{++} -

Al(Ga)N backward diode integrated visible and ultraviolet LEDs have been successfully demonstrated without polarization engineering [259, 268, 276]. Still, extensive studies on the intrinsic performance of stand-alone AlGaN-based nanowire tunnel junctions or backward diodes have been remained elusive, and extensive studies are required to carefully examine the critical parameters for low resistance, high efficiency tunnel junctions/backward diodes.

6.1 Design and Growth

In this work, we have studied four different types of Al(Ga)N backward diodes, including n^{++} -GaN/Al/ p^+ -Al_{0.15}Ga_{0.85}N, n^{++} -GaN/Al/ p^+ -Al_{0.50}Ga_{0.50}N, n^+ -Al_{0.50}Ga_{0.50}N/Al/ p^+ -Al_{0.50}Ga_{0.50}N, n^+ -AlN/Al/ p^+ -AlN illustrated in Fig. 6.1a, which are denoted as BD A, BD B, BD C and BD D. Here, we have studied all the backward diode structures in n - p - n configuration, where heavily doped n^{++} -Al(Ga)N/Al/ p^+ -Al(Ga)N backward diode is serially connected to a GaN-based p - n junction.

It is worthwhile mentioning that such n - p - n backward diode is not limited by high p -contact

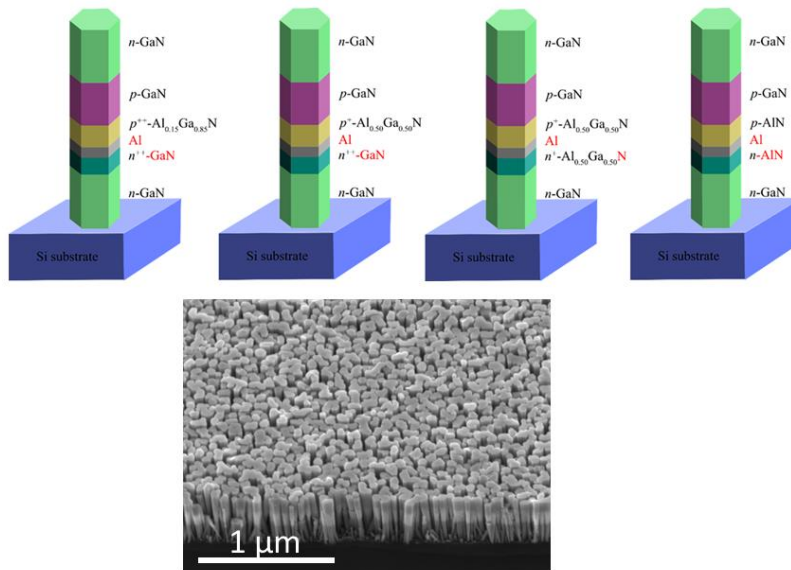


Figure 6.1: (a) Schematic diagram of four different composition AlGaN backward diodes (BD A, BD B, BD C, BD D) (b) An SEM image of AlGaN backward diode taken with a 45° angle.

resistance, and therefore, it is envisioned that the intrinsic carrier transport of the backward diode can be better comprehended. It was also demonstrated that heavily Mg-doped p -GaN up nanowire structures generally exhibits relatively poor crystalline quality including non-uniform nanowire density, height, and rough surface morphology [197, 277]. Therefore, subsequent device processing becomes difficult due to contact planarization and metallization issues.

All the backward diode structures were grown on n -Si (111) substrate under nitrogen rich condition without using any external metal catalyst. As can be seen in Fig. 6.1a, the n - p - n tunnel junction device structure consists of ~ 200 nm Si-doped n -GaN base layer, ~ 40 nm Al(Ga)N/Al/Al(Ga)N backward diode segment (varying Al compositions in p^+ -AlGaN), ~ 100 nm Mg-doped p -GaN layer, ~ 200 nm Si-doped n -GaN capping layer and ~ 15 nm heavily Si-doped n^{++} -GaN contact layer for subsequent ohmic contact formation during device processing. The substrate temperature was ~ 780 °C for n -GaN and 770 °C for p -GaN segments. Doping concentration and degeneracy in the whole n - p - n backward diode structure were controlled by the Si (n -doping) and Mg (p -doping) effusion cell temperatures, associated beam equivalent pressure and growth temperature. The Al layer was grown at ~ 450 °C and was subsequently capped with a thin layer of Ga. In this process, the nitrogen plasma was turned off to avoid the formation of large bandgap AlN or AlGaN. The substrate temperature was then increased to 650 °C for the growth of p^+ -AlGaN (~ 15 nm). Ga and Al beam equivalent pressures (BEPs) of $\sim 2.5 \times 10^{-8}$ and 4.3×10^{-9} Torr were used for BD A. However, Al BEP of 1.2×10^{-8} Torr was used for BD B, BD C, BD D. Si and Mg doping concentrations in the heavily doped n -Al(Ga)N and p -Al(Ga)N segments of the tunnel junction were in the ranges of 5×10^9 and 1×10^{20} cm $^{-3}$, respectively. A relatively low nitrogen flow rate ~ 0.4 sccm was used during the AlGaN growth, which, together with the relatively high substrate temperature, is found to be highly beneficial to enhance Al adatom migration and to suppress

defect formation [202, 278]. Such growth conditions were obtained based on extensive studies of the fabrication and testing of Al(Ga)N/Al/Al(Ga)N nanowire tunnel junctions.

Details of the GaN/Al/Al(Ga)N and GaN/InGaN/GaN growth and its integration with visible and deep ultraviolet LEDs can be found in previous chapters [264, 268]. Illustrated in Fig. 6.1b is the scanning electron microscopy (SEM) image of n^{++} -GaN/Al/ p^+ -AlGaN backward diode (BD A). As can be seen, the nanowires are vertically aligned on the Si substrate and exhibit relatively uniform height and size distribution (nanowire lateral sizes in the range of 100-120 nm). Nanowires in BD B, BD C and BD D exhibit similar structural properties (height, density, and diameter). Nanowires in all the tunnel junction structures were grown along the c -axis and possess N-polarity.

6.2 Schematic Band Diagram

The schematic band diagrams of different Al/Al(Ga)N backward diodes are shown in Fig. 6.2 a,b,c,d. As can be seen in Fig. 6.2a and 6.2b, Al metal (work function 4.08 eV) can readily form an ohmic tunnel contact to heavily doped n^{++} -Al(Ga)N. On the other hand, with heavy Mg-doping, the depletion width at Al/Al_{0.15}Ga_{0.85}N interface is decreased. It is worthwhile mentioning that the carrier tunneling probability critically depends on the depletion width at metal/ p^+ -Al(Ga)N interface. As shown, carrier can efficiently tunnel from the filled valence band of p^+ -Al(Ga)N through the epitaxial Al metal layer due to the reduced depletion width. This transport mechanism is similar to field emission (FE) while the p -type Al(Ga)N is heavily doped ($N_A > 2 \times 10^{19} \text{ cm}^{-3}$) [245]. In addition, at room temperature, due to the presence of deep level defect (DLD) bands in p^+ -Al(Ga)N and interfacial traps, carrier tunneling from p^+ -Al(Ga)N to Al is significantly enhanced in a similar manner like trap-assisted tunneling (TAT) [245, 259, 279].

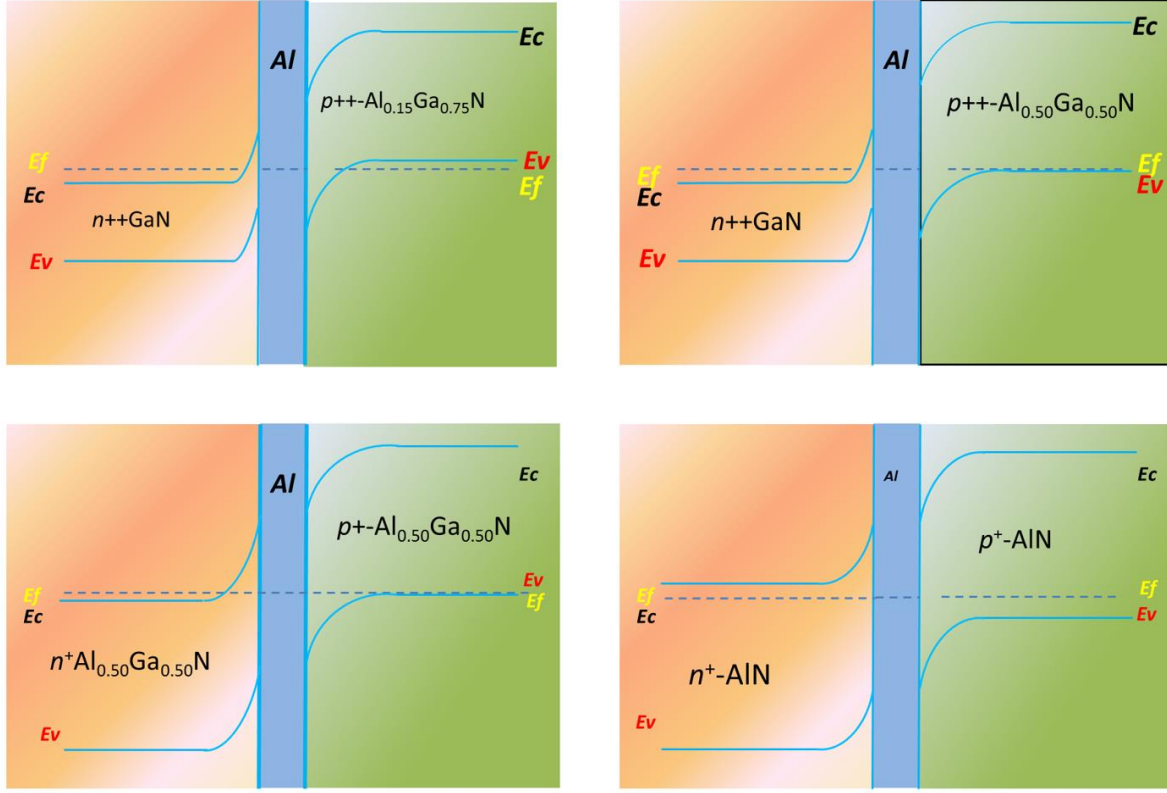


Figure 6.2: Schematic energy band diagram of (a) n^{++} -GaN/Al/ p^{+} -Al_{0.15}Ga_{0.85}N backward diode structures (BD A) (b) n^{++} -GaN/Al/ p^{+} -Al_{0.50}Ga_{0.50}N backward structure (BD B) (c) n^{+} -Al_{0.50}Ga_{0.50}N /Al/ p^{+} -Al_{0.50}Ga_{0.50}N backward structure (BD C) (d) n^{+} -AlN/Al/ p^{+} -AlN backward structure (BD D).

As shown in Fig. 6.2b, due to the moderate p -type doping ($\sim 1 \times 10^{18} \text{ cm}^{-3}$) in Al_{0.50}Ga_{0.50}N, the depletion width (at Al/ p^{+} -Al_{0.50}Ga_{0.50}N interface) and barrier height is increased that result in limited carrier tunneling. However, for n^{+} -AlGa_{0.50}N/Al/ p^{+} -AlGa_{0.50}N and n^{+} -AlN/Al/ p^{+} -AlN the depletion width and barrier height are further increased (in both of the interfaces) due to inefficient doping (both Mg and Si) and large band gaps. It is surmised that thermionic emission (TE) is dominant due to such large band gaps and related high potential barrier [245, 277].

6.3 Device Fabrication

During the TJ device fabrication process, the nanowire arrays were first planarized using a polyimide resist layer, followed by O₂ plasma etching to expose the nanowire top surface. Thick Ti(40 nm)/Au (200 nm) and Ti (20 nm)/Au (100 nm) metal layers were then deposited on the nanowire surface and the backside of the Si substrates to serve as *p*- and *n*-metal contacts, respectively. Contrary to III-nitride nanowire LED fabrication, sufficiently thick metal layers were deposited on both sides, since backward diodes are not limited by visible/UV light absorption in the thick metal layers. It was found that current injection to the nanowire devices are critically dependent on the thickness and step-coverage of the metal layers. The fabricated devices with metal contacts were annealed at ~500 °C for 5 mins in nitrogen ambient.

6.4 Current-Voltage Characteristics

Current-voltage characteristics of all the backward diode nanowire structures (BD A, B, C and D) were measured under continuous wave (CW) biasing conditions at room temperature. During the measurement, a negative bias was applied on the top surface for *n*-GaN (since all the structures are in *n-p-n* configuration). As such, the *p-n* junction was forward biased (a resistor) and serially connected backward diode was reverse biased. Shown in Fig. 6.3a and 6.4, All the devices exhibit clearly rectifying backward diode characteristics (the semi-log scale I-V characteristics are also shown in the insets of Fig. 6.3a and 6.4). The measured device areal size is 500×500 μm², and the nanowire filling factor is ~30%. Shown in Fig. 6.3a, the *n-p-n* backward diode device (BD A) shows clear rectifying characteristics (the reverse current is much higher than forward current) with a sharp turn-on voltage of ~2.7 V. Shown in Fig. 6.3b, the device total specific resistivity

estimated from the linear region of the forward I-V characteristics is $\sim 9 \times 10^{-4} \Omega \cdot \text{cm}^2$ or less, for the backward diode nanowire device (BD A).

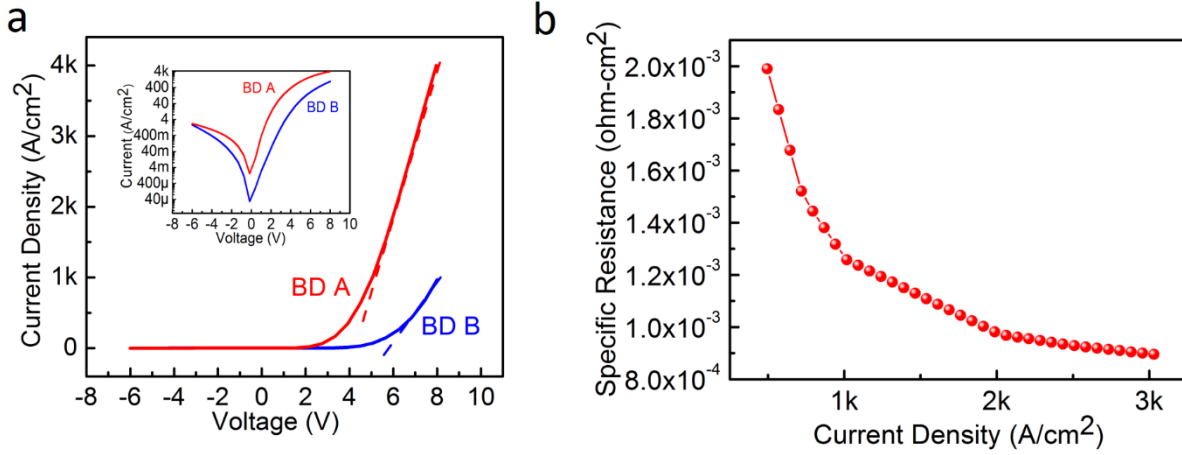


Figure 6.3: a) I-V characteristics comparison of n^{++} -GaN/Al/ p^{++} -Al_{0.15}Ga_{0.85}N backward diode structure (BD A) and n^{++} -GaN/Al/ p^{++} -Al_{0.50}Ga_{0.50}N (BD B), the inset shows the I-V plots in semi-log scale. b) Specific resistance vs Current density plot of n^{++} -GaN/Al/ p^{++} -Al_{0.15}Ga_{0.85}N backward diode structure (BD A).

This specific device resistivity for different devices includes p - and n -contact resistance, resistance of p -/ n - junction and resistance of backward diode itself. Taking these factors into account, the upper limit of n^{++} -GaN/Al/ p^{++} -Al_{0.15}Ga_{0.85}N backward diode resistance (BD A) is estimated to be $\sim 1.5 \times 10^{-4} \Omega \cdot \text{cm}^2$, or less. In this estimation, the contact resistance for the top and bottom contacts was estimated to be $\sim 2 \times 10^{-4} \Omega \cdot \text{cm}^2$ and $\sim 3 \times 10^{-4} \Omega \cdot \text{cm}^2$ [242]. The series resistance of the p -GaN layer was estimated to be $3 \times 10^{-4} \Omega \cdot \text{cm}^2$, however, the series resistance of n -GaN layer is ignored. Additionally, the backward diode device resistance is further limited by the presence of a SiN_x layer at the Si and GaN nanowire interface [211-213]. Specific resistivity values in the range of 10^{-4} to $10^{-2} \Omega \cdot \text{cm}^2$ have been previously reported in different AlGaN/InGaN, GaN/InGaN and Al/Al(Ga)N based planar and nanowire tunnel junction devices [144, 218, 221, 223, 225, 242, 259, 267-273, 275, 280-283] (shown in Table 6.1). In addition, the device showed only ~ 3 V forward voltage drop at 100 A/cm^2 . Such excellent device properties are attributed to the efficient p -type

doping, nearly defect free growth, reduced barrier height at Al/ p^{++} -Al(Ga)N interface, excellent current transport through the epitaxial Al metal layer, and due to the elimination of resistive p -Al(Ga)N contact. As shown in Fig. 6.3a, the total specific resistivity for BD B is $\sim 1 \times 10^{-3} \Omega \cdot \text{cm}^2$, and therefore, the upper limit of n^{++} -GaN/Al/ p^{++} -Al_{0.50}Ga_{0.50}N is $\sim 9 \times 10^{-4} \Omega \cdot \text{cm}^2$. This result suggests that efficient inter-band conduction critically depends on the barrier height at Al/ p^{++} -Al(Ga)N interface. Furthermore, different turn-on voltages in the devices are also attributed to the increased barrier height/depletion width at p^+ -Al(Ga)N/Al interfaces and therefore, increased reverse bias was needed for efficient inter-band tunneling.

Table 6.1 Specific resistivity values of different planar/nanowire tunnel junction devices

Journal	Tunnel Junction (TJ)	TJ resistance ($\Omega \cdot \text{cm}^2$)	Device resistance ($\Omega \cdot \text{cm}^2$)	Structure	Method
<i>APL</i> , 105,141104, 2014	InGaN/GaN	5×10^{-4}	2×10^{-2}	Planar , TJ LED	PA-MBE
<i>Nano Lett</i> , 13, 2570-2575, 2013	GdN/GaN	1.3×10^{-3}	N/A	Planar , TJ p-n device	PA-MBE
<i>Nano Lett</i> , 13, 2570-2575, 2013	p^{++} -GaN/ n^{++} -GaN	22.5×10^{-2}	N/A	Planar TJ device	PA-MBE
<i>IEEE EDL</i> , 36, 4, 2015	InGaN/GaN	6.05×10^{-3}	2.38×10^{-2}	Planar TJ LED	MOCVD
<i>IEEE JQE</i> , 51, 8, 2015	AlGaIn/InGaN	1.95×10^{-3}	1.97×10^{-2}	Planar TJ LED	MOCVD
<i>APEX</i> , 8, 082103, 2015	InGaN/GaN	5×10^{-4}	0.3×10^{-2}	Planar , cascaded TJ LED	PA-MBE
<i>APL</i> , 107,051107, 2015	p^{++} -GaN/ n^{++} -GaN	N/A	3.7×10^{-4}	Planar , TJ LED	Ammonia MBE
<i>Nano Lett.</i> , 15,10,6696,2015	InGaN/GaN	N/A	3×10^{-2}	Nanowire , TJ LED	PA-MBE
<i>Nano Lett.</i> , 16(2) 1076,2016	Al/GaN	$\sim 10^{-3}$	0.4×10^{-2}	Nanowire , TJ LED	PA-MBE
<i>APL</i> , 99, 233504, 2011	InGaN/GaN	$\sim 10^{-4}$	N/A	Planar , TJ device	PA-MBE

Journal	Tunnel Junction (TJ)	TJ resistance ($\Omega \cdot \text{cm}^2$)	Device resistance ($\Omega \cdot \text{cm}^2$)	Structure	Method
<i>APL</i> , 106, 141103, 2015	$\text{Al}_{0.3}\text{Ga}_{0.7}\text{N}/\text{In}_{0.25}\text{Ga}_{0.75}\text{N}$	5.6×10^{-4}	NA	<i>Planar</i> , TJ UV LED	PA-MBE
<i>APL</i> , 109, 121102, 2016	$\text{Al}_{0.55}\text{Ga}_{0.45}\text{N}/\text{In}_{0.2}\text{Ga}_{0.8}\text{N}$	9.4×10^{-4}	N/A	<i>Planar</i> , TJ p-n device	PA-MBE
<i>APEX</i> , 9, 052102, 2016	$\text{Al}_{0.3}\text{Ga}_{0.7}\text{N}/\text{In}_{0.25}\text{Ga}_{0.75}\text{N}$	5.6×10^{-4}	N/A	<i>Planar</i> TJ device	PA-MBE
<i>APL</i> , 110, 201102, 2017	$\text{Al}_{0.75}\text{Ga}_{0.025}\text{N}/\text{In}_{0.2}\text{Ga}_{0.8}\text{N}$	$>1 \times 10^{-3}$	N/A	<i>Planar</i> TJ LED	PAMBE
<i>APL</i> , 108, 072102 (2016)	$\text{p}^{++}\text{GaN}/\text{n}^{++}\text{GaN}$	2×10^{-3}	N/A	<i>Planar</i> TJ Device	Ammonia MBE
<i>APEX</i> , 9, 022102, 2016	$\text{p}^{++}\text{GaN}/\text{n}^{++}\text{GaN}$	1.5×10^{-4}	0.3×10^{-2}	<i>Planar</i> , TJ LED	PA-MBE
<i>APL</i> , 108, 131103, 2016	$\text{p}^{++}\text{-GaN}/\text{n}^{++}\text{-GaN}$	3.1×10^{-4}	N/A	<i>Planar</i> , TJ Device	PA-MBE
<i>NanoLett.</i> , 17 (2), 1212, 2017	$\text{Al}/\text{Al}(\text{Ga})\text{N}$	$\sim 1 \times 10^{-3}$	3×10^{-2}	<i>Nanowire</i> , TJ LED	PA-MBE
<i>This work</i>	Al/AlGaN	$\sim 10^{-3}$	0.4×10^{-2}	<i>Nanowire</i> , TJ Device	PA-MBE

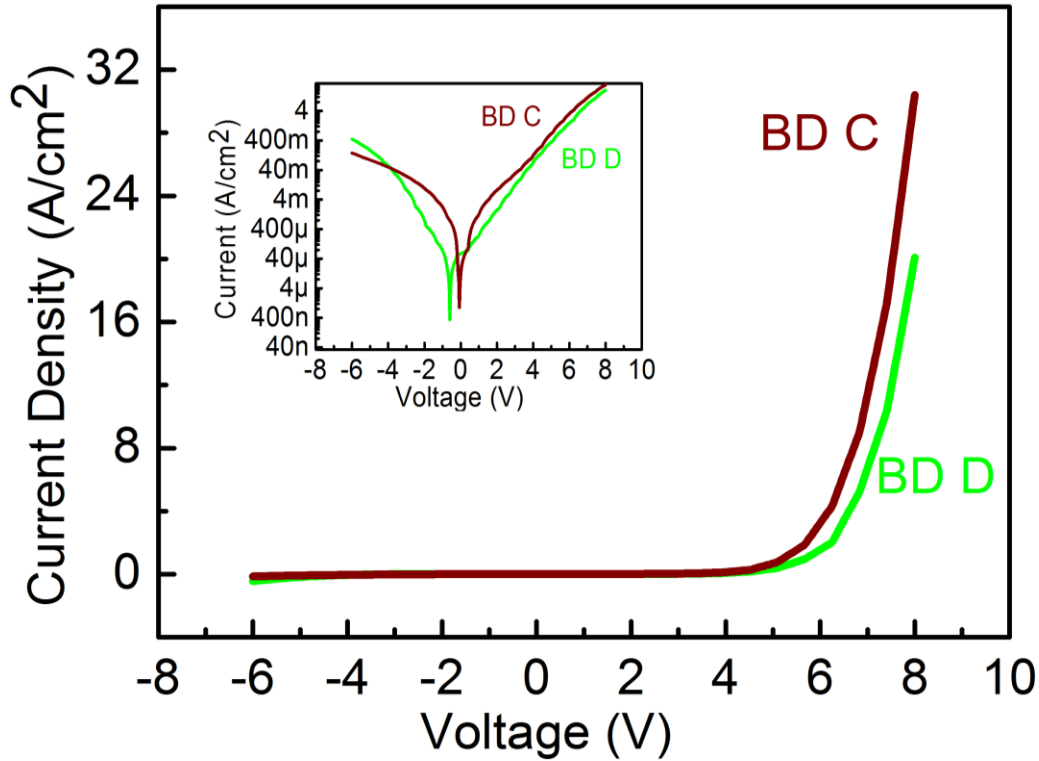


Figure 6.4: I-V characteristics comparison of n^+ - Al_{0.50}Ga_{0.50}N /Al/ p^+ -Al_{0.50}Ga_{0.50}N backward structure (BD C) and n^+ -AlN/Al/ p^+ -AlN backward structure (BD D), the inset shows the I-V plots in semi-log scale.

Shown in Fig. 6.4, For BD C and BD D, the turn-on voltage and specific resistivity is significantly increased with the increase of Al mole fraction and addition of n -AlGa_{0.50}N layer at the bottom interface. It confirms that inter-band tunneling not only depends on the Al/ p^+ -Al(Ga)N interface and Al mole fraction, but also depends on the n^+ -AlGa_{0.50}N/Al interface. This also suggests that efficient ohmic/quasi-ohmic contact formation at the interfaces is critical for monolithic metal/wide bandgap AlGa_{0.50}N nanowire tunnel junction. It is envisioned that with further optimization of the design, doping and epitaxy process, both the turn-on voltage and differential resistivity of different Al mole fraction, Al/Al(Ga)N backward diodes can be further reduced.

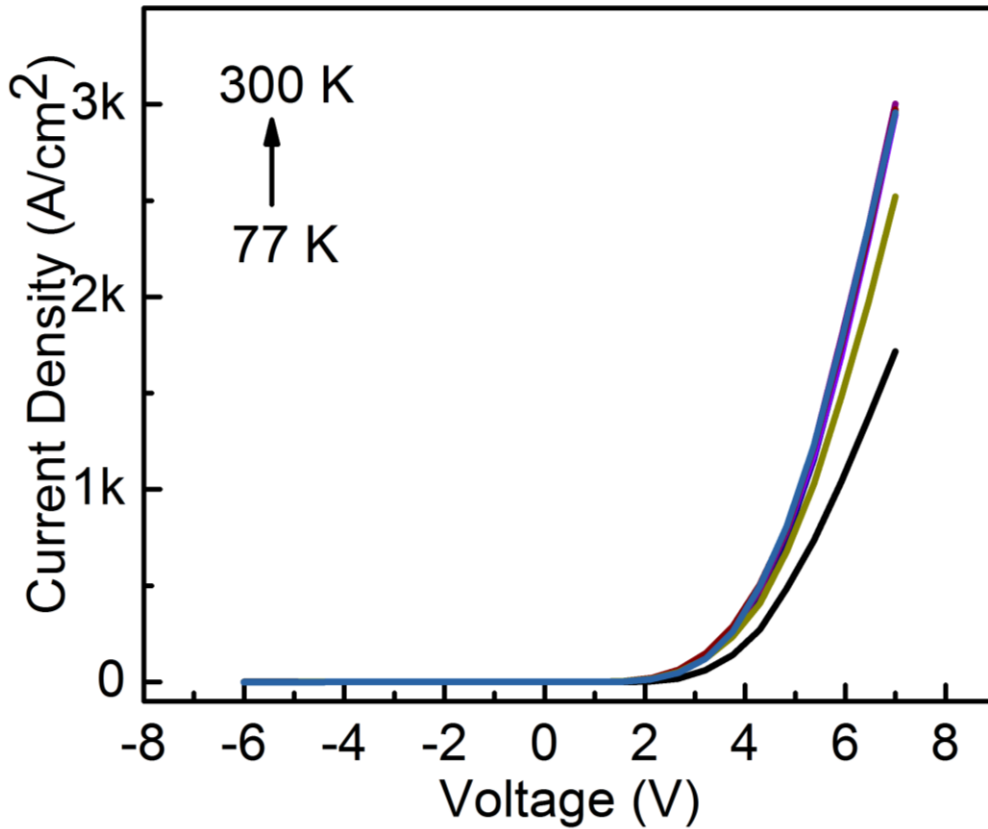


Figure 6.5: (a) Temperature dependent I-V characteristics comparison of n^{++} -GaN/Al/ p^+ -Al_{0.15}Ga_{0.85}N backward diode structure (BD A).

Fig. 6.5, shows the temperature-dependent I-V curves for the backward diode A (measured device areal size is $500 \times 500 \mu\text{m}^2$). An important figure of merit for backward diode is the curvature co-

efficient at zero voltage defined as $\gamma = \frac{\delta^2 I}{\delta V^2} \frac{\delta V}{\delta I}$ [272]. The measured γ is 14 V^{-1} at 300 K for BD A, and

this is insensitive to temperature as γ remains constant even at low temperature ($\gamma = 15 \text{ V}^{-1}$ at 77 K). It is worthwhile mentioning that such constant figure of merit, γ is lower than thermal limit value $\sim 40 \text{ V}^{-1}$ and consistent with the previously reported III-nitride backward diodes [171, 272].

Significantly lower and consistent γ value further suggests that carrier transport is not limited by

Schottky barrier at either interface. Such low γ value is attributed to excellent dopant incorporation in *n*- and *p*-sides of low-dimensional nanowires.

6.5 Summary

In conclusion, we have demonstrated the design, epitaxy, and device performance of different Al composition Al/AlGa_N nanowire backward diodes by MBE. The low-resistance backward diode integrated with a *p-n* junction eliminates the need of polarization engineering, and therefore It shows that Al composition up to 50% can perform efficient inter-band tunneling. Our comprehensive study suggests that specific resistivity critically depends on the Al molar fraction, *p*-/*n*-doping and related depletion width. The lowest specific resistivity $\sim 1.5 \times 10^{-4} \Omega \cdot \text{cm}^2$ was measured with a turn-on voltage ~ 2.7 V. Such a new class of AlGa_N-based nanowire backward diode offers a unique approach for achieving ultra-high efficiency III-nitride electronic devices.

Chapter 7

Monolithically Integrated Metal/Semiconductor Tunnel Junction Nanowire Light Emitting Diodes

The results of this chapter were previously published in *Nano Lett.*, 2016, 16 (2), pp 1076–1080 [284].

As discussed in Chapter 1 and in previous chapters, the scheme of tunnel junction has been employed in a broad range of electronic and optoelectronic devices. However, its application in wide bandgap devices, such as GaN and AlN based light emitting diodes (LEDs) and lasers has been limited. To date, however, it has remained challenging to form an efficient, low resistance tunnel junction using wide bandgap GaN-based materials [285]. Illustrated in Fig. 7.1a is the schematic energy band diagram of a conventional n^{++} -GaN/ p^{++} -GaN tunnel junction.

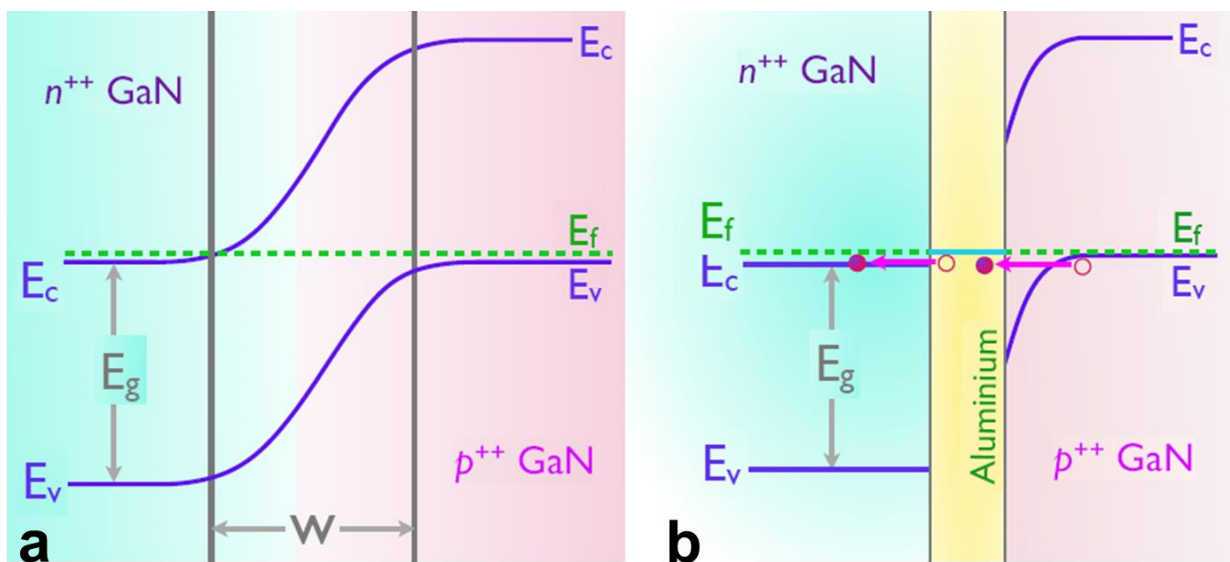


Figure 7.1: Schematic energy band diagram of (a) conventional p^{++}/n^{++} GaN tunnel junction and (b) n^{++} -GaN/Al/ p^{++} -GaN tunnel junction structures.

The inefficient *p*-type doping in GaN and AlN, due to the low acceptor ionization efficiency,[286] leads to a large depletion region width (wide tunnel barrier thickness) that inhibits efficient inter-band tunneling. In this context, the inherent spontaneous and piezoelectric polarization of wurtzite GaN-based heterostructures has been exploited to enable efficient inter-band tunneling. Several tunnel junction designs, including GaN/AlN/GaN [173, 287], GaN/InGaN/GaN [145, 218, 221, 222, 267, 288, 289] AlGaIn/InGaIn,[242, 290] AlGaIn/GaN,[150, 151] and GaN/InGaIn [218, 224] have been demonstrated. Although promising results have been achieved using these tunnel junctions in planar devices, it has remained challenging to incorporate these designs in emerging nanowire structures. Due to the inherent strain relaxation, polarization-induced sheet charge at the heterointerface of nanowire structures is significantly reduced. Consequently, polarization engineered tunnel junctions may exhibit a higher voltage drop in nanowire-based devices [218]. In addition, the successful incorporation of such tunnel junctions by and large depends on the crystal polarity (N-face or Ga-face) [222, 291]. Despite the reduction in tunnel barrier width over conventional tunnel junctions, the afore-described AlN/GaN and InGaIn/GaN based tunnel junctions still suffer from comparatively low inter-band tunneling conduction as well as optical absorption loss.

Alternatively, tunnel junction devices that incorporate rare earth materials GdN [225] or semi metallic MnAs [292] and ErAs [293, 294] nanoparticles have been demonstrated under forward and reverse bias, wherein tunneling is enhanced by the presence of mid-gap states. In this context, we have proposed and demonstrated, for the first time, a monolithically integrated metal/semiconductor nanowire tunnel junction LED, wherein the tunnel junction consists of n^{++} -GaN/Al/ p^{++} -GaN, schematically shown in Fig. 7.1b. With a work function of 4.08 eV, Al metal

can form an ohmic contact to n -GaN [295]. The presence of defects at the Al/ p^{++} -GaN interface, partly due to the very high Mg-doping ($N_A \sim 1 \times 10^{20} \text{ cm}^{-3}$) [296-298], results in deep energy levels, which can significantly enhance carrier transport from p -GaN to Al in a similar manner to conventional trap-assisted tunneling [299]. As such, it is expected that the epitaxial Al/ p^{++} -GaN can exhibit quasi-ohmic contact characteristics [300, 301]. Consequently, the effective tunneling barrier width is minimized, thereby enabling efficient inter-band conduction from p -GaN to n -GaN through the Al interconnect. The back-to-back Al quasi-ohmic/ohmic contacts to the p^{++} and n^{++} -GaN layers eliminate the need for polarization engineering at the interface to shrink the depletion region for efficient tunneling. With the use of molecular beam epitaxy (MBE), we have demonstrated the monolithic integration of nearly defect-free GaN/Al/GaN tunnel junction LED heterostructures. Unique to the Al-based tunnel junction is that the Al layer, with appropriate thickness, can serve as a mirror to reflect light emitted from the active region [302, 303], given its high reflectivity ($\sim 90\%$) in the visible and UV spectral range, which is in direct contrast to the light absorption induced by polarization engineered tunnel junctions in previous reports [218, 221]. We have further shown that the incorporation of such tunnel junction in InGaN/GaN dot-in-a-wire LEDs can lead to significantly improved light output power and lower operation voltage, compared to identical nanowire devices without the use of tunnel junctions or with the incorporation of n^{++} -GaN/ p^{++} -GaN tunnel junctions.

7.1 Design and Growth

In this work, we have investigated three different types of InGaN/GaN nanowire LED structures, including a) n^{++} -GaN/Al/ p^{++} -GaN tunnel junction LEDs (LED A), b) n^{++} -GaN/ p^{++} -GaN tunnel junction LEDs (LED B), and c) conventional nanowire LEDs without the use of any tunnel junction (LED C). Schematics for LED A, LED B, and LED C are shown in Fig. 7.2a. The tunnel

junction of LED A consists of n^{++} -GaN (7 nm), Al (2 nm), and p^{++} -GaN (10 nm). The tunnel junction of LED B is identical to that of A but without the incorporation of the Al layer. The active regions of LEDs A, B, and C consist of ten self-organized InGaN (3 nm)/GaN (3 nm) quantum dots [134, 304, 305]. Each quantum dot layer is modulation doped p -type to enhance the hole injection and transport in the device active region [134, 305]. In order to examine the intrinsic properties of the tunnel junction dot-in-a-wire LEDs, no AlGaN electron blocking layers were incorporated. All the LED structures were grown by plasma-assisted MBE on n -Si (111) substrate under nitrogen-rich conditions without using any external metal catalyst [77, 141]. Prior to the growth, native oxide on the Si substrate was removed by hydrofluoric acid (10%), and further *in situ* desorbed at ~ 770 °C. The N_2 flow rate was kept at 1.0 standard cubic centimeter per minute (sccm) with a forward plasma power of ~ 350 W during the growth. The substrate temperature was ~ 780 °C for n -GaN and 750 °C for p -GaN segments. Doping concentration and degeneracy in the tunnel junction were controlled by the Si (n -doping) and Mg (p -doping) effusion cell temperatures. The Al layer was grown at ~ 450 °C and was subsequently capped with a thin layer of Ga. In this process, the nitrogen plasma was turned off to avoid the formation of AlN. The substrate temperature was then increased to 650 °C for the growth of p^{++} -GaN (10 nm). Such optimum growth conditions were obtained based on extensive studies of the LED performance by varying the Al thickness (~ 1 to 6 nm) and growth temperature (~ 300 to 650 °C) and by changing the Si and Mg-doping concentrations. It was observed that a high quality pure Al metal layer could be grown *in situ* on GaN nanowires without any metal agglomeration and void formation. Moreover, detailed structural characterization (to be described later) further confirmed that defect-free nanowires could be grown directly on an epitaxial Al layer [306].

7.2 Characterization of Nanowire Heterostructure

The three nanowire LED structures exhibited nearly identical photoluminescence (PL) characteristics. Shown in Fig. 7.2b is the PL spectrum of LED A measured at room temperature with a 405 nm laser excitation. A single PL emission peak at ~534 nm corresponds to emission from the quantum dot active region. Inhomogeneous broadening seen in the PL emission is largely due to In compositional variations inside the quantum dots. Structural properties of nanowire LEDs were characterized by field emission scanning electron microscopy (SEM). Shown in Fig. 7.2c is

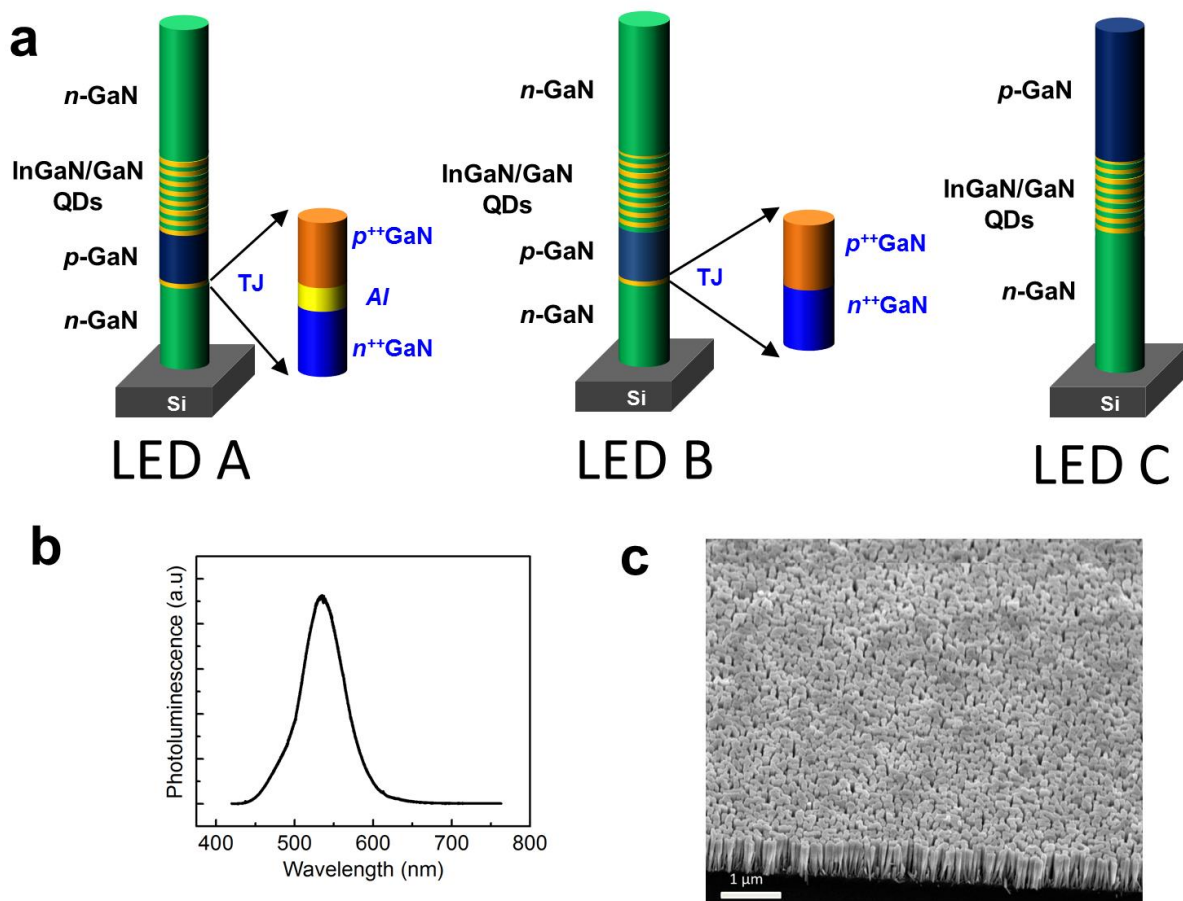


Figure 7.2: (a) Schematic diagram of Al tunnel junction (TJ) dot-in-a-wire LED (LED A), n^{++} -GaN/ p^{++} -GaN tunnel junction LED (LED B), conventional nanowire LEDs without the use of any tunnel junction (LED C) grown on a Si substrate. (b) PL spectra of Al TJ dot-in-a-wire LEDs (LED A) measured at room temperature. (c) An SEM image of Al-interconnect TJ dot-in-a-wire LEDs (LED A) taken with a 45° angle.

a 45° tilted image of the Al-based tunnel junction nanowire structure (LED A). The nanowires are vertically aligned on the substrate, with diameters and densities in the range of 40 to 100 nm and $1 \times 10^{10} \text{ cm}^{-2}$, respectively.

Scanning transmission electron microscopy (STEM) and high-resolution transmission electron microscopy (HR-TEM) studies were further performed to characterize the tunnel junction thickness and composition. The nanowires were first dispersed on a Cu grid. A JEOL JEM-2100F equipped with a field emission gun with an accelerating voltage of 200 kV was used to obtain

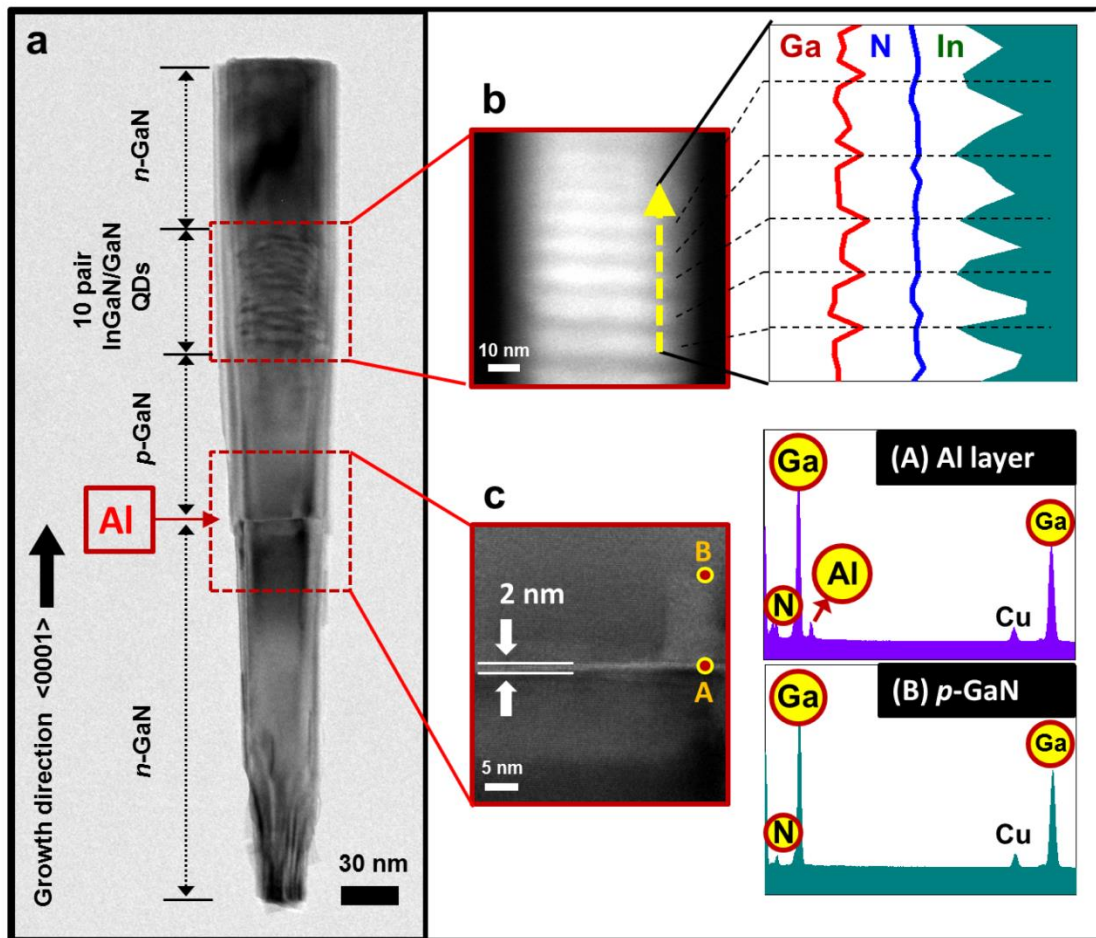


Figure 7.3: (a) STEM image of a single Al tunnel nanowire LED structure (LED A). (b) HAADF (left) and EDXS line profile (right) across the InGaN/GaN quantum dots. (c) HR-TEM image of the Al tunnel junction (left) and EDXS point profiles (right) of the tunnel junction region and p -GaN region.

bright-field TEM images. For STEM and high angle annular dark field (HAADF) imaging, the same equipment with a cold field emission emitter operated at 200 kV and with an electron beam diameter of approximately 0.1 nm was used. Illustrated in Fig. 7.3a is the STEM image of a tunnel junction nanowire structure, wherein the different segments are identified. It is seen that InGaN/GaN quantum dots are positioned in the center of the nanowires due to the strain-induced self-organization. Also, no noticeable stacking faults and threading dislocations were observed. Energy dispersive X-ray spectroscopy (EDXS) analysis was performed along the InGaN/GaN quantum dot active region. The HAADF image and EDXS analysis of the quantum dot active region is further illustrated in Fig. 7.3b, showing the signal variations of Ga and In (dips and peaks) across the active region (quantum dots) along the growth direction (*c*-axis). The HR-TEM image of the tunnel junction is illustrated in Fig. 7.3c. It is seen that the thickness of the Al layer is ~2 nm. EDXS analysis was further performed to study the compositional variations of the n^{++} -GaN/Al/ p^{++} -GaN tunnel junction. An EDXS point profile taken in the vicinity of the Al-layer provided unambiguous evidence for the presence of Al. The thin Al layer is surrounded by relatively thick *p*- and *n*-GaN. Even though the beam was directed toward the Al-layer, Ga and N signals were also detected from the surrounding GaN layers due to the enlarged beam size. It is worthwhile mentioning that due to the high atomic number (atom density) of Ga compared to Al, EDXS analysis gives greater sensitivity to Ga. Point profile measurement away from the Al-layer (*p*-GaN region) shows no measureable trace of Al (Fig. 7.3c).

7.3 Device Fabrication

During the LED fabrication process, the nanowire arrays were first planarized using a polyimide resist layer, followed by contact metallization and thermal annealing. For LEDs A and B, Ti/Au (8 nm/8 nm) and Ti/Au (20 nm/120 nm) layers were deposited on the nanowire surface and the backside of the Si substrate as the top and back metal contact layers, respectively. For LED C, the top metal contact consists of Ni (8 nm)/Au (8 nm). 120 nm indium tin oxide (ITO) was subsequently deposited on the top surface to serve as a transparent current spreading layer. Details about the nanowire LED fabrication process were also described elsewhere and in the previous chapters[134, 226, 307].

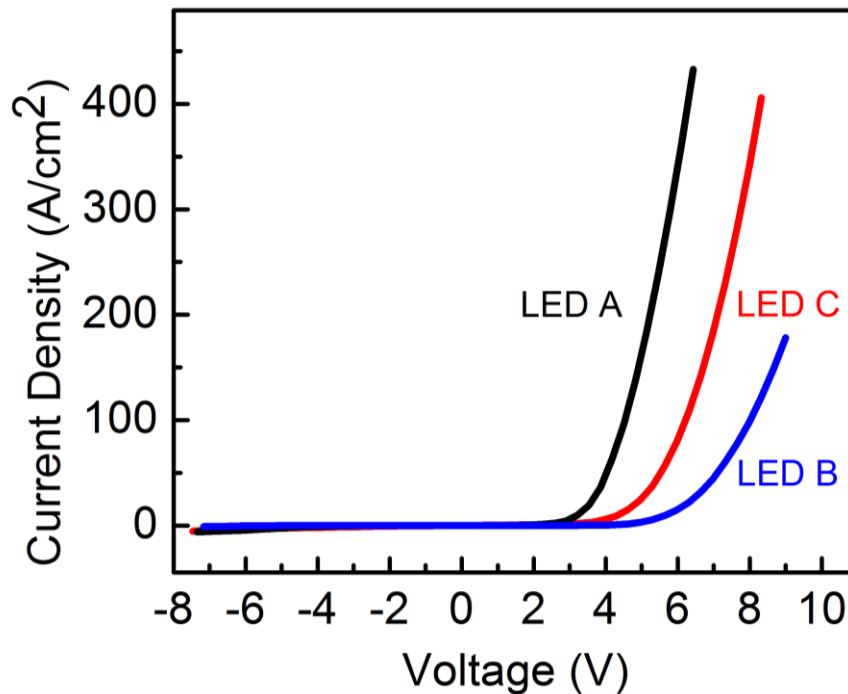


Figure 7.4: I-V characteristics of the Al tunnel junction dot-in-a-wire LED (LED A), n^{++} -GaN/ p^{++} -GaN tunnel junction LED (LED B), and conventional nanowire LED without the use of any tunnel junction (LED C).

7.4 Electrical and Optical Characterizations

Current-voltage characteristics of the nanowire LEDs were measured under continuous wave biasing conditions at room temperature. During the measurements, a negative bias was applied on the top surface for *n*-GaN up LEDs (LEDs A and B). As such, the LED was forward biased and the tunnel junction was reverse biased. Conversely, a positive bias was applied on the top surface for *p*-GaN up device (LED C, without the use of tunnel junction). Shown in Fig. 7.4, the Al tunnel junction device (LED A) shows clear rectifying characteristics with a sharp turn-on voltage of ~ 2.9 V. The device areal size is $500 \mu\text{m} \times 500 \mu\text{m}$, and the nanowire filling factor is $\sim 30\%$. The device specific resistivity estimated from the linear portion of the forward characteristics is $\sim 4 \times 10^{-3} \Omega \cdot \text{cm}^2$ at 400 A/cm^2 . Both the turn-on voltage and resistance is much smaller than that of the conventional nanowire LEDs grown and fabricated under similar conditions but without the use of tunnel junction (LED C). For comparison, the n^{++} -GaN/ p^{++} -GaN tunnel junction LED (LED B) showed significantly larger turn-on voltage ~ 5.5 V and higher resistivity $\sim 5 \times 10^{-2} \Omega \cdot \text{cm}^2$, due to the wide depletion region width formed between n^{++} -GaN and p^{++} -GaN regions and the resulting low tunneling efficiency.

It is also worthwhile mentioning that the specific resistivity of $4 \times 10^{-3} \Omega \cdot \text{cm}^2$ for LED A includes not only the Al tunnel junction resistance, but also the contact resistance and series resistance of the *p*- and *n*-GaN layers. In addition, the device resistance is further limited by the presence of a SiN_x layer at the Si and GaN nanowire interface [211-213] and nonuniform contact to the nanowire arrays due to variations of nanowire heights [210]. In deriving the specific resistance, it is important to take into account the fill factor (surface coverage) of nanowires, which is estimated to be $\sim 30\%$. It is seen the device specific resistivity is in the range of $4 \times 10^{-3} \Omega \cdot \text{cm}^2$ based on the I-V characteristics shown in Fig. 7.4. This specific resistivity includes not only the Al tunnel

junction resistance, but also the metal/semiconductor contact resistance and resistance of the p - and n -GaN layers. Taking these factors into account, we estimated that the specific resistivity for the Al tunnel junction is in the range of $10^{-3} \Omega \cdot \text{cm}^2$, or smaller. Specific resistivity values in the range of 10^{-4} to $10^{-2} \Omega \cdot \text{cm}^2$ have been previously reported in GaN-based planar tunnel junction devices [218, 221, 223, 225, 267, 271, 288, 290]. Given the identical design, growth and fabrication processes for the three LEDs, the significantly reduced turn-on voltage and resistance of LED A provides unambiguous evidence that the n^{++} -GaN/Al/ p^{++} -GaN can serve as a low resistivity tunnel junction.

The Al tunnel junction LED also showed significantly improved light intensity compared to the conventional nanowire device (LED C) and n^{++} -GaN/ p^{++} -GaN tunnel junction device (LED B), illustrated in Fig. 7.5a. These devices were measured under pulsed bias (10% duty cycle) to minimize junction heating effect. The significantly improved light intensity is largely due to the

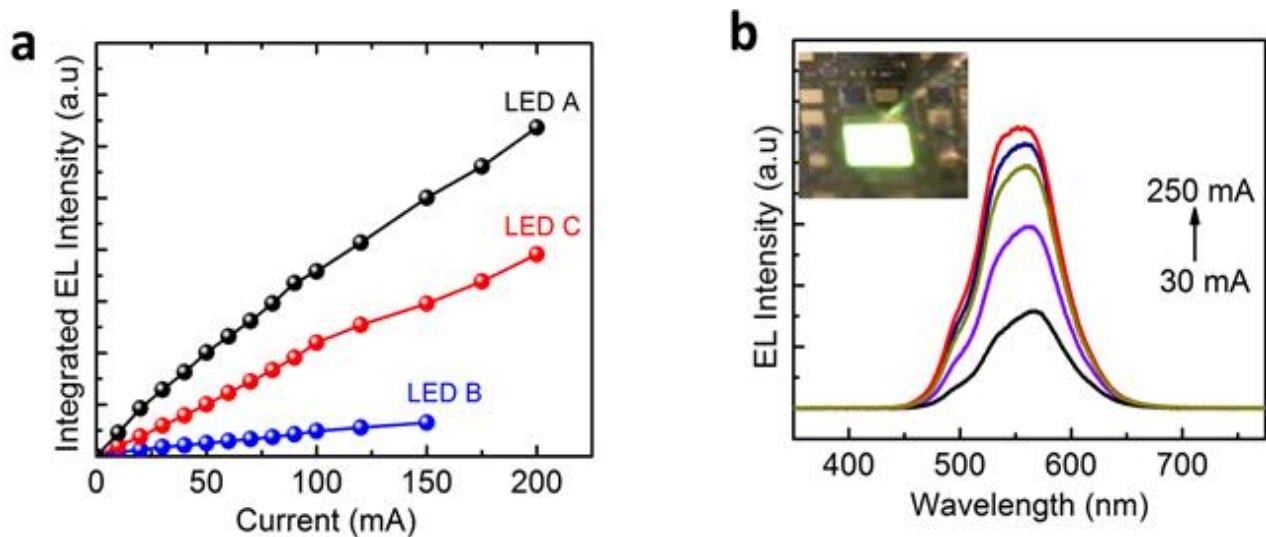


Figure 7.5: (a) L-I characteristics of the Al tunnel junction (TJ) dot-in-a-wire LED (LED A), n^{++} -GaN/ p^{++} -GaN tunnel junction LED (LED B), and conventional nanowire LED without the use of any tunnel junction (LED C). (b) Electroluminescence (EL) spectra of the Al tunnel junction dot-in-a-wire LED (LED A) under pulsed biasing condition (10% duty cycle). Inset: the optical micrograph of the Al tunnel junction dot-in-a-wire LED (LED A) showing strong green light emission.

efficient tunnel injection of holes into the active region. The output spectra of LED A measured from 30 mA to 250 mA are shown in Fig. 7.5b. An optical micrograph of the device is shown in

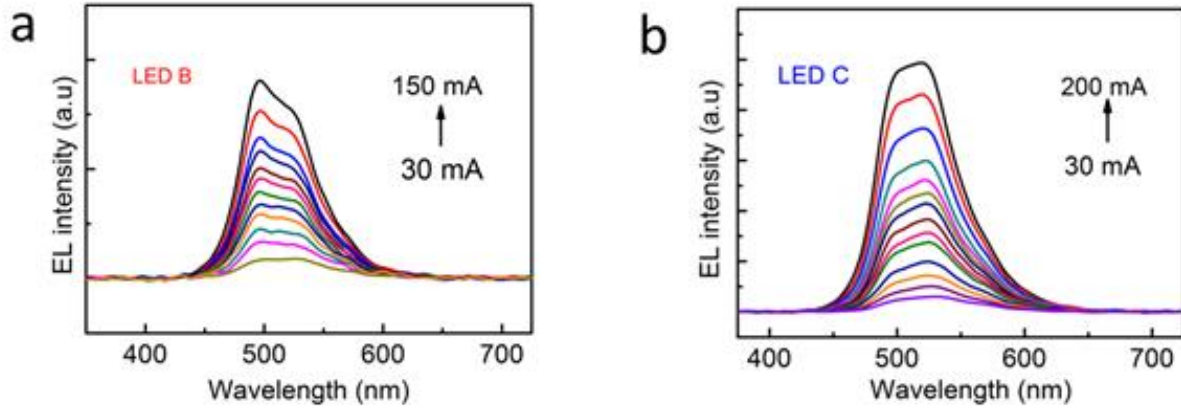


Figure 7.6: Electroluminescence (EL) spectra of LED B and LED C under pulsed biasing condition (10% duty cycle).

the inset of Fig. 7.5b. Output spectra of LED B and LED C are also shown in Fig. 7.6.

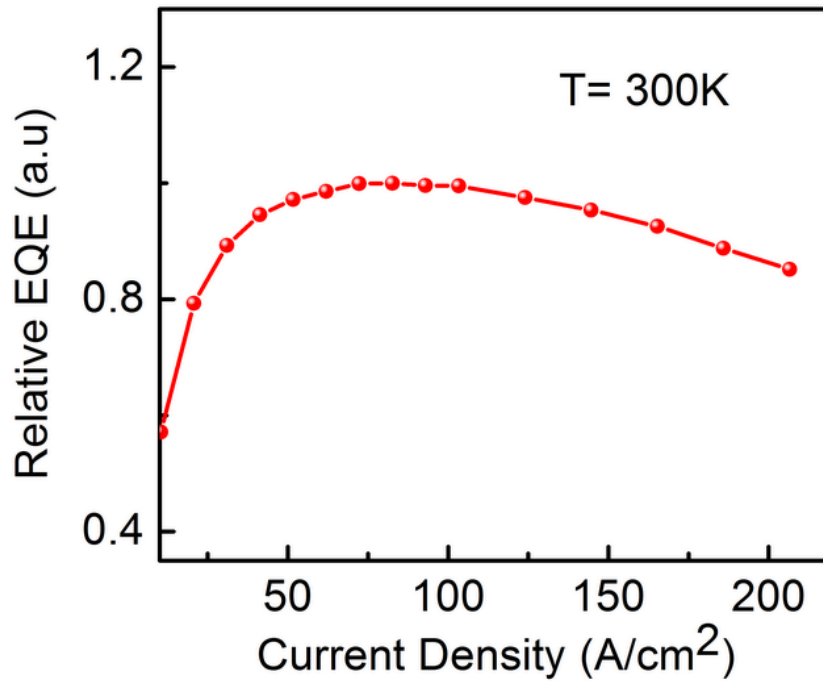


Figure 7.7: Relative external quantum efficiency (EQE) of the Al-tunnel junction nanowire LEDs (LED A) measured under CW biasing condition.

The measured external quantum efficiency (EQE) is also shown Fig. 7.7. There was no noticeable shift in the peak position with increasing current. Such highly stable emission characteristics are a direct consequence of the highly efficient and uniform hole injection in the quantum dot active region. It is further expected that, by suppressing nonradiative surface recombination with the incorporation of core-shell quantum dot active regions [141, 241, 308], the Al tunnel junction nanowire LEDs can lead to high power operation.

7.5 Summary

In summary, we have demonstrated low resistance Al tunnel junction integrated dot-in-a-wire LEDs, enabling *p*-contact free devices with significantly improved hole injection efficiency. Compared to previously reported polarization engineered tunnel junctions, the presented Al tunnel junction completely eliminates the use of either a low bandgap InGaN or a large bandgap Al(Ga)N layer in the tunnel junction design that often leads to undesired optical absorption and/or high voltage loss. Such an Al tunnel junction may also be implemented in either N-face or Ga-face III-nitride quantum well and nanowire LEDs. It also holds tremendous promise for applications in the emerging non-polar and semi-polar GaN optoelectronic devices. Moreover, the seamless integration of defect-free nanowire structures with various metal layers offers a unique approach for achieving high performance nanoscale electronic and photonic devices that were not previously possible.

Chapter 8

An AlGaN Core-Shell Tunnel Junction Nanowire Light Emitting Diode Operating in the Ultraviolet-C Band

The results of this chapter were previously published in *Nano Lett.*, 2017, 17 (2), pp 1212–1218 [268].

As described in chapter 1, high efficiency AlGaN light-emitting diodes (LEDs) operating in the ultraviolet (UV)-C band (100-280 nm) are in demand for a broad range of applications including water purification, disinfection, and medical diagnostics [309-315]. To date, the best reported wall-plug efficiency for semiconductor LEDs operating at ~280 nm is ~10% or less, [100, 310, 316-319] and the efficiency values decrease drastically with further decreasing wavelengths [114, 313, 320-322]. The performance of LEDs in the UV-C band has been severely limited by the presence of extended defects and dislocations, extremely poor current conduction, and TM polarized emission of Al-rich AlGaN quantum well heterostructures [122, 313, 323, 324]. Among these issues, the use of highly resistive and absorptive *p*-(Al)GaN contact layers not only leads to large optical and electrical loss but also generates severe heating effect, resulting in further efficiency degradation at high injection levels [218, 242, 282, 315, 316, 325, 326]. To this end, several design schemes, including polarization doping, transparent *p*-AlGaN, and *p*-AlGaN/GaN superlattices have been studied to enhance hole injection and to minimize light absorption [282, 315, 327-330]. Moreover, it has been demonstrated that tunnel injection of *non-equilibrium* holes can significantly improve the hole injection efficiency and the associated

carrier recombination in the LED active region [218, 242, 259, 269, 275, 282, 289]. To date, however, there have been few reports on the incorporation of tunnel junction in quantum well UV LEDs, and these studies have been limited to devices operating in the wavelength range of 290 to 340 nm [242, 269, 275, 282, 289]. The underlying challenge for achieving tunnel junction quantum well LEDs operating in the UV-C band includes the extremely inefficient *p*-type doping of Al-rich AlGa_N, due to the prohibitively large ionization energy (up to 600 meV) for Mg-dopant and the formation of extensive compensating defects in the conventional planar structures [226, 269, 326]. The resulting small hole concentration creates large depletion region widths and leads to significantly reduced tunneling probability.

Recent studies have shown that III-nitride nanowires offer a unique approach to address the efficiency bottleneck of UV-C optoelectronic devices [331] [202, 264]. Due to the effective lateral stress relaxation, nearly defect-free AlGa_N nanowires can be formed directly on Si, or other foreign substrates [179, 202, 259, 264]. With the use of plasma-assisted molecular beam epitaxy (MBE), their emission wavelengths can be controllably tuned from ~210 nm to 365 nm [179, 202, 226, 264, 278, 289, 291, 325, 332, 333]. Recent studies have further shown, both theoretically and experimentally, that significantly enhanced Mg-dopant incorporation and large hole concentration can be achieved in low dimensional Al-rich AlGa_N nanowires, compared to their planar counterparts, due to the reduced Mg-dopant formation energy and the suppression of defect/impurity incorporation [202, 226] [334]. To date, however, there have been few studies on nanowire UV LEDs, which generally exhibit extremely low output power (in the range of nW to 100 μW) and small external quantum efficiency (< 0.005%) [202, 264, 278, 289].

In this context, we have investigated the design, epitaxy, and performance characteristics of large area AlGa_N tunnel junction core-shell nanowire deep UV LEDs, wherein an epitaxial Al layer

serves as the tunnel junction. During the epitaxy process, an Al-rich AlGa_N shell is spontaneously formed, which provides effective carrier confinement in the nanowire LED active region and suppresses nonradiative surface recombination. The nearly defect-free nanowire heterostructures exhibit very high internal quantum efficiency (up to 80%) at room temperature, with the absence of defect-related emission that is commonly measured in AlGa_N quantum wells [313, 322]. With the incorporation of an epitaxial Al tunnel junction, the *p*-(Al)Ga_N contact-free nanowire deep UV LEDs showed nearly one order of magnitude reduction in the device resistance, compared to the conventional AlGa_N nanowire *p-i-n* devices. The unpackaged Al tunnel junction deep UV LEDs exhibit an output power >8 mW and a peak external quantum efficiency (EQE) ~0.4%, which are nearly one to two orders of magnitude higher than previously reported AlGa_N nanowire UV LEDs [202, 264, 278, 289]. Our detailed studies further suggest that the maximum achievable efficiency is limited by electron overflow and poor light extraction efficiency due to the TM polarized emission.

8.1 Design and Growth

In this work, we have studied two different types of AlGa_N nanowire LEDs, including a metal/semiconductor tunnel junction integrated AlGa_N nanowire UV LED and a conventional *p-i-n* device, illustrated in Fig. 8.1a and 8.1b, which are denoted as LED A and LED B, respectively. LED A consists of 340 nm *n*-Ga_N, *n*⁺⁺-Ga_N (25 nm)/Al (2.6 nm)/*p*⁺⁺-Al_{0.15}Ga_{0.85}N (25 nm) tunnel junction, 30 nm *p*-Al_{0.15}Ga_{0.85}N, 55 nm *p*-Al_{0.60}Ga_{0.40}N, 55 nm undoped Al_{0.50}Ga_{0.50}N, 55 nm *n*-Al_{0.60}Ga_{0.40}N, and a very thin (10 nm) *n*-Ga_N contact layer. The epitaxial Al layer forms an ohmic contact to *n*-Ga_N and a quasi-ohmic contact to *p*-AlGa_N, as shown in previous studies,[108, 259, 295-298, 301] enabling efficient inter-band conduction from *p*-AlGa_N to *n*-Ga_N. The design of

LED B is similar to LED A, except without the incorporation of Al tunnel junction and with the use of p -GaN contact layer on the top surface.

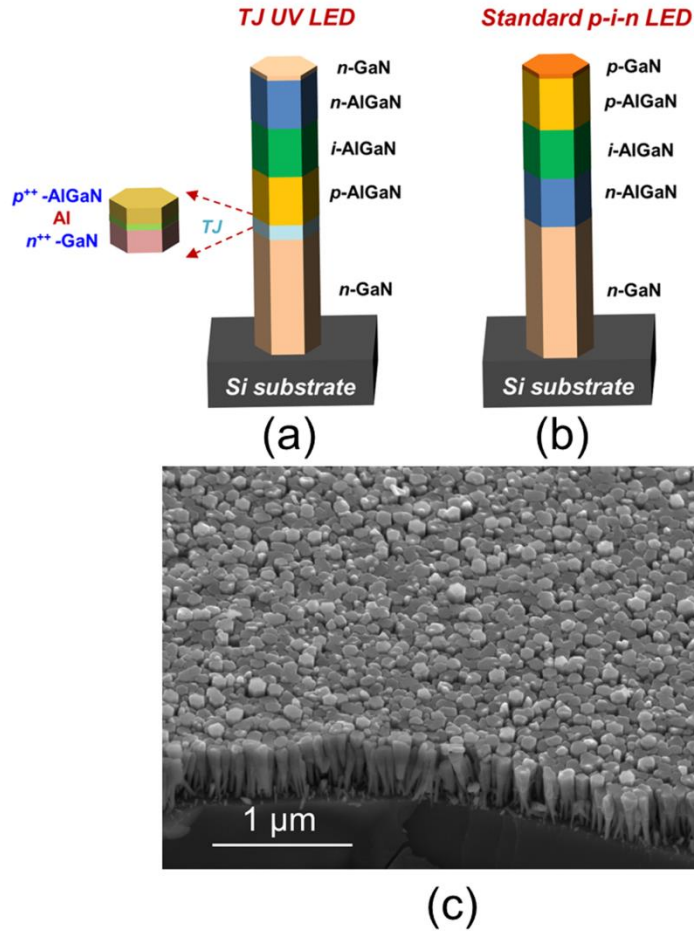


Figure 8.1: (a) Schematic diagram of Al tunnel junction (TJ) AlGaN UV LED (LED A). (b) Schematic diagram of standard p - i - n AlGaN UV LED without the use of any tunnel junction (LED B). (c) An SEM image of nanowires in an Al TJ AlGaN UV LED structure taken with a 45° angle.

The nanowire arrays are grown directly on Si substrate using a Veeco Genxplor MBE system equipped with a radio frequency plasma-assisted nitrogen source. The growth temperature for the AlGaN segments was in the range of $\sim 840^\circ\text{C}$, whereas a relatively low substrate temperature ($\sim 460^\circ\text{C}$) was used for the growth of Al tunnel junction. Ga and Al beam equivalent pressures (BEPs) of $\sim 2.5 \times 10^{-8}$ and 2.3×10^{-8} Torr, and 2×10^{-8} and 2.6×10^{-8} Torr were used for the AlGaN

active region and cladding layers, respectively. A relatively low nitrogen flow rate ~ 0.4 sccm was used during the AlGa_N growth, which, together with the relatively high substrate temperature, is found to be highly beneficial to enhance Al adatom migration and to suppress defect formation [202, 278]. Such growth conditions were obtained based on extensive studies of the fabrication and testing of AlGa_N nanowire LEDs operating in the UV-C band [202, 264]. Si and Mg doping concentrations in the *n*-Ga_N and *p*-AlGa_N segments of the tunnel junction were in the ranges of $5 \times 10^{19} \text{ cm}^{-3}$ and $1 \times 10^{20} \text{ cm}^{-3}$, respectively. Details of the Al-tunnel junction and Al-rich AlGa_N active region growth can be found in previous publications [202, 259]. Illustrated in Fig. 8.1c is the scanning electron microscopy (SEM) image of Al tunnel junction integrated AlGa_N nanowire deep UV LED structure (LED A). The nanowires are vertically aligned on the Si substrate and exhibit relatively uniform height and size distribution (nanowire lateral sizes in the range of 100-120 nm). Nanowires in LED B exhibit similar structural properties. Nanowires in both LED structures were grown along the *c*-axis and possess N-polarity [202, 207, 326].

8.2 Photoluminescence Characterization

Photoluminescence properties of AlGa_N tunnel junction nanowire arrays were measured using a 193 nm ArF excimer laser. Shown in Fig. 8.2a, the nanowire heterostructure exhibits strong emission at ~ 280 nm at room temperature. Emission from the underlying Ga_N nanowire segment can also be observed. The internal quantum efficiency is estimated by comparing the photoluminescence emission intensity at room temperature with that measured at low temperature (20 K). Shown in Fig. 8.2b, a very high internal quantum efficiency $\sim 80\%$ is derived at room temperature, which surpasses that of conventional AlGa_N quantum wells in this wavelength Range [275, 313, 335]. The inset of Fig. 8.2b shows the PL spectra at temperature 293 K and 15 K under

an excitation power of 0.13 mW. However, the photoluminescence efficiency by and large depends on the excitation power and other non-radiative mechanisms at low temperature [336].

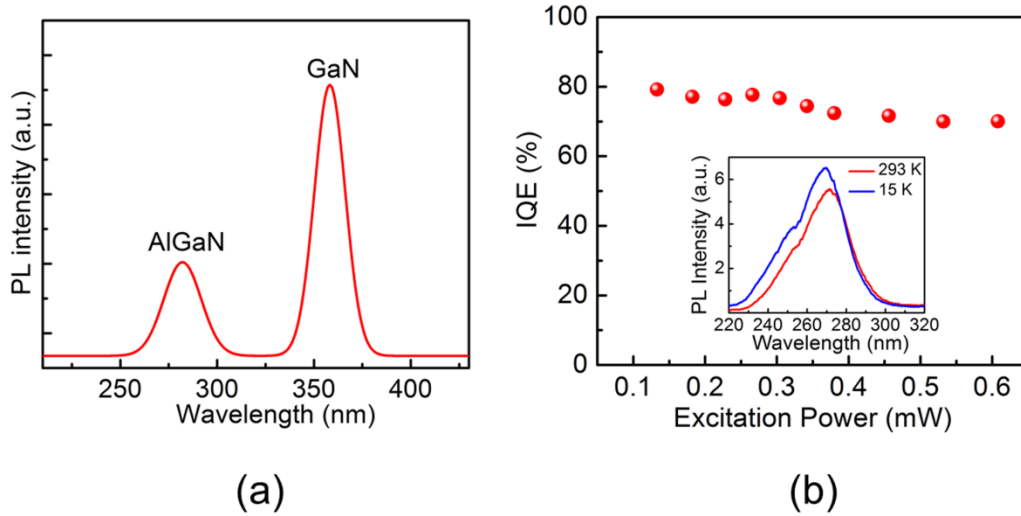


Figure 8.2: (a) Room temperature photoluminescence spectrum, and (b) Internal quantum efficiency vs. excitation power measured at room temperature for the AlGaN tunnel junction nanowire LED heterostructure. The inset shows the PL spectra measured under an excitation power of 0.13 mW at 293 K and 15 K.

In this context, it is important to derive the accurate IQE over a broad range of excitation power [207, 226, 336]. As can be seen in the Fig: 8.2b, the IQE stays in the range of 70%-80% over a large range of excitation power. The high luminescence efficiency is directly related to the significantly reduced defect densities in AlGaN nanowires and the formation of an Al-rich AlGaN shell structure that minimizes nonradiative surface recombination (to be described next) [203, 337]. Similar optical properties were also measured from AlGaN nanowire arrays without the incorporation of Al tunnel junction.

8.3 Structural Characterization

Structural properties of the Al tunnel junction integrated nanowire LED heterostructure were subsequently investigated by scanning transmission electron microscopy (STEM) and high resolution transmission electron microscopy (HR-TEM) using a JEOL JEM-2100F equipped with a field emission gun operated at 200 kV. The sample was prepared by dispersing AlGa_N nanowires on a Cu grid, and high angle annular dark field (HAADF) STEM imaging was measured with an electron beam diameter of approximately 0.2 to 0.7 nm. Illustrated in Fig. 8.3a is the STEM image of an Al tunnel junction integrated AlGa_N nanowire LED structure, wherein the different segments are identified. HR-TEM analysis further confirmed there were no noticeable stacking faults or threading dislocations formed at the interface between the epitaxial Al layer and subsequent *p*-AlGa_N layer. In a high-magnification STEM image shown in Fig. 8.3(b), the Al tunnel junction layer is clearly observed with ~2.6 nm thickness. Energy dispersive X-ray spectroscopy (EDXS) analysis was further performed to study the compositional variations of the *n*⁺⁺-Ga_N/Al/*p*⁺⁺-AlGa_N tunnel junction. An EDXS point analysis was done in the vicinity of the Al-layer, shown in Fig. 8.3c, which provided clear evidence for the presence of Al. Here, the Ga_N nanowire with Al tunnel junction is surrounded by an AlGa_N shell which was formed during the epitaxy of subsequent *p*- and *n*-AlGa_N segments. In consequence, even though the beam was directed toward the Al-layer, Ga and Cu signals were also detected from the surrounding AlGa_N shell structure and Cu grid due to the transmitted beam. The EDX data

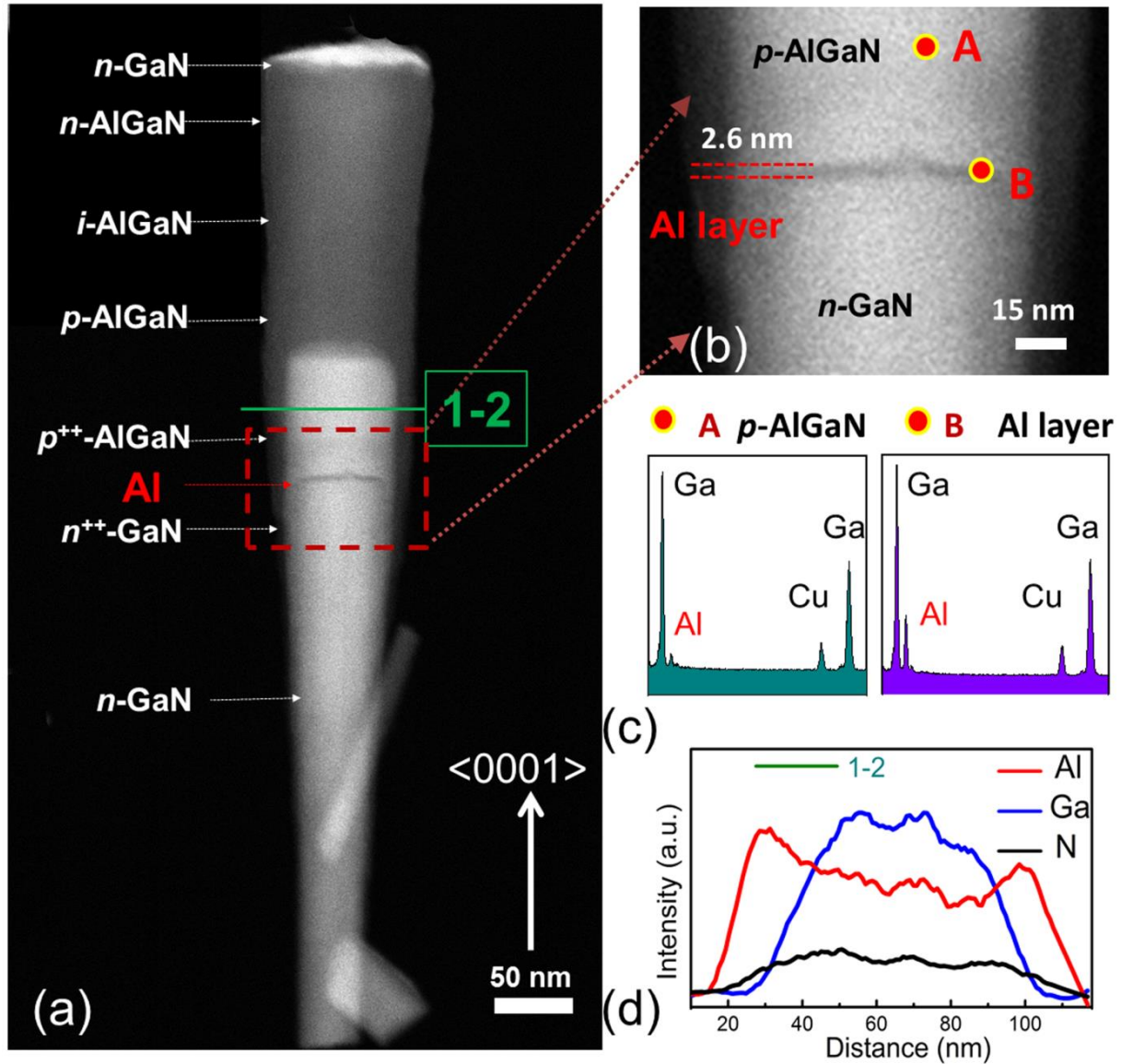


Figure 8.3: (a) STEM image of a single Al tunnel junction AlGaN UV LED structure (LED A). (b) STEM image of the Al-tunnel junction. (c) EDXS point analysis of the tunnel junction region (point B in b) and *p*-AlGaN region (point A in b). (d) EDXS line profile analysis along the lateral dimension of the *p*-AlGaN segment (line 1-2 in a).

detected from region A of *p*-AlGaN in Fig. 8.3b shows much lesser trace of Al content compared to region B in the Al tunnel junction layer. This analysis confirms the presence of Al tunnel junction in the nanowire structure. EDXS line profile analysis was further performed along the lateral dimension of the nanowire structure (line 1-2) to identify the presence of Al-rich AlGaN

shell structure. Shown in Fig. 8.3d, the Ga composition peak intensity is at its maximum in the center region and drops toward the sidewalls of the nanowire. In contrast, Al signals show a clear peak in the sidewall region and drop toward the center of the nanowire. This provides unambiguous evidence for the presence of Al-rich AlGaN core-shell double heterostructure, which was also observed in previous studies [141, 241, 305, 337] [203, 207]. The unique core-shell heterostructures can effectively suppress nonradiative surface recombination and lead to high efficiency emission [141, 241, 305].

8.4 Device Fabrication and Electrical Characterization

The fabrication of AlGaN nanowire deep UV LEDs involves the use of standard photolithography and contact metallization techniques. For the tunnel junction device (LED A), Ti (5 nm)/Au (10 nm) and Ti (15 nm)/Au (100 nm) layers were deposited on the nanowire top surface and the backside of the Si substrate, respectively. The top metal layers were deposited using a tilting angle deposition technique [202].

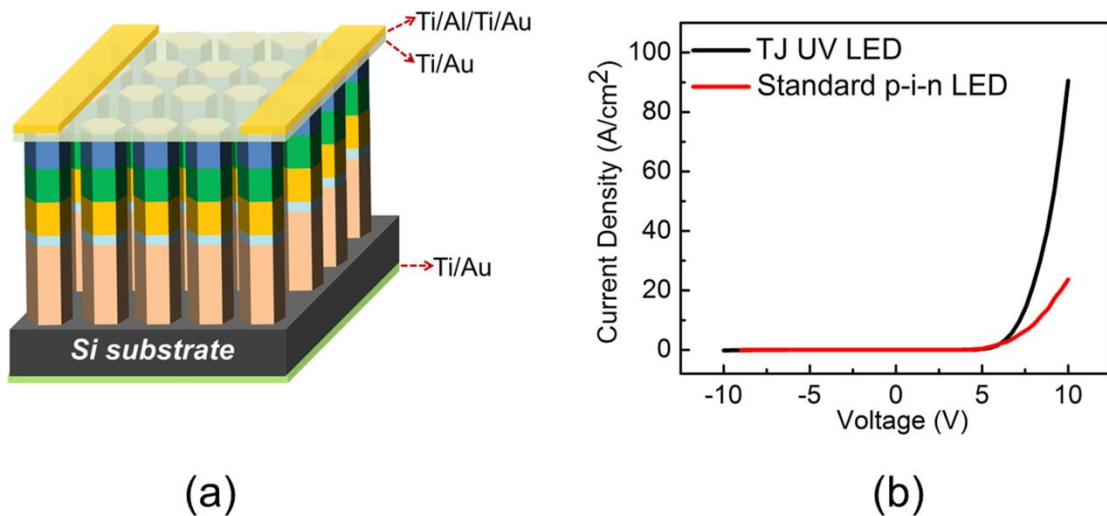


Figure 8.4: (a) Schematic illustration of the fabricated large area AlGaN nanowire tunnel junction UV LED. (b) I-V characteristics of the AlGaN tunnel junction UV LED (LED A) and the standard *p-i-n* UV LED without the use of any tunnel junction (LED B).

It is worthwhile mentioning that no filling materials were used to avoid the absorption of UV photons. Ti (20 nm)/Al (150 nm)/Ti (20 nm)/Au (80 nm) metal grid contacts were also deposited on the device top surface to facilitate current spreading. The device mesa sizes are in the range of $300 \times 300 \mu\text{m}^2$ to $1 \times 1 \text{mm}^2$. The fabricated tunnel junction nanowire LED device is schematically shown in Fig. 8.4a. The fabrication process of the conventional AlGaN *p-i-n* device (LED B) is similar to that of LED A, except Ni (5 nm)/Au (10 nm) layers were deposited on the nanowire surface to form *p*-metal contact. Current-voltage characteristics of both the tunnel junction nanowire UV device (LED A) and standard *p-i-n* nanowire device (LED B) were measured under continuous wave (CW) biasing conditions. Shown in Fig. 8.4b, both nanowire devices exhibit clearly rectifying characteristics. The measured device areal size is $500 \times 500 \mu\text{m}^2$. The device specific resistance estimated from the linear region of the forward I-V characteristics (between 7 V and 9.5 V) is $\sim 35 \Omega$ for the tunnel junction nanowire UV device (LED A), whereas the resistance for LED B is $\sim 230 \Omega$. The nearly one order of magnitude reduction in the device resistance is attributed to the significantly reduced contact resistance, due to the elimination of *p*-(Al)GaN for Al tunnel junction nanowire LED, and the resulting efficient hole transport and injection in the device active region. This specific device resistance for the Al tunnel junction device includes *p*- and *n*-contact resistance, resistance of AlGaN double heterostructure active region, and resistance of tunnel junction itself. Taking these factors into account, the upper limit of tunnel junction resistance is estimated to be $\sim 1 \times 10^{-3} \Omega \cdot \text{cm}^2$, or less [259]. Interestingly, both nanowire LEDs exhibit similar turn-on voltages. This may be partly explained by the additional resistance at the $\text{Al}_{0.60}\text{Ga}_{0.40}\text{N}/\text{Al}_{0.15}\text{Ga}_{0.85}\text{N}$ hetero-interface for Al tunnel junction device. It is expected that, with further optimization of the design and epitaxy process, both the turn-on voltage and resistance of Al tunnel junction UV LEDs can be further reduced.

8.5 Electroluminescence Characterization:

Shown in Fig. 8.5a is the electroluminescence (EL) spectra measured under various injection currents under CW biasing condition for LED A.

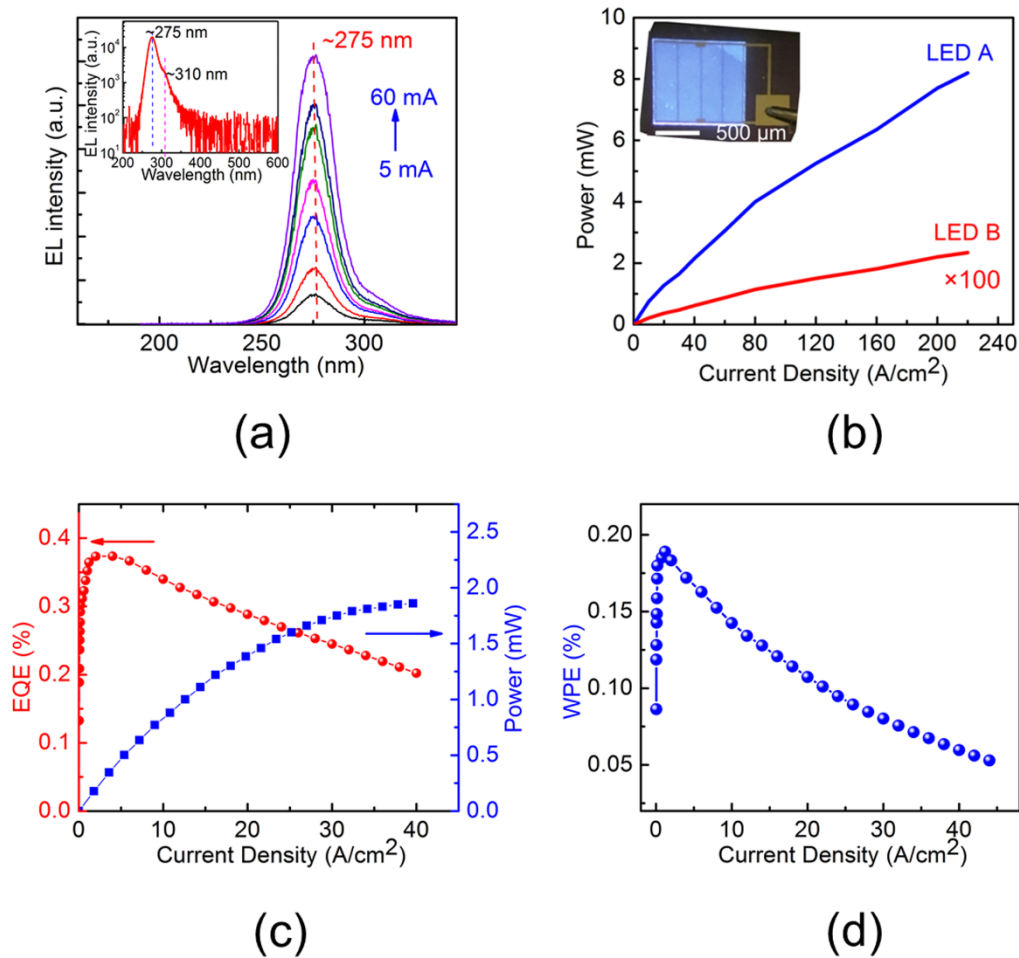


Figure 8.5: (a) Electroluminescence (EL) spectra of the Al tunnel junction AlGaIn UV LED (LED A) under CW biasing condition. The inset shows the EL spectrum in log scale. (b) Output power vs injection current for Al tunnel junction AlGaIn UV LED (LED A) and standard *p-i-n* AlGaIn UV LED (LED B) under pulsed biasing (2% duty cycle). The inset shows an optical image of LED A under an injection current of 8 A/cm^2 . (c) External quantum efficiency (EQE) and output power of Al tunnel junction AlGaIn UV LED under CW condition. (d) Wall plug efficiency (WPE) of Al tunnel junction AlGaIn UV LED under CW condition.

A relatively narrow emission peak centered at 275 nm was measured. The spectral linewidth (full-width-at-half-maximum – FWHM) is ~18 nm, which is comparable to that measured from AlGaIn quantum wells in this wavelength range [269, 316, 338, 339]. No significant shift in the emission wavelength was measured with increasing injection current, which is directly related to the use of double heterostructures and the resulting small, or negligible quantum-confined Stark effect. Significantly, defect-related emission in the UV or visible spectral range that was commonly observed in conventional AlGaIn quantum wells is absent in the presented AlGaIn nanowires, shown in the inset of Fig. 8.5a [338, 340]. The 310 nm weak EL emission is likely due to the radiative recombination (electron overflow) in the thin p -Al_{0.15}Ga_{0.85}N capping layer inserted next to the p^{++} -Al_{0.15}Ga_{0.85}N tunnel junction. Output power of nanowire LEDs was measured directly on wafer without any packaging. Shown in Fig. 8.5b, an output power (up to 8 mW) was measured under pulsed biasing condition. Also shown in Fig. 8.5b is the output power vs. injection current for the standard p - i - n nanowire device (LED B), which exhibits a maximum output power in the range of 20-30 μ W. Given the similar optical properties of both nanowire devices under optical pumping, the drastically improved output power for LED A is attributed to the significantly enhanced hole transport and injection into the device active region, due to the incorporation of Al tunnel junction, and the elimination of resistive and absorptive p -GaIn contact layer. Variations of the EQE of Al tunnel junction device (LED A) vs. current under CW operation are shown in Fig 8.5c. It is seen that the EQE first shows an increasing trend with current and reaches a peak value (~0.4%) at 2 A/cm², followed a drop with further increasing current. The measured EQE of 0.4% is nearly a factor of 50 to 100 times higher than previously reported nanowire LEDs operating in the UV-B or UV-C bands [202, 264, 278, 289] [226, 325]. The severe efficiency droop has been commonly measured in AlGaIn quantum well devices. The underlying cause may include Auger

recombination and electron overflow [289, 313, 322, 341, 342]. In this study, a relatively thick AlGaIn double heterostructure was employed as the active region and, therefore, the carrier density in the LED active region is expected to be significantly smaller, compared to that of a conventional quantum well device. Consequently, Auger recombination may play a very small, or negligible role in the measured efficiency droop. Alternatively, the efficiency degradation with increasing current can be well explained by the increased electron overflow, due to the highly asymmetric transport properties for electrons and holes in AlGaIn [343, 344] [71, 345]. The efficiency droop can be minimized by incorporating an AlGaIn electron blocking layer and by *p*-type modulation doping to enhance the hole injection and transport in the active region [134, 322, 341, 343]. The maximum wall-plug efficiency (WPE) is ~0.2% (shown in Fig. 8.5d). For the presented Al tunnel junction LED, the maximum EQE and WPE is primarily limited by the poor light extraction associated with the TM polarized emission (to be described next) and the photon absorption by the top metal contact and the underlying Si substrate.

8.6 Polarization Measurement

We have further investigated the polarization properties of light emission of Al tunnel junction deep UV device. In this measurement, the light emission was collected from the lateral surface of nanowire LEDs, and was polarization resolved by a Glan-Taylor prism. The polarization resolved EL spectra measured under a current density of 8 A/cm² are shown in Fig. 8.6a. Variations of the light intensity vs. injection current for TM and TE polarized emission are further shown in Fig. 8.6b.

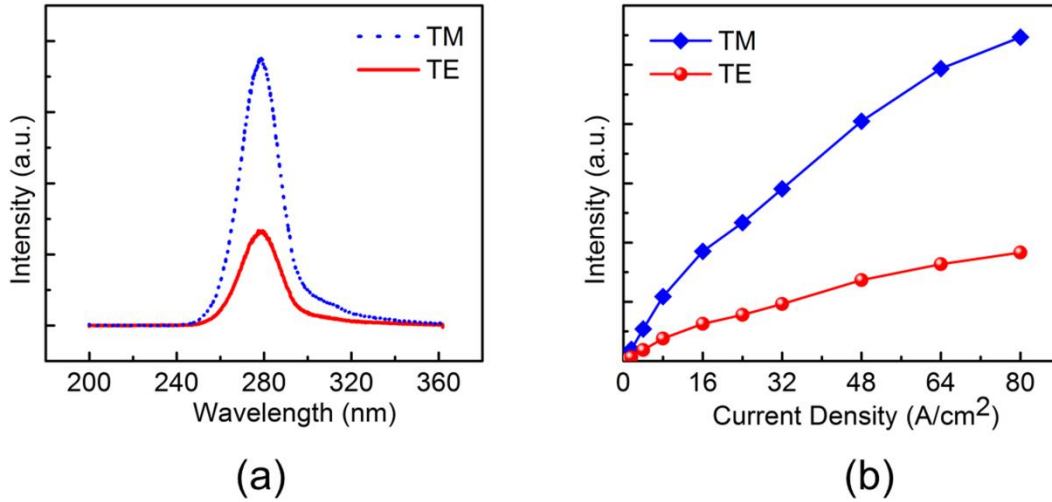


Figure 8.6: (a) Electroluminescence spectra of LED A under an injection current of 8 A/cm² for TM and TE polarized emission. (b) Light intensity vs. injection current for TM and TE polarized emission.

It is seen that the emission is predominantly TM polarized, wherein TM polarization is defined as the electrical field parallel to the nanowire c -axis ($E // c$). The polarization ratio is defined by $(I_{\text{TM}} - I_{\text{TE}})/(I_{\text{TM}} + I_{\text{TE}})$, where I_{TM} and I_{TE} are the integrated EL intensity for TM and TE polarizations, respectively. For the presented nanowire LEDs, a polarization ratio ~ 0.33 was measured. It is worthwhile mentioning that TM polarized emission has been measured from AlGaIn quantum wells in this wavelength range [122, 346, 347]. Moreover, previous studies also showed TM polarized emission from single and ensemble InGaIn based visible LEDs, due to the nanowire geometric effect [348, 349].

8.7 Summary

In this chapter, we have demonstrated a new class of deep UV LEDs, with the use of AlGaIn tunnel junction core-shell nanowire heterostructures. It is observed that nearly dislocation-free Al-rich AlGaIn nanowire heterostructures can be formed on an epitaxial Al tunnel junction. The resulting

core-shell nanowire arrays exhibit high luminescence efficiency (~80%) in the UV-C band at room temperature. Such p -(Al)GaN contact-free deep UV LEDs showed nearly one order of magnitude reduction in the device resistance and more than two orders of magnitude enhancement in the output power. Detailed studies further suggest that the maximum achievable efficiency is limited by electron overflow and poor light extraction efficiency due to the TM polarized emission. The device performance can be further improved by optimizing the tunnel junction and device active region, including the use of quantum dots/disks and the incorporation of electron blocking layer. It is further envisioned that the Al tunnel junction, with optimized design, can be exploited to significantly enhance the light reflection and extraction, which, together with a precise control of the nanowire size and spacing, can lead to deep UV LEDs with significantly improved performance [350].

Chapter 9

Sub-milliwatt AlGa_N Nanowire Tunnel Junction Deep Ultraviolet Light Emitting Diodes on Silicon Operating at 240 nm

The results of this chapter were previously published in Applied Physics Letters, 109, 201106 (2016) [264].

Compared to the high performance GaN-based blue/near-UV LEDs, AlGa_N quantum well LEDs in the UV-C band (200-280 nm) have remained immature, in particular for devices with emission wavelengths around 240 nm or shorter. Such devices are generally characterized by very low external quantum efficiencies (EQEs) and large operation voltages, which is attributed to the commonly measured large dislocation and defect densities, poor hole transport, and low light extraction efficiency [14, 313, 351-354]. As an alternative approach, AlGa_N nanostructures have been investigated in the past decade. These nanostructures include ternary AlGa_N nanowires, [278, 355, 356] Ga(Al)N quantum disks/dots embedded in Al(Ga)N nanowires [205, 357, 358], and spontaneously formed AlGa_N quantum-dot-like nanostructures [207, 359, 360]. AlN LEDs operating at ~207 nm and AlGa_N nanowire LEDs with emission wavelengths as short as 236 nm have been achieved [202, 226, 278, 325, 329, 337, 361]. However, the output power of these devices has remained extremely low. For example, for a device operating at 250 nm, the maximum peak power is only 220 nW at an injection of 400 mA. With the use of the p^+ -Ga_N/InGa_N/ n^+ -Ga_N tunnel junction (TJ) and p^+ AlGa_N/InGa_N/ n^+ -AlGa_N TJ, improved electrical performance and output power have been demonstrated in InGa_N and AlGa_N quantum

well LEDs for visible [221] and UV emissions [267], respectively. Moreover, InGaN/GaN dot-in-a-nanowire LEDs with the incorporation of p^+ -GaN/InGaN/ n^+ -GaN and n^+ -GaN/Al/ p^+ -AlGaN TJs have also been demonstrated [218, 259]. In this letter, we investigate AlGaN nanowire deep UV LEDs on Si substrate with the incorporation of an n^+ -GaN/Al/ p^+ -AlGaN TJ. It is found that the device resistance is reduced by nearly a factor of ten, and the output power is enhanced by more than two orders of magnitude compared to AlGaN nanowire deep UV LEDs without such a TJ. An output of 0.37 mW is measured for an unpackaged AlGaN nanowire TJ UV LEDs emitting at 242 nm, with a maximum EQE of 0.012%. These performance characteristics are comparable to previously reported AlGaN quantum well LEDs operating in the similar wavelength range [14, 313, 351].

9.1 Design, Growth and Optical Characterization

Fig. 9.1a shows the schematic of AlGaN nanowire LED structure on Si substrate, which consists of n -GaN contact layer, AlGaN double-heterojunction, and p -GaN contact layer along the growth direction. The active region thickness is around 40 nm, and both n -AlGaN and p -AlGaN cladding layers are around 60 nm. We define such an AlGaN nanowire LED structure as *Standard UV LED Structure*. Illustrated in Fig. 9.1b is the device structure with the incorporation of n^+ -GaN/Al/ p^+ -AlGaN TJ, which is referred to as *TJ UV LED*. The AlGaN active region and cladding layers in TJ UV LED structure have the same thickness as those in the standard UV LED structure. Both device structures were grown by radio-frequency plasma-assisted molecular beam epitaxy (MBE) on n -Si substrate. Growth conditions for the standard UV LED structure included a growth temperature of 850 °C for AlGaN segments, a nitrogen flow rate of 0.4 sccm, and Ga and Al beam equivalent pressures (BEPs) 2×10^{-8} Torr and 1.5×10^{-8} Torr in the device active region and 1.5×10^{-8} and 2×10^{-8} Torr in the cladding layers, respectively.

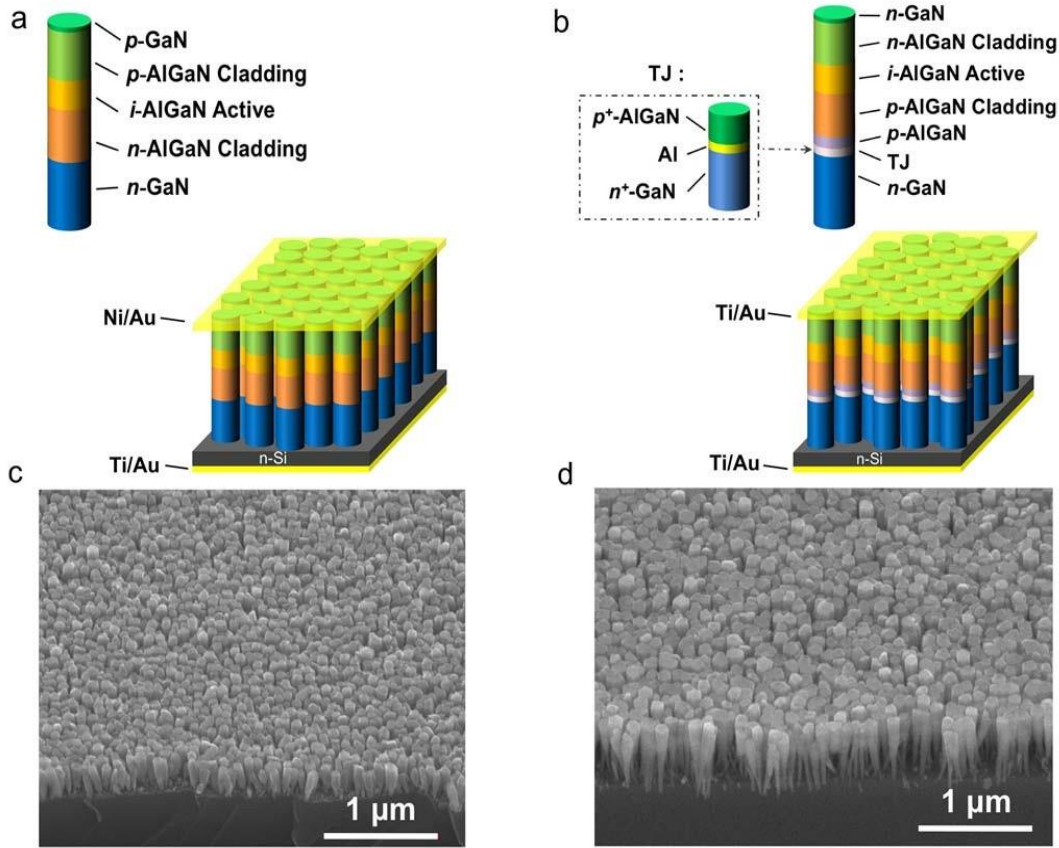


Figure 9.1: (a) Schematic of AlGaIn nanowire standard UV LED structure. (b) Schematic of AlGaIn nanowire TJ UV LED structure. (c) SEM image of AlGaIn nanowires in the standard UV LED structure. (d) SEM image of AlGaIn nanowires in the TJ UV LED structure. The images were taken with a 45-degree tilting angle. The scale bar in both images are 1 μm.

More details about the growth process were described in chapter 2. The Si and Mg dopant concentrations in the *n*-AlGaIn and *p*-AlGaIn cladding layers were estimated to be in the range of $5 \times 10^{19} \text{ cm}^{-3}$ and $5 \times 10^{20} \text{ cm}^{-3}$, respectively [19, 30, 31]. Growth conditions for the TJ UV LED structure were similar to those of the standard UV LED, except that relatively low growth temperatures were used for Al layer (460 °C) and *p*⁺-AlGaIn layer (640 °C). Detailed TJ growth process was explained in previous chapter [259]. The scanning electron microscope (SEM) images of AlGaIn nanowires in both structures are shown in Fig. 9.1c and 9.1d, respectively. It

is seen that in both structures, highly uniform and dense nanowires are formed, which is important for the fabrication of large area devices. We have further performed photoluminescence (PL) experiments on standard UV LED and TJ UV LED structures. In this experiment, the samples were excited by a 193 nm ArF excimer laser. Shown in Fig. 9.2, similar PL intensity and spectral linewidth are measured from both LED structures under the same excitation condition, suggesting a similar optical quality for these two LED structures. The small emission peak around 210 nm is attributed to the emission from AlN shell and/or Al-rich AlGaN shell surrounding the nanowires.

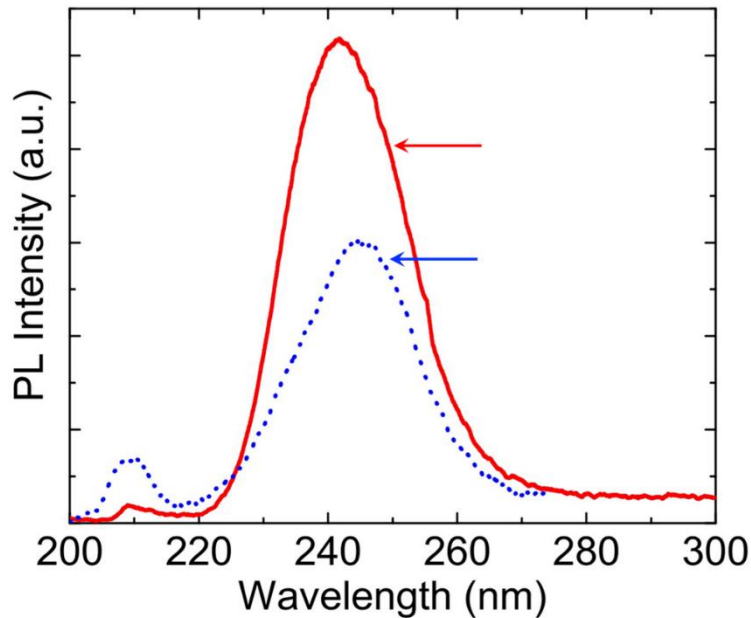


Figure 9.2: Room-temperature PL spectra measured from AlGaN nanowire standard and TJ UV LED structures.

9.2 Device Fabrication and Electrical Characterization

The device fabrication process included standard photolithography and metallization and is similar to that of conventional quantum well LEDs. To avoid any deep UV light absorption, no surface passivation or planarization was performed. Thin metal grids were used to improve

current spreading. The detailed fabrication procedure was reported elsewhere [259, 326]. Fig. 9.3a shows the I-V characteristics of standard and TJ UV LED devices, with the inset showing the plot in a semi-log scale. It is seen that excellent diodes are formed. As shown by the dashed lines in Fig. 9.3a, the device resistance of the standard UV LED and TJ UV LED is estimated to be 352.9 Ω and 42.8 Ω , respectively. The significantly improved electrical performance of TJ UV LEDs is mainly attributed to more efficient carrier (hole) injection with the use of TJ, and the reduced contact resistance due to the removal of *p*-GaN layer.

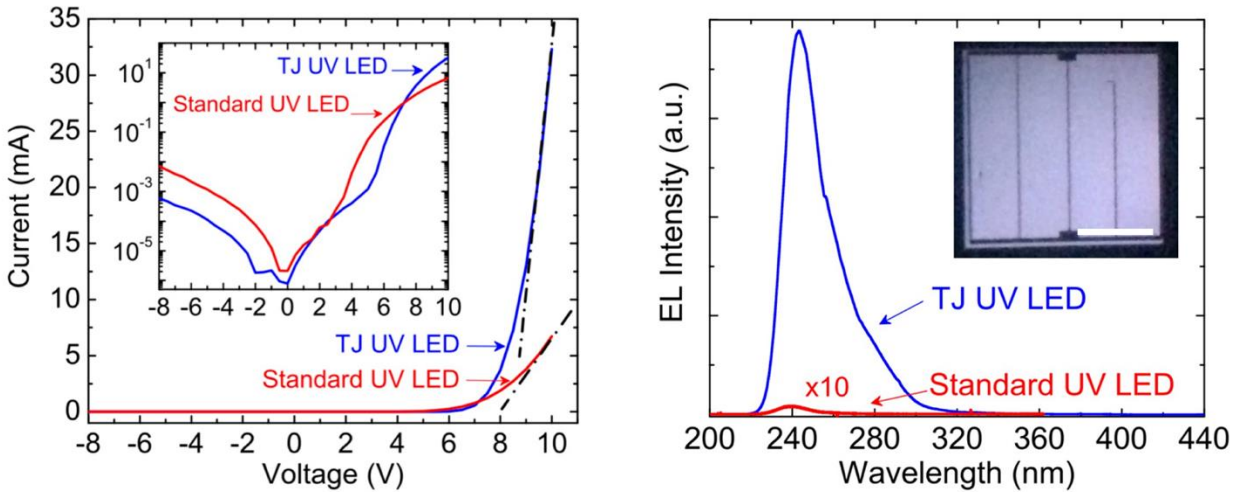


Figure 9.3: (a) Room-temperature I-V characteristics of standard and TJ UV LEDs, with the inset showing the plots in a semi-log scale. (b) Room-temperature EL spectra measured from standard and TJ UV LEDs, with the inset showing the optical image of light emission from the device top. Device size: 500 μm \times 500 μm .

9.3 Electroluminescence Characterization

Fig. 9.3b shows the electroluminescence (EL) spectra measured from standard and TJ UV LEDs. An optical image of the TJ UV LED is shown in the inset of Fig. 9.3b. The output spectra were taken under an injection of 20 mA under continuous wave (CW) biasing conditions. In this experiment, the emitted light was collected from the device top surface with an optical fiber. Compared to the standard UV LED, the EL intensity of the TJ UV LED is enhanced by a factor

of 400 times. Given the similar optical quality of these two LED structures as indicated by Fig. 9.2, the significantly enhanced EL intensity is thus largely due to the improved electrical performance of TJ UV LEDs as discussed above.

Detailed characterization of TJ UV LEDs is described subsequently. Fig. 9.4a shows the room-temperature EL emission spectra of a device under CW biasing with currents varying from 2 to 60 mA.

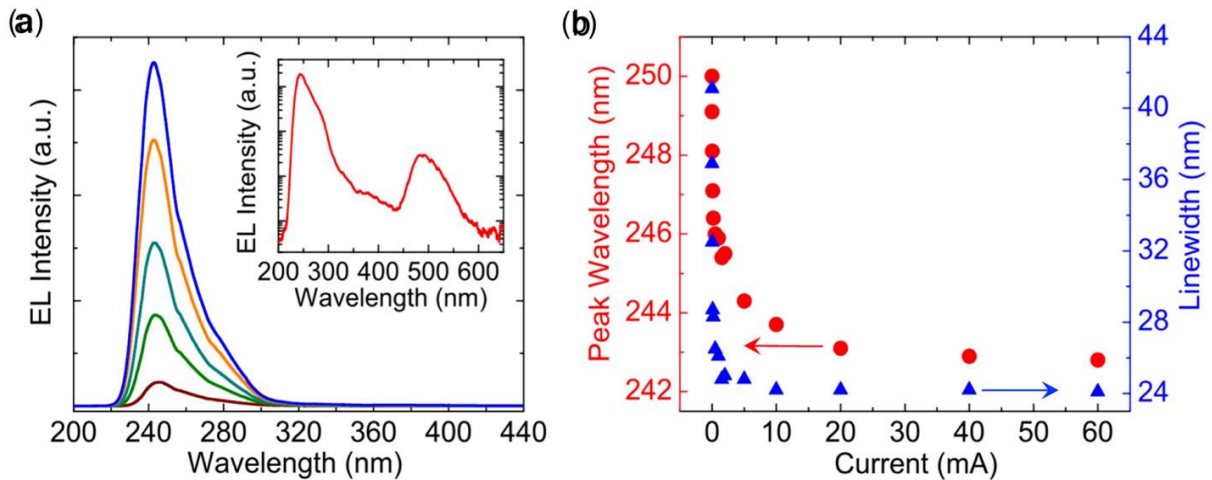


Figure 9.4: (a) Room-temperature EL spectra measured from a TJ UV LED under CW biasing, with injection currents varying from 2 to 60 mA. The device size is $500\ \mu\text{m} \times 500\ \mu\text{m}$. The inset shows a scan up to 650 nm under an injection of 20 mA. (b) The derived EL peak position (filled circles) and spectral linewidth (filled triangles) as a function of injection current.

The inset of Fig. 9.4a shows an EL spectrum under an injection current of 20 mA plotted in a semi-log scale. It is seen that there does not exist any defect-related emission in the UV band (below 400 nm). Only a weak emission around 480 nm, with the intensity two orders of magnitude lower compared to the emission peak around 242 nm, is measured, suggesting excellent material quality of the presented AlGaIn nanowire LED structures. Fig. 9.4b shows the EL peak position and linewidth as a function of injection current. It is seen that as the injection current increases, a strong blue shift of the peak wavelength, accompanied by the narrowing of

the spectral linewidth, is measured, which is attributed to the quantum-confined Stark effect, due to the presence of quantum-dot-like nanostructures in AlGaIn nanowires [207, 359]. Similar peak wavelength vs. injection current dependence is also measured from standard UV LEDs. We have further estimated the built-in polarization field of AlGaIn nanowires. For the device shown in Fig. 9.4, the peak position becomes nearly constant for injection currents above 20 mA. Based on a nanowire fill factor of 50% and that the current path is mostly through the nanowire center region due to the presence of Al-rich AlGaIn shell [207], the polarization field is derived to be ~ 0.2 MV/cm. This number agrees reasonably well with what is commonly measured from AlGaIn quantum well structures [362-364].

9.4 Optical Polarization

The optical polarization of TJ UV LEDs is further investigated. In this experiment, the light was collected from the device lateral surface, and the polarization was resolved by a Glan-Taylor prism.

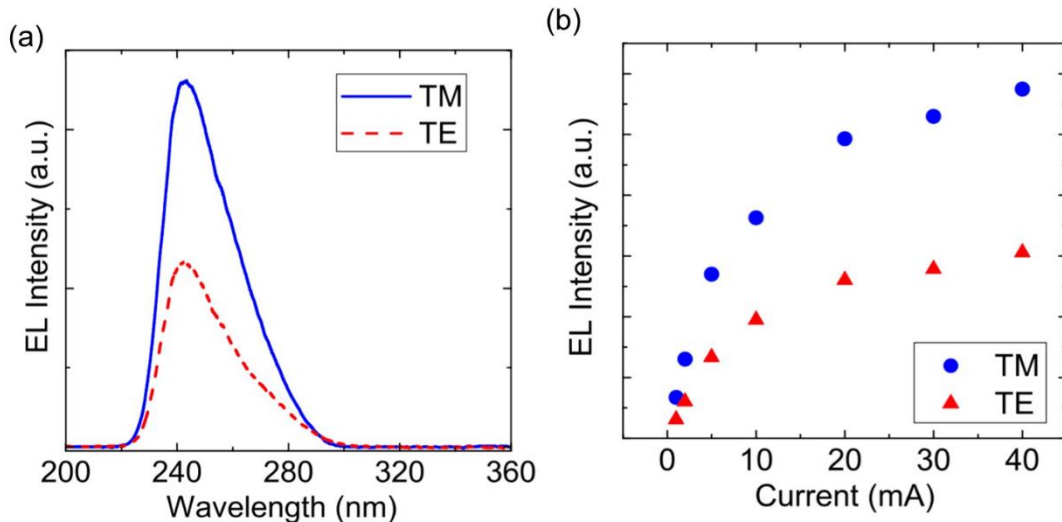


Figure 9.5: (a) EL spectra under an injection of 20 mA for TM and TE polarizations. (b) Light intensity vs. injection current for TM and TE polarizations.

The TM polarization is defined as the electrical field parallel to the nanowire c -axis ($E // c$). The EL spectra measured under an injection of 20 mA and the light output vs. injection current for TM and TE polarizations are shown in Fig. 9.5a and 9.5b, respectively. It is seen that the light is predominantly TM polarized for all injection currents. The polarization ratio, which is defined by $(I_{TM}-I_{TE})/(I_{TM}+I_{TE})$ where I_{TM} and I_{TE} are the integrated EL intensity for TM and TE polarizations, respectively, is estimated to be around 0.35. TM polarized emission has also been commonly measured from AlGaIn quantum well LEDs in this wavelength range [126, 365]. Moreover, it is worthwhile mentioning that, due to the influence of nanowire geometric effect, TM polarization has also been measured from InGaIn nanowire structures [289, 366].

9.5 Output Power and EQE

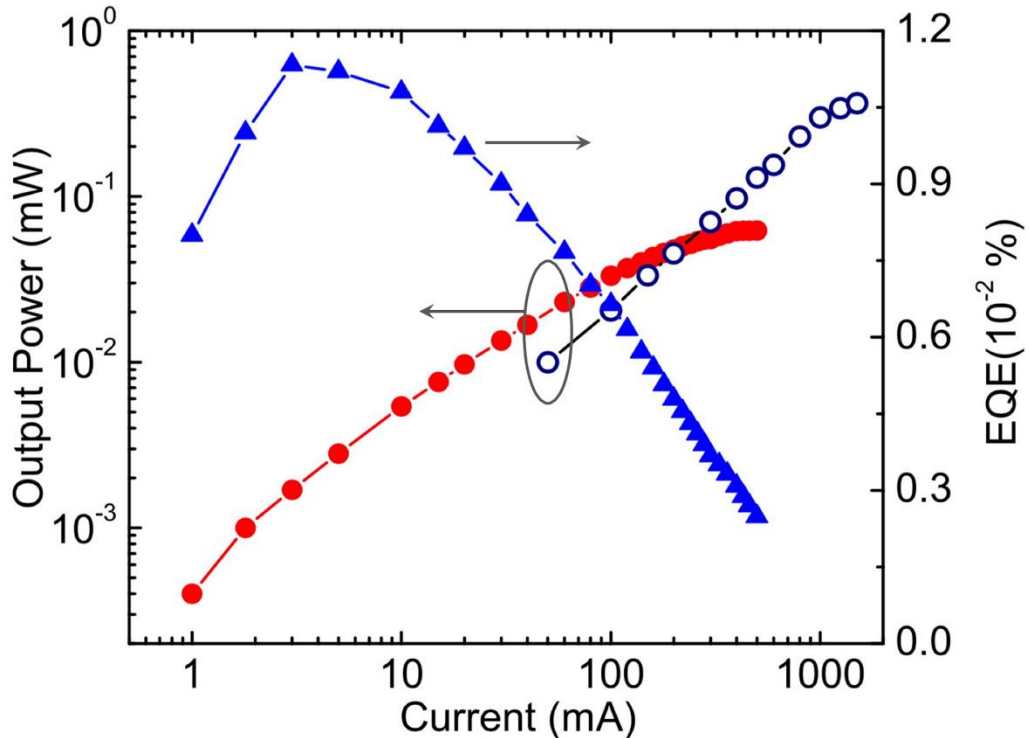


Figure 9.6: Room-temperature output power and EQE of TJ UV LEDs. Symbols: filled and open circles are for output power under CW and pulse biasing, respectively; filled triangles are for EQE under CW biasing. Device size: 1 mm \times 1 mm.

The output power of TJ UV LEDs has been further measured. The results under CW biasing are first presented. Filled circles in Fig. 9.6 are the light output power vs. injection current for a device emitting at 242 nm. With the increase of injection current, the light output power increases nearly linearly up to 50 mA, and then gradually saturates around 400 mA, limited by electron overflow and heating effect. A maximum output power of 62 μW is measured. The corresponding EQE, which is defined by the ratio of emitted photon number over the injected electron number, is further derived. As illustrated by the filled triangles in Fig. 9.6, the EQE increases up to around 3 mA, and then followed by a decrease. The peak EQE of 0.012% is derived, and is comparable to AlGaIn quantum well LEDs emitting in this wavelength range. Improved light output power is obtained under pulse biasing (2% duty cycle, 100 kHz), by minimizing the heating effect at high injection currents. The open circles in Fig. 9.6 show the light output power vs. injection current for a device emitting at 242 nm. Under pulsed biasing, light output power increases almost linearly up to 800 mA. An output power up to 0.37 mW is measured, and is comparable to AlGaIn quantum well LEDs operating in the similar wavelength range [313, 353]. In the end, we discuss the underlying mechanism for efficiency droop and limiting factor for EQE. For the presented TJ UV devices, the efficiency droop occurs only around 0.3 A/cm², which is much lower compared to the current density where droop is measured from AlGaIn quantum well LEDs emitting in the similar wavelength range [367]. At this low injection level, heating effect and Auger recombination are not likely the dominant causes. We attribute the efficiency droop mainly to electron overflow, due to the highly asymmetric electron and hole transport in Al-rich AlGaIn and the absence of electron blocking layer. Regarding to the limiting factor for EQE, it is largely ascribed to the extremely low light extraction efficiency, which is estimated to be below 0.1% considering the presence of light localization effect from randomly arranged nanowires,

the use of relatively thick metal contact, and photon absorption by the underlying Si substrate [203, 207, 326, 334].

9.6 Summary

In this chapter, we have investigated the MBE growth and characterization of AlGaIn nanowire deep UV LED structures on Si substrate. It is found that with the utilization of n^+ - GaN/Al/ p^+ - AlGaIn TJ, both electrical performance and light output power can be drastically improved, due to the removal of the resistive p -GaN contact layer and the more efficient charge carrier (hole) injection into the device active region. Noticeably, for AlGaIn nanowire TJ UV LEDs, output power of 0.37 mW and EQE of 0.012% have been measured for emission wavelength at 242 nm.

Chapter 10

Conclusions and Future Works

10.1 Summary

The presented work in this thesis has extensively focused on design, molecular beam epitaxial growth, device fabrication, and optical/electrical characterization of various InGaN/Al(Ga)N dot-in-a-wire and AlGaN double heterostructure nanowire visible/ultraviolet LEDs. This work has by and large solved some of the long-standing bottlenecks of III-nitride nanowire visible LEDs, including resistive *p*-type contact resistance, efficiency droop, efficient *p*-type dopant incorporation, etc. Also, this work has demonstrated for the first time metal/semiconductor nanowire tunnel junction monolithically integrated with InGaN/GaN dot-in-a-wire LEDs. Furthermore, this thesis demonstrated, for the first time, alternating current (AC) operated InGaN/GaN nanowire LEDs on Si substrate. The presented work also included high efficiency, relatively high power AlGaN core-shell deep ultraviolet LEDs operated in the challenging sub-280 nm and ~ 240 nm spectral ranges. It is worthwhile mentioning that majority of the innovations in the designs and development of the presented work was done with the use of various low resistance III-nitride nanowire tunnel junctions. We have also studied the epitaxial growth and characterization of aluminum (Al)/Al(Ga)N metal-semiconductor heterojunctions. This thesis also highlighted on the monolithic metal/large band gap AlGaN nanowire backward diodes grown on Si substrate.

In Chapter 2, we have described our approach on the MBE growth, device fabrication and structural/optical/electrical characterization of InGaN/(Al)GaN nanowire LEDs presented in this thesis. In chapter 3, we have demonstrated tunnel junction InGaN/GaN dot-in-a-wire LEDs, that can eliminate the need of resistive p -GaN contact layer, leading to reduced voltage loss and improved hole injection into the device active region. Also, we have demonstrated multiple-active-region nanowire LEDs connected by low resistance GaN/InGaN/GaN tunnel junction. Such multiple-active-region nanowire LEDs showed significantly improved light intensity as compared to single-active region LEDs and reduced efficiency droop. In chapter 4, we have demonstrated AC operated nanowire LEDs on Si platform that eliminates the use of an AC/DC converter.

In Chapter 5, we have demonstrated MBE growth and characterization of Al metal on Al(Ga)N nanowires and vice-versa. We have analyzed the epitaxy of Al(Ga)N/Al/Al(Ga)N nanowire heterostructure by STEM, HRTEM and XRD. In Chapter 6, we have presented low resistance Al-tunnel junction integrated dot-in-a-wire LED with overall better performance. Compared to previously reported polarization engineered tunnel junctions, the presented monolithic metal tunnel junction design eliminates the use of either a low band gap InGaN or a large band gap AlN/Al(Ga)N interlayer that often leads to optical absorption and unwanted voltage loss.

In Chapter 7, we have demonstrated a monolithic n^{++} -GaN/Al/ p^{++} -Al(Ga)N nanowire backward diode, wherein an epitaxial Al layer serves as the tunnel junction. Such an Al(Ga)N-based n - p - n nanowire backward diode exhibits record low resistivity ($<1.5 \times 10^{-4} \Omega \cdot \text{cm}^2$) and low turn-on voltage ~ 2.7 V. Associated with this efficient p -type doping, excellent carrier transport was enabled due to back to back ohmic/quasi-ohmic contact to n -GaN/ p -(Al)GaN. Such a low-resistance backward diode exhibited a current density of 100 A/cm^2 at ~ 3 V. Associated with this

efficient *p*-type doping, excellent carrier transport was enabled due to back to back ohmic/quasi ohmic contact to *n*-GaN/*p*-(Al)GaN.

In Chapters 8 and 9, we have demonstrated a new class of deep UV LEDs (operating in the spectral range of ~275 nm and ~242 nm) with the use of AlGa_N tunnel junction core-shell nanowire heterostructure. We show that nearly dislocation free Al-rich AlGa_N nanowire heterostructures can be formed on an epitaxial Al/AlGa_N tunnel junction. The resulting core-shell nanowire arrays exhibit high luminescence efficiency (~80%) in the UV-C band. The unpackaged Al tunnel junction deep UV LEDs operating in the ~275 nm spectral range exhibit an output power > 8 mW and a peak external quantum efficiency ~0.4%. For UV LED emission wavelength at 242 nm, an output power of 0.37 mW and EQE of 0.012% have been measured. Detailed measurement suggests that light emission from the AlGa_N based deep UV devices is predominantly TM polarized, and identified as one of the reasons for relatively low efficiency in the challenging UV-C band.

10.2 Suggested Future Works

10.2.1 Self-organized Al(Ga)N/AlN Quantum Dots/Discs in Nanowires

In this thesis work, we have investigated the MBE growth and device performance of various AlGa_N based core-shell double heterostructure LEDs. Although we have demonstrated significantly improved performance including light output power, EQE, device resistance, etc., yet this is not even close to the best-reported value in this spectral range. It was envisioned that the maximum achievable efficiency is limited by electron overflow and poor light extraction efficiency due to the TM polarized light emission. The light polarization switching from TE to TM occurs when the Al mole fraction increases. Nevertheless, the device performance can be further

improved by optimizing device active region, including the use of quantum dots/disks for better carrier confinement and the incorporation of an electron blocking layer. Until recent years, however, the successful incorporation of quantum dots/disks and improved device performance has not been demonstrated in the ultraviolet-C band. In this context, AlGa_N quantum dots embedded in AlGa_N nanowires will by and large solve the afore-mentioned challenges. Further to better carrier confinement, by varying the Al composition in quantum dot and barrier, the emission wavelength can be readily tuned. Another primary challenge for high-performance deep UV light emitters is the QCSE. Moreover, it was reported that with the use of semipolar/non-polar AlGa_N quantum wells, QCSE can be reduced due to the elimination of spontaneous polarization field, leading to improved light output.

Further optimization in the growth process of AlGa_N/AlN quantum dots, such that semipolar/nonpolar AlGa_N quantum dots can be formed through controlling the growth parameters including substrate temperature, nitrogen flow, and Al and Ga fluxes. Such QCSE-free AlGa_N quantum dots will drastically improve the luminescence efficiency and reduce efficiency droop. In addition, the TM polarization associated with high Al-composition can be largely mitigated by further optimizing AlGa_N quantum dot lateral size, height, and barrier compositions. As such, it is expected that, the desired optical TE polarization can be realized and light extraction efficiency can be significantly improved. The device schematic is shown in Fig. 10.1.

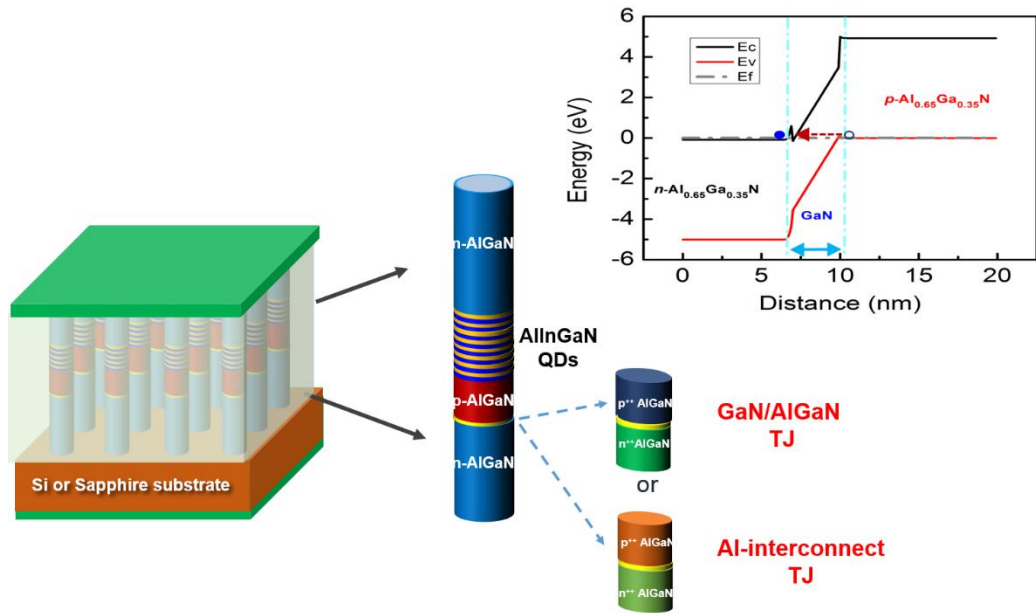


Figure 10.1 Schematic illustration of High Power Tunnel Junction AlInGaN/AlN QDs UV nanowire LEDs on Si or Sapphire substrate. Band diagram of the GaN/AlGaN tunnel junction is also shown.

10.2.2 Tunnel Junction III-Nitride Visible Nanowire Laser Diodes

As described in chapter 1, the current solid-state lighting technology still relies on the blue light-emitting diode (LEDs) and use of phosphors to down convert GaN-based blue lights to green and red light. Associated with this down-conversion is an energy loss of ~30% or more, low color rendering index, and Stokes fluorescence loss. Driven by the need for reduced power consumption and enhanced efficiency and functionality, future ultra-high resolution display and smart lighting technologies require the development of small size, high-efficiency, multi-color laser sources. To date, however, there are no efficient semiconductor lasers in the deep visible (green/red) spectral range. The challenges for realizing planar InGaN-based green and yellow/red lasers include large densities of lattice misfit dislocations as well as strain-induced quantum-confined Stark effect (QCSE) [218, 259, 268]. Recently, significant progress has been made in InGaN nanowire

heterostructures, which are virtually free of dislocations and exhibit a small strain field. In addition, previously it was reported that in self-organized InGaN/GaN quantum dots, In incorporation can be significantly enhanced and QCSE can be drastically reduced. To date, however, the development of electrically injected, full-color InGaN/GaN quantum-dot-in-nanowire edge emitting laser has been limited.

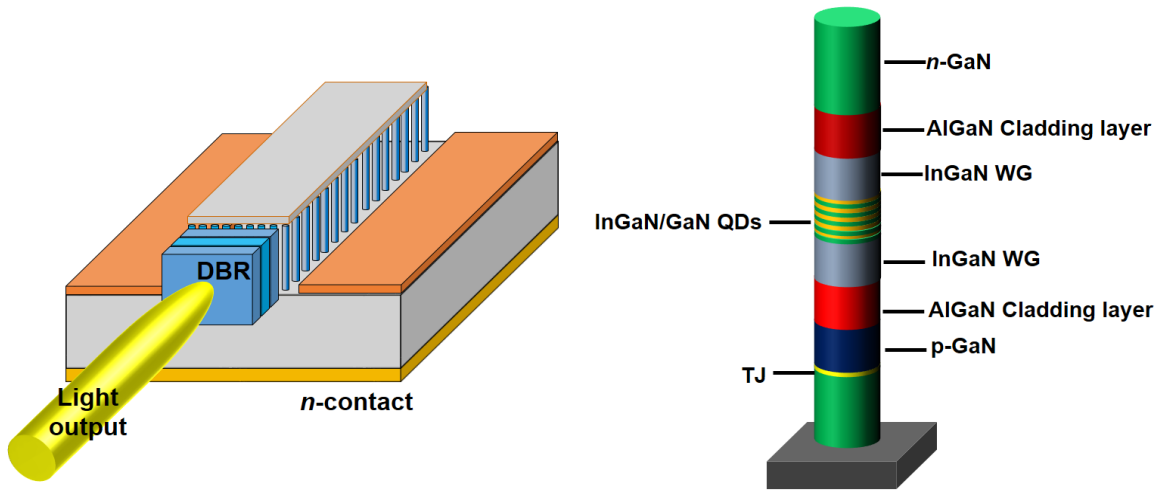


Figure 10.2: Schematic illustration of InGaN/GaN QDs visible nanowire edge-emitting

The overall development of electrically injected laser includes the achievement of low threshold current density, reasonably high light output power, weak temperature dependence of the threshold, large modal, differential gain etc. However, for both nanowire and planar III-nitride devices, highly resistive *p*-GaN contact remains a bottleneck. As described in previous chapters, due to inefficient Mg dopant ionization and heavy hole effective mass, the specific contact resistance and layer resistivity are very high. Additionally, *p*-GaN work function is very high, and it is challenging to form a low resistance ohmic contact. Therefore, conventional GaN-based *p-i-n* laser diodes suffer from high operation voltage and low wall plug efficiency. Tunnel junction integration can by and large solve the afore-described issues. In tunnel junction III-nitride laser

diodes, the p -type cladding and the p -type contact layers can be replaced by low resistance n -type cladding and n -type contact layers. In addition, tunnel junction of *non-equilibrium* holes can be significantly enhanced, and thereby laser output power will be dramatically increased. The device schematic of edge-emitting visible nanowire laser array is shown in Fig. 10.2.

10.2.3 Tunnel Junction III-Nitride UV Nanowire Laser Diodes

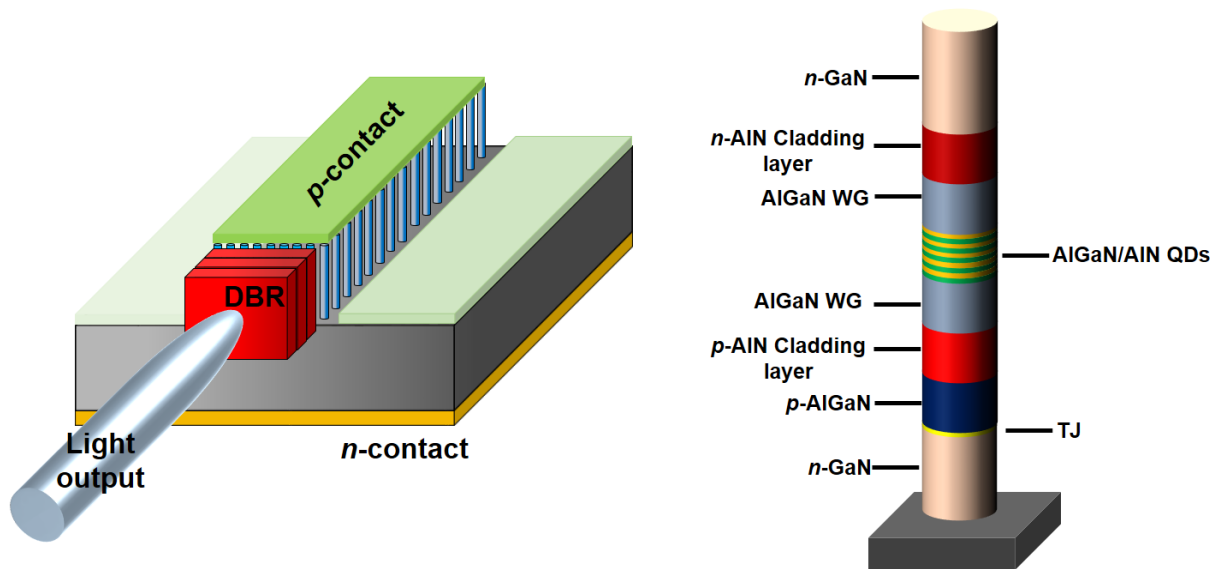


Figure 10.3 Schematic illustration of AlGaN/AlN QDs UV nanowire edge emitting laser.

To date, the shortest wavelength electrically pumped semiconductor edge-emitting lasers is ~ 336 nm. The realization of electrically injected coherent light sources in the deep ultraviolet band has been fundamentally limited by the presence of extensive defects, dislocations, and cracks due to the lattice mismatch between GaN and AlN ($\sim 3\%$), and the extremely inefficient p -type doping in Al-rich AlGaN due to the large ionization energy of Mg dopant (~ 600 meV in AlN). As mentioned in previous chapters, An efficient light source in the deep UV band (< 280 nm) is required for a wide range of applications, including water purification, sterilization, and chemical

and biological analysis. The current technology is limited to mercury vapor lamps, a few gas lasers, and lasers based on frequency conversion. In this context, we propose a tunnel junction edge-emitting UV laser operating below 280 nm spectral wavelength. The device structure is schematically shown in Fig. 10.3. We will integrate a low resistance tunnel junction in the UV laser structure to replace the resistive p -Al(Ga)N contact.

10.2.4 Tunnel Junction III-nitride Solar Cells

In addition to LED and laser diode applications, III-nitride materials system is attractive for photovoltaic applications. Direct bandgap InGaN-based alloys can absorb a broad range of solar spectrum ranging from ultraviolet to infrared, therefore, it potentially can cover the full solar spectrum. Additionally, strong photon absorption capability of InGaN alloys allows to absorb a large fraction of the incident photons in a very thin InGaN layer. To date, however, the development of InGaN-based solar cells is limited due to several factors. First, it is very challenging to grow high In-content, high crystalline quality InGaN layer and to date, InGaN solar cell devices were limited to In content (~2-5%) [368]. Second, due to large lattice mismatch between InN and GaN, thick InGaN layer cannot be grown on lattice mismatched materials.[369] However, due to effective lateral stress relaxation low dimensional III-nitride nanowire can potentially solve these issues. Here, we propose single junction and multi-junction InGaN nanowire solar cells on a Si platform. Such InGaN nanowire solar cell will absorb a broad solar spectrum by effectively changing the In-concentration in different junctions connected by a low resistance tunnel junction. However, the external quantum efficiency (EQE) of the single junction solar cell is low in the GaN- band gap energy range. The low EQE is partly due to the absorption

of UV photon in the top p -GaN. Nevertheless, decrease in p -GaN thickness will further increase the p -GaN spreading resistance.

Tunnel junction integration with solar cell can replace resistive p -GaN with a thin low resistance n -GaN layer transparent to UV light. Single junction solar cell is limited by thin InGaN layer and full solar spectrum cannot be absorbed. Therefore, cascaded multi-junction solar cell connected by a low resistance tunnel junction can cover the full solar spectrum. The structure will be more or less similar to the cascaded multiple wavelength LEDs described in chapter 3. However, tandem multi-junction nanowire solar cell requires careful optimization in the unit cells. This can be done by optimizing growth condition and designs. The schematics for single junction and three-junction solar cells are shown in Fig. 10.4. The open circuit voltage, V_{oc} can be increased by the series connection of each unit cell connected by a tunnel junction.

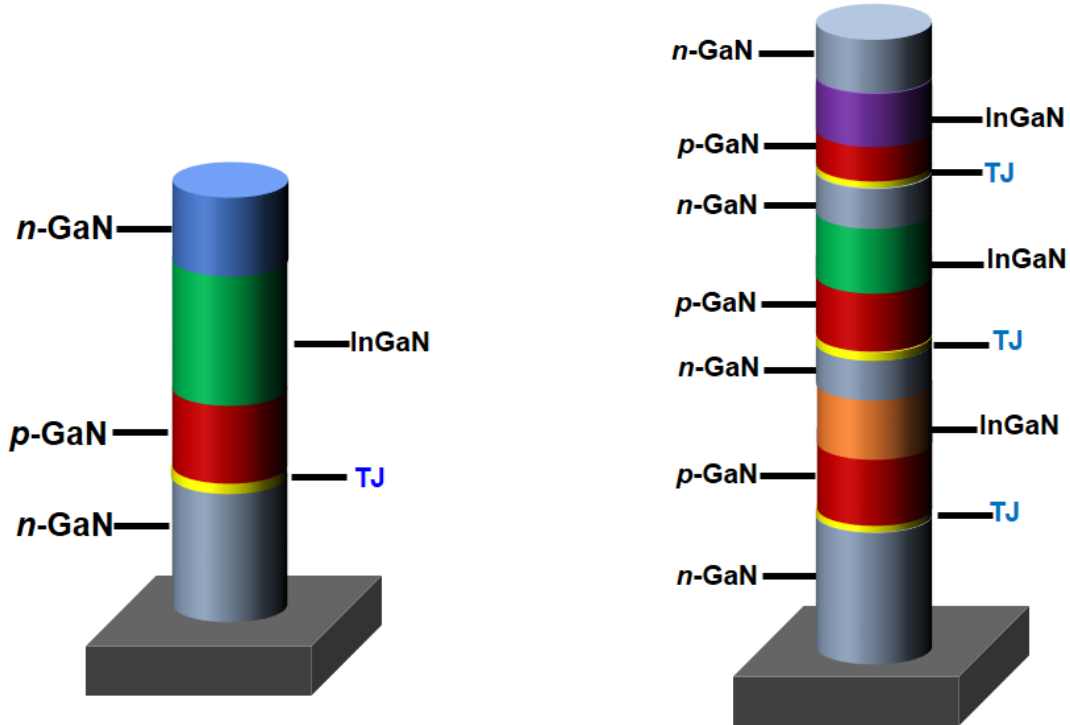


Figure 10.4 Schematic illustration of single junction and multi-junction InGaN nanowire solar cell.

10.2.5 GaN Nanowire Vertical Transistor on Si Substrate

In addition to III-nitride's ubiquitous applications in optoelectronics, GaN is very attractive for electronic device applications due to wide bandgap, high saturation velocity and large critical electric field strength [370, 371]. However, current lateral GaN-based FET devices suffer from increased devices operation voltage with the increase of device dimension, non-uniform heat dissipation, unavailability of the normally-off transistor, high leakage current, etc. [370, 371]. In this context, vertical GaN-transistor offers significant promise to overcome the afore-described problems associated with lateral GaN-transistors. The enormous promise of vertically aligned GaN nanowires for optoelectronics is discussed in this dissertation. We also discussed GaN-nanowire backward diodes. GaN-nanowire is very promising for vertical transistor applications for several reasons [371]. First, vertical nanowire allows large current densities per unit chip size. Second, due to effective stress relaxation, and high surface to volume ratio, an excellent quality non-polar surface can be achieved. Third, efficient gate control can be enabled using a wraparound gate formed on the vertical nanowires [370]. Such vertical III-nitride nanowire FETs with both enhancement mode and depletion mode operation on the same chip could be a promising building block for high-temperature logic circuits. Here, we propose to demonstrate vertical GaN-nanowire transistor grown on Si/GaN-on Sapphire by MBE. For the growth, first, we grow 300-400 nm Si-doped GaN (source layer) on commercially available GaN-on Sapphire substrate/Si substrate. Then another intrinsic 700-800 nm GaN will be grown as the channel layer, and finally 200-300 nm heavily Si-doped GaN will be grown as drain layer. The vertical nanowire growth and device fabrication are schematically shown in Fig. 10.5.

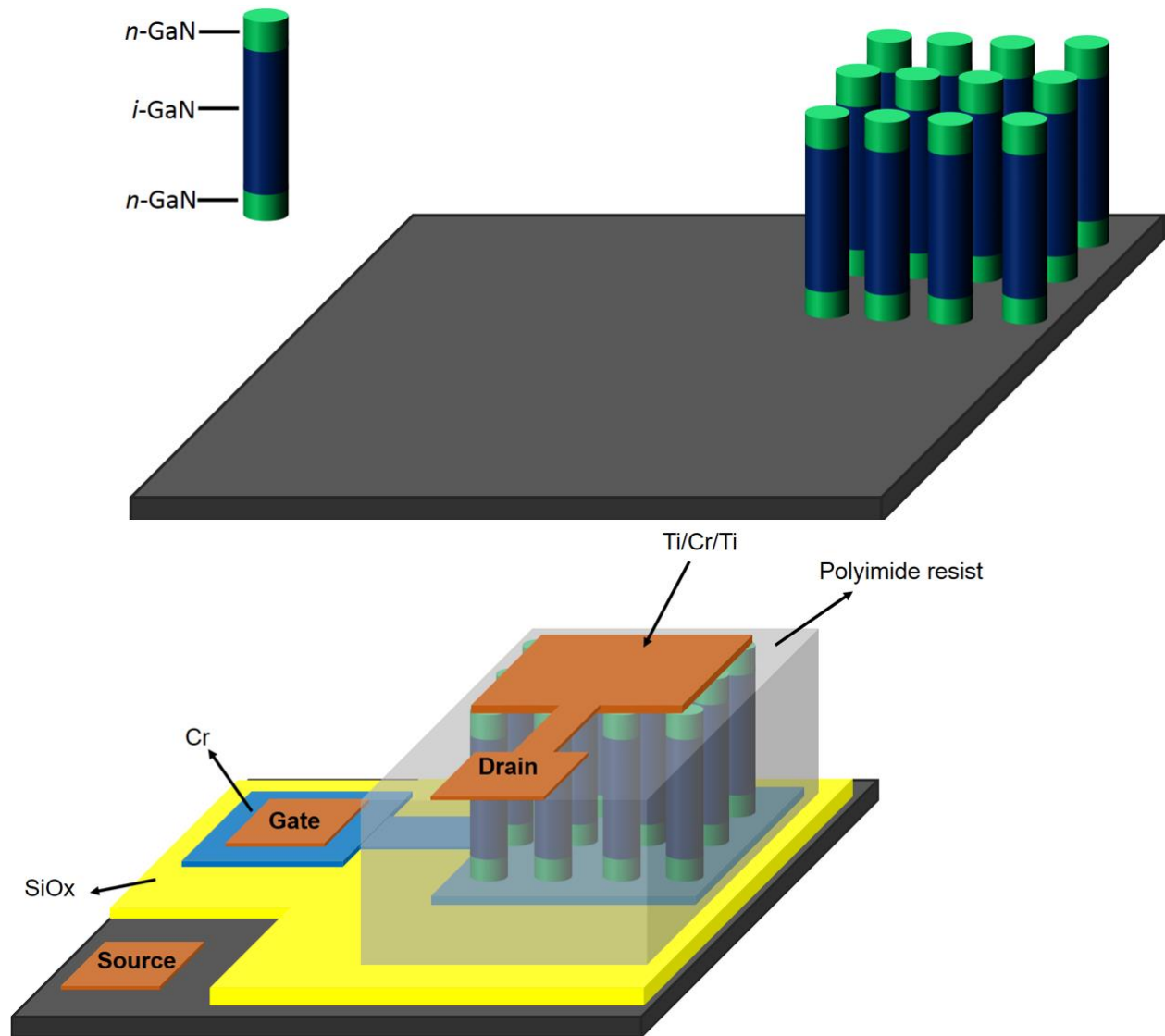


Figure 10.5 (a) Schematic illustration of vertical n-GaN/i-GaN/n-GaN nanowire growth on Si substrate. (b) Illustration of vertical nanowire transistor fabrication.

As shown in Fig. 10.5, the vertical nanowire transistor device fabrication involves the following steps. First, a 20 nm-50 nm SiO₂ is deposited by plasma enhanced chemical vapor deposition (PECVD) to form a dielectric layer on the nanowire sidewalls. Then an e-beam evaporated non-stoichiometric SiO_x (~200 nm-300 nm) will be deposited as a passivation layer between the heavily doped source layer and the metal gate layer. Subsequently, a ~300 nm Cr layer is deposited at a

tilting angle to form a wrap-around gate contact. Afterwards, a polyimide resist layer will be deposited to fully cover the nanowires, followed by a O_2 plasma etching to expose the nanowire top surface. Finally, a Ti/Cr/Au layer stack will be deposited by e-beam evaporation on the nanowires to form the drain contact.

10.2.6 Selective Area Growth of Tunnel Junction InGaN/Al(Ga)N Core-Shell LEDs

Compared to edge emitting lasers, vertical cavity surface emitting lasers (VCSELs) offer advantages such as lower threshold, circular and low-divergence output beam, and single longitudinal mode emission.^{2,3} Such quantum-confined nanowire heterostructures will be grown by selective area epitaxy using plasma-assisted molecular beam epitaxy (MBE). In these structures, small strain field, reduced dislocation densities, and the three-dimensional quantum confinement of charge carrier and the resulting near-discrete density of states leads to large gain and differential gain. To date, however, the realization of high-performance GaN-based VCSELs has remained elusive, and there have been no commercial GaN-based VCSELs.

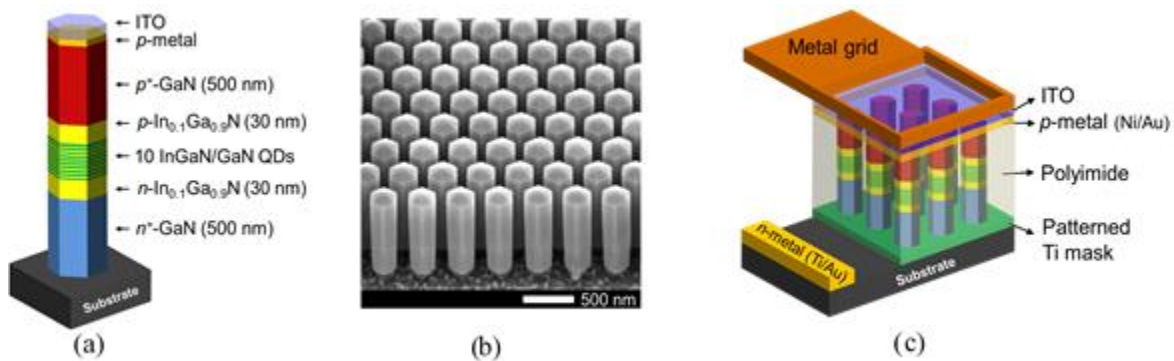


Figure 10.6 a) Schematic illustration of InGaN/GaN dot-in-a-wire heterostructures for photonic crystal laser. (b) SEM image of hexagonally packed nanowires which have diameters ~ 260 nm, and pitch ~ 345 nm. (c) Illustration of the fabrication of electrically injected dot-in-nanowire photonic crystal lasers.

The large threshold is due to the relatively low reflectivity of the distributed Bragg reflectors (DBRs) and the presence of extensive defects and dislocations in the active region. Our idea is to demonstrate InGaN nanowire photonic crystal band edge lasers, wherein surface laser emission can be achieved without the use of distributed Bragg reflectors. The device heterostructure is schematically shown in Fig. 10.6a. Each nanowire consists of ~500 nm n^+ -GaN, 30 nm n -In_{0.1}Ga_{0.9}N guiding layer, ten vertically aligned InGaN/GaN quantum dots, 30 nm p -In_{0.1}Ga_{0.9}N guiding layer, and 500 nm p^+ -GaN cladding and contact layer. The resulting nanowire sidewalls are perfectly vertical and have atomic scale roughness, which inherently avoids major contributions to loss in top-down PhC cavities. The representative SEM image is shown in Fig. 10.6b. The fabrication process for electrically injected nanowire photonic crystal lasers involves the use of standard photolithography, dry etching, and contact metallization techniques (shown in Fig. 10.6c).

List of Publications

Referred Journal Articles:

1. An AlGa_N Core-Shell Tunnel Junction Nanowire Light Emitting Diode Operating in the ultraviolet C-band. **S. M. Sadaf**, S. Zhao, Y. Wu, Y.-H Ra and Z. Mi **Nano Letters** 17 (2), 1212-1218 (2017) (IF=13.78)
2. Molecular Beam Epitaxial Growth and Characterization of n-GaN/Al/p-Al(Ga)_N Tunnel Junction Nanowire Heterostructure. **S. M. Sadaf**, S. Zhao, I. Shih and Z. Mi (in preparation for **APL Materials**) (2017).
3. Record Low Resistance AlGa_N Nanowire Backward Diode for High Efficiency III-Nitride Photonic Devices. **S.M. Sadaf**, Y.-H. Ra, T. Szkopek, I. Shih and Z. Mi. (submitted to **Applied Physics Letters**) (2017).
4. Monolithically Integrated Metal/Semiconductor Tunnel Junction Nanowire Light Emitting Diodes **S. M. Sadaf**, Y.-H, Ra, T. Szkopek, Z. Mi: **Nano Letters** 16 (2), 1076-1080 (2016) (IF=13.78)
5. Alternating-Current InGa_N/Ga_N Tunnel Junction Nanowire White-Light Emitting Diodes. **S. M. Sadaf**, Y.-H. Ra, H. P. T. Nguyen, M. Djavid, Z. Mi: **Nano Letters** 15 (10), 6696-6701. (2015) (IF=13.78).
6. Sub-milliwatt AlGa_N Nanowire Deep Ultraviolet Light Emitting Diodes on Silicon Operating around 240 nm. S. Zhao*, **S. M. Sadaf***, S. Vanka, Y. Wang, R. Rashid and Z. Mi. (* contributed equally). **Applied Physics Letters** 109, 201106 (2016) (IF=3.142)
7. Optically Active Dilute-Antimonide III-Nitride Nanostructures for Optoelectronic Devices. F. A. Chowdhury, **S. M. Sadaf**, Q. Shi, Y.C Chen, H. Guo, Z. Mi., **Applied Physics Letters** (2017) (accepted) (IF=3.142)
8. Full-Color Single Nanowire Projection Displays. Y.-H Ra, R. Wang, S. Y. Woo, M. Djavid **S. M. Sadaf**, J. Lee, G.A Botton, Z. Mi. **Nano Letters** 16 (7), 4608-4615 (2016) (IF=13.78)
9. AlGa_N nanowire light-emitting diodes: breaking the efficiency bottleneck of deep

- ultraviolet light sources. Z. Mi, S. Zhao. **S.M. Sadaf**. (invited paper). **SPIE OPTO**. (2017)
10. Molecular Beam Epitaxy Growth of Al-rich AlGa_N Nanowires for Deep Ultraviolet Optoelectronics. S. Zhao, S. Yu, **S. M. Sadaf**, Y. Wu, D. Laleyen, R. Rashid, G.A. Botton and Z. Mi. **APL Materials**. 4, 8, 086115-2. (2016) (IF=4.323)
 11. Optical and electrical properties of Mg-doped AlN nanowires grown by molecular beam epitaxy. A.T. Connie, S. Zhao, **S. M. Sadaf**, I. Shih, Z. Mi, X. Du, J. L. Jiang: **Applied Physics Letters** 106 (21), 213105. (2015) (IF=3.142).
 12. Aluminum nitride nanowire light emitting diodes: Breaking the fundamental bottleneck of deep ultraviolet light sources. S. Zhao, A. T. Connie, M. H. T. Dastjerdi, X. H. Kong, Q. Wang, M. Djavid, **S. M. Sadaf**, X. D. Liu, I. Shih, H. Guo, Z. Mi **Scientific Reports** 5, 8332. (2015) (IF=5.228)
 13. Engineering the Carrier Dynamics of InGa_N Nanowire White Light-Emitting Diodes by Distributed p-AlGa_N Electron Blocking Layers. H. T. P. Nguyen, M. Djavid, S. Y. Woo, X. Liu, A. T. Connie, **S. M. Sadaf**, Q. Wang, G. A. Botton, I. Shih, Z. Mi: **Scientific Reports** 5, 7744. (2015) (IF=5.228)
 14. Engineering the color rendering index of phosphor-free InGa_N/(Al)Ga_N nanowire white light emitting diodes grown by molecular beam epitaxy. A.T. Connie, H. P.T. Nguyen, **S. M. Sadaf**,, Ishiang Shih, Zetian Mi. **Journal of vacuum science & technology. B**, Microelectronics and nanometer structures: processing, measurement, and phenomena: an official journal of the American Vacuum Society. 32 (2), 02C113. (2014) (IF=1.398).
 15. Highly efficient, spectrally pure 340 nm ultraviolet emission from Al_xGa_{1-x}N nanowire based light emitting diodes. Q Wang, A T Connie, H P T Nguyen, M G Kibria, S Zhao, **S. M. Sadaf**, I Shih, Z Mi. **Nanotechnology** 24 (34), 345201 (2013) (IF=3.573).
 16. High Power Phosphor-Free InGa_N/Ga_N/AlGa_N Core-Shell Nanowire White Light Emitting Diodes on Si Substrates. Z. Mi, H P T Nguyen, M. Djavid, S. Zhang, A.T. Connie, **S.M. Sadaf**, Q. Wang. S. Zhao, I. Shih. **ECS Trans**. 2014 61(5): 9-15;

Conference Presentations:

1. Molecular Beam Epitaxial Growth and Characterization of n-GaN/Al/p-Al(GaN) Tunnel Junction Nanowire Heterostructure. **S. M. Sadaf**, S. Zhao , I. Shih and Z. Mi. **International Symposium on Semiconductor Light-Emitting Diodes (ISSLED)** , Banff, Canada, 2017.
2. Bandgap Tuning of Optically Active Dilute-Antimonide GaSbN Nanowire Heterostructures for Visible Light Emitting Diodes. M. F. Choudhury, Q. Shi, **S.M. Sadaf**, H. Guo and Z.Mi. **Electronic Materials Conference**, University of Notredame, South Bend , IN, 2017.
3. Monolithically Integrated GaN/Al/GaN Tunnel Junction Nanowire Visible and Deep UV Light Emitting Diodes. **S. M. Sadaf**, Y.-H.Ra, S.Zhao and Z.Mi. **Electronic Materials Conference**, Newark, Delaware. USA, 2016.
4. Molecular Beam Epitaxial Growth and Characterization of AlGaIn Nanowires for 240 nm Emitting UV LEDs and Lasers. S. Zhao, **S. M. Sadaf**, X. Liu and Z. Mi. **North American Molecular Beam Epitaxy (NAMBE)** 2016, New York, USA.
5. Alternating current operated InGaIn/GaN tunnel junction nanowire phosphor-free white-light emitting diodes **S. M. Sadaf**, Y.-H.Ra, H.P.T.Nguyen and Z.Mi. **MRS, Fall Meeting**, Boston, USA. December, 2015
6. Tunnel Junction Enhanced High Power Deep Ultraviolet Nanowire Light-Emitting Diodes. **S. M. Sadaf**, S. Zhao, Y. Wu, Y.-H. Ra, X. Liu, and Z. Mi. **North American Molecular Beam Epitaxy NAMBE** 2016, New York, USA
7. InGaIn/GaN Tunnel Junction Dot-in-a-wire Light Emitting Diodes. **S. M. Sadaf**, Y.-H.Ra, H.P.T.Nguyen, M. Djavid and Z.Mi. **MRS Spring meeting**, Sanfrancisco, USA, April, 2015.
8. Polarization doped core-shell InGaIn-GaN dot-in-a wire white light emitting diodes. **S. M. Sadaf**, H. Nguyen, A. Connie. I. Shih, Z. Mi . **Electronic Materials Conference**, Indiana, USA, June,2013.

9. Engineering the Color Rendering Index of Phosphor-free InGaN/(Al)GaN Nanowire White Light Emitting Diodes Grown by Molecular Beam Epitaxy, A.T. Connie, H.P.T. Nguyen, **S. M. Sadaf**, I. Shih, and Z. Mi. 30th **NAMBE** Conference, Banff, Alberta, October 5-11, 2013.
10. High Power Phosphor-Free InGaN/GaN/AlGaN Core-Shell Nanowire White Light Emitting Diodes on Si. Z. Mi, H. Nguyen, M. Djavid, S. Zhang, A. Connie, **S. M. Sadaf**, Q. Wang, S. Zhao, and I. Shih (McGill University), **225th ECS Meeting** (May 11-16, 2014).

Bibliography

- [1] J. Piprek, "Efficiency droop in nitride-based light-emitting diodes," *Phys. Status Solidi A*, vol. 207, pp. 2217-2225, 2010.
- [2] J. H. Tae-Yeon Seong, Hiroshi Amano, Hadis Markoc, *III-Nitride Based Light Emitting Diodes and Applications*. Singapore: Springer, 2017.
- [3] E. F. S. a. J. K. Kim, "Solid-State Light Sources Getting Smart," *Science*, vol. 308, 2005.
- [4] J. Cho, E. F. Schubert, and J. K. Kim, "Efficiency droop in light-emitting diodes: Challenges and countermeasures," *Laser & Photonics Reviews*, vol. 7, pp. 408-421, 2013.
- [5] S. Nakamura, "Nobel Lecture: Background story of the invention of efficient blue InGaN light emitting diodes," *Rev. Modern Phys.*, vol. 87, p. 1139, 2015.
- [6] S. P. DenBaars, D. Feezell, K. Kelchner, S. Pimputkar, C.-C. Pan, C.-C. Yen, *et al.*, "Development of gallium-nitride-based light-emitting diodes (LEDs) and laser diodes for energy-efficient lighting and displays," *Acta Mater.*, vol. 61, pp. 945-951, 2013.
- [7] D. C. F. M. Steranka J. Bhat, L. Cook, M. G. Craford, R. Fletcher, N. Gardner, P. Grillot, W. Goetz, M. Keuper, R. Khare, A. Kim, M. Krames, G. Harbers, M. Ludowise, P. S. Martin, M. Misra, G. Mueller, , S. R. R. Mueller-Mach, Y.-C. Shen, D. Steigerwald, S. Stockman, , and T. T. S. Subramanya, and J. J. Wierer, "High Power LEDs – Technology Status and Market Applications" *Phys. Status Solidi A*, vol. 194, pp. 380-388, 2002.
- [8] G. O. M. Regina Mueller-Mach, Michael R. Krames, and Troy Trottier, "High-Power Phosphor-Converted Light-Emitting Diodes Based on III-Nitrides," *IEEE J. Sel. Topics Quantum Electron.*, vol. 8, 2002.
- [9] S. W. Kaun, M. H. Wong, U. K. Mishra, and J. S. Speck, "Molecular beam epitaxy for high-performance Ga-face GaN electron devices," *Semicond. Sci. Technol.*, vol. 28, p. 074001, 2013.
- [10] P. T. Barletta, E. Acar Berkman, B. F. Moody, N. A. El-Masry, A. M. Emar, M. J. Reed, *et al.*, "Development of green, yellow, and amber light emitting diodes using InGaN multiple quantum well structures," *Appl. Phys. Lett.*, vol. 90, p. 151109, 2007.
- [11] Y. L. Chang, J. L. Wang, F. Li, and Z. Mi, "High efficiency green, yellow, and amber emission from InGaN/GaN dot-in-a-wire heterostructures on Si(111)," *Appl. Phys. Lett.*, vol. 96, p. 013106, 2010.
- [12] M. H. Crawford, "LEDs for Solid-State Lighting: Performance Challenges and Recent Advances," *IEEE J. Sel. Topics Quantum Electron.*, vol. 15, pp. 1028-1040, 2009.
- [13] B. Damilano, N. Grandjean, J. Massies, L. Siozade, and J. Leymarie, "InGaN/GaN quantum wells grown by molecular-beam epitaxy emitting from blue to red at 300 K," *Appl. Phys. Lett.*, vol. 77, p. 1268, 2000.
- [14] M. Kneissl, T. Kolbe, C. Chua, V. Kueller, N. Lobo, J. Stellmach, *et al.*, "Advances in group III-nitride-based deep UV light-emitting diode technology," *Semicond. Sci. Technol.*, vol. 26, p. 014036, 2011.

- [15] M. R. Krames, O. B. Shchekin, R. Mueller-Mach, G. O. Mueller, L. Zhou, G. Harbers, *et al.*, "Status and Future of High-Power Light-Emitting Diodes for Solid-State Lighting," *J. Display Technol.*, vol. 3, pp. 160-175, 2007.
- [16] M. A. Khan, M. Shatalov, H. P. Maruska, H. M. Wang and E. Kuokstis, "III-Nitride UV Devices," *Jpn. J. Appl. Phys.*, vol. 44, 2005.
- [17] S. Nakamura, M. Senoh, S.-i. Nagahama, N. Iwasa, T. Yamada, T. Matsushita, *et al.*, "InGaN/GaN/AlGaIn-based laser diodes with modulation-doped strained-layer superlattices grown on an epitaxially laterally overgrown GaN substrate," *Appl. Phys. Lett.*, vol. 72, p. 211, 1998.
- [18] S. Nakamura, M. Senoh, S.-i. Nagahama, N. Iwasa, T. Yamada, T. Matsushita, *et al.*, "Room-temperature continuous-wave operation of InGaN multi-quantum-well structure laser diodes with a lifetime of 27 hours," *Appl. Phys. Lett.*, vol. 70, p. 1417, 1997.
- [19] Y. Narukawa, Y. Kawakami, M. Funato, S. Fujita, S. Fujita, and S. Nakamura, "Role of self-formed InGaIn quantum dots for exciton localization in the purple laser diode emitting at 420 nm," *Appl. Phys. Lett.*, vol. 70, p. 981, 1997.
- [20] D. s. e. Queren, A. Avramescu, G. Brüderl, A. Breidenassel, M. Schillgalies, S. Lutgen, *et al.*, "500 nm electrically driven InGaIn based laser diodes," *Appl. Phys. Lett.*, vol. 94, p. 081119, 2009.
- [21] O. Jani, I. Ferguson, C. Honsberg, and S. Kurtz, "Design and characterization of GaInGa solar cells," *Appl. Phys. Lett.*, vol. 91, p. 132117, 2007.
- [22] C. J. Neufeld, N. G. Toledo, S. C. Cruz, M. Iza, S. P. DenBaars, and U. K. Mishra, "High quantum efficiency InGaIn/GaN solar cells with 2.95 eV band gap," *Appl. Phys. Lett.*, vol. 93, p. 143502, 2008.
- [23] Z. H. C. Y. B. Tang, H. S. Song, C. S. Lee., H. T. Cong, H. M. Cheng, W. J. Zhang, I. Bello, and S. T. Lee, "Vertically Aligned p-Type Single-Crystalline GaIn Nanorod Arrays on n-Type Si for Heterojunction Photovoltaic Cells" *Nano Lett.*, vol. 8, 2008.
- [24] B. T. Yajie Dong, Thomas J. Kempa, and Charles M. Lieber, "Coaxial Group III-Nitride Nanowire Photovoltaics" *Nano Lett.*, vol. 9, 2009.
- [25] X. Zhang, X. Wang, H. Xiao, C. Yang, J. Ran, C. Wang, *et al.*, "Simulation of In_{0.65}Ga_{0.35}N single-junction solar cell," *J. Phys. D: Appl. Phys.*, vol. 40, pp. 7335-7338, 2007.
- [26] F. Binet, J. Y. Duboz, E. Rosencher, F. Scholz, and V. Härle, "Mechanisms of recombination in GaIn photodetectors," *Appl. Phys. Lett.*, vol. 69, p. 1202, 1996.
- [27] E. M. E Munoz, J L Pau, F Calle, F Omnes and P Gibart, "III nitrides and UV detection," *J. Phys.: Condens. Matter*, vol. 13 pp. 7115–7137, 2001.
- [28] E. Miyazaki, S. Itami, and T. Araki, "Using a light-emitting diode as a high-speed, wavelength selective photodetector," *Rev. Sci. Instrum.*, vol. 69, p. 3751, 1998.
- [29] A. Osinsky, S. Gangopadhyay, R. Gaska, B. Williams, M. A. Khan, D. Kuksenkov, *et al.*, "Low noise p- π -n GaIn ultraviolet photodetectors," *Appl. Phys. Lett.*, vol. 71, p. 2334, 1997.
- [30] M. Razeghi and A. Rogalski, "Semiconductor ultraviolet detectors," *J. Appl. Phys.*, vol. 79, p. 7433, 1996.
- [31] S. J. Chang, T. K. Ko, Y. K. Su, Y. Z. Chiou, C. S. Chang, S. C. Shei, *et al.*, "GaIn-based p-i-n sensors with ITO contacts," *IEEE Sens. J.*, vol. 6, pp. 406-411, 2006.

- [32] J. A. Jose Luis Pau, Carlos Rivera, Álvaro Navarro, Isabel Álava, Marcos Redondo, and Elías Muñoz, "Optical sensors based on III-nitride photodetectors for flame sensing and combustion monitoring" *Appl. Opt.*, vol. 45, 2006.
- [33] M. Shur, "Physics of Semiconductor Devices," USA, 1990.
- [34] Shreepad Karmalkar and Umesh K. Mishra, "Enhancement of Breakdown Voltage in AlGaIn/GaN High Electron Mobility Transistors Using a Field Plate," *IEEE Trans. Electron. Devices*, vol. 48, 2001.
- [35] J. D. Albrecht, R. P. Wang, P. P. Ruden, M. Farahmand, and K. F. Brennan, "Electron transport characteristics of GaN for high temperature device modeling," *J. Appl. Phys.*, vol. 83, pp. 4777-4781, 1998.
- [36] J. n. Kolník, I. s. H. Oğuzman, K. F. Brennan, R. Wang, P. P. Ruden, and Y. Wang, "Electronic transport studies of bulk zincblende and wurtzite phases of GaN based on an ensemble Monte Carlo calculation including a full zone band structure," *J. Appl. Phys.*, vol. 78, p. 1033, 1995.
- [37] M. Asif Khan, A. Bhattarai, J. N. Kuznia, and D. T. Olson, "High electron mobility transistor based on a GaN-Al_xGa_{1-x}N heterojunction," *Appl. Phys. Lett.*, vol. 63, p. 1214, 1993.
- [38] M. Asif Khan, J. N. Kuznia, D. T. Olson, W. J. Schaff, J. W. Burm, and M. S. Shur, "Microwave performance of a 0.25 μm gate AlGaIn/GaN heterostructure field effect transistor," *Appl. Phys. Lett.*, vol. 65, p. 1121, 1994.
- [39] T. Palacios, A. Chakraborty, S. Heikman, S. Keller, S. P. DenBaars, and U. K. Mishra, "AlGaIn/GaN high electron mobility transistors with InGaIn back-barriers," *IEEE Electron Device Lett.*, vol. 27, pp. 13-15, 2006.
- [40] P. D. Ye, B. Yang, K. K. Ng, J. Bude, G. D. Wilk, S. Halder, *et al.*, "GaN metal-oxide-semiconductor high-electron-mobility-transistor with atomic layer deposited Al₂O₃ as gate dielectric," *Appl. Phys. Lett.*, vol. 86, p. 063501, 2005.
- [41] Y. Zhang and J. Singh, "Charge control and mobility studies for an AlGaIn/GaN high electron mobility transistor," *J. Appl. Phys.*, vol. 85, pp. 587-594, 1999.
- [42] "Energy Information Administration. Annual Energy Outlook 2015 with Projections to 2040. Energy Information Administration, U.S. Department of Energy. Washington, DC : s.n., 2015. Available at: [http://www.eia.gov/forecasts/archive/aeo15/pdf/0383\(2015\).pdf](http://www.eia.gov/forecasts/archive/aeo15/pdf/0383(2015).pdf)
- [43] "DOE SSL Program. Solid-State Lighting R&D Plan. [Online] June 2016. Available at: http://energy.gov/sites/prod/files/2016/06/f32/ssl_rd-plan_%20jun2016_2.pdf."
- [44] "Energy Savings Forecast of Solid-State Lighting in General Illumination Applications, 2016. https://energy.gov/sites/prod/files/2016/09/f33/energysavingsforecast16_2.pdf.
- [45] N. Holonyak and S. F. Bevacqua, "Coherent (visible) light emission from Ga(As_{1-x}P_x) junctions," *Appl. Phys. Lett.*, vol. 1, p. 82, 1962.
- [46] M. Gershenson and R. M. Mikulyak, "Electroluminescence at p-n Junctions in Gallium Phosphide," *J. Appl. Phys.*, vol. 32, p. 1338, 1961.
- [47] H. P. Maruska and J.J. Tietjen, "The preparation and properties of vapor-deposited single-crystalline GaN," *Appl. Phys. Lett.*, vol. 15, p. 327, 1969.

- [48] S. Yoshida, "Improvements on the electrical and luminescent properties of reactive molecular beam epitaxially grown GaN films by using AlN-coated sapphire substrates," *Appl. Phys. Lett.*, vol. 42, p. 427, 1983.
- [49] H. Amano, N. Sawaki, I. Akasaki, and Y. Toyoda, "Metalorganic vapor phase epitaxial growth of a high quality GaN film using an AlN buffer layer," *Appl. Phys. Lett.*, vol. 48, p. 353, 1986.
- [50] M. K. Hiroshi Amano, Kazumasa Hiramatsu, Isamu Akasaki, "P-Type Conduction in Mg-Doped GaN Treated with Low-Energy Electron Beam Irradiation," *Jpn. J. Appl. Phys.*, vol. 28, pp. L2112-L2114, 1989.
- [51] T. M. S. Nakamura, M. Senoh, N. Iwasa., "Thermal Annealing Effects on P-Type Mg-Doped GaN Films," *Jpn. J. Appl. Phys.*, vol. 31, pp. L139-L142, 1992.
- [52] T. M. S. Nakamura, M. Senoh, ",High-Power GaN P-N junction Blue Light emitting Diodes," *Jpn. J. Appl. Phys.*, vol. 30, pp. L1998-L2001, 1991.
- [53] M. S. S. Nakamura, T. Mukai, "P-GaN-N-InGaN-N-GaN Double-Heterostructure Blue-Light-Emitting Diodes " *Jpn. J. Appl. Phys.*, vol. 32, pp. L8-L11, 1993.
- [54] S. Nakamura, T. Mukai, and M. Senoh, "Candela-class high-brightness InGaN/AlGaIn double-heterostructure blue-light-emitting diodes," *Appl. Phys. Lett.*, vol. 64, p. 1687, 1994.
- [55] M. S. S. Nakamura, N. Iwasa, S. Nagahama, "High-Brightness InGaN Blue, Green and Yellow Light-Emitting Diodes with Quantum Well," *Jpn. J. Appl. Phys.*, vol. 34, pp. L797-L799, 1995.
- [56] M. S. S. Nakamura, N. Iwasa, S. Nagahama, T. Yamada, T. Mukai, "Superbright Green InGaN Single-Quantum-Well-Structure Light-Emitting Diodes," *Jpn. J. Appl. Phys.*, vol. 34, pp. L1332-L1335, 1995.
- [57] M. S. S. Nakamura, S. Nagahama, N. Iwasa, T. Yamada, T. Matsushita, H. Kiyoku, Y. Sugimoto, " InGaN-Based Multi-Quantum-Well-Structure Laser Diodes," *Jpn. J. Appl. Phys.*, vol. 35, pp. L74-L76, 1996.
- [58] B. K. Y. Noguchi, K. Sakamoto, and Y. Shimizu, "Development of high bright and pure LED Lamps," *Tech. Digest. Phosphor Res. Soc.*, 264th Meeting, 1996.
- [59] D. J. Colin Wood, *Polarization Effects in Semiconductors From Ab Initio Theory to Device Applications*. US: Springer, 2008.
- [60] G. Li, W. Wang, W. Yang, Y. Lin, H. Wang, Z. Lin, *et al.*, "GaN-based light-emitting diodes on various substrates: a critical review," *Rep. Prog. Phys.*, vol. 79, p. 056501, May 2016.
- [61] C.-C. Pan, S. Tanaka, F. Wu, Y. Zhao, J. S. Speck, S. Nakamura, *et al.*, "High-Power, Low-Efficiency-Droop Semipolar (20-2-1) Single-Quantum-Well Blue Light-Emitting Diodes," *Appl. Phys. Express*, vol. 5, p. 062103, 2012.
- [62] M. Auf der Maur, A. Pecchia, G. Penazzi, W. Rodrigues, and A. Di Carlo, "Efficiency Drop in Green InGaIn/GaN Light Emitting Diodes: The Role of Random Alloy Fluctuations," *Phys. Rev. Lett.*, vol. 116, p. 027401, Jan 15 2016.
- [63] D. Zhu, D. J. Wallis, and C. J. Humphreys, "Prospects of III-nitride optoelectronics grown on Si," *Rep. Prog. Phys.*, vol. 76, p. 106501, Oct 2013.
- [64] G. Verzellesi, D. Saguatti, M. Meneghini, F. Bertazzi, M. Goano, G. Meneghesso, *et al.*, "Efficiency droop in InGaIn/GaN blue light-emitting diodes: Physical mechanisms and remedies," *J. Appl. Phys.*, vol. 114, p. 071101, 2013.

- [65] V. R. C. D. Lee, A. Sagar, R. M. Feenstra, D. W. Greve, W. L. Sarney, L. Salamanca-Riba, D. C. Look, S. Bai, W. J. Choyke, and R. P. Devaty, "Properties of GaN epitaxial layers grown on 6HSiC(0001) by plasma-assisted molecular beam epitaxy" *J. Elec. Mater.*, vol. 30, pp. 162-169, 2001.
- [66] M. Haerberlen, D. Zhu, C. McAleese, M. J. Kappers, and C. J. Humphreys, "Dislocation reduction in MOVPE grown GaN layers on (111)Si using SiNx and AlGaIn layers," *Journal of Physics: Conference Series*, vol. 209, p. 012017, 2010.
- [67] H.-Y. Shin, S. K. Kwon, Y. I. Chang, M. J. Cho, and K. H. Park, "Reducing dislocation density in GaN films using a cone-shaped patterned sapphire substrate," *J. Cryst. Growth*, vol. 311, pp. 4167-4170, 2009.
- [68] B. Monemar and B. E. Sernelius, "Defect related issues in the "current roll-off" in InGaIn based light emitting diodes," *Appl. Phys. Lett.*, vol. 91, p. 181103, 2007.
- [69] M. Meneghini, N. Trivellin, G. Meneghesso, E. Zanoni, U. Zehnder, and B. Hahn, "A combined electro-optical method for the determination of the recombination parameters in InGaIn-based light-emitting diodes," *J. Appl. Phys.*, vol. 106, p. 114508, 2009.
- [70] K. A. Bulashevich and S. Y. Karpov, "Is Auger recombination responsible for the efficiency rollover in III-nitride light-emitting diodes?," *Phys. Status Solidi C*, vol. 5, pp. 2066-2069, 2008.
- [71] M.-H. Kim, M. F. Schubert, Q. Dai, J. K. Kim, E. F. Schubert, J. Piprek, *et al.*, "Origin of efficiency droop in GaN-based light-emitting diodes," *Appl. Phys. Lett.*, vol. 91, p. 183507, 2007.
- [72] A. Laubsch, M. Sabathil, J. Baur, M. Peter, and B. Hahn, "High-Power and High-Efficiency InGaIn-Based Light Emitters," *IEEE Trans. Electron Devices*, vol. 57, pp. 79-87, 2010.
- [73] A. Laubsch, M. Sabathil, W. Bergbauer, M. Strassburg, H. Lugauer, M. Peter, *et al.*, "On the origin of IQE-'droop' in InGaIn LEDs," *Phys. Status Solidi C*, vol. 6, pp. S913-S916, 2009.
- [74] J. Xie, X. Ni, Q. Fan, R. Shimada, U. m. Özgür, and H. Morkoç, "On the efficiency droop in InGaIn multiple quantum well blue light emitting diodes and its reduction with p-doped quantum well barriers," *Appl. Phys. Lett.*, vol. 93, p. 121107, 2008.
- [75] M. Zhang, P. Bhattacharya, J. Singh, and J. Hinckley, "Direct measurement of auger recombination in In_{0.1}Ga_{0.9}N/GaN quantum wells and its impact on the efficiency of In_{0.1}Ga_{0.9}N/GaN multiple quantum well light emitting diodes," *Appl. Phys. Lett.*, vol. 95, p. 201108, 2009.
- [76] W. Guo, M. Zhang, A. Banerjee, and P. Bhattacharya, "Catalyst-free InGaIn/GaN nanowire light emitting diodes grown on (001) silicon by molecular beam epitaxy," *Nano Lett.*, vol. 10, pp. 3355-9, Sep 8 2010.
- [77] H. P. Nguyen, K. Cui, S. Zhang, M. Djavid, A. Korinek, G. A. Botton, *et al.*, "Controlling electron overflow in phosphor-free InGaIn/GaN nanowire white light-emitting diodes," *Nano Lett.*, vol. 12, pp. 1317-23, Mar 14 2012.
- [78] J. Piprek and S. Li, "Electron leakage effects on GaN-based light-emitting diodes," *Opt. Quant. Electron.*, vol. 42, pp. 89-95, 2011.
- [79] C. H. Wang, J. R. Chen, C. H. Chiu, H. C. Kuo, Y. L. Li, T. C. Lu, *et al.*, "Temperature-Dependent Electroluminescence Efficiency in Blue InGaIn-GaN Light-Emitting Diodes With Different Well Widths," *IEEE Photon. Technol. Lett.*, vol. 22, pp. 236-238, 2010.

- [80] J. Wang, L. Wang, W. Zhao, Z. Hao, and Y. Luo, "Understanding efficiency droop effect in InGaN/GaN multiple-quantum-well blue light-emitting diodes with different degree of carrier localization," *Appl. Phys. Lett.*, vol. 97, p. 201112, 2010.
- [81] S. Nakamura, T. Mukai, and M. Senoh, "In situ monitoring and Hall measurements of GaN grown with GaN buffer layers," *J. Appl. Phys.*, vol. 71, p. 5543, 1992.
- [82] N. I. S. Nakamura, M. Senoh, T. Mukai, "Hole Compensation Mechanism of P-Type GaN Films," *Jpn. J. Appl. Phys.*, vol. 31, pp. 1258-1266, 1992.
- [83] G. Namkoong, E. Trybus, K. K. Lee, M. Moseley, W. A. Doolittle, and D. C. Look, "Metal modulation epitaxy growth for extremely high hole concentrations above 10^{19} cm⁻³ in GaN," *Appl. Phys. Lett.*, vol. 93, p. 172112, 2008.
- [84] M. Zhang, P. Bhattacharya, W. Guo, and A. Banerjee, "Mg doping of GaN grown by plasma-assisted molecular beam epitaxy under nitrogen-rich conditions," *Appl. Phys. Lett.*, vol. 96, p. 132103, 2010.
- [85] M. Kneissl, "A Brief Review of III-Nitride UV Emitter Technologies and Their Applications," in *III-Nitride Ultraviolet Emitters Technology and Applications*. M. Kneissl and J. Rass, Ed., ed: Springer, 2016.
- [86] F. Brunner, H. Protzmann, M. Heuken, A. Knauer, M. Weyers, and M. Kneissl, "High-temperature growth of AlN in a production scale $11 \times 2'$ MOVPE reactor," *Phys. Status Solidi C*, vol. 5, pp. 1799-1801, 2008.
- [87] O. Reentilä, F. Brunner, A. Knauer, A. Mogilatenko, W. Neumann, H. Protzmann, *et al.*, "Effect of the AlN nucleation layer growth on AlN material quality," *J. Cryst. Growth*, vol. 310, pp. 4932-4934, 2008.
- [88] V. Kueller, A. Knauer, F. Brunner, A. Mogilatenko, M. Kneissl, and M. Weyers, "Investigation of inversion domain formation in AlN grown on sapphire by MOVPE," *Phys. Status Solidi C*, vol. 9, pp. 496-498, 2012.
- [89] S. F. Chichibu, A. Uedono, T. Onuma, B. A. Haskell, A. Chakraborty, T. Koyama, *et al.*, "Origin of defect-insensitive emission probability in In-containing (Al,In,Ga)N alloy semiconductors," *Nat Mater*, vol. 5, pp. 810-6, Oct 2006.
- [90] S. Y. Karpov and Y. N. Makarov, "Dislocation effect on light emission efficiency in gallium nitride," *Appl. Phys. Lett.*, vol. 81, p. 4721, 2002.
- [91] M. I. Satoshi Kamiyama, Nobuaki Hayashib, Tetsuya Takeuchib, Hiroshi Amano, c, Isamu Akasakia, c, Satoshi Watanabed, Yawara Kanekod, Norihide Yamadad, "Low-temperature-deposited AlGaIn interlayer for improvement of AlGaIn/GaN heterostructure" *J. Cryst. Growth*, vol. 223, pp. 83-91, 2000.
- [92] J. Han, K. E. Waldrip, S. R. Lee, J. J. Figiel, S. J. Hearne, G. A. Petersen, *et al.*, "Control and elimination of cracking of AlGaIn using low-temperature AlGaIn interlayers," *Appl. Phys. Lett.*, vol. 78, p. 67, 2001.
- [93] M. Asif Khan, J. N. Kuznia, D. T. Olson, T. George, and W. T. Pike, "GaIn/AlN digital alloy short-period superlattices by switched atomic layer metalorganic chemical vapor deposition," *Appl. Phys. Lett.*, vol. 63, p. 3470, 1993.
- [94] M. Asif Khan, J. N. Kuznia, R. A. Skogman, D. T. Olson, M. Mac Millan, and W. J. Choyke, "Low pressure metalorganic chemical vapor deposition of AlN over sapphire substrates," *Appl. Phys. Lett.*, vol. 61, p. 2539, 1992.

- [95] M. Asif Khan, R. A. Skogman, J. M. Van Hove, D. T. Olson, and J. N. Kuznia, "Atomic layer epitaxy of GaN over sapphire using switched metalorganic chemical vapor deposition," *Appl. Phys. Lett.*, vol. 60, p. 1366, 1992.
- [96] K. Hiramatsu, "Epitaxial lateral overgrowth techniques used in group III nitride epitaxy," *J. Phys.: Condens. Matter*, vol. 13, pp. 6961–6975, 2001.
- [97] Z. R. Zytewicz, "Laterally overgrown structures as substrates for lattice mismatched epitaxy" *Thin Solid Films*, vol. 412, pp. 64-75, 2002.
- [98] O.-H. Nam, M. D. Bremser, T. S. Zheleva, and R. F. Davis, "Lateral epitaxy of low defect density GaN layers via organometallic vapor phase epitaxy," *Appl. Phys. Lett.*, vol. 71, p. 2638, 1997.
- [99] M. Kim, T. Fujita, S. Fukahori, T. Inazu, C. Pernot, Y. Nagasawa, *et al.*, "AlGa_N-Based Deep Ultraviolet Light-Emitting Diodes Fabricated on Patterned Sapphire Substrates," *Applied Physics Express*, vol. 4, p. 092102, 2011.
- [100] P. Dong, J. Yan, J. Wang, Y. Zhang, C. Geng, T. Wei, *et al.*, "282-nm AlGa_N-based deep ultraviolet light-emitting diodes with improved performance on nano-patterned sapphire substrates," *Appl. Phys. Lett.*, vol. 102, p. 241113, 2013.
- [101] V. Kueller, A. Knauer, C. Reich, A. Mogilatenko, M. Weyers, J. Stellmach, *et al.*, "Modulated Epitaxial Lateral Overgrowth of AlN for Efficient UV LEDs," *IEEE Photon. Technol. Lett.*, vol. 24, pp. 1603-1605, 2012.
- [102] M. L. Nakarmi, K. H. Kim, M. Khizar, Z. Y. Fan, J. Y. Lin, and H. X. Jiang, "Electrical and optical properties of Mg-doped Al_{0.7}Ga_{0.3}N alloys," *Appl. Phys. Lett.*, vol. 86, p. 092108, 2005.
- [103] K. B. Nam, M. L. Nakarmi, J. Li, J. Y. Lin, and H. X. Jiang, "Mg acceptor level in AlN probed by deep ultraviolet photoluminescence," *Appl. Phys. Lett.*, vol. 83, p. 878, 2003.
- [104] V. P. John Simon, Chuanxin Lian, Huili Xing, Debdeep Jena, "Polarization-Induced Hole Doping in Wide-Band-Gap Uniaxial Semiconductor Heterostructures" *Science*, vol. 327, 2010.
- [105] M. L. Nakarmi, N. Nepal, J. Y. Lin, and H. X. Jiang, "Photoluminescence studies of impurity transitions in Mg-doped AlGa_N alloys," *Appl. Phys. Lett.*, vol. 94, p. 091903, 2009.
- [106] X. T. Trinh, D. Nilsson, I. G. Ivanov, E. Janzén, A. Kakanakova-Georgieva, and N. T. Son, "Stable and metastable Si negative-U centers in AlGa_N and AlN," *Appl. Phys. Lett.*, vol. 105, p. 162106, 2014.
- [107] A. Kakanakova-Georgieva, D. Nilsson, X. T. Trinh, U. Forsberg, N. T. Son, and E. Janzén, "The complex impact of silicon and oxygen on the n-type conductivity of high-Al-content AlGa_N," *Appl. Phys. Lett.*, vol. 102, p. 132113, 2013.
- [108] J. R. Grandusky, J. A. Smart, M. C. Mendrick, L. J. Schowalter, K. X. Chen, and E. F. Schubert, "Pseudomorphic growth of thick n-type Al_xGa_{1-x}N layers on low-defect-density bulk AlN substrates for UV LED applications," *J. Cryst. Growth*, vol. 311, pp. 2864-2866, 2009.
- [109] B. Cheng, S. Choi, J. E. Northrup, Z. Yang, C. Knollenberg, M. Teepe, *et al.*, "Enhanced vertical and lateral hole transport in high aluminum-containing AlGa_N for deep ultraviolet light emitters," *Appl. Phys. Lett.*, vol. 102, p. 231106, 2013.

- [110] A. A. Allerman, M. H. Crawford, M. A. Miller, and S. R. Lee, "Growth and characterization of Mg-doped AlGa_N-AlN short-period superlattices for deep-UV optoelectronic devices," *J. Cryst. Growth*, vol. 312, pp. 756-761, 2010.
- [111] M. L. Nakarmi, K. H. Kim, J. Li, J. Y. Lin, and H. X. Jiang, "Enhanced p-type conduction in GaN and AlGa_N by Mg- δ -doping," *Appl. Phys. Lett.*, vol. 82, p. 3041, 2003.
- [112] T. Kolbe, F. Mehnke, M. Guttman, C. Kuhn, J. Rass, T. Wernicke, *et al.*, "Improved injection efficiency in 290 nm light emitting diodes with Al(Ga)_N electron blocking heterostructure," *Appl. Phys. Lett.*, vol. 103, p. 031109, 2013.
- [113] F. Mehnke, C. Kuhn, M. Guttman, C. Reich, T. Kolbe, V. Kueller, *et al.*, "Efficient charge carrier injection into sub-250 nm AlGa_N multiple quantum well light emitting diodes," *Appl. Phys. Lett.*, vol. 105, p. 051113, 2014.
- [114] H. Hirayama, Y. Tsukada, T. Maeda, and N. Kamata, "Marked Enhancement in the Efficiency of Deep-Ultraviolet AlGa_N Light-Emitting Diodes by Using a Multiquantum-Barrier Electron Blocking Layer," *Appl. Phys. Express*, vol. 3, p. 031002, 2010.
- [115] K. B. Asif Khan, Tom Katona, "Ultraviolet light-emitting diodes based on group three nitrides" *Nat. Photon.*, vol. 2, 2008.
- [116] V. Adivarahan, A. Heidari, B. Zhang, Q. Fareed, S. Hwang, M. Islam, *et al.*, "280 nm Deep Ultraviolet Light Emitting Diode Lamp with an AlGa_N Multiple Quantum Well Active Region," *Appl. Phys. Express*, vol. 2, p. 102101, 2009.
- [117] L. Zhou, J. E. Epler, M. R. Krames, W. Goetz, M. Gherasimova, Z. Ren, *et al.*, "Vertical injection thin-film AlGa_N/AlGa_N multiple-quantum-well deep ultraviolet light-emitting diodes," *Appl. Phys. Lett.*, vol. 89, p. 241113, 2006.
- [118] T. N. Oder, K. H. Kim, J. Y. Lin, and H. X. Jiang, "III-nitride blue and ultraviolet photonic crystal light emitting diodes," *Appl. Phys. Lett.*, vol. 84, p. 466, 2004.
- [119] T. Gessmann, E. F. Schubert, J. W. Graff, K. Streubel, and C. Karnutsch, "Omnidirectional reflective contacts for light-emitting diodes," *IEEE Electron Device Letters*, vol. 24, pp. 683-685, 2003.
- [120] N. Lobo, H. Rodriguez, A. Knauer, M. Hoppe, S. Einfeldt, P. Vogt, *et al.*, "Enhancement of light extraction in ultraviolet light-emitting diodes using nanopixel contact design with Al reflector," *Appl. Phys. Lett.*, vol. 96, p. 081109, 2010.
- [121] J. Li, K. B. Nam, M. L. Nakarmi, J. Y. Lin, H. X. Jiang, P. Carrier, *et al.*, "Band structure and fundamental optical transitions in wurtzite AlN," *Appl. Phys. Lett.*, vol. 83, p. 5163, 2003.
- [122] K. B. Nam, J. Li, M. L. Nakarmi, J. Y. Lin, and H. X. Jiang, "Unique optical properties of AlGa_N alloys and related ultraviolet emitters," *Appl. Phys. Lett.*, vol. 84, p. 5264, 2004.
- [123] R. G. Banal, M. Funato, and Y. Kawakami, "Optical anisotropy in [0001]-oriented Al_xGa_{1-x}N/AlN quantum wells ($x > 0.69$)," *Phys. Rev. B*, vol. 79, 2009.
- [124] H. Kawanishi, M. Senuma, and T. Nukui, "Anisotropic polarization characteristics of lasing and spontaneous surface and edge emissions from deep-ultraviolet ($\lambda \approx 240$ nm) AlGa_N multiple-quantum-well lasers," *Appl. Phys. Lett.*, vol. 89, p. 041126, 2006.
- [125] H. Kawanishi, M. Senuma, M. Yamamoto, E. Niikura, and T. Nukui, "Extremely weak surface emission from (0001) c-plane AlGa_N multiple quantum well structure in deep-ultraviolet spectral region," *Appl. Phys. Lett.*, vol. 89, p. 081121, 2006.
- [126] T. Kolbe, A. Knauer, C. Chua, Z. Yang, S. Einfeldt, P. Vogt, *et al.*, "Optical polarization characteristics of ultraviolet (In)(Al)Ga_N multiple quantum well light emitting diodes," *Appl. Phys. Lett.*, vol. 97, p. 171105, 2010.

- [127] J. C. J. Heon-Jin Choi, Rongrui He, Sang-Kwon Lee, Franklin Kim, Peter Pauzauskie, Joshua Goldberger, Richard J. Saykally, Peidong Yang, "Self-Organized GaN Quantum Wire UV Lasers," *J. Phys. Chem. B*, vol. 107, pp. 8721-8725, 2003.
- [128] B. T. Yajie Dong, Thomas J. Kempa, Charles M. Lieber, "Coaxial Group III-Nitride Nanowire Photovoltaics," *Nano Lett.*, vol. 9, pp. 2183-2187, 2009.
- [129] S. G. a. Fang Qian, Yat Li, Cheng-Yen Wen, Charles M. Lieber, "Core/Multishell Nanowire Heterostructures as Multicolor, High-Efficiency Light-Emitting Diodes," *Nano Lett.*, vol. 5, pp. 2287-2291, 2005.
- [130] S. D. Hersee, A. K. Rishinaramangalam, M. N. Fairchild, L. Zhang, and P. Varangis, "Threading defect elimination in GaN nanowires," *J. Mater. Res.*, vol. 26, pp. 2293-2298, 2011.
- [131] K. S. Nicolas Thillozen, Hilde Hardtdegen, Ralph Meijers, Raffaella Calarco, Simone Montanari, Nicoleta Kaluza, Jurgen Gutowski, Hans Luth, "The State of Strain in Single GaN Nanocolumns As Derived from Micro-Photoluminescence Measurements " *Nano Lett.*, vol. 6, pp. 704-708, 2006.
- [132] E. Ertekin, P. A. Greaney, D. C. Chrzan, and T. D. Sands, "Equilibrium limits of coherency in strained nanowire heterostructures," *J. Appl. Phys.*, vol. 97, p. 114325, 2005.
- [133] F. Glas, "Critical dimensions for the plastic relaxation of strained axial heterostructures in free-standing nanowires," *Phys. Rev. B*, vol. 74, 2006.
- [134] H. P. Nguyen, S. Zhang, K. Cui, X. Han, S. Fatholouloumi, M. Couillard, *et al.*, "p-Type modulation doped InGaN/GaN dot-in-a-wire white-light-emitting diodes monolithically grown on Si(111)," *Nano Lett.*, vol. 11, pp. 1919-24, May 11 2011.
- [135] J. Verma, P. K. Kandaswamy, V. Protasenko, A. Verma, H. Grace Xing, and D. Jena, "Tunnel-injection GaN quantum dot ultraviolet light-emitting diodes," *Appl. Phys. Lett.*, vol. 102, p. 041103, 2013.
- [136] A. T. Sarwar, S. D. Carnevale, F. Yang, T. F. Kent, J. J. Jamison, D. W. McComb, *et al.*, "Semiconductor Nanowire Light-Emitting Diodes Grown on Metal: A Direction Toward Large-Scale Fabrication of Nanowire Devices," *Small*, vol. 11, pp. 5402-8, Oct 28 2015.
- [137] M. Wolz, C. Hauswald, T. Flissikowski, T. Gotschke, S. Fernandez-Garrido, O. Brandt, *et al.*, "Epitaxial Growth of GaN Nanowires with High Structural Perfection on a Metallic TiN Film," *Nano Lett.*, vol. 15, pp. 3743-7, Jun 10 2015.
- [138] C. Zhao, T. K. Ng, N. Wei, A. Prabaswara, M. S. Alias, B. Janjua, *et al.*, "Facile Formation of High-Quality InGaN/GaN Quantum-Disks-in-Nanowires on Bulk-Metal Substrates for High-Power Light-Emitters," *Nano Lett.*, vol. 16, pp. 1056-63, Feb 10 2016.
- [139] K. Goodman, V. Protasenko, J. Verma, T. Kosel, G. Xing, and D. Jena, "Molecular beam epitaxial growth of gallium nitride nanowires on atomic layer deposited aluminum oxide," *J. Cryst. Growth*, vol. 334, pp. 113-117, 2011.
- [140] S. Zhao, M. G. Kibria, Q. Wang, H. P. Nguyen, and Z. Mi, "Growth of large-scale vertically aligned GaN nanowires and their heterostructures with high uniformity on SiO(x) by catalyst-free molecular beam epitaxy," *Nanoscale*, vol. 5, pp. 5283-7, Jun 21 2013.
- [141] H. P. Nguyen, S. Zhang, A. T. Connie, M. G. Kibria, Q. Wang, I. Shih, *et al.*, "Breaking the carrier injection bottleneck of phosphor-free nanowire white light-emitting diodes," *Nano Lett.*, vol. 13, pp. 5437-42, 2013.
- [142] L. Esaki, "New Phenomenon in Narrow Germanium-p-n Junctions," *Phys. Rev.*, vol. 109, pp. 603-604, 1958.

- [143] S. K. Siddharth Rajan, and Fatih Akyol, "Gallium Nitride-Based Interband Tunnel Junctions" in *Gallium Nitride (GaN): Physics, Devices, and Technology*, F. Medjdoub, Ed., ed: CRC Press, 2015.
- [144] S.-J. Chang, W.-H. Lin, and W.-S. Chen, "Cascaded GaN Light-Emitting Diodes With Hybrid Tunnel Junction Layers," *IEEE J. Quant. Electron.*, vol. 51, pp. 1-5, 2015.
- [145] F. Akyol, S. Krishnamoorthy, and S. Rajan, "Tunneling-based carrier regeneration in cascaded GaN light emitting diodes to overcome efficiency droop," *Appl. Phys. Lett.*, vol. 103, p. 081107, 2013.
- [146] M. Yamaguchi, T. Takamoto, K. Araki, and N. Ekins-Daukes, "Multi-junction III–V solar cells: current status and future potential," *Sol. Energ.*, vol. 79, pp. 78-85, 2005.
- [147] S.-R. Jeon, Y.-H. Song, H.-J. Jang, G. M. Yang, S. W. Hwang, and S. J. Son, "Lateral current spreading in GaN-based light-emitting diodes utilizing tunnel contact junctions," *Appl. Phys. Lett.*, vol. 78, p. 3265, 2001.
- [148] U. K. M. M. J. Grundmann, "Multi-color light emitting diode using polarization-induced tunnel junctions" *Phys. Status Solidi C*, vol. 4, pp. 2830–2833, 2007.
- [149] J. Simon, Z. Zhang, K. Goodman, H. Xing, T. Kosel, P. Fay, *et al.*, "Polarization-Induced Zener Tunnel Junctions in Wide-Band-Gap Heterostructures," *Phys. Rev. Lett.*, vol. 103, 2009.
- [150] K. Zhang, H. Liang, Y. Liu, R. Shen, W. Guo, D. Wang, *et al.*, "Low Al-composition p-GaN/Mg-doped Al_{0.25}Ga_{0.75}N/n⁺-GaN polarization-induced backward tunneling junction grown by metal-organic chemical vapor deposition on sapphire substrate," *Sci Rep*, vol. 4, p. 6322, Sep 10 2014.
- [151] K. Zhang, H. Liang, R. Shen, D. Wang, P. Tao, Y. Liu, *et al.*, "Negative differential resistance in low Al-composition p-GaN/Mg-doped Al_{0.15}Ga_{0.85}N/n⁺-GaN hetero-junction grown by metal-organic chemical vapor deposition on sapphire substrate," *Appl. Phys. Lett.*, vol. 104, p. 053507, 2014.
- [152] X. Guo, G.-D. Shen, Y. Ji, X.-Z. Wang, J.-Y. Du, D.-S. Zou, *et al.*, "Thermal property of tunnel-regenerated multiactive-region light-emitting diodes," *Appl. Phys. Lett.*, vol. 82, p. 4417, 2003.
- [153] I. Ozden, E. Makarona, A. V. Nurmikko, T. Takeuchi, and M. Krames, "A dual-wavelength indium gallium nitride quantum well light emitting diode," *Appl. Phys. Lett.*, vol. 79, p. 2532, 2001.
- [154] X. Guo, G.-D. Shen, G.-H. Wang, W.-J. Zhu, J.-Y. Du, G. Gao, *et al.*, "Tunnel-regenerated multiple-active-region light-emitting diodes with high efficiency," *Appl. Phys. Lett.*, vol. 79, p. 2985, 2001.
- [155] J. Piprek, "Blue light emitting diode exceeding 100% quantum efficiency," *Phys. Status Solidi (RRL) - Rapid Res. Lett.*, vol. 8, pp. 424-426, 2014.
- [156] J. Piprek, "Origin of InGaN/GaN light-emitting diode efficiency improvements using tunnel-junction-cascaded active regions," *Appl. Phys. Lett.*, vol. 104, p. 051118, 2014.
- [157] J. S. O. Ambacher, J. R. Shealy, N. G. Weimann, K. Chu, M. Murphy, W. J. Schaff, L. F. Eastman, R. Dimitrov, L. Wittmer, M. Stutzmann, W. Rieger, J. Hilsenbeck, "Two-dimensional electron gases induced by spontaneous and piezoelectric polarization charges in N- and Ga-face AlGaIn/GaN heterostructures" *J. Appl. Phys.*, vol. 85, p. 3222, 1999.

- [158] O. Ambacher, "Growth and applications of Group III-nitrides," *J. Phys. D: Appl. Phys.*, vol. 31, 1998.
- [159] R. D. O. Ambacher, M. Stutzmann, B. E. Foutz, M. J. Murphy, J. A. Smart, J. R. Shealy, N. G. Weimann, K. Chu, M. Chumbes, B. Green, A. J. Sierakowski, W. J. Schaff and L. F. Eastman, "Role of Spontaneous and Piezoelectric Polarization Induced Effects in Group-III Nitride Based Heterostructures and Devices," *Phys. Status Solidi B*, 1999.
- [160] J. S. O. Ambacher, J. R. Shealy, N. G. Weimann, K. Chu, M. Murphy, W. J. Schaff, L. F. Eastman, R. Dimitrov, L. Wittmer, M. Stutzmann, W. Rieger, J. Hilsenbeck, "Two-dimensional electron gases induced by spontaneous and piezoelectric polarization charges in N- and Ga-face AlGa_N/Ga_N heterostructures" *J. Appl. Phys.*, vol. 85, p. 3222, 1999.
- [161] F. Bernardini and V. Fiorentini, "Nonlinear macroscopic polarization in III-V nitride alloys," *Phys. Rev. B*, vol. 64, 2001.
- [162] F. B. a. V. Fiorentini, "Macroscopic polarization and band offsets at nitride heterojunctions," *Phys. Rev. B*, vol. 57, p. 9427, 1998.
- [163] A. E. Romanov, T. J. Baker, S. Nakamura, J. S. Speck, and E. J. U. Group, "Strain-induced polarization in wurtzite III-nitride semipolar layers," *J. Appl. Phys.*, vol. 100, p. 023522, 2006.
- [164] F. B. Vincenzo Fiorentini, "Effects of macroscopic polarization in III-V nitride multiple quantum wells," *Phys. Rev. B*, vol. 60, p. 8849, 1999.
- [165] L. F. E. a. U. K. Mishra, "The toughest transistor yet (Ga_N transistors)," *IEEE Spectrum* vol. 39, pp. 28-33, 2002.
- [166] O. Ambacher, B. Foutz, J. Smart, J. R. Shealy, N. G. Weimann, K. Chu, *et al.*, "Two dimensional electron gases induced by spontaneous and piezoelectric polarization in undoped and doped AlGa_N/Ga_N heterostructures," *J. Appl. Phys.*, vol. 87, p. 334, 2000.
- [167] J. P. Ibbetson, P. T. Fini, K. D. Ness, S. P. DenBaars, J. S. Speck, and U. K. Mishra, "Polarization effects, surface states, and the source of electrons in AlGa_N/Ga_N heterostructure field effect transistors," *Appl. Phys. Lett.*, vol. 77, p. 250, 2000.
- [168] I. P. Smorchkova, C. R. Elsass, J. P. Ibbetson, R. Vetury, B. Heying, P. Fini, *et al.*, "Polarization-induced charge and electron mobility in AlGa_N/Ga_N heterostructures grown by plasma-assisted molecular-beam epitaxy," *J. Appl. Phys.*, vol. 86, p. 4520, 1999.
- [169] V. T. Lester F. Eastman, J. Smart, Bruce M. Green, Eduardo M. Chumbes, Roman Dimitrov, Hyungtak Kim, Oliver S. Ambacher, N. Weimann, T. Prunty, Michael Murphy, William J. Schaff, and James R. Shealy, "Undoped AlGa_N/Ga_N HEMTs for Microwave Power Amplification" *IEEE Trans. Electron Devices*, vol. 48, 2002.
- [170] M. Singh, Y. Zhang, J. Singh, and U. Mishra, "Examination of tunnel junctions in the AlGa_N/Ga_N system: Consequences of polarization charge," *Appl. Phys. Lett.*, vol. 77, p. 1867, 2000.
- [171] J. Simon, Z. Zhang, K. Goodman, H. Xing, T. Kosel, P. Fay, *et al.*, "Polarization-induced Zener tunnel junctions in wide-band-gap heterostructures," *Phys. Rev. Lett.*, vol. 103, p. 026801, Jul 10 2009.
- [172] C. Wetzel, T. Takeuchi, H. Amano, and I. Akasaki, "Piezoelectric Franz-Keldysh effect in strained GaInN/Ga_N heterostructures," *J. Appl. Phys.*, vol. 85, p. 3786, 1999.
- [173] M. F. Schubert, "Interband tunnel junctions for wurtzite III-nitride semiconductors based on heterointerface polarization charges," *Phys. Rev. B*, vol. 81, 2010.

- [174] T. Frost, S. Jahangir, E. Stark, S. Deshpande, A. Hazari, C. Zhao, *et al.*, "Monolithic electrically injected nanowire array edge-emitting laser on (001) silicon," *Nano Lett.*, vol. 14, pp. 4535-41, Aug 13 2014.
- [175] F. Gonzalez-Posada, R. Songmuang, M. Den Hertog, and E. Monroy, "Room-temperature photodetection dynamics of single GaN nanowires," *Nano Lett.*, vol. 12, pp. 172-6, Jan 11 2012.
- [176] L. Rigutti, M. Tchernycheva, A. De Luna Bugallo, G. Jacopin, F. H. Julien, L. F. Zagonel, *et al.*, "Ultraviolet photodetector based on GaN/AlN quantum disks in a single nanowire," *Nano Lett.*, vol. 10, pp. 2939-43, Aug 11 2010.
- [177] T. J. K. a. C. M. L. Bozhi Tian, "Single nanowire photovoltaics," *Chem. Soc. Rev.*, vol. 38, pp. 16-24, 2008.
- [178] Z. H. C. Y. B. Tang, H. S. Song, C. S. Lee, H. T. Cong, H. M. Cheng, W. J. Zhang, I. Bello, and S. T. Lee, "Vertically Aligned p-Type Single-Crystalline GaN Nanorod Arrays on n-Type Si for Heterojunction Photovoltaic Cells" *Nano Lett.*, vol. 8, pp. 4191-4195, 2008.
- [179] B. J. May, A. T. M. G. Sarwar, and R. C. Myers, "Nanowire LEDs grown directly on flexible metal foil," *Appl. Phys. Lett.*, vol. 108, p. 141103, 2016.
- [180] S. Li and A. Waag, "GaN based nanorods for solid state lighting," *J. Appl. Phys.*, vol. 111, p. 071101, 2012.
- [181] S. Fernández-Garrido, J. Grandal, E. Calleja, M. A. Sánchez-García, and D. López-Romero, "A growth diagram for plasma-assisted molecular beam epitaxy of GaN nanocolumns on Si(111)," *J. Appl. Phys.*, vol. 106, p. 126102, 2009.
- [182] V. G. Dubrovskii, V. Consonni, A. Trampert, L. Geelhaar, and H. Riechert, "Scaling thermodynamic model for the self-induced nucleation of GaN nanowires," *Phys. Rev. B*, vol. 85, 2012.
- [183] V. Consonni, M. Hanke, M. Knelangen, L. Geelhaar, A. Trampert, and H. Riechert, "Nucleation mechanisms of self-induced GaN nanowires grown on an amorphous interlayer," *Phys. Rev. B*, vol. 83, 2011.
- [184] V. Consonni, "Self-induced growth of GaN nanowires by molecular beam epitaxy: A critical review of the formation mechanisms," *Phys. Status Solidi (RRL) - Rapid Res. Lett.*, vol. 7, pp. 699-712, 2013.
- [185] R. J. M. R. Calarco, R. K. Debnath, T. Stoica, E. Sutter, H. Lüth, "Nucleation and growth of GaN nanowires on Si(111) performed by molecular beam epitaxy" *Nano Lett.*, vol. 7, 2007.
- [186] J. Ristić, E. Calleja, S. Fernández-Garrido, L. Cerutti, A. Trampert, U. Jahn, *et al.*, "On the mechanisms of spontaneous growth of III-nitride nanocolumns by plasma-assisted molecular beam epitaxy," *J. Cryst. Growth*, vol. 310, pp. 4035-4045, 2008.
- [187] R. K. Debnath, R. Meijers, T. Richter, T. Stoica, R. Calarco, and H. Lüth, "Mechanism of molecular beam epitaxy growth of GaN nanowires on Si(111)," *Appl. Phys. Lett.*, vol. 90, p. 123117, 2007.
- [188] C. Chèze, L. Geelhaar, B. Jenichen, and H. Riechert, "Different growth rates for catalyst-induced and self-induced GaN nanowires," *Appl. Phys. Lett.*, vol. 97, p. 153105, 2010.
- [189] V. Consonni, V. G. Dubrovskii, A. Trampert, L. Geelhaar, and H. Riechert, "Quantitative description for the growth rate of self-induced GaN nanowires," *Phys. Rev. B*, vol. 85, 2012.

- [190] S. Fernandez-Garrido, V. M. Kaganer, K. K. Sabelfeld, T. Gotschke, J. Grandal, E. Calleja, *et al.*, "Self-regulated radius of spontaneously formed GaN nanowires in molecular beam epitaxy," *Nano Lett.*, vol. 13, pp. 3274-80, Jul 10 2013.
- [191] M. Tchernycheva, C. Sartel, G. Cirlin, L. Travers, G. Patriarche, J. C. Harmand, *et al.*, "Growth of GaN free-standing nanowires by plasma-assisted molecular beam epitaxy: structural and optical characterization," *Nanotechnology*, vol. 18, p. 385306, 2007.
- [192] R. Songmuang, O. Landré, and B. Daudin, "From nucleation to growth of catalyst-free GaN nanowires on thin AlN buffer layer," *Appl. Phys. Lett.*, vol. 91, p. 251902, 2007.
- [193] K. A. Bertness, A. Roshko, L. M. Mansfield, T. E. Harvey, and N. A. Sanford, "Mechanism for spontaneous growth of GaN nanowires with molecular beam epitaxy," *J. Cryst. Growth*, vol. 310, pp. 3154-3158, 2008.
- [194] V. Consonni, M. Knelangen, U. Jahn, A. Trampert, L. Geelhaar, and H. Riechert, "Effects of nanowire coalescence on their structural and optical properties on a local scale," *Appl. Phys. Lett.*, vol. 95, p. 241910, 2009.
- [195] S. Fernandez-Garrido, V. M. Kaganer, C. Hauswald, B. Jenichen, M. Ramsteiner, V. Consonni, *et al.*, "Correlation between the structural and optical properties of spontaneously formed GaN nanowires: a quantitative evaluation of the impact of nanowire coalescence," *Nanotechnology*, vol. 25, p. 455702, Nov 14 2014.
- [196] K. A. Grossklaus, A. Banerjee, S. Jahangir, P. Bhattacharya, and J. M. Millunchick, "Misorientation defects in coalesced self-catalyzed GaN nanowires," *J. Cryst. Growth*, vol. 371, pp. 142-147, 2013.
- [197] F. Limbach, R. Caterino, T. Gotschke, T. Stoica, R. Calarco, L. Geelhaar, *et al.*, "The influence of Mg doping on the nucleation of self-induced GaN nanowires," *AIP Advances*, vol. 2, p. 012157, 2012.
- [198] J. Arbiol, S. Estrade, J. D. Prades, A. Cirera, F. Furtmayr, C. Stark, *et al.*, "Triple-twin domains in Mg doped GaN wurtzite nanowires: structural and electronic properties of this zinc-blende-like stacking," *Nanotechnology*, vol. 20, p. 145704, Apr 08 2009.
- [199] S. Fan, S. Zhao, X. Liu, and Z. Mi, "Study on the coalescence of dislocation-free GaN nanowires on Si and SiO₂," *J. Vac. Sci. Technol. B, Nanotechnology and Microelectronics: Materials, Processing, Measurement, and Phenomena*, vol. 32, p. 02C114, 2014.
- [200] V. Consonni, M. Knelangen, A. Trampert, L. Geelhaar, and H. Riechert, "Nucleation and coalescence effects on the density of self-induced GaN nanowires grown by molecular beam epitaxy," *Appl. Phys. Lett.*, vol. 98, p. 071913, 2011.
- [201] S. Deshpande, T. Frost, L. Yan, S. Jahangir, A. Hazari, X. Liu, *et al.*, "Formation and nature of InGa_{0.5}N quantum dots in GaN nanowires," *Nano Lett.*, vol. 15, pp. 1647-53, Mar 11 2015.
- [202] S. Zhao, S. Y. Woo, S. M. Sadaf, Y. Wu, A. Pofelski, D. A. Laleyan, *et al.*, "Molecular beam epitaxy growth of Al-rich AlGa_{0.5}N nanowires for deep ultraviolet optoelectronics," *APL Materials*, vol. 4, p. 086115, 2016.
- [203] K. H. Li, X. Liu, Q. Wang, S. Zhao, and Z. Mi, "Ultralow-threshold electrically injected AlGa_{0.5}N nanowire ultraviolet lasers on Si operating at low temperature," *Nat Nanotechnol.*, vol. 10, pp. 140-4, Feb 2015.
- [204] E. Iliopoulos and T. D. Moustakas, "Growth kinetics of AlGa_{0.5}N films by plasma-assisted molecular-beam epitaxy," *Appl. Phys. Lett.*, vol. 81, pp. 295-297, 2002.
- [205] C. Himwas, M. den Hertog, L. S. Dang, E. Monroy, and R. Songmuang, "Alloy inhomogeneity and carrier localization in AlGa_{0.5}N sections and AlGa_{0.5}N/AlN nanodisks in nanowires with 240–350 nm emission," *Appl. Phys. Lett.*, vol. 105, p. 241908, 2014.

- [206] A. Pierret, C. Bougerol, S. Murcia-Mascaros, A. Cros, H. Renevier, B. Gayral, *et al.*, "Growth, structural and optical properties of AlGa_N nanowires in the whole composition range," *Nanotechnology*, vol. 24, p. 115704, Mar 22 2013.
- [207] S. Zhao, S. Y. Woo, M. Bugnet, X. Liu, J. Kang, G. A. Botton, *et al.*, "Three-Dimensional Quantum Confinement of Charge Carriers in Self-Organized AlGa_N Nanowires: A Viable Route to Electrically Injected Deep Ultraviolet Lasers," *Nano Lett.*, vol. 15, pp. 7801-7, Dec 09 2015.
- [208] "InGa_N/Ga_N nanorod array white light-emitting diode," *Appl. Phys. Lett.*, vol. 97, p. 073101, 2010.
- [209] A. L. Bavencove, G. Tourbot, J. Garcia, Y. Desieres, P. Gilet, F. Levy, *et al.*, "Submicrometre resolved optical characterization of green nanowire-based light emitting diodes," *Nanotechnology*, vol. 22, p. 345705, Aug 26 2011.
- [210] F. Limbach, C. Hauswald, J. Lahnemann, M. Wolz, O. Brandt, A. Trampert, *et al.*, "Current path in light emitting diodes based on nanowire ensembles," *Nanotechnology*, vol. 23, p. 465301, Nov 23 2012.
- [211] M. Musolino, A. Tahraoui, F. Limbach, J. Lahnemann, U. Jahn, O. Brandt, *et al.*, "Understanding peculiarities in the optoelectronic characteristics of light emitting diodes based on (In,Ga)_N/Ga_N nanowires," *Appl. Phys. Lett.*, vol. 105, p. 083505, 2014.
- [212] E. Calleja, J. Ristić, S. Fernández-Garrido, L. Cerutti, M. A. Sánchez-García, J. Grandal, *et al.*, "Growth, morphology, and structural properties of group-III-nitride nanocolumns and nanodisks," *Phys. Status Solidi B* vol. 244, pp. 2816-2837, 2007.
- [213] T. Stoica, E. Sutter, R. J. Meijers, R. K. Debnath, R. Calarco, H. Luth, *et al.*, "Interface and wetting layer effect on the catalyst-free nucleation and growth of Ga_N nanowires," *Small*, vol. 4, pp. 751-4, Jun 2008.
- [214] S. Jahangir, M. Mandl, M. Strassburg, and P. Bhattacharya, "Molecular beam epitaxial growth and optical properties of red-emitting ($\lambda = 650$ nm) InGa_N/Ga_N disks-in-nanowires on silicon," *Appl. Phys. Lett.*, vol. 102, p. 071101, 2013.
- [215] C. Netzel, V. Hoffmann, T. Wernicke, A. Knauer, M. Weyers, M. Kneissl, *et al.*, "Temperature and excitation power dependent photoluminescence intensity of GaIn_N quantum wells with varying charge carrier wave function overlap," *J. Appl. Phys.*, vol. 107, p. 033510, 2010.
- [216] S. Watanabe, N. Yamada, M. Nagashima, Y. Ueki, C. Sasaki, Y. Yamada, *et al.*, "Internal quantum efficiency of highly-efficient In_xGa_{1-x}N-based near-ultraviolet light-emitting diodes," *Appl. Phys. Lett.*, vol. 83, p. 4906, 2003.
- [217] L. Ya-Ju, C. Ching-Hua, K. Chih Chun, L. Po Chun, L. Tien-Chang, K. Hao-Chung, *et al.*, "Study of the Excitation Power Dependent Internal Quantum Efficiency in InGa_N/Ga_N LEDs Grown on Patterned Sapphire Substrate," *IEEE J. Sel. Topics Quant. Electron.*, vol. 15, pp. 1137-1143, 2009.
- [218] S. M. Sadaf, Y. H. Ra, H. P. Nguyen, M. Djavid, and Z. Mi, "Alternating-Current InGa_N/Ga_N Tunnel Junction Nanowire White-Light Emitting Diodes," *Nano Lett.*, vol. 15, pp. 6696-701, Oct 14 2015.
- [219] M. Kaga, T. Morita, Y. Kuwano, K. Yamashita, K. Yagi, M. Iwaya, *et al.*, "GaIn_N-Based Tunnel Junctions in n-p-n Light Emitting Diodes," *Jpn. J. Appl. Phys.*, vol. 52, p. 08JH06, 2013.
- [220] S. Krishnamoorthy, F. Akyol, P. S. Park, and S. Rajan, "Low resistance Ga_N/InGa_N/Ga_N tunnel junctions," *Appl. Phys. Lett.*, vol. 102, p. 113503, 2013.

- [221] S. Krishnamoorthy, F. Akyol, and S. Rajan, "InGaN/GaN tunnel junctions for hole injection in GaN light emitting diodes," *Applied Physics Letters*, vol. 105, p. 141104, 2014.
- [222] S. Krishnamoorthy, D. N. Nath, F. Akyol, P. S. Park, M. Esposito, and S. Rajan, "Polarization-engineered GaN/InGaN/GaN tunnel diodes," *Appl. Phys. Lett.*, vol. 97, p. 203502, 2010.
- [223] S. Krishnamoorthy, P. S. Park, and S. Rajan, "Demonstration of forward inter-band tunneling in GaN by polarization engineering," *Appl. Phys. Lett.*, vol. 99, p. 233504, 2011.
- [224] Z.-H. Zhang, S. Tiam Tan, Z. Kyaw, Y. Ji, W. Liu, Z. Ju, *et al.*, "InGaN/GaN light-emitting diode with a polarization tunnel junction," *Appl. Phys. Lett.*, vol. 102, p. 193508, 2013.
- [225] S. Krishnamoorthy, T. F. Kent, J. Yang, P. S. Park, R. C. Myers, and S. Rajan, "GdN nanoisland-based GaN tunnel junctions," *Nano Lett*, vol. 13, pp. 2570-5, Jun 12 2013.
- [226] S. Zhao, A. T. Connie, M. H. Dastjerdi, X. H. Kong, Q. Wang, M. Djavid, *et al.*, "Aluminum nitride nanowire light emitting diodes: Breaking the fundamental bottleneck of deep ultraviolet light sources," *Sci. Rep.*, vol. 5, p. 8332, 2015.
- [227] S. Zhao, S. Fathololoumi, K. H. Bevan, D. P. Liu, M. G. Kibria, Q. Li, *et al.*, "Tuning the surface charge properties of epitaxial InN nanowires," *Nano letters*, vol. 12, pp. 2877-82, Jun 13 2012.
- [228] S. Zhao, B. H. Le, D. P. Liu, X. D. Liu, M. G. Kibria, T. Szkopek, *et al.*, "p-Type InN nanowires," *Nano Lett.*, vol. 13, pp. 5509-13, 2013.
- [229] Y. H. Ra, R. Navamathavan, J. H. Park, and C. R. Lee, "Coaxial In(x)Ga(1-x)N/GaN multiple quantum well nanowire arrays on Si(111) substrate for high-performance light-emitting diodes," *Nano letters*, vol. 13, pp. 3506-16, Aug 14 2013.
- [230] S. G. Fang Qian, Yat Li, Cheng-Yen Wen, and Charles M. Lieber, "Core/Multishell Nanowire Heterostructures as Multicolor, High-Efficiency Light-Emitting Diodes" *Nano Lett.*, vol. 5, pp. 2287-2291, 2005.
- [231] J. Ristić, C. Rivera, E. Calleja, S. Fernández-Garrido, M. Povoloskyi, and A. Di Carlo, "Carrier-confinement effects in nanocolumnar GaN/Al_xGa_{1-x}N quantum disks grown by molecular-beam epitaxy," *Phys. Rev. B*, vol. 72, 2005.
- [232] K. Kishino, K. Nagashima, and K. Yamano, "Monolithic Integration of InGaN-Based Nanocolumn Light-Emitting Diodes with Different Emission Colors," *Appl. Phys. Express*, vol. 6, p. 012101, 2013.
- [233] H.-W. Lin, Y.-J. Lu, H.-Y. Chen, H.-M. Lee, and S. Gwo, "InGaN/GaN nanorod array white light-emitting diode," *Appl. Phys. Lett.*, vol. 97, p. 073101, 2010.
- [234] K. Kishino and S. Ishizawa, "Selective-area growth of GaN nanocolumns on Si(111) substrates for application to nanocolumn emitters with systematic analysis of dislocation filtering effect of nanocolumns," *Nanotechnology*, vol. 26, p. 225602, Jun 5 2015.
- [235] J. Naka, Y. Inose, H. Kunugita, V. Ramesh, A. Kikuchi, K. Kishino, *et al.*, "Optical properties of InGaN/GaN nanocolumns in yellow-to-red region," *Phys. Status Solidi C*, vol. 9, pp. 2477-2480, 2012.
- [236] R. Armitage and K. Tsubaki, "Multicolour luminescence from InGaN quantum wells grown over GaN nanowire arrays by molecular-beam epitaxy," *Nanotechnology*, vol. 21, p. 195202, May 14 2010.
- [237] H. P. T. Nguyen, M. Djavid, S. Y. Woo, X. Liu, A. T. Connie, S. Sadaf, *et al.*, "Engineering the Carrier Dynamics of InGaN Nanowire White Light-Emitting Diodes by Distributed p-AlGaN Electron Blocking Layers," *Sci. Rep.*, vol. 5, p. 7744, 2015.

- [238] S. Fernandez-Garrido, X. Kong, T. Gotschke, R. Calarco, L. Geelhaar, A. Trampert, *et al.*, "Spontaneous nucleation and growth of GaN nanowires: the fundamental role of crystal polarity," *Nano Lett.*, vol. 12, pp. 6119-25, Dec 12 2012.
- [239] K. Hestroffer, C. Leclere, C. Bougerol, H. Renevier, and B. Daudin, "Polarity of GaN nanowires grown by plasma-assisted molecular beam epitaxy on Si(111)," *Phys. Rev. B*, vol. 84, 2011.
- [240] Y. Park, S. Jahangir, Y. Park, P. Bhattacharya, and J. Heo, "InGaN/GaN nanowires grown on SiO₂ and light emitting diodes with low turn on voltages," *Opt. Express*, vol. 23, pp. A650-6, Jun 1 2015.
- [241] R. Wang, X. Liu, I. Shih, and Z. Mi, "High efficiency, full-color AlInGaN quaternary nanowire light emitting diodes with spontaneous core-shell structures on Si," *Appl. Phys. Lett.*, vol. 106, p. 261104, 2015.
- [242] Y. Zhang, S. Krishnamoorthy, J. M. Johnson, F. Akyol, A. Allerman, M. W. Moseley, *et al.*, "Interband tunneling for hole injection in III-nitride ultraviolet emitters," *Appl. Phys. Lett.*, vol. 106, p. 141103, 2015.
- [243] S. Neugebauer, M. P. Hoffmann, H. Witte, J. Bläsing, A. Dadgar, A. Strittmatter, *et al.*, "All metalorganic chemical vapor phase epitaxy of p/n-GaN tunnel junction for blue light emitting diode applications," *Appl. Phys. Lett.*, vol. 110, p. 102104, 2017.
- [244] G. A. Onushkin, L. Young-Jin, Y. Jung-Ja, K. Hyung-Kun, S. Joong-Kon, P. Gil-Han, *et al.*, "Efficient Alternating Current Operated White Light-Emitting Diode Chip," *IEEE Photonics Technology Letters*, vol. 21, pp. 33-35, 2009.
- [245] H. Okumura, D. Martin, and N. Grandjean, "Low p-type contact resistance by field-emission tunneling in highly Mg-doped GaN," *Appl. Phys. Lett.*, vol. 109, p. 252101, 2016.
- [246] I. Ferguson, Y.-w. Liu, M. H. Kane, A. Jayawardena, T. R. Klein, N. Narendran, *et al.*, "Estimating the junction temperature of AC LEDs," vol. 7784, p. 778409, 2010.
- [247] H.-H. Yen, W.-Y. Yeh, and H.-C. Kuo, "GaN alternating current light-emitting device," *Phys. Status Solidi A*, vol. 204, pp. 2077-2081, 2007.
- [248] J.-H. Zhang, B.-Q. Wu, T.-M. Shih, Y.-J. Lu, Y.-L. Gao, R. Ru-Gin Chang, *et al.*, "Thermal analyses of alternating current light-emitting diodes," *Appl. Phys. Lett.*, vol. 103, p. 153505, 2013.
- [249] C. J. Palmstrm, "Epitaxy of Dissimilar Materials," *Annu. Rev. Mater. Sci.*, vol. 25, pp. 389-415, 1995.
- [250] S. Pezzagna, S. Vézian, J. Brault, and J. Massies, "Layer-by-layer epitaxial growth of Mg on GaN(0001)," *Appl. Phys. Lett.*, vol. 92, p. 233111, 2008.
- [251] Q. Z. Liu, S. S. Lau, N. R. Perkins, and T. F. Kuech, "Room temperature epitaxy of Pd films on GaN under conventional vacuum conditions," *Appl. Phys. Lett.*, vol. 69, pp. 1722-1724, 1996.
- [252] M. Missous, E. H. Rhoderick, and K. E. Singer, "Thermal stability of epitaxial Al/GaAs Schottky barriers prepared by molecular-beam epitaxy," *J. Appl. Phys.*, vol. 59, pp. 3189-3195, 1986.
- [253] J.E. Oh, P.K. Bhattacharya, J. Singh, W. Dos Passos, R. Clarke, N. Mestres, R. Merlin, K.H. Chang, R. Gibala, "Epitaxial growth and characterization of GaAs/Al/GaAs heterostructures," *Surf. Sci.*, vol. 228, pp. 16-19, 1990.

- [254] P. Krogstrup, N. L. Ziino, W. Chang, S. M. Albrecht, M. H. Madsen, E. Johnson, *et al.*, "Epitaxy of semiconductor-superconductor nanowires," *Nat Mater*, vol. 14, pp. 400-6, Apr 2015.
- [255] Q. Z. Liu, L. Shen, K. V. Smith, C. W. Tu, E. T. Yu, S. S. Lau, *et al.*, "Epitaxy of Al films on GaN studied by reflection high-energy electron diffraction and atomic force microscopy," *Appl. Phys. Lett.*, vol. 70, pp. 990-992, 1997.
- [256] T. M. Uitsu Tanaka, Katsuhiro Akimoto, "Epitaxial growth of GaN/Pd/GaN sandwich structure," *J. Cryst. Growth*, vol. 2001, pp. 444-447, 1999.
- [257] V. M. Bermudez, R. Kaplan, M. A. Khan, and J. N. Kuznia, "Growth of thin Ni films on GaN(0001)-(1×1)," *Phys. Rev. B*, vol. 48, pp. 2436-2444, 1993.
- [258] V. M. Bermudez, T. M. Jung, K. Doverspike, and A. E. Wickenden, "The growth and properties of Al and AlN films on GaN(0001)-(1×1)," *J. Appl. Phys.*, vol. 79, pp. 110-119, 1996.
- [259] S. M. Sadaf, Y. H. Ra, T. Szkopek, and Z. Mi, "Monolithically Integrated Metal/Semiconductor Tunnel Junction Nanowire Light-Emitting Diodes," *Nano Lett.*, vol. 16, pp. 1076-80, Feb 10 2016.
- [260] M. F. P.D. Browna, N. Bock, S. Marlafeka, T.S. Chengb, S.V. Novikov, C.S. Davis, R.P. Campion, C.T. Foxon, "Structural characterisation of Al grown on group III-nitride layers and sapphire by molecular beam epitaxy" *J. Cryst. Growth*, vol. 234, pp. 384-390, 2000.
- [261] R. Meijers, R. Calarco, N. Kaluza, H. Hardtdegen, M. v. d. Ahe, H. L. Bay, *et al.*, "Epitaxial growth and characterization of Fe thin films on wurtzite GaN(0001)," *J. Cryst. Growth*, vol. 283, pp. 500-507, 2005.
- [262] J. T. Leonard, E. C. Young, B. P. Yonkee, D. A. Cohen, T. Margalith, S. P. DenBaars, *et al.*, "Demonstration of a III-nitride vertical-cavity surface-emitting laser with a III-nitride tunnel junction intracavity contact," *Appl. Phys. Lett.*, vol. 107, p. 091105, 2015.
- [263] V. Kumaresan, L. Largeau, A. Madouri, F. Glas, H. Zhang, F. Oehler, *et al.*, "Epitaxy of GaN Nanowires on Graphene," *Nano Lett.*, vol. 16, pp. 4895-902, Aug 10 2016.
- [264] S. Zhao, S. M. Sadaf, S. Vanka, Y. Wang, R. Rashid, and Z. Mi, "Sub-milliwatt AlGaIn nanowire tunnel junction deep ultraviolet light emitting diodes on silicon operating at 242 nm," *Appl. Phys. Lett.*, vol. 109, p. 201106, 2016.
- [265] S. M. Sadaf, S. Zhao, Y. Wu, Y. H. Ra, X. Liu, S. Vanka, *et al.*, "An AlGaIn Core-Shell Tunnel Junction Nanowire Light-Emitting Diode Operating in the Ultraviolet-C Band," *Nano Lett.*, Jan 18 2017.
- [266] Y. H. Ra, R. Wang, S. Y. Woo, M. Djavid, S. M. Sadaf, J. Lee, *et al.*, "Full-Color Single Nanowire Pixels for Projection Displays," *Nano Lett.*, vol. 16, pp. 4608-15, Jul 13 2016.
- [267] F. Akyol, S. Krishnamoorthy, Y. Zhang, and S. Rajan, "GaN-based three-junction cascaded light-emitting diode with low-resistance InGaIn tunnel junctions," *Appl. Phys. Express*, vol. 8, p. 082103, 2015.
- [268] S. M. Sadaf, S. Zhao, Y. Wu, Y. H. Ra, X. Liu, S. Vanka, *et al.*, "An AlGaIn Core-Shell Tunnel Junction Nanowire Light-Emitting Diode Operating in the Ultraviolet-C Band," *Nano Lett.*, vol. 17, pp. 1212-1218, Feb 08 2017.
- [269] Y. Zhang, S. Krishnamoorthy, F. Akyol, A. A. Allerman, M. W. Moseley, A. M. Armstrong, *et al.*, "Design and demonstration of ultra-wide bandgap AlGaIn tunnel junctions," *Appl. Phys. Lett.*, vol. 109, p. 121102, 2016.

- [270] F. Akyol, S. Krishnamoorthy, Y. Zhang, J. Johnson, J. Hwang, and S. Rajan, "Low-resistance GaN tunnel homojunctions with 150 kA/cm² current and repeatable negative differential resistance," *Applied Physics Letters*, vol. 108, p. 131103, 2016.
- [271] M. Malinverni, D. Martin, and N. Grandjean, "InGaN based micro light emitting diodes featuring a buried GaN tunnel junction," *Appl. Phys. Lett.*, vol. 107, p. 051107, 2015.
- [272] H. Okumura, D. Martin, M. Malinverni, and N. Grandjean, "Backward diodes using heavily Mg-doped GaN growth by ammonia molecular-beam epitaxy," *Appl. Phys. Lett.*, vol. 108, p. 072102, 2016.
- [273] E. C. Young, B. P. Yonkee, F. Wu, S. H. Oh, S. P. DenBaars, S. Nakamura, *et al.*, "Hybrid tunnel junction contacts to III–nitride light-emitting diodes," *Appl. Phys. Express*, vol. 9, p. 022102, 2016.
- [274] X. Yan, W. Li, S. M. Islam, K. Pourang, H. Xing, P. Fay, *et al.*, "Polarization-induced Zener tunnel diodes in GaN/InGaN/GaN heterojunctions," *Appl. Phys. Lett.*, vol. 107, p. 163504, 2015.
- [275] Y. Zhang, S. Krishnamoorthy, F. Akyol, A. A. Allerman, M. W. Moseley, A. M. Armstrong, *et al.*, "Design of p-type cladding layers for tunnel-injected UV-A light emitting diodes," *Appl. Phys. Lett.*, vol. 109, p. 191105, 2016.
- [276] T. M. Shuji Nakamura, Masayuki Senoh, "High Power GaN P-N junction Blue Light emitting Diodes," *Jpn. J. Appl. Phys.*, vol. 30, pp. L1998-L2001, 1991.
- [277] G. Miceli and A. Pasquarello, "Self-compensation due to point defects in Mg-doped GaN," *Phys. Rev. B*, vol. 93, 2016.
- [278] T. F. Kent, S. D. Carnevale, A. T. Sarwar, P. J. Phillips, R. F. Klie, and R. C. Myers, "Deep ultraviolet emitting polarization induced nanowire light emitting diodes with Al_xGa(1-x)N active regions," *Nanotechnology*, vol. 25, p. 455201, Nov 14 2014.
- [279] D. Mahaveer Sathaiya and S. Karmalkar, "Thermionic trap-assisted tunneling model and its application to leakage current in nitrided oxides and AlGaIn/GaN high electron mobility transistors," *J. Appl. Phys.*, vol. 99, p. 093701, 2006.
- [280] S.-J. Chang, W.-H. Lin, and C.-T. Yu, "GaN-Based Multiquantum Well Light-Emitting Diodes With Tunnel-Junction-Cascaded Active Regions," *IEEE Electron Device Lett.*, vol. 36, pp. 366-368, 2015.
- [281] D. Takasuka, Y. Akatsuka, M. Ino, N. Koide, T. Takeuchi, M. Iwaya, *et al.*, "GaInN-based tunnel junctions with graded layers," *Appl. Phys. Express*, vol. 9, p. 081005, 2016.
- [282] Y. Zhang, A. A. Allerman, S. Krishnamoorthy, F. Akyol, M. W. Moseley, A. M. Armstrong, *et al.*, "Enhanced light extraction in tunnel junction-enabled top emitting UV LEDs," *Appl. Phys. Express*, vol. 9, p. 052102, 2016.
- [283] Y. Zhang, S. Krishnamoorthy, F. Akyol, S. Bajaj, A. A. Allerman, M. W. Moseley, *et al.*, "Tunnel-injected sub-260 nm ultraviolet light emitting diodes," *Appl. Phys. Lett.*, vol. 110, p. 201102, 2017.
- [284] S. M. Sadaf, Y. H. Ra, T. Szkopek, and Z. Mi, "Monolithically Integrated Metal/Semiconductor Tunnel Junction Nanowire Light-Emitting Diodes," *Nano Lett.*, vol. 16, pp. 1076-1080, 2016.
- [285] Z. Z. John Simon, Kevin Goodman, Huili Xing, Thomas Kosel, Patrick Fay, Debdeep Jena, "Polarization-Induced Zener Tunnel Junctions in Wide-Band-Gap Heterostructures," *Phys. Rev. Lett.*, vol. 103, p. 026801, 2009.
- [286] B. Monemar, P. Paskov, G. Pozina, C. Hemmingsson, J. Bergman, T. Kawashima, *et al.*, "Evidence for Two Mg Related Acceptors in GaN," *Phys. Rev. Lett.*, vol. 102, 2009.

- [287] U. K. M. Michael J. Grundmann, "Multi-color light emitting diode using polarization-induced tunnel junctions," *Phys. Status Solidi C*, vol. 4, pp. 2830–2833, 2007.
- [288] W.-H. L. Shoou-Jinn Chang, Chun-Ta Yu, "GaN-Based Multiquantum Well Light-Emitting Diodes With Tunnel-Junction-Cascaded Active Regions," *IEEE Electron Device Lett.*, vol. 36, pp. 366-368, 2015.
- [289] A. T. M. G. Sarwar, B. J. May, J. I. Deitz, T. J. Grassman, D. W. McComb, and R. C. Myers, "Tunnel junction enhanced nanowire ultraviolet light emitting diodes," *Applied Physics Letters*, vol. 107, p. 101103, 2015.
- [290] C. Shoou-Jinn, L. Wei-Heng, and C. Wei-Shou, "Cascaded GaN Light-Emitting Diodes With Hybrid Tunnel Junction Layers," *IEEE J. Quant. Electron.*, vol. 51, pp. 1-5, 2015.
- [291] A. T. Connie, S. Zhao, S. M. Sadaf, I. Shih, Z. Mi, X. Du, *et al.*, "Optical and electrical properties of Mg-doped AlN nanowires grown by molecular beam epitaxy," *Applied Physics Letters*, vol. 106, p. 213105, 2015.
- [292] F. L. Bloom, A. C. Young, R. C. Myers, E. R. Brown, A. C. Gossard, and E. G. Gwinn, "Tunneling through MnAs particles at a GaAs p[⁺]n[⁺] junction," *J. Vac. Sci. Technol. B: Microelectronics and Nanometer Structures*, vol. 24, p. 1639, 2006.
- [293] J. M. O. Zide, A. Kleiman-Shwarsstein, N. C. Strandwitz, J. D. Zimmerman, T. Steenblock-Smith, A. C. Gossard, *et al.*, "Increased efficiency in multijunction solar cells through the incorporation of semimetallic ErAs nanoparticles into the tunnel junction," *Appl. Phys. Lett.*, vol. 88, p. 162103, 2006.
- [294] H. P. Nair, A. M. Crook, and S. R. Bank, "Enhanced conductivity of tunnel junctions employing semimetallic nanoparticles through variation in growth temperature and deposition," *Appl. Phys. Lett.*, vol. 96, p. 222104, 2010.
- [295] J. S. Foresi and T. D. Moustakas, "Metal contacts to gallium nitride," *Applied Physics Letters*, vol. 62, p. 2859, 1993.
- [296] J. S. Kwak, "Temperature-dependent contact resistivity of the nonalloyed ohmic contacts to p-GaN," *J. Appl. Phys.*, vol. 95, p. 5917, 2004.
- [297] W. Götz, N. M. Johnson, and D. P. Bour, "Deep level defects in Mg-doped, p-type GaN grown by metalorganic chemical vapor deposition," *Appl. Phys. Lett.*, vol. 68, p. 3470, 1996.
- [298] M. Smith, G. D. Chen, J. Y. Lin, H. X. Jiang, A. Salvador, B. N. Sverdlov, *et al.*, "Mechanisms of band-edge emission in Mg-doped p-type GaN," *Appl. Phys. Lett.*, vol. 68, p. 1883, 1996.
- [299] L. S. Yu, D. Qiao, L. Jia, S. S. Lau, Y. Qi, and K. M. Lau, "Study of Schottky barrier of Ni on p-GaN," *Appl. Phys. Lett.*, vol. 79, p. 4536, 2001.
- [300] L. J. L. S. Yu, D. Qiao, S. S. Lau, J. Li, J. Y. Lin, and H. X. Jiang, "The Origins of Leaky Characteristics of Schottky Diodes on p-GaN" *IEEE Trans. Electron. Devices*, vol. 50, 2003.
- [301] J.-K. Ho, C.-S. Jong, C. C. Chiu, C.-N. Huang, K.-K. Shih, L.-C. Chen, *et al.*, "Low-resistance ohmic contacts to p-type GaN achieved by the oxidation of Ni/Au films," *J. Appl. Phys.*, vol. 86, p. 4491, 1999.
- [302] J.-O. Song, W.-K. Hong, Y. Park, J. S. Kwak, and T.-Y. Seong, "Low-resistance Al-based reflectors for high-power GaN-based flip-chip light-emitting diodes," *Appl. Phys. Lett.*, vol. 86, p. 133503, 2005.

- [303] K.-P. Hsueh, K.-C. Chiang, Y.-M. Hsin, and C. J. Wang, "Investigation of Cr- and Al-based metals for the reflector and Ohmic contact on n-GaN in GaN flip-chip light-emitting diodes," *Appl. Phys. Lett.*, vol. 89, p. 191122, 2006.
- [304] H. P. Nguyen, M. Djavid, K. Cui, and Z. Mi, "Temperature-dependent nonradiative recombination processes in GaN-based nanowire white-light-emitting diodes on silicon," *Nanotechnology*, vol. 23, p. 194012, May 17 2012.
- [305] H. P. Nguyen, M. Djavid, S. Y. Woo, X. Liu, A. T. Connie, S. Sadaf, *et al.*, "Engineering the carrier dynamics of InGaN nanowire white light-emitting diodes by distributed p-AlGaN electron blocking layers," *Sci Rep*, vol. 5, p. 7744, Jan 16 2015.
- [306] A. G. Sarwar, S. D. Carnevale, F. Yang, T. F. Kent, J. J. Jamison, D. W. McComb, *et al.*, "Semiconductor Nanowire Light-Emitting Diodes Grown on Metal: A Direction Toward Large-Scale Fabrication of Nanowire Devices," *Small*, Aug 25 2015.
- [307] A. T. Connie, H. P. T. Nguyen, S. M. Sadaf, I. Shih, and Z. Mi, "Engineering the color rendering index of phosphor-free InGaN/(Al)GaN nanowire white light emitting diodes grown by molecular beam epitaxy," *J. Vac. Sci. Technol. B: Microelectronics and Nanometer Structures*, vol. 32, p. 02C113, 2014.
- [308] S. F. Zhang, A. T. Connie, D. A. Laleyan, H. P. T. Nguyen, Q. Wang, J. Song, *et al.*, "On the Carrier Injection Efficiency and Thermal Property of InGaN/GaN Axial Nanowire Light Emitting Diodes," *IEEE J. Quant. Electron.*, vol. 50, pp. 483-490, Jun 2014.
- [309] G.-D. Hao, M. Taniguchi, N. Tamari, and S.-i. Inoue, "Enhanced wall-plug efficiency in AlGaIn-based deep-ultraviolet light-emitting diodes with uniform current spreading-electrode structures," *J. Phys. D: Appl. Phys.*, vol. 49, p. 235101, 2016.
- [310] M. Shatalov, W. Sun, R. Jain, A. Lunev, X. Hu, A. Dobrinsky, *et al.*, "High power AlGaIn ultraviolet light emitters," *Semicond. Sci. Technol.*, vol. 29, p. 084007, 2014.
- [311] J. Close, J. Ip, and K. H. Lam, "Water recycling with PV-powered UV-LED disinfection," *Renewable Energy*, vol. 31, pp. 1657-1664, 2006.
- [312] M. A. Wurtele, T. Kolbe, M. Lipsz, A. Kulberg, M. Weyers, M. Kneissl, *et al.*, "Application of GaN-based ultraviolet-C light emitting diodes--UV LEDs--for water disinfection," *Water Res.*, vol. 45, pp. 1481-9, Jan 2011.
- [313] H. Hirayama, N. Maeda, S. Fujikawa, S. Toyoda, and N. Kamata, "Recent progress and future prospects of AlGaIn-based high-efficiency deep-ultraviolet light-emitting diodes," *Jpn. J. Appl. Phys.*, vol. 53, p. 100209, 2014.
- [314] H. Sun, J. Woodward, J. Yin, A. Moldawer, E. F. Pecora, A. Y. Nikiforov, *et al.*, "Development of AlGaIn-based graded-index-separate-confinement-heterostructure deep UV emitters by molecular beam epitaxy," *J. Vac. Sci. Technol. B: Microelectronics and Nanometer Structures*, vol. 31, p. 03C117, 2013.
- [315] M. Jo, N. Maeda, and H. Hirayama, "Enhanced light extraction in 260 nm light-emitting diode with a highly transparent p-AlGaIn layer," *Appl. Phys. Express*, vol. 9, p. 012102, 2016.
- [316] M. Shatalov, W. Sun, A. Lunev, X. Hu, A. Dobrinsky, Y. Bilenko, *et al.*, "AlGaIn Deep-Ultraviolet Light-Emitting Diodes with External Quantum Efficiency above 10%," *Appl. Phys. Express*, vol. 5, p. 082101, 2012.
- [317] M. Ichikawa, A. Fujioka, T. Kosugi, S. Endo, H. Sagawa, H. Tamaki, *et al.*, "High-output-power deep ultraviolet light-emitting diode assembly using direct bonding," *Appl. Phys. Express*, vol. 9, p. 072101, 2016.

- [318] A. Fujioka, T. Misaki, T. Murayama, Y. Narukawa, and T. Mukai, "Improvement in Output Power of 280-nm Deep Ultraviolet Light-Emitting Diode by Using AlGa_N Multi Quantum Wells," *Appl. Phys. Express*, vol. 3, p. 041001, 2010.
- [319] T. Mino, H. Hirayama, T. Takano, K. Tsubaki, and M. Sugiyama, "Realization of 256–278 nm AlGa_N-Based Deep-Ultraviolet Light-Emitting Diodes on Si Substrates Using Epitaxial Lateral Overgrowth AlN Templates," *Appl. Phys. Express*, vol. 4, p. 092104, 2011.
- [320] J. R. Grandusky, J. Chen, S. R. Gibb, M. C. Mendrick, C. G. Moe, L. Rodak, *et al.*, "270 nm Pseudomorphic Ultraviolet Light-Emitting Diodes with Over 60 mW Continuous Wave Output Power," *Appl. Phys. Express*, vol. 6, p. 032101, 2013.
- [321] T. Kinoshita, T. Obata, T. Nagashima, H. Yanagi, B. Moody, S. Mita, *et al.*, "Performance and Reliability of Deep-Ultraviolet Light-Emitting Diodes Fabricated on AlN Substrates Prepared by Hydride Vapor Phase Epitaxy," *Appl. Phys. Express*, vol. 6, p. 092103, 2013.
- [322] H. Hirayama, N. Noguchi, and N. Kamata, "222 nm Deep-Ultraviolet AlGa_N Quantum Well Light-Emitting Diode with Vertical Emission Properties," *Appl. Phys. Express*, vol. 3, p. 032102, 2010.
- [323] J.-I. Chyi, H. Fujioka, H. Morkoç, J. Rass, T. Kolbe, N. Lobo-Ploch, *et al.*, "High-power UV-B LEDs with long lifetime," *Proc. of SPIE*, vol. 9363, p. 93631K, 2015.
- [324] S. M. Islam, V. Protasenko, S. Rouvimov, H. Xing, and D. Jena, "Sub-230 nm deep-UV emission from GaN quantum disks in AlN grown by a modified Stranski–Krastanov mode," *Jpn. J. Appl. Phys.*, vol. 55, p. 05FF06, 2016.
- [325] S. Zhao, M. Djavid, and Z. Mi, "Surface Emitting, High Efficiency Near-Vacuum Ultraviolet Light Source with Aluminum Nitride Nanowires Monolithically Grown on Silicon," *Nano Lett.*, vol. 15, pp. 7006-9, Oct 14 2015.
- [326] S. Zhao, X. Liu, S. Y. Woo, J. Kang, G. A. Botton, and Z. Mi, "An electrically injected AlGa_N nanowire laser operating in the ultraviolet-C band," *Appl. Phys. Lett.*, vol. 107, p. 043101, 2015.
- [327] Y. Taniyasu, M. Kasu, and T. Makimoto, "An aluminium nitride light-emitting diode with a wavelength of 210 nanometres," *Nature*, vol. 441, pp. 325-8, May 18 2006.
- [328] S. D. Carnevale, T. F. Kent, P. J. Phillips, M. J. Mills, S. Rajan, and R. C. Myers, "Polarization-induced pn diodes in wide-band-gap nanowires with ultraviolet electroluminescence," *Nano Lett.*, vol. 12, pp. 915-20, Feb 8 2012.
- [329] S. D. Carnevale, T. F. Kent, P. J. Phillips, A. T. Sarwar, C. Selcu, R. F. Klie, *et al.*, "Mixed polarity in polarization-induced p-n junction nanowire light-emitting diodes," *Nano Lett.*, vol. 13, pp. 3029-35, Jul 10 2013.
- [330] J. Verma, S. M. Islam, V. Protasenko, P. Kumar Kandaswamy, H. Xing, and D. Jena, "Tunnel-injection quantum dot deep-ultraviolet light-emitting diodes with polarization-induced doping in III-nitride heterostructures," *Appl. Phys. Lett.*, vol. 104, p. 021105, 2014.
- [331] S. Zhao, H. P. T. Nguyen, M. G. Kibria, and Z. Mi, "III-Nitride nanowire optoelectronics," *Prog. Quant. Electron.*, vol. 44, pp. 14-68, 2015.
- [332] A. T. Sarwar, B. J. May, M. F. Chisholm, G. J. Duscher, and R. C. Myers, "Ultrathin GaN quantum disk nanowire LEDs with sub-250 nm electroluminescence," *Nanoscale*, Mar 29 2016.
- [333] T. F. Kent, S. D. Carnevale, and R. C. Myers, "Atomically sharp 318 nm Gd:AlGa_N ultraviolet light emitting diodes on Si with low threshold voltage," *Appl. Phys. Lett.*, vol. 102, p. 201114, 2013.

- [334] Z. Mi, S. Zhao, S. Y. Woo, M. Bugnet, M. Djavid, X. Liu, *et al.*, "Molecular beam epitaxial growth and characterization of Al(Ga)N nanowire deep ultraviolet light emitting diodes and lasers," *J. Phys. D: Appl. Phys.*, vol. 49, p. 364006, 2016.
- [335] Y. Liao, C. Thomidis, C.-k. Kao, and T. D. Moustakas, "AlGa_N based deep ultraviolet light emitting diodes with high internal quantum efficiency grown by molecular beam epitaxy," *Appl. Phys. Lett.*, vol. 98, p. 081110, 2011.
- [336] E. Matioli and C. Weisbuch, "Direct measurement of internal quantum efficiency in light emitting diodes under electrical injection," *J. Appl. Phys.*, vol. 109, p. 073114, 2011.
- [337] Q. Wang, A. T. Connie, H. P. Nguyen, M. G. Kibria, S. Zhao, S. Sharif, *et al.*, "Highly efficient, spectrally pure 340 nm ultraviolet emission from Al_xGa(1-x)N nanowire based light emitting diodes," *Nanotechnology*, vol. 24, p. 345201, Aug 30 2013.
- [338] K. Mayes, A. Yasan, R. McClintock, D. Shiell, S. R. Darvish, P. Kung, *et al.*, "High-power 280 nm AlGa_N light-emitting diodes based on an asymmetric single-quantum well," *Appl. Phys. Lett.*, vol. 84, p. 1046, 2004.
- [339] J. Yun, J.-I. Shim, and H. Hirayama, "Analysis of efficiency droop in 280-nm AlGa_N multiple-quantum-well light-emitting diodes based on carrier rate equation," *Appl. Phys. Express*, vol. 8, p. 022104, 2015.
- [340] X. Li, S. Sundaram, P. Disseix, G. Le Gac, S. Bouchoule, G. Patriarche, *et al.*, "AlGa_N-based MQWs grown on a thick relaxed AlGa_N buffer on AlN templates emitting at 285 nm," *Opt. Mat. Express*, vol. 5, p. 380, 2015.
- [341] H. Hirayama, N. Noguchi, T. Yatabe, and N. Kamata, "227 nm AlGa_N Light-Emitting Diode with 0.15 mW Output Power Realized using a Thin Quantum Well and AlN Buffer with Reduced Threading Dislocation Density," *Appl. Phys. Express*, vol. 1, p. 051101, 2008.
- [342] R. Vaxenburg, E. Lifshitz, and A. L. Efros, "Suppression of Auger-stimulated efficiency droop in nitride-based light emitting diodes," *Appl. Phys. Lett.*, vol. 102, p. 031120, 2013.
- [343] H. Hirayama, S. Fujikawa, N. Noguchi, J. Norimatsu, T. Takano, K. Tsubaki, *et al.*, "222-282 nm AlGa_N and InAlGa_N-based deep-UV LEDs fabricated on high-quality AlN on sapphire," *Physica Status Solidi A*, vol. 206, pp. 1176-1182, 2009.
- [344] Y. S. Jicai Zhang, Takashi Egawa, "Study on the Electron Overflow in 264 nm AlGa_N Light-Emitting Diodes," *IEEE J. Quant. Electron.*, vol. 46, pp. 1854-1859, 2010.
- [345] Q. Dai, Q. Shan, J. Wang, S. Chhajed, J. Cho, E. F. Schubert, *et al.*, "Carrier recombination mechanisms and efficiency droop in GaInN/GaN light-emitting diodes," *Appl. Phys. Lett.*, vol. 97, p. 133507, 2010.
- [346] J. W. Lee, D. Y. Kim, J. H. Park, E. F. Schubert, J. Kim, J. Lee, *et al.*, "An elegant route to overcome fundamentally-limited light extraction in AlGa_N deep-ultraviolet light-emitting diodes: Preferential outcoupling of strong in-plane emission," *Sci. Rep.*, vol. 6, p. 22537, Mar 03 2016.
- [347] A. Atsushi Yamaguchi, "Valence band engineering for remarkable enhancement of surface emission in AlGa_N deep-ultraviolet light emitting diodes," *Physica Status Solidi C*, vol. 5, pp. 2364-2366, 2008.
- [348] K. H. Li, Q. Wang, H. P. T. Nguyen, S. Zhao, and Z. Mi, "Polarization-resolved electroluminescence study of InGa_N/Ga_N dot-in-a-wire light-emitting diodes grown by molecular beam epitaxy," *Physica Status Solidi A*, vol. 212, pp. 941-946, 2015.

- [349] Y.-J. Lu, H.-W. Lin, H.-Y. Chen, Y.-C. Yang, and S. Gwo, "Single InGaN nanodisk light emitting diodes as full-color subwavelength light sources," *Appl. Phys. Lett.*, vol. 98, p. 233101, 2011.
- [350] M. Djavid and Z. Mi, "Enhancing the light extraction efficiency of AlGaIn deep ultraviolet light emitting diodes by using nanowire structures," *Appl. Phys. Lett.*, vol. 108, p. 051102, 2016.
- [351] K. B. a. T. K. Asif Khan, "Ultraviolet light-emitting diodes based on group three nitrides " *Nature Photonics* /, vol. 2, 2008.
- [352] Y. Muramoto, M. Kimura, and S. Nouda, "Development and future of ultraviolet light-emitting diodes: UV-LED will replace the UV lamp," *Semicond. Sci. Technol.*, vol. 29, p. 084004, 2014.
- [353] M. Knissel, J. Rass, "III-Nitride Ultraviolet Emitters " *Springer*, 2016.
- [354] M. S. Shur and R. Gaska, "Deep-Ultraviolet Light-Emitting Diodes," *IEEE Transactions on Electron Devices*, vol. 57, pp. 12-25, 2010.
- [355] K. A. Bertness, A. Roshko, N. A. Sanford, J. M. Barker, and A. V. Davydov, "Spontaneously grown GaN and AlGaIn nanowires," *J. Cryst. Growth*, vol. 287, pp. 522-527, 2006.
- [356] J. Su, M. Gherasimova, G. Cui, H. Tsukamoto, J. Han, T. Onuma, *et al.*, "Growth of AlGaIn nanowires by metalorganic chemical vapor deposition," *Appl. Phys. Lett.*, vol. 87, p. 183108, 2005.
- [357] M. J. Holmes, K. Choi, S. Kako, M. Arita, and Y. Arakawa, "Room-temperature triggered single photon emission from a III-nitride site-controlled nanowire quantum dot," *Nano Lett.*, vol. 14, pp. 982-6, Feb 12 2014.
- [358] J. Renard, R. Songmuang, G. Tourbot, C. Bougerol, B. Daudin, and B. Gayral, "Evidence for quantum-confined Stark effect in GaN/AlN quantum dots in nanowires," *Phys. Rev. B*, vol. 80, 2009.
- [359] A. Pierret, C. Bougerol, B. Gayral, M. Kociak, and B. Daudin, "Probing alloy composition gradient and nanometer-scale carrier localization in single AlGaIn nanowires by nanocathodoluminescence," *Nanotechnology*, vol. 24, p. 305703, Aug 02 2013.
- [360] J. Ristic, E. Calleja, A. Trampert, S. Fernandez-Garrido, C. Rivera, U. Jahn, *et al.*, "Columnar AlGaIn/GaN nanocavities with AlN/GaN Bragg reflectors grown by molecular beam epitaxy on Si(111)," *Phys. Rev. Lett.*, vol. 94, p. 146102, Apr 15 2005.
- [361] A. T. Sarwar, B. J. May, M. F. Chisholm, G. J. Duscher, and R. C. Myers, "Ultrathin GaN quantum disk nanowire LEDs with sub-250 nm electroluminescence," *Nanoscale*, vol. 8, pp. 8024-32, Apr 21 2016.
- [362] N. Grandjean, B. Damilano, S. Dalmaso, M. Leroux, M. Laügt, and J. Massies, "Built-in electric-field effects in wurtzite AlGaIn/GaN quantum wells," *J. Appl. Phys.*, vol. 86, pp. 3714-3720, 1999.
- [363] E. Kuokstis, C. Q. Chen, M. E. Gaevski, W. H. Sun, J. W. Yang, G. Simin, *et al.*, "Polarization effects in photoluminescence of C- and M-plane GaN/AlGaIn multiple quantum wells," *Appl. Phys. Lett.*, vol. 81, pp. 4130-4132, 2002.
- [364] S.-H. Park and S.-L. Chuang, "Spontaneous polarization effects in wurtzite GaN/AlGaIn quantum wells and comparison with experiment," *Appl. Phys. Lett.*, vol. 76, pp. 1981-1983, 2000.

- [365] J. E. Northrup, C. L. Chua, Z. Yang, T. Wunderer, M. Kneissl, N. M. Johnson, *et al.*, "Effect of strain and barrier composition on the polarization of light emission from AlGa_N/AlN quantum wells," *Appl. Phys. Lett.*, vol. 100, p. 021101, 2012.
- [366] Y.-C. Y. Hung-Ying Chen, Hon-Way Lin, Shih-Cheng Chang, and Shangjr Gwo, "Polarized photoluminescence from single GaN nanorods: Effects of optical confinement" *Opt. Express*, vol. 16, p. 13465, 2008.
- [367] W. Sun, M. Shatalov, J. Deng, X. Hu, J. Yang, A. Lunev, *et al.*, "Efficiency droop in 245–247 nm AlGa_N light-emitting diodes with continuous wave 2 mW output power," *Appl. Phys. Lett.*, vol. 96, p. 061102, 2010.
- [368] N. G. Toledo and U. K. Mishra, "InGa_N solar cell requirements for high-efficiency integrated III-nitride/non-III-nitride tandem photovoltaic devices," *J. Appl. Phys.*, vol. 111, p. 114505, 2012.
- [369] S. Liu, Q. Wang, H. Xiao, K. Wang, C. Wang, X. Wang, *et al.*, "Optimization of growth and fabrication techniques to enhance the InGa_N/Ga_N multiple quantum well solar cells performance," *Superlattices Microstruct.*, 2017.
- [370] F. Yu, D. Rümmler, J. Hartmann, L. Caccamo, T. Schimpke, M. Strassburg, *et al.*, "Vertical architecture for enhancement mode power transistors based on Ga_N nanowires," *Appl. Phys. Lett.*, vol. 108, p. 213503, 2016.
- [371] F. Yu, S. Yao, F. Romer, B. Witzigmann, T. Schimpke, M. Strassburg, *et al.*, "Ga_N nanowire arrays with nonpolar sidewalls for vertically integrated field-effect transistors," *Nanotechnology*, vol. 28, p. 095206, Mar 03 2017.
- [372] Online. https://www.tf.uni-kiel.de/matwis/amat/semi_en/kap_5/backbone/r5_1_2.html.